Year : 2023

The role of myeloid cells in the brain tumor microenvironment

Maas Roeltje

Maas Roeltje, 2023, The role of myeloid cells in the brain tumor microenvironment

Illustrations generated using BioRender

Originally published at : Thesis, University of Lausanne

Posted at the University of Lausanne Open Archive http://serval.unil.ch
Document URN : urn:nbn:ch:serval-BIB_343F3CD466446

UNIL | Université de Lausanne

Faculté de biologie
et de médecine

Département d'oncologie fondamentale

The role of myeloid cells in the brain tumor microenvironment

Thèse de doctorat ès sciences de la vie (PhD)

présentée à la

Faculté de biologie et de médecine
de l'Université de Lausanne

par

Roeltje MAAS

Médecin diplômé, l'Université de Radboud, Nijmegen, Les Pays-Bas

Jury

Prof. Johanna A. Joyce, Directrice de thèse
Prof. Caroline Pot, Présidente
Prof. Fabienne Tacchini-Cottier, Experte
Prof. Karin de Visser, Experte

Lausanne, 2023

UNIL | Université de Lausanne

Faculté de biologie
et de médecine

Département d'oncologie fondamentale

The role of myeloid cells in the brain tumor microenvironment

Thèse de doctorat ès sciences de la vie (PhD)

présentée à la

Faculté de biologie et de médecine
de l'Université de Lausanne

par

Roeltje MAAS

Médecin diplômé, l'Université de Radboud, Nijmegen, Les Pays-Bas

Jury

Prof. Johanna A. Joyce, Directrice de thèse
Prof. Caroline Pot, Présidente
Prof. Fabienne Tacchini-Cottier, Experte
Prof. Karin de Visser, Experte

Lausanne, 2023

UNIL | Université de Lausanne
Faculté de biologie
et de médecine

Ecole Doctorale
Doctorat ès sciences de la vie

Imprimatur

Vu le rapport présenté par le jury d'examen, composé de

Président·e	Madame	Prof.	Caroline	**Pot**
Directeur·trice de thèse	Madame	Prof.	Johanna A.	**Joyce**
Expert·e·s	Madame	Prof.	Fabienne	**Tacchini-Cottier**
	Madame	Prof.	Karin	**de Visser**

le Conseil de Faculté autorise l'impression de la thèse de

Roeltje Renée Maas

Master of Science in Medicine, Université de Radboud, Nijmegen, Pays-Bas

intitulée

The role of myeloid cells in the brain tumor microenvironment

Date de l'examen : 10 octobre 2022

Date d'émission de l'imprimatur : Lausanne, le 13 juin 2023

pour le Doyen
de la Faculté de biologie et de médecine

Prof. Niko GELDNER
Directeur de l'Ecole Doctorale

Table of Contents

1. Acknowledgements 4

2. Abstract 7

3. Resumé 9

4. Abbreviations 11

5. Introduction 12

5.1 The brain as a unique organ 12

5.2 Brain malignancies 14

5.2.1 The different types of brain malignancies 14

5.2.2 Clinical appearance and symptoms 15

5.2.3 Current treatment strategies and their prognosis 16

5.3 The brain tumor microenvironment 17

5.4 The myeloid cell compartment 21

5.4.1 Tumor-associated macrophages 21

5.4.2 Neutrophils and tumor-associated neutrophils 22

5.5 The lymphoid cell compartment 26

5.6 New therapeutic approaches 27

5.7 Aims of the thesis 30

6. Summary of results and contributions 31

7. Results 35

7.1 An integrated pipeline for comprehensive analysis of immune cells in human brain tumor clinical samples 35

7.2 Interrogation of the microenvironmental landscape in brain tumors reveals disease-specific alterations of immune cells 68

7.3 The local microenvironment drives activation of neutrophils in human brain tumors 104

7.3.1 Summary 105

7.3.2 Introduction 105

7.3.3 Results 107

7.3.4 Discussion 118

7.3.5 Acknowledgments 120

7.3.6 Author Contributions 121

7.3.7 Declaration of Interests 121

7.3.8 Methods 121

7.3.9 Figures 137

7.3.10 Supplementary figures 151

7.4 Phenotypic diversity of T-cells in primary and metastatic brain tumors revealed by multiomic interrogation 165

7.5 Immunogenomic analysis of human brain metastases reveals diverse immune landscapes across genetically distinct tumors 167

8. Discussion 168

8.1 An integrated pipeline to investigate human brain TIME.....169

8.2 The brain TIME composition and transcriptional alterations in MG and MDMs are driven by tumor subtype.....171

8.3 The human brain TIME stimulates an immunosuppressive and pro-angiogenic TAN phenotype.....173

9. References 181

1. Acknowledgements

This chapter is dedicated to all my teammates, whether you were with me on the field, coaching me behind the scenes or cheering me on from the bleachers. Without you I wouldn't have been able to finish my PhD!

First, I would like to thank all the **patients** and **healthy donors** that have donated tissue used in this thesis. Without the patients and the department of neurosurgery, oncology, and pathology who helped us get access to this clinical material, this research would not have been possible. In this regard I would in particular like to thank **Prof. Monika Hegi**, who put a lot of effort into building up and running the brain tumor biobank here at CHUV.

I would also like to thank my PhD advisor **Prof. Johanna Joyce** for your guidance and feedback throughout the PhD. Thank you so much for welcoming me into your lab – a stimulating research environment that allowed me to work together with so many inspiring people. Throughout my PhD you gave me your trust and the freedom to develop myself both personally and scientifically. You taught me many facets of science, set the bar high, pushed me to reach for the stars, and showed me how to ignore glass ceilings. In addition to Prof. Johanna Joyce, I would also like to thank my other committee members, **Prof. Fabienne Tacchini-Coti**er, **Prof. Caroline Pot** and **Prof. Karin de Visser**, for their scientific feedback and support during my PhD. It is a sad state of affairs that it is still noteworthy that I had a fully female thesis committee, but I like to look at it as a sign that equality is on its way even in academia.

This stimulating research environment wouldn't have been the same without all my lab mates. I would especially like to thank **Klara**, **Mara**, and **Nadine**, who have stood by me throughout this sometimes-difficult journey. I have learned so much from you, both scientifically and personally. I probably will not miss the late-night experiments, but I will miss all our good conversations. **Sabine** and **Johanna**, I would like to thank for having brought so much fresh energy to the work floor and for brightening my workdays. **Joanna** for being such a solid friend on whom I can always count, whether high on caffeine or sick from a vaccine. **Matteo** for your endless enthusiasm and for being there when it really mattered. **Anoek** for never letting me get lost and being my home beacon in the lab. **Florian** for teaching me my first steps

in R. **Damien** and **Elena**, interns in the lab, for all your inspiring questions. It was a delight to work with you all.

Big thanks to my friends and fellow PhD students **Davide**, **Vlad**, **Paola** and **Rui** with whom I shared the PhD journey. There were so many good moments of laughter, whether in the lab, on the ski slopes or paddleboarding/swimming/fishing for keys on the lake. Infinite thanks to **Paola** for carrying me through the roughest moments and making it okay to not be okay. For me, it made a night and day difference having you all with me on this journey.

Thanks also to the C.R.A.B.S. members, **Giulia**, **Victor**, **Rui**, **Bruno** and **Spencer**, swimming across lac Léman pushed me to my athletic height and kept me sane while trying to submit my PhD thesis. I loved every second of our race (at least looking back at it), the time spent in the water and on the boat trying to keep moral up.

Life outside of the lab was such a blast thanks to my Franco-Suisse family from Château 33. You've given me a home away from home, with coloc dinners, costume parties, beer brewing, game nights, ice hockey, and outdoor adventures. Thank you so much **Paul**, **Ece**, **John**, **Lucie**, **Clea and Julian**. I would like to specifically thank **Josephine**, **Pierre** and **Manu**, as you made it so easy to be myself around you. Chatting with you always gave a positive spin to my mood and lifted my spirit.

I cannot thank the Pumpernickeltjes members, **Alex**, **Enrico**, **Vivek**, and **Rhythima**, enough for being such welcoming and considerate people, except maybe when playing first-person shooter games. I'm extremely happy to call you my friends and look forward to sharing more adventures and dinners with you.

My friends **Linda**, **Geert**, **Jessica**, **Jon**, **Chrissy**, and **Friða**, for being the first to show me that science is fun, each in a different way, and that there is no shame in taking a long time to finish your PhD.

I would also like to thank my friends from back home and way back when, you all helped shape who I am. We don't see each other often, but it never feels as if you are far away. **Matt**, **Rikkie**, **Robin**, **Falco** and **Rene**, you know me through and through and I really cherish our moments together when we shift gears between intense in-depth conversations, slapstick, staredowns on the tatami or cozy motorcycle tours. Thank you, **Anouk**, **Yvette, Eline**, **Steef** and **Janna**, for having such a grounding effect on me and always putting a smile on my face!

An immense thank you to my family, who has been so supportive my entire life and so defining to who I am today. To my parents, **Chris** and **Dineke**, who were always there for me, gave me the impression that whatever I set my mind to, could become possible, and for stimulating me to look at the world as my playground. To **Chris**, for teaching me that every problem can be fixed by dissecting it to the smallest screw/component, for showing me that being humble is mostly a good character trait and that adding a bit of humor to the day makes all the difference! You (literally) provided me with a toolbox to face life and it hurts intensely not having you with us anymore. Luckily, all you taught me I'll keep applying to life on a daily, keeping you close. And the precious lesson we both learned from a very wise barbie, will never ever grow old, nor loose its truth: "Wij zijn vriendjes - Ik hou van jou".

To **Dineke** in particular, for showing me from a young age that being independent is not scary but empowering and who even when our world comes crashing down still manages to stay somehow positive and never loses faith in our abilities. To my big sis, **Rikkertje**, for paving the way for me, keeping me sharp, whether during karate battles or in real life, and for being my number one protector. We stood stronger when we were the four of us, but even with the three of us I'm confident we can somehow face it all. **Antoine** for being such a caring person and who is infinitely patient with my French, and **Nouk**, my little niece, for putting a smile on our faces even in times when that seems impossible. My homegirl and cousin **Marthe**, who helped me fight off so many demons both figuratively and literally in our grandma's basement.

I am especially grateful to **Fabs** with whom life is never dull and always full of laughter. You have the magical capacity to make life look lighter and brighter on both good and bad days. I am so thankful that we got to do this chapter of our lives from start till end together and I am very much looking forward to all the adventures yet to come, wherever they may take place!

Thank you!

Roeltje

2. Abstract

Malignant brain tumors are lethal cancers that can be classified into primary and metastatic disease. While primary brain tumors comprise of low- and high-grade gliomas, brain metastasis (BrM) can occur with any cancer type. Approximately 20% of cancer patients, and especially those with primary lung-, breast-cancer or melanomas are at a particularly high risk of developing BrMs. Standard of care therapy, especially for gliomas, has only improved modestly over the past decade. Novel therapeutic strategies are increasingly focused on evaluating immunotherapies; however, they are effective in only a subset of BrM patients and show virtually no response in glioma patients. A plausible hypothesis posits that the limited efficacy of immunotherapy is in part due to immunosuppressive traits of the brain tumor immune microenvironment (TIME).

In this thesis, we aimed to test this hypothesis by exploring the role of myeloid cells in the TIME in human gliomas, and BrMs. We developed an extensive framework of orthogonal methods to study the spatial, phenotypic, and transcriptional changes in different brain TIMEs, which we applied to two separate studies.

In the first study, we explored the brain TIME and found striking differences in its composition across distinct brain tissue types. While the TIME of low-grade gliomas predominantly contain microglia (MG), in high-grade gliomas and particularly BrMs there is a considerable influx of recruited immune cells (e.g., monocyte derived macrophages (MDMs), tumor-associated neutrophils (TANs), and T-cells). Furthermore, transcriptional analysis of MG and MDMs delineated both cell type- and disease-specific alterations.

In the second study, we focused on TANs, and revealed an immunosuppressive and pro-angiogenic phenotype, combined with a prolonged survival for both glioma and BrM TANs. Transcriptionally, inflammatory tumor type-specific alterations were also uncovered, which were most pronounced in BrMs. Induction of the TAN phenotype was predominantly orchestrated by TNF-a produced by MG and MDMs.

Together these studies revealed that the myeloid niche contributes to an immunosuppressive brain TIME, which could explain the limited response of brain tumors to immunotherapies to date. Furthermore, we identified several potential

therapeutic targets that may render the brain TIME less immunosuppressive, which will be important to evaluate in future studies.

3. Resumé

Les tumeurs cérébrales malignes sont des cancers mortels qui peuvent être classés en maladies primaires et métastatiques. Les tumeurs cérébrales primaires comprennent les gliomes de bas et haut grade. Les métastases cérébrales (BrM) peuvent survenir avec tous types de cancer. Environ 20 % des patients avec un cancer, et en particulier ceux qui ont un cancer primaire du poumon, du sein ou un mélanome, présentent un risque élevé de développer des BrM. Le traitement ne s'est que modestement amélioré au cours de la dernière décennie, en particulier pour les gliomes. Les nouveaux traitements d'immunothérapie ne sont efficaces que chez une fraction des patients avec des BrMs et ne montrent pratiquement aucune réponse dans les gliomes. L'efficacité limitée de l'immunothérapie est potentiellement liée aux caractéristiques immunosuppressives du microenvironnement immunitaire des tumeurs (TIME) cérébrales.

Dans cette thèse, nous avons testé cette hypothèse en explorant le rôle des cellules myéloïdes dans le TIME des gliomes et BrMs humains. Nous avons développé un pipeline de méthodes orthogonales pour étudier les changements spatiaux, phénotypiques et transcriptionnels dans les différents TIME du cerveau, que nous avons appliqué à deux études distinctes.

Dans la première étude, nous avons exploré le TIME et constaté des différences frappantes dans sa composition entre les différentes tumeurs cérébrales. Alors que le TIME des gliomes de bas grade contient principalement de la microglie (MG), dans les gliomes de haut grade et en particulier dans les BrMs, il y a un afflux considérable de cellules immunitaires recrutées (macrophages dérivés des monocytes (MDMs), neutrophiles associés à la tumeur (TANs), et cellules T). En outre, l'analyse transcriptionnelle des MDMs et MG a mis en évidence des altérations spécifiques au type de cellule et à la maladie.

Dans la deuxième étude, nous avons révélé que les TANs ont un phénotype plus immunosuppresseur et pro-angiogénique, associé à leur survie prolongée dans la tumeur. Nous avons également découvert des altérations transcriptionnelles pro-inflammatoires dans les TANs, particulièrement prononcées dans les BrMs.

L'induction du phénotype TAN semble principalement orchestrée par le TNF-a produit par les MDMs et MG.

L'ensemble de ces études a révélé que la niche myéloïde contribue à un TIME cérébral immunosuppresseur, ce qui pourrait expliquer la réponse limitée des tumeurs cérébrales à l’immunothérapie. De plus, nous avons identifié plusieurs cibles thérapeutiques potentielles pour rendre le TIME cérébral moins immunosuppresseur, ce qu'il sera important d'évaluer dans des études futures.

4. Abbreviations

APC = Antigen-presenting cell
Arg1 = Arginase 1
BBB = Blood-brain barrier
BrM = Brain metastasis
CAR = Chimeric antigen receptor
CM = Conditioned media
CNS = Central nervous system
CSF-1R = Colony stimulating factor-1 receptor
CTLA-4 = Cytotoxic T-lymphocyte-associated protein 4
CyTOF = Mass cytometry by time-of-flight
DC = Dendritic cell
FAC-sorting = Fluorescence activated cell sorting
FCM = Flow cytometry
G-CSF = Granulocyte-colony stimulating factor
GBM = Glioblastoma
GM-CSF = Granulocyte macrophage-colony stimulating factor
HBMEC = Human brain microvascular endothelial cell
ICB = Immune-checkpoint blockade
IDH = Isocitrate hydrogenase 1 and 2
IF = Immunofluorescence
MDM = Monocyte-derived macrophage
MDSC = Myeloid-derived suppressor cell
MEC = Microenvironmental culture
MG = Microglia
MGMT = O6-methylguanine-methyltransferase
MHC = Major histocompatibility complex
MMP = metalloprotease
MPO = Myeloperoxidase
Mut = Mutant
NE = Neutrophil elastase
NET = Neutrophil extracellular traps
NLR = Neutrophil to lymphocyte ratio
PBN = Peripheral blood neutrophil
PD-1 = Programmed cell death receptor 1
PD-L1 = Programmed death ligand 1
ROS = Reactive oxygen species
RNAseq = RNA sequencing
scRNAseq = Single cell RNA sequencing
TAM = Tumor-associated macrophage
TAN = Tumor-associated neutrophil
TCR = T-cell receptor
TIME = Tumor immune microenvironment
TME = Tumor microenvironment
Treg = $CD4^+$ regulatory T-cells
VEGF = Vascular endothelial growth factor
WES = Whole exome sequencing
Wt = Wild-type

5. Introduction

5.1 The brain as a unique organ

For every step we take, for every word we speak and for every thought we shape, our central nervous system (CNS) plays a crucial role. The CNS comprises the brain and the spinal cord. While the spinal cord serves as a highway passing information rapidly between the brain on one end and the peripheral nervous system on the other, the brain has a much more complex function (1). The brain processes all sensory information it receives from the periphery and organizes and initiates locomotion and speech. In our brain our personality is also hardwired, as well as our emotions and our memory. In other words, we are our brain.

The distinct functions of the brain are assigned to different anatomic regions. Firstly, the brain can be divided into the cerebellum ("small brain") and the cerebrum ("large brain"). In the highly neuronal cerebellum, coordination of movements is organized (1). In the cerebrum, all other neurological functions are scattered over several lobes: the frontal, parietal, temporal, and occipital lobe (1). In brief, the frontal lobe is associated with emotional regulation, and contains the primary motor cortex, which is responsible for all voluntary movements (1). The parietal lobe is associated with the processing of sensory input such as touch. In the temporal lobe auditive information, speech, as well as memories are localized (1). The visual processing takes place in the occipital lobe (1). These four lobes are found within the two hemispheres that make up the cerebrum and when it comes to sensory-motor functions the left and right side of the body are directed by the opposite hemisphere (1). The left hemisphere is additionally more dominant in language, logic, and math abilities, whereas the right hemisphere is associated with creativity and intuition (1). As the brain has these distinct anatomic regions linked to functionality, localized dysfunction of the brain can present with a large range of different symptoms. This is further amplified by the limited plasticity of the brain in adults, which rapidly leads to permanent loss of function (2).

The CNS is built up of a tight-knit network of neuronal cells executing different brain functions (1). These neurons receive signals via their dendritic synapses, and with

their long protruding and branching axons they can rapidly transmit these electric signals over a long distance to other neurons (1). Neurons are supported by a plethora of glial cells, which can be divided in oligodendrocytes, astrocytes and microglia (MG) (3). Oligodendrocytes produce myelin sheaths around neuronal axons, increasing the impulse conduction speed (3). Astrocytes are a major support for neuronal cells metabolically (4, 5) and regulate neuronal function amongst others by modulating the signal intensity of neurotransmitters in the axonal synapse (6). Lastly, MG aid the other glial cells in remodeling the neuronal network and the brain vasculature (3, 7). In the adult brain, MG patrol the CNS to quickly act on inflammation and tissue damage by phagocytosing apoptotic cells and debris (7).

Given the importance of the brain for our being and functioning, it is crucial to protect this organ from any possibly hostile foreign influences. Throughout the body, the interface between circulating blood and tissue is made up of a monolayer of endothelial cells attached to the basal lamina, a layer of extracellular matrix secreted by the endothelial cells themselves (8). In the brain, however, the vascular wall has additional reinforcement and tight junctions to increase the regulation of components passing through (9). This blood-brain barrier (BBB) is built of specialized human brain microvascular endothelial cells (HBMECs), which have more tight junctions with their neighboring cells. As elsewhere in the body, endothelial cells in the brain are connected to the basal lamina; however the brain basal lamina is produced by pericytes and astrocytes in addition to HBMECs (9). Pericytes and astrocyte endfeet make up the abluminal side of the BBB, increasing the selective permeability of the BBB (9).

The tightly regulated permeability of the BBB reduces the chance of pathogens, circulating tumor cells, or potentially toxic factors to enter the brain (10). At the same time the brain is consequently also an organ that is challenging for circulating immune cells to access in case of an infection or tumor development. Moreover, once brain disease occurs this organ is complex to treat as most therapeutics do not pass through the BBB very efficiently (11). Until recently the brain was thought to be an immune privileged organ (12), however through the brain's meningeal lymphatics system it is

in contact with the peripheral immune system. Lymphatic vessels were found in the dura mater, the outer layer of the meninges which separate the skull from the brain (13). Through these vessels, brain-derived soluble waste is transported to the deep cervical lymph nodes, where they come into contact with the peripheral immune system (14). The lymphatic system has been implicated in several neuro-inflammatory diseases as well as brain tumors (15, 16).

5.2 Brain malignancies

In healthy well-functioning tissue, an optimal homeostasis between cell division and cell death must take place. On the cellular level, several mechanisms exist to control cell division and maintain this delicate balance. Via cell cycle checkpoints, errors in DNA replication can be identified and cells subsequently forced into senescence or apoptosis (17). In cancer cells, however, proliferative signaling is one of their key hallmarks (18). Due to an accumulation of mutations in exactly those pathways associated with cell cycle checkpoints, cancer cells no longer undergo senescence and apoptosis and rather continue proliferating (17). These cells, if not recognized and eradicated by the immune system, will continue to multiply, and form a tumor mass. This process can occur in any organ and is unfortunately also not an uncommon occurrence in the brain.

5.2.1 The different types of brain malignancies

Primary brain tumors are newly diagnosed in 24 per 100.000 people each year (19). They can be divided into different subtypes based on histology, genetics, epigenetics, and molecular diagnostics (Fig. 1). This classification is continuously updated based on the latest research findings (20). Approximately one-third of brain tumors are malignant, and of those the vast majority are gliomas (~80%) (19). Gliomas are tumors that originate from either astrocytes or oligodendrocytes, which leads to several subtypes of gliomas with varying severity grade. Gliomas can be broadly divided into two groups based on the occurrence of isocitrate dehydrogenase 1 and 2 (*IDH*) mutation (20). *IDH* mutant (mut) gliomas are generally low-grade gliomas (grade 1-3), associated with astrocytomas (originating from astrocytes) and oligodendrogliomas (originating from oligodendrocytes) (20). The latter can be

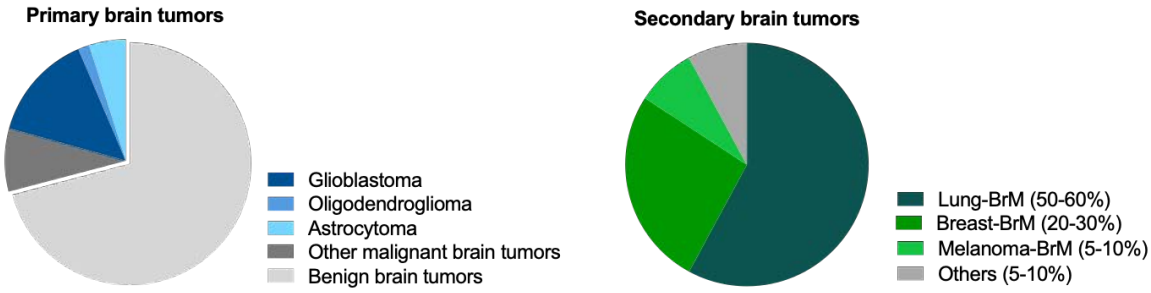

Tumor type	Tumor subtype	Grade	Genetic alterations	Clinically relevant markers/mutations	Mean survival (months)
Glioma	Astrocytoma	1-3	*IDH* mut		20-59
	Oligodendroglioma	1-3	*IDH* mut, 1p/19q co-deletion		199
	Glioblastoma	4	*IDH* wt	*MGMT* methylation	8
BrM	Lung-BrM	4	-	*EGFR, ALK*	4-10
	Breast-BrM	4	-	*HER2*	10
	Melanoma-BrM	4	-	*BRAF*-V600E	6

***Figure 1: Classification of brain malignancies**. Approximately 20% of primary brain tumors, and 80% of malignant primary brain tumors, are gliomas. BrMs mostly originate from lung, breast and melanoma primary tumors (21). The table shows the classification of brain tumors with their genetic alterations used for diagnostics, clinically relevant markers, and mean survival (19, 20, 22-24).*

identified by an additional 1p/19q co-deletion (Fig. 1). *IDH* wild-type (wt) gliomas are predominantly high grade (grade 4) glioblastomas (GBMs), and tumor cells are from the astrocyte lineage (20) (Fig. 1).

More common, however, is the occurrence of brain metastasis (BrMs), as an estimated 20% of cancer patients develop metastatic lesions in the brain (25, 26). The primary tumor types that are most prone to metastasize to the brain are melanoma (10%-73% of patients) lung (30%-58% of patients), and breast cancer (18%-30% of patients) (22, 25, 27, 28) (Fig.1).

5.2.2 Clinical appearance and symptoms

The clinical manifestation of brain tumors can present with both generalized and/or focal symptoms. Symptoms include headaches, seizures, cognitive dysfunction, and focal deficits (29). Epileptic seizures occur in >50% of glioma patients (30), whereas

BrM patients are only affected by seizures in 15% of cases (31). Cognitive dysfunction can present itself as memory loss or changes in personality and may be subtle. Focal deficits can range from muscular weakness, sensory loss, aphasia (loss of comprehension of speech or capacity to speak), and visual-spatial dysfunction and is highly dependent on the anatomic location of the tumor (32). The majority of gliomas are solitary lesions, which are distributed across the frontal (40%), temporal (29%), parietal (14%), and occipital lobes (3%), with only 14% located in the deeper brain structures (33). BrMs are often located close to the cortex and are multifocal in 85% of patients (34). The development of symptoms usually progresses more rapidly in GBMs and BrMs compared to low-grade gliomas, as tumor growth is more aggressive (34, 35).

5.2.3 Current treatment strategies and their prognosis

The optimal treatment of primary brain tumors requires tissue diagnosis by a pathologist. Therefore, it is common to start upfront with either a stereotactic biopsy or surgical tumor resection, which is followed by radiotherapy of the tumor bed for gliomas (36). Patients with grade 2 astrocytoma or oligodendroglioma generally receive a combination of alkylating chemotherapies (lomustine, procarbazine and vincristine) that pass the BBB (36). Upon recurrence of the tumor after resection, patients' chemotherapeutic treatment regimen will be changed to Temozolomide. With this treatment patients can survive 2-16 years (19), and currently there is no curative treatment available. Patients with a grade 3 astrocytoma or GBM have a much grimmer prognosis. They immediately receive Temozolomide post-surgical resection (36), regardless of the methylation status of the O^6-methylguanine-methyltransferase (MGMT) promoter. However, patients with an unmethylated MGMT promotor status rarely respond to Temozolomide (37). Given the aggressiveness of GBMs, the mean survival is only 8 months (19). Moreover, the standard of care treatment for GBMs has not improved since it was first introduced in 2009 by investigators at the CHUV Lausanne (38), regardless of extensive efforts in both the scientific and clinical fields.

BrMs are often detected at or after diagnosis of a primary tumor (28), hence resection of the BrM is rarely required for diagnostic purposes. Local therapy to control

BrM growth is delivered in the form of either surgical resection or stereotactic radiosurgery (23). Adjuvant targeted therapy has shown some survival benefits in the case of specific mutations such as *EGFR* or *ALK* mutations in lung-BrM, HER2+ breast-BrM and *BRAF*-V600E mut melanoma-BrM (Fig. 1) (23, 24). Unfortunately, none of the targeted therapies to date achieve complete response in the brain. Survival of patients with BrMs is extremely poor with a median survival of 5 months (22). However, survival is highly dependent on the primary tumor type and the mutational landscape of the BrMs and therefore falls within a range of 2-10 months when stratified by primary tumor type (Fig. 1) (22).

The poor survival of patients with high-grade gliomas and BrMs is evidently linked to the mediocre efficacy of the treatment options currently available. Compared to extra-cranial tumors, the treatment efficacy in intra-cranial tumors is lagging. This is predominantly due to our poor understanding of the interplay between these brain malignancies and the non-tumoral cells in their environment, which together shape the tumor microenvironment (TME). Hence it is crucial for further improvement of survival as well as quality of life of patients to study the brain TME in more detail.

5.3 The brain tumor microenvironment

Our efforts to understand cancer started by focusing on the tumor cells themselves. Cancer was predominantly perceived as a disease where cells lose the communication with their surroundings and keep proliferating. This is also depicted in the first version of “The Hallmarks of Cancer” (39), where acquired capabilities of cancer cells such as self-sufficiency in growth signals, insensitivity to anti-growth signals, limitless replicative potential and evading apoptosis were highlighted. As tumors were additionally shown to stimulate angiogenesis to adapt to their increased nutritional needs, an image can be envisaged of tumor cells that are completely self-sufficient and functioning independently from their tissue microenvironment. However, we now appreciate that cancer is a much more complex disease, and tumor cells are, unlike initially thought, highly dependent on the non-malignant cells in the TME (40). This was also underlined in the consecutive Hallmarks of Cancer (18, 41), where non-

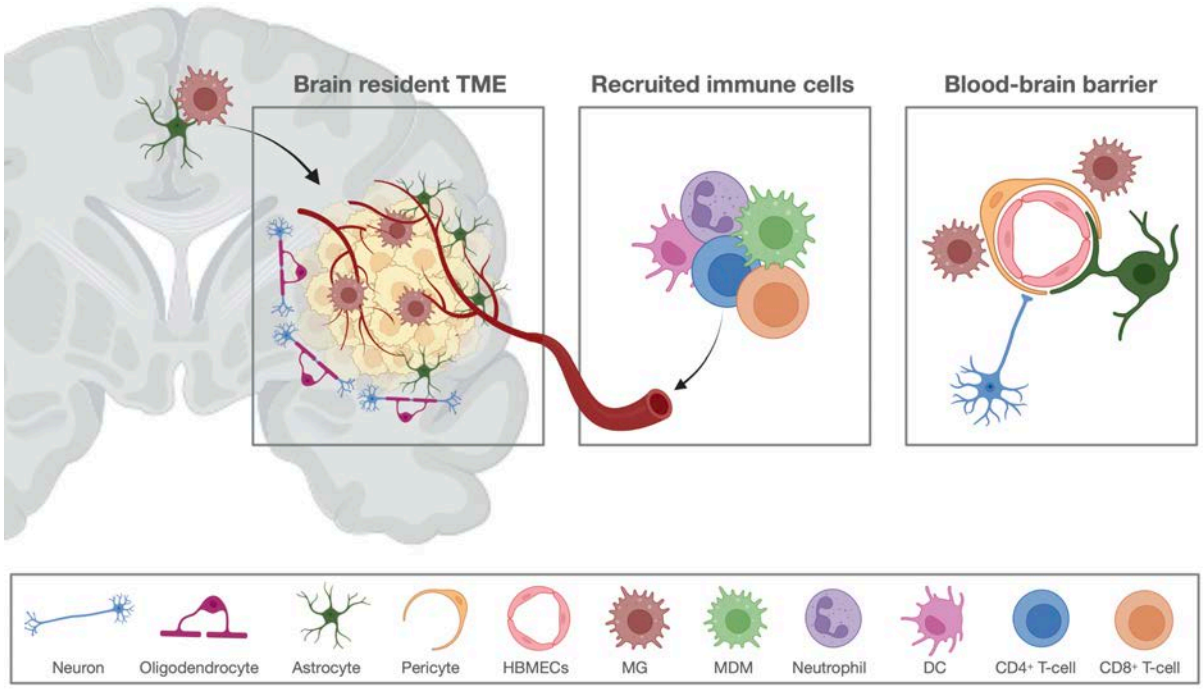

Figure 2: The brain tumor microenvironment (TME). *The TME of brain tumors consists of both brain-resident cells (e.g., neurons, oligodendrocytes, astrocytes, pericytes, HBMECs, and MG) and recruited immune cells (e.g., neutrophils, MDMs, DCs, $CD4^+$, and $CD8^+$ T-cells). Immune cell recruitment from the periphery is hampered by the blood-brain barrier (BBB). Adapted from (42) and created with BioRender.*

malignant TME cells were described as crucial for the support of cancer growth and the evasion from the immune system.

The brain TME consists of all brain resident cells (e.g., neurons, oligodendrocytes, astrocytes, microglia, HBMECs and pericytes), the tumor cells, and immune cells recruited from the circulation (42, 43) (Fig. 2). A developing brain tumor can increase the permeability of the BBB, through disruption of the pericyte and astrocyte endfeet distribution along the vascular wall (44, 45) and by the production of pro-angiogenic molecules such as vascular endothelial growth factors (VEGF) (9). The BBB in tumors is hence more porous, which allows peripheral immune cells to enter the brain and further add to the composition and complexity of the brain TME.

The tumor immune microenvironment (TIME) can be broadly divided into myeloid and lymphoid cell compartments (46). The myeloid compartment is a crucial pillar of the innate immune system, which is responsible for mounting a rapid response

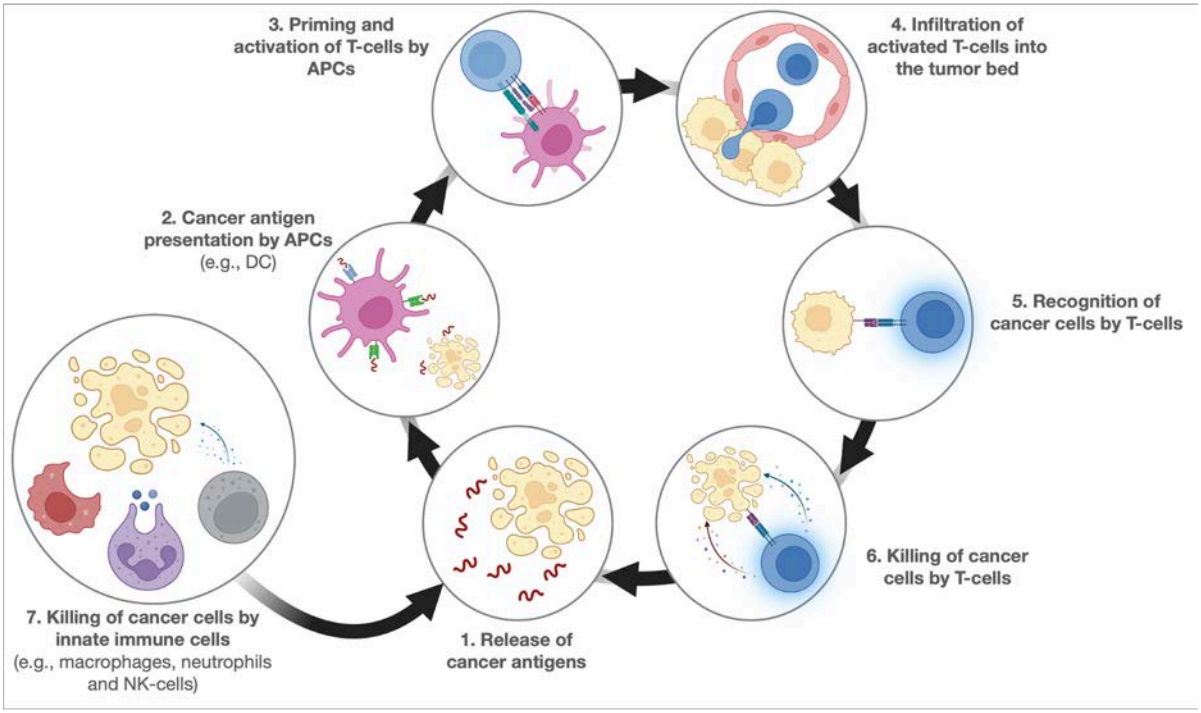

Figure 3: The cancer immunity cycle. *The cycle can be divided in several different steps and starts with [1] the release of cancer specific antigens. [2] These antigens are presented by antigen-presenting cells (APCs) [3] to naïve T-cells. They get primed for the cancer antigens and will [4] enter the tumor and [5] recognize tumor cells expressing this antigen. Next, [6] they will kill the tumor cell, which releases more tumor antigen and the cycle restarts. [7] Cells from the innate immune system (e.g., macrophages, neutrophils, and NK-cells) can also directly kill tumor cells and help release cancer antigens. Adapted from (47) and created with BioRender.*

against infectious agents (48). Cells of the innate immune system include macrophages, dendritic cells (DCs), neutrophils and other granulocytes from the myeloid compartment, as well as NK-cells from the lymphoid compartment (48). They scavenge the body for molecular alterations in cells and pathogens, indicative of an infection or signs of apoptosis. These cells then launch an effector response and destroy the affected cell by either phagocytosis or excretion of cytotoxic particles (48). Additionally, several innate immune cells (macrophages and DCs) are antigen-presenting cells (APCs), which present antigens from the phagocytosed cells on their surface and prime the adaptive immune system to recognize these specific antigens (47). The adaptive immune system consists of B- and T-cells from the lymphoid compartment (48). These cells are specialized in recognizing and eliminating very specific pathogens and cells based on the antigens that they present (48). As the adaptive immune system builds up a memory, future encounters with the same

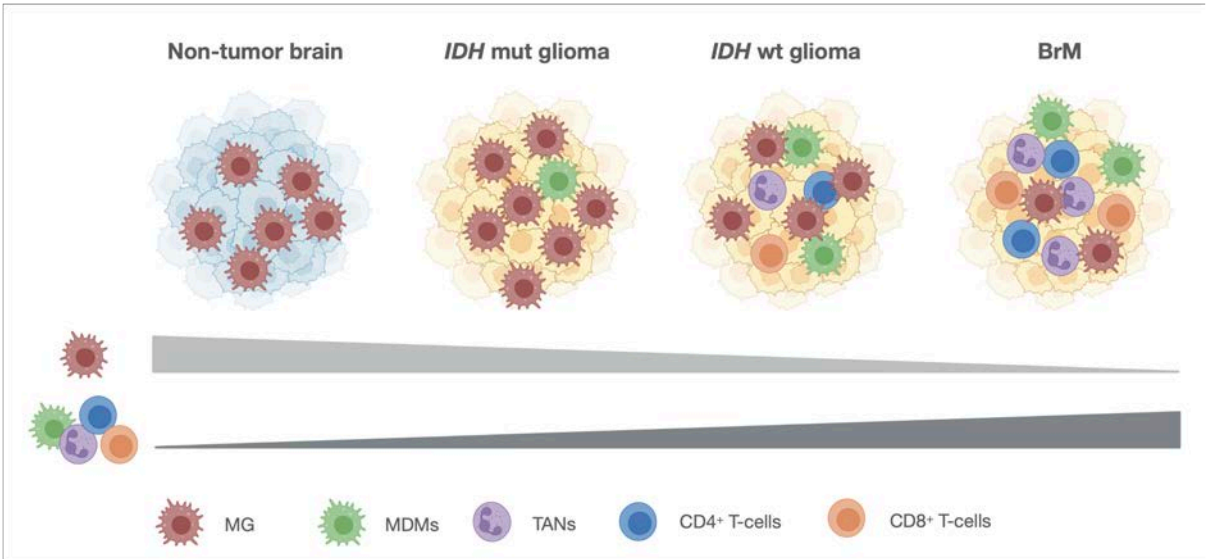

Figure 4: The tumor immune microenvironment (TIME) in different brain tissues*. In non-tumor brain and IDH mut glioma predominantly MG are present, while in IDH wt glioma and BrMs there is a large proportion of immune cells recruited from the periphery. Created with BioRender, based on results from (Chapter 7.2 and (49, 50)).*

pathogen or cell type generate a faster and more efficient response (48). The interplay between the innate and adaptive immune system is crucial for an effective immune response against pathogens but also cancer cells (Fig. 3). Since cancer cells present tumor-specific antigens on their cell surface, they can be recognized by the adaptive immune system and eradicated, however this does require an effective priming of T-cells by a well-functioning innate immune system (47, 51).

To understand how to engage the immune system in eradicating brain tumors it is thus crucial to first interrogate the composition and functions of the TIME. Depending on the brain tumor type the TIME changes drastically (Chapter 7.2 and (49, 50)) (Fig. 4). In non-tumor brain and *IDH* mut gliomas, MG are the predominant immune cells in the TIME, with only a very minor recruitment of peripheral immune cells such as monocyte-derived macrophages (MDMs), tumor-associated neutrophils (TANs) or T-cells (Chapter 7.2 and (49, 50)). In *IDH* wt GBMs, however, there is a very diverse TIME with a large influx of both MDMs and TANs, and even few T-cells can be found (Chapter 7.2 and (49, 50)). In BrMs, the recruitment of immune cells from the periphery is further increased, especially regarding TANs and T-cells (Chapter 7.2 and (49, 50)). These alterations in the TIME between the different brain tumor entities are crucial to

understand the potential interactions that cancer cells have with their environment and how the TIME can be used to our advantage when aiming to treat brain malignancies more efficiently. This requires us to better understand the roles of the individual cell types present in their tumor-specific context.

5.4 The myeloid cell compartment

In healthy brain, gliomas, and BrMs the myeloid cell compartment, predominantly composed of MG, MDMs, and neutrophils, represents 60-95% of the immune cell landscape (49, 50). Given their high abundance in these tissues, they potentially play a crucial role in tumor growth and development. Although all three cell populations are derived from the myeloid lineage, MG are derived from the yolk sac and migrate to the brain during early development (52), whereas MDMs and neutrophils differentiate from hematopoietic stem cells in the bone marrow. More importantly, they serve very distinct functions in both health and disease.

5.4.1 Tumor-associated macrophages

Under homeostatic conditions the brain contains virtually only tissue-specific long-living resident macrophages, i.e., MG. In brain cancers, MG can be actively recruited to the tumor site and expand further via *in situ* proliferation (53-55). During tumor formation, this pool of resident macrophages is complemented by MDMs recruited from the periphery. Until recently it was not possible to distinguish the two ontogenically distinct phagocytic tumor-associated macrophage (TAM) populations in the human brain, as robust markers in both mouse and human were lacking. Under homeostatic conditions it was established that P2Y12, TMEM119, CX3CR1 are specifically expressed in murine MG and not in MDMs (56, 57), however in the context of cancer the adaptation of MDMs to the brain TME increases the expression levels of ‘MG-specific’ genes such as *CX3CR1* (58). And even MG-specific gene expression is altered upon activation in the context of neuroinflammatory (59, 60) and oncogenic disease (61). Recently, thanks to the use of genetic lineage-tracing mouse models, the MDM specific marker CD49D/*ITGA4* was identified in a cancer context (gliomas and BrMs) and consequently validated in human samples (58). Using this cell surface

marker, the field now has a method to investigate the phenotype, functional roles, and transcriptional alterations in MG and MDMs separately.

Considering that this effective distinction within the brain TAM compartment is a relatively recent development, most literature investigated the functional roles of TAMs as one entity. TAMs across multiple cancers were historically categorized using a binary M1/M2 classification, where the M1-like TAM is considered pro-inflammatory and anti-tumorigenic and the M2-like TAM pro-tumorigenic. However, this dichotomous categorization has since been much debated, and we now consider the TAM spectrum to be much more complex, diverse, and plastic (62, 63). Nonetheless, in both murine gliomas and BrMs, TAMs are generally considered to support tumor development and growth (64-68) by generating an immunosuppressive environment (53, 69-71) and pro-angiogenic niche (72, 73). Consequently, increased infiltration of tumors with TAMs is also correlated with poor survival in the majority of cancers (63) , including gliomas (73). Studies investigating the difference of MG and MDMs in the human brain TME are few and report that the tumor type (glioma vs. BrM) shapes the differentiation of both types of macrophages distinctly (Chapter 7.2 and (49, 50)). However, the functional interactions of MG and MDMs with the human brain TME has not been studied to this end and is clearly of importance to further our understanding of their contribution to tumor growth and novel therapeutic targets.

5.4.2 Neutrophils and tumor-associated neutrophils

In humans, neutrophils are the most abundant circulating immune cell. Approximately 50-70% of all blood leukocytes are peripheral blood neutrophils (PBNs) (74). They are produced in vast quantities in the bone marrow (> 10^{11} per day) as the lifespan of circulating neutrophils is limited (half-life ~ 7 hours in mice) (74, 75). While it has been challenging to accurately assess their lifespan in humans (76-78), a recent study shed light on the fact that neutrophils in different mouse organs exhibit a different half-life than in blood under homeostatic conditions (79). Neutrophils' short lifespan is also one reason why they have been largely overlooked with regards to tumorigenesis. Only in recent years has the contribution of neutrophils to cancer been under active investigation and the neutrophil to lymphocyte ratio (NLR) has been linked to poor

prognoses in many cancers including BrMs and gliomas (80-83). In mouse models, tumor cells are able to stimulate the release of neutrophils from the bone marrow via the production of granulocyte-colony stimulating factor (G-CSF) (84-86) or granulocyte macrophage-colony stimulating factor (GM-CSF) (87-89), and actively recruit them to the tumor site (90-92), and in the brain specifically via G-CSF (93) (Fig. 5). Furthermore, G-CSF induced an immunosuppressive phenotype in TANs (85). Fortunately, considering the potential for unwanted side-effects, systemic G-CSF administration, a treatment against neutropenia, did not increase the risk of BrMs in *de novo* stage IV breast cancer patients (94).

Given their short lifespan, neutrophils are extremely fast-acting cells, and highly sensitive to alterations in their environment (95) They have distinct granules, containing cytotoxic and antimicrobial factors, metalloproteases (MMPs), myeloperoxidase (MPO), arginase 1 (Arg1) and neutrophil elastase (NE), which can be released to the extracellular space through exocytosis (95). Via excretion of these factors, neutrophils can execute their most important effector function, eradicating bacterial intruders and supporting the wound healing process (96, 97). However, several excreted factors have also been linked to aiding tumor development and the formation of metastasis. For example, NE was shown to stimulate tumor cell proliferation (98). MMP9 and NE share the capacity to stimulate the formation of metastasis by breaking down the vascular basal lamina and thereby facilitating the extravasation of tumor cells (95, 99) (Fig. 5). MMP9 additionally stimulates angiogenesis in cancers (100) (Fig. 5). Moreover, once tumor cells are in the circulation, neutrophils can protect them from elimination by the immune system (101) (Fig. 5).

In addition to exocytosis, neutrophils can also excrete granular content by the formation of neutrophil extracellular traps (NETs) (102). NETosis is a unique form of programmed cell death, characterized by the expulsion of extracellular DNA fibers coated with granular proteins such as MPO and NE (102). NETs can capture and kill foreign microbes, but in mouse cancer models they were additionally shown to trap circulating tumor cells and support the formation of metastasis (103-107) (Fig. 5).

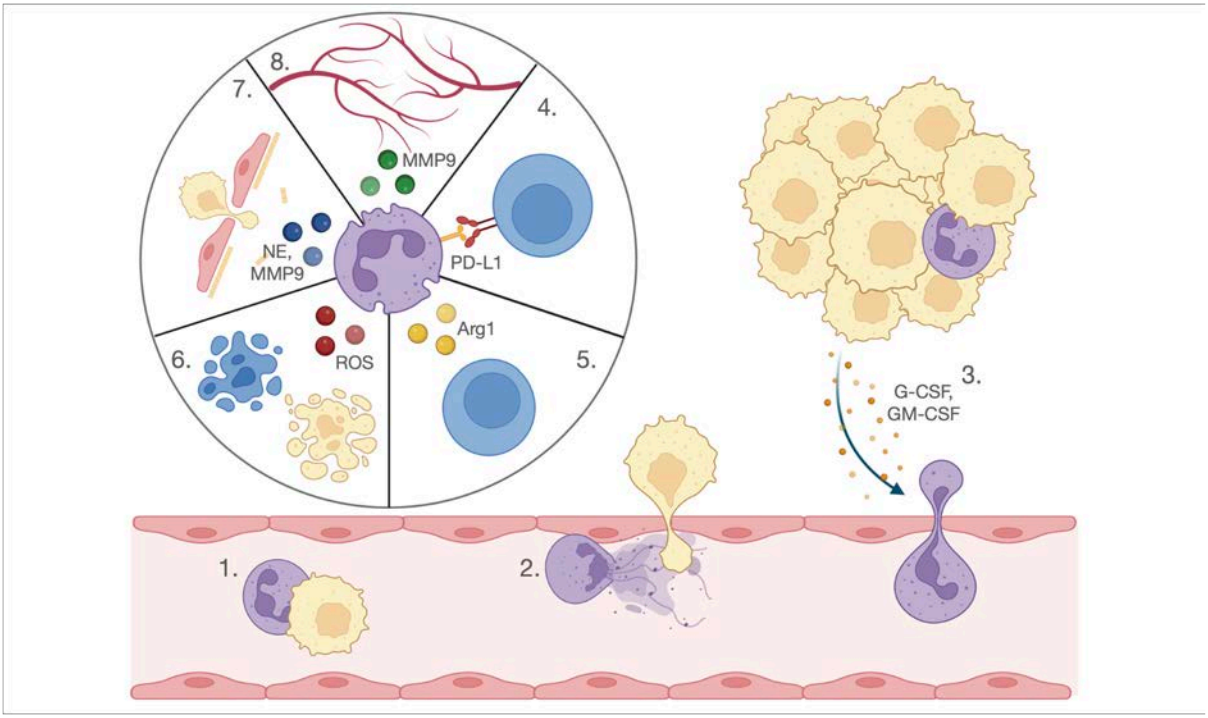

Figure 5. Neutrophil functions in cancer: *[1] Neutrophils have been shown to bind circulating tumor cells and protect them from eradication by the immune system (101). [2] Through the process of NETosis, neutrophils can bind circulating tumor cells and help them extravasate and form metastasis (103-107).[3] Neutrophils themselves are recruited by tumor cells to the tumor site (93). In the tumor, TANs have mostly been described to be pro-tumorigenic and via [4] the expression PD-L1 directly bind T-cells and inhibit their tumor cytotoxic effector function. Through exocytosis of granules neutrophils can excrete [5] Arg1 which depletes arginine and suppresses T-cell function (99), [6] ROS, a cytotoxic agent and suppresser of T-cells (108-110), [7] NE and MMP9 which stimulate the breakdown of the vascular structure supporting the formation of tumor cell extravasation (95, 99), [8]. Additionally, MMP9 can stimulate angiogenesis in cancer (100). Created with BioRender.*

Furthermore, NETs can promote cancer cell proliferation (103, 111, 112) and awaken dormant tumor cells (113). In patients, circulating NET levels are increased in conjunction with their metastatic burden (104).

The formation of NETs can be induced by the production of reactive oxygen species (ROS) (105), another canonical mechanism for the neutrophil's antimicrobial defense. Neutrophils are one of the main producers of MPO-mediated ROS, which are highly cytotoxic including for tumor cells (108-110) (Fig. 5). Neutrophil ROS production might even be a requirement for the cancer cell cytotoxicity observed after radiotherapy (114). However, neutrophil-derived ROS can equally suppress T-cell

function and thereby exert a pro-tumoral effect (115-117) (Fig. 5). Additionally, through the excretion of Arg1 or expression of programmed death ligand 1 (PD-L1), neutrophils can further inhibit T-cell function (99) (Fig. 5). Arg1 depletes the amino acid arginine, which is essential for T-cells, leaving them unable to exert their effector functions against tumor cells (118, 119). Moreover, PD-L1 can bind to programmed cell death protein 1 (PD-1), an inhibitory receptor on T-cells, which suppresses their cytotoxic function (Fig. 5). This immunosuppressive phenotype was observed in a subset of neutrophils, and initially led to the identification of a separate cell type called myeloid-derived suppressor cell (MDSC) (120). However, as there are currently no markers that can definitively distinguish MDSCs from neutrophils with an immunosuppressive capacity, we consider them herein as neutrophils (120).

Considering that neutrophils are short-lived cells and have a fast-acting post-transcriptional granule release, it was long thought that the neutrophil transcriptome would contribute little to their functionality and phenotype. Indeed, neutrophils show lower transcriptional activity compared to other immune cells (121), nevertheless recent advances in single cell RNA sequencing (scRNAseq) have been able to capture their transcriptional heterogeneity in cancer (122-124), including in BrM-bearing patients (125). Even though neutrophils can be observed in a continuum at the transcriptional level, TAN-specific clusters were observed, which are mostly driven by pro-inflammatory alterations (e.g., IL-8 and S100A8/9) (125).

In general, only very few studies have been conducted on neutrophils in brain tumors and the formation of BrMs specifically. Mouse models of glioma and BrMs showed mostly pro-tumoral roles by suppressing T-cell function (93, 126, 127). In BrMs, neutrophils were shown to infiltrate the brain to prepare the premetastatic niche and recruit circulating tumor cells (128). By contrast, a study in GBM-bearing mice showed that neutrophils have a cytotoxic effect on cancer cells via the MPO-ROS cascade (110). However, it is crucial to keep in mind that there are several intrinsic differences between murine and human neutrophils (e.g. abundance in the circulation, cell surface markers and chemokine receptor expression, granule content and cytokine production), which can make it challenging to translate findings in mouse

models to the clinic (129). Hence it is critical to study neutrophil function in the most valid physiological context; in human glioma and BrMs (74). In glioma-bearing patients the few observations to date indicated a pro-tumoral role of neutrophils via their stimulation of angiogenesis by MMP9 production (130) and induction of cancer cell proliferation via S100A4 (131). In BrMs, a correlation was observed between the expression of pro-inflammatory protein S100A8 by TANs and overall patient survival (93). With so few studies performed in human brain malignancies, there is evidently a need to comprehensively interrogate the role of neutrophils in this context.

5.5 The lymphoid cell compartment

Lymphoid cells broadly comprise T-cells, B-cells, and NK-cells. In human brain tumors (both gliomas and BrMs) B-cells and NK-cells are rather rare, however T-cells are quite abundant in BrMs (Chapter 7.2 and (49, 50)). T-cells are generated in the bone marrow and migrate to the thymus where they further mature and differentiate into $CD4^+$, $CD8^+$ and $CD4^+$ regulatory T-cells (Tregs) (48). T-cells express T-cell receptors (TCRs) on their cell surface, which bind to the major histocompatibility complex (MHC) present on APCs of the innate immune system (48). Through this connection APCs can prime T-cells for a specific antigen. $CD4^+$ T-cells bind to MHC-II and once activated support $CD8^+$ T-cell function as well as the production of large quantities of monoclonal antibodies generated by B-cells (48). $CD8^+$ T-cells have a high affinity to MHC-I molecules, which can be expressed on both APCs and tumor cells (47, 48). Once primed by APCs against a specific antigen, $CD8^+$ T-cells will bind tumor cells presenting this antigen via MHC-I and consequently eradicate these cells (47, 48).

There are several negative and positive feedback loops in place which ensure that the adaptive immune system does not become overly reactive and cause auto-immune diseases. Cell types such as Tregs are specialized in suppressing T-cell cytotoxicity and proliferation and thereby maintaining immunogenic homeostasis (48). Furthermore, persistent exposure of $CD8^+$ T-cells to tumor antigens can induce sustained expression of immune-checkpoint molecules which subsequently drive $CD8^+$ T-cells into an exhausted or apoptotic state (132). Immune-checkpoint

molecules are inhibitory receptors on T-cells, which ensure fine-tuning of the immune response. The most prominent checkpoint molecules are PD-1 and cytotoxic T-lymphocyte-associated protein 4 (CTLA-4) (133). Their ligands, PD-L1 and B7.1, respectively, can be expressed by other immune cells (e.g., macrophages and neutrophils) as well as by tumor cells, allowing them to use T-cell checkpoint inhibition as an immune escape (133).

5.6 New therapeutic approaches

Understanding the TIME in brain malignancies can allow us to venture into new potential therapeutic options. Conventional treatment strategies are predominantly focused on targeting the tumor cells directly. These treatments either make use of the high proliferative capacity (radiotherapy and chemotherapy) or biological characteristics (targeted therapy and hormone therapy) of cancerous cells. Since tumor cells are often highly mutated, selection pressure under especially targeted and hormone therapy will promote the selection of tumor cell subclones that are resistant to these therapies (134). By contrast, the TIME cells are genomically stable, therefore targeting these cells by bolstering their anti-tumorigenic effects could have a more long-lasting effect, as this should not be susceptible to genetic selection. Strategies targeting the myeloid and lymphoid compartment are currently at distinct stages of clinical implementation, where thus far the focus has concentrated on stimulating the functions of T-cells. However, reeducating the immunosuppressive TIME might hold considerable promise, as proposed, and pioneered by several investigators in our field.

With regards to harnessing T-cell function, the most mature and successful immunotherapy options to date involve immune-checkpoint blockade (ICB). This monoclonal antibody therapy targets the T-cells' immune-inhibitory receptors (e.g., anti-PD-1, anti-CTLA-4) (133). This can revitalize exhausted $CD8^+$ T-cells and enhance their cytotoxic anti-tumor response (132). ICB has greatly improved the survival of patients with several extracranial solid tumors, predominantly those with a high mutagenic load (135). Phase II clinical trials in patients with metastatic intra-cranial disease from primary lung cancer and melanoma also revealed a positive

response to ICB, with increased overall and progression-free survival in a subset of patients (136-140). However, in gliomas they have shown no evident improvement compared to standard of care therapy (141, 142). Other approaches have focused on generating engineered chimeric antigen receptor (CAR) T-cells designed to recognize and target adult GBM-specific tumor antigens (e.g., EGFRvIII, IL13Rα2) (143, 144). Although these studies showed trafficking of CAR T-cells to the brain tumor, an increased immunosuppressive response was measured *in situ*, thus hampering the treatment efficacy (143). And lastly, there have been several attempts to boost the effectiveness of the adaptive immune system by optimizing their priming to tumor antigens with the help of peptide or APC vaccines (145). Thus far the few clinical trials performed in GBM have shown induced T-cell responses with limited effects on overall survival (146-150). The poor efficacy of these therapies might in part be due to the overall immunosuppressive TIME present in brain tumors. Of note, many patients with brain tumors receive corticosteroids to reduce brain edema, with the potential side effects of suppressing the immune system further (151).

With regards to immunosuppressive TAMs, several approaches are being investigated in murine models of glioma and BrMs. Both MG and MDMs express colony stimulating factor-1 receptor (CSF-1R), which is a key regulator of macrophage functions (63). CSF-1R binds to the growth factors CSF-1 and IL-34, and regulates macrophage differentiation, proliferation and survival (63). Inhibition of CSF-1R in murine models of GBM (64-66) and BrM (67) resulted in depolarization or depletion of TAMs (152), leading to reduced tumor growth and invasion. Hence targeting TAMs is a promising approach in murine brain tumors, particularly with highly potent and selective CSF-1R inhibitors such as BLZ945. This specific CSF-1R inhibitor has revealed promising preliminary results in a phase I study, where patients bearing advanced solid tumors, including GBMs, are being treated with BLZ945 alone or in combination with anti-PD-1 (153). However, in human recurrent GBMs only very mild effects were observed in a phase II study using PLX3397 (154), which is a less potent and poorly brain-penetrant inhibitor of CSF-1R. This is a clear example of how the BBB can negatively affect treatment efficacy. Other approaches that are actively being investigated include the targeting of TAM recruitment via IL-33 inhibition (68) or

reeducation of their immunosuppressive phenotype via monoamine oxidase A (69). Additionally, combination therapies are being investigated where the cytotoxic and phagocytic capacity of TAMs is exploited by blocking the anti-phagocytosis molecule CD47 on tumor cells while treating with conventional Temozolomide chemotherapy (155). This approach increases the cytotoxicity and antigen presentation potential of TAMs and stimulates the adaptive immune system (155). Several clinical trials are underway studying the effect of the different TAM-targeting approaches in cancer (43), of which few are ongoing in brain malignancies (153).

The therapeutic targeting of TANs is still in its infancy compared to T-cells and TAMs. There are four proposed strategies that thus far have only been evaluated in mouse models: i) broad neutrophil depletion, ii) blocking neutrophil development, iii) blocking neutrophil recruitment and iv) inhibition of their immunosuppressive function (156). These strategies are not without caveats, as first of all, robust and durable depletion of neutrophils in mice has been very challenging (157). Secondly, the development of neutrophil targeting therapies is hindered by their high turnover and important antimicrobial function (156). Consequently, treatment modalities that target neutrophils too broadly would leave patients unprotected against a range of lethal infections. Therefore, a better understanding of specific TAN targets is required before such therapeutics could be developed and make the transition to the clinic.

In parallel, there are human studies that do not necessarily aim to exploit the brain TIME per se, but rather attempt to impede the oxygenation and nutritional supply of tumors. At the tumor site, the vasculature changes as increased nutritional demands of cancer cells require them to co-opt vessels and stimulate angiogenesis (9). Tumor cells can achieve this through the expression of VEGF. Anti-VEGF therapy remodels the tumor vasculature, so that it then resembles healthy brain vasculature (158). This leads to a decrease in tumor volume, angiogenesis, and tumor oxygenation in GBMs (159). However, anti-VEGF therapy only prolonged progression-free survival in phase III clinical trials in GBM patients, but did not improve overall survival compared to standard of care therapy (160, 161). Interestingly, MMP9 plasma levels released by neutrophils, was deemed predictive of an effective response in these patients and

showed a negative correlation with overall survival (130). This suggests a therapy-resistance feedback loop via the production of pro-angiogenic factors by neutrophils.

5.7 Aims of the thesis

Over the last decade in particular, the TIME has been increasingly studied across a range of different cancers, which has led to promising new therapeutic strategies, such as ICB. The clinical advances that were achieved with ICB in extracranial solid tumors have not been translated to all intracranial tumors to date. Consequently, investigating the brain TIME in more depth is critical to determine why brain tumors respond poorly to ICB, how we can alter this and, perhaps more importantly, to investigate whether brain tumors have other TIME-related weaknesses that can be exploited therapeutically. Hence, the aim of this thesis was to interrogate the TIME in both human gliomas and BrMs, and specifically focus on the highly abundant yet understudied myeloid cell compartment. Considering the limited access to non-tumor brain tissue and clinical brain tumor material, a large body of this thesis centers around optimizing and establishing a human brain tissue pipeline. This pipeline includes a diverse set of experimental methods and analyses allowing for an orthogonal investigation of the brain TIME (Chapter 7.1 (162)), which allowed us to address the following topics in this thesis:

i) Characterizing the immune landscape in human non-tumor brain tissue, gliomas and BrMs.
ii) Investigating MG and MDMs as separate entities in human brain (tumor) tissue by analyzing their transcriptome, protein expression and spatial orientation.
iii) Exploring the roles of neutrophils by analyzing their phenotypic, transcriptomic, and functional alterations upon entry into the brain tumor niche, while considering their spatial localization.

6. Summary of results and contributions

The data generated and presented for this thesis can be divided into five separate studies, which are included either as sub-chapters of the Results section, or as abstracts at the end of this chapter. The studies presented in Chapters 7.1 (162) and 7.2 (49) have already been published in peer-reviewed journals. The study described in Chapter 7.3 will shortly be submitted to a peer-reviewed journal. The two remaining manuscripts, where I am a co-author, have recently been submitted for peer review and are included as part of my thesis only in the form of an abstract.

The publication in Chapter 7.1 (Maas*, Soukup*, Klemm* et al, *Nature Protocols*, 2021 (162)) details the comprehensive experimental pipeline that we developed and optimized for the orthogonal analysis of immune cells in human brain tumors, non-tumor brain tissue, and matched blood samples (162). The various techniques that we described in this publication allow researchers to investigate immune cells on a phenotypic, transcriptional as well as functional level, and to use the different techniques for cross-method validation.

For this publication the collection and processing of human patient samples was performed by myself, K. Soukup, F. Klemm, R. Bowman, M. Kornete, and D.N. Marie. Optimization of the diverse techniques was performed by myself, K. Soukup, M. Kornete. Whole exome sequencing (WES) analysis was performed by A.F. Álvarez-Prado. Flow cytometry (FCM) support and sorting was provided by R. Bedel, D. Labes, and A. Wilson. Human tissue used in the study was obtained through our collaboration with R.T. Daniel and M.E. Hegi. Pathology review was performed by J-P. Brouland. Figures were prepared by myself and K. Soukup. Statistical analysis was performed by me. The manuscript was written by myself, K. Soukup, F. Klemm, and J.A. Joyce, and subsequently reviewed and/or revised by all co-authors. This project was supervised by J.A. Joyce.

The publication in Chapter 7.2 (Klemm, Maas et al, *Cell*, 2020 (49)) presents a comprehensive interrogation of the immune landscape of both primary and metastatic

brain malignancies, with a focus on analyzing potential similarities or distinctions between resident MG and recruited MDMs (49). The major discoveries presented in this study are that the brain TME shapes the phenotypes and activation of immune cells, and our identification of converging transcriptional trajectories in MG and MDMs in a disease-specific manner.

For this study, the collection and processing of human patient samples was performed by F. Klemm, myself, R. Bowman, M. Kornete, and K. Soukup. The RNA sequencing (RNAseq) analysis was performed by F. Klemm. Immunofluorescence (IF) staining was executed by myself and M. Kornete, and the spatial quantification was performed by me. FCM analysis for Fig 1A and 1F was performed by me and F. Klemm, FCM analysis for Fig 2B, S2B, and 4C was performed by me. *In vitro* generation and analysis of MDMs was performed by K. Soukup. Protein isolation and downstream enzyme-linked immunosorbent assays were performed by F. Klemm. Statistical analyses associated with RNAseq and proteomics analyses were performed by F. Klemm (Figs. 2D, S3C, S3E, 4I-J, S4C, S4F-G, S6C-D, 7C-D, 7G, S7B), and for the figure panels associated with FCM and IF analysis, these were performed by me (Figs. 1B, 1F, 2C, S2D, 3E, 4A, 4C), and the mixed effect model used in Fig 4B was executed by S. Nassiri. Human tissue was received through our collaboration with C.A. Iacobuzio-Donahue, C. Brennan, V. Tabar, P.H. Gutin, R.T. Daniel, and M.E. Hegi. Pathology review was performed by J-P. Brouland. Figures were generated by F. Klemm and me. The manuscript was written by F. Klemm and J.A. Joyce, and reviewed and/or revised by all authors. This project was supervised by J.A. Joyce.

The third study (Chapter 7.3) focuses on our investigation of the functions and phenotypes of neutrophils in brain malignancies. The major findings of this study are that neutrophils are phenotypically, transcriptionally, and functionally altered following their entry into brain tumors. Brain TANs show a prolonged survival, along with immunosuppressive and pro-angiogenic phenotypes. The alterations we uncovered are predominantly mediated by soluble factors produced by the myeloid cell compartment, consisting of neutrophils, MG and MDMs.

The author contributions for this manuscript are listed below. The collection and processing of human patient samples was performed by myself, K. Soukup, S. Galland, M. Kornete, D.N. Marie, and V. Wischnewski. *Ex vivo* culture assays were executed by myself, K. Soukup, and S. Galland. Mouse studies were performed by K. Soukup, D. Croci, M. Massara, and myself. Single round standard IF staining and image quantification, shown in Figs. 1D-G, S7A, was performed by me. Sequential IF stainings were performed by myself, S. Galland, and J. Lilja. Downstream cellular identification using QuPath, depicted in Figs. 4I, S4F-G, and 7A was executed by S. Galland, and the image quantifications and analyses were performed by me. Whole exome sequencing analysis was executed by A.F. Álvarez-Prado. The RNA sequencing library was prepared by A. Wirapati and analysis of RNAseq was executed by N. Fournier and J. Lourenco, in collaboration with myself and K. Soukup. Mathematical modeling of the murine neutrophil survival, shown in Fig. 5D,E and S5E, was generated by R. Marcone and G. Fernández-Calvo, in collaboration with myself and K. Soukup. We received the human tissue used in this study through our collaboration with A. Hottinger, R.T. Daniel, and M.E. Hegi. Pathology review was performed by J-P. Brouland. Figures were prepared by myself, N. Fournier, S. Galland and K. Soukup. Statistical analysis was performed by myself (Figs. 1B-C, 2A, S2A, 4B-C, 4E-H, S4A, S4C-E, S4H, 5A, 5F, 5H-J, S5A-D, S5H, 6C-D, 6G-H, S6D-E, 7D, 7G, S7B-C, S7E) and N. Fournier (Figs. 2D, 2F, 3A, 3F, S6H, 7E). The manuscript was written by myself, K. Soukup, S. Galland, and J.A. Joyce, and subsequently reviewed and/or revised by all co-authors. The project was supervised by J.A. Joyce.

The fourth and fifth manuscripts, for which the abstracts can be found below, study the role of T-cells (Chapter 7.4) and the effect of different mutations on the immune landscape in brain malignancies (Chapter 7.5). These two studies were led by V. Wischnewski and A.F. Álvarez-Prado, respectively, and supervised by J.A. Joyce; I was not involved in the conception of these projects. For both studies, I, together with K. Soukup, M. Kornete, and A.F. Álvarez-Prado generated the bulk RNAseq dataset. For both studies, I also executed and analyzed the immune cell landscape as performed by FCM. For the study in Chapter 7.4, P. Guerrero, J. Lilja, S. Galland, and

I performed sequential IF staining, for which P. Guerrero and I performed the image quantification and statistical analyses. P. Guerrero, V. Wischnewski, and I performed the *ex vivo* T-cell proliferation assay in this same study. I did not assist in the preparation of the final figures nor the writing of either manuscript. I reviewed both final manuscripts, and suggested edits and modifications.

7. Results

7.1 An integrated pipeline for comprehensive analysis of immune cells in human brain tumor clinical samples

nature protocols

PROTOCOL

https://doi.org/10.1038/s41596-021-00594-2

Check for updates

An integrated pipeline for comprehensive analysis of immune cells in human brain tumor clinical samples

Roeltje R. Maas[1,2,3,4,8], Klara Soukup[1,2,8], Florian Klemm[1,2,8], Mara Kornete[1,2], Robert L. Bowman[5], Romain Bedel[6], Damien N. Marie[1,2], Ángel F. Álvarez-Prado[1,2], Danny Labes[6], Anne Wilson[1,6], Jean-Philippe Brouland[7], Roy T. Daniel[4], Monika E. Hegi[3,4] and Johanna A. Joyce[1,2]✉

Human tissue samples represent an invaluable source of information for the analysis of disease-specific cellular alterations and their variation between different pathologies. In cancer research, advancing a comprehensive understanding of the unique characteristics of individual tumor types and their microenvironment is of considerable importance for clinical translation. However, investigating human brain tumor tissue is challenging due to the often-limited availability of surgical specimens. Here we describe a multimodule integrated pipeline for the processing of freshly resected human brain tumor tissue and matched blood that enables analysis of the tumor microenvironment, with a particular focus on the tumor immune microenvironment (TIME). The protocol maximizes the information yield from limited tissue and includes both the preservation of bulk tissue, which can be performed within 1 h following surgical resection, as well as tissue dissociation for an in-depth characterization of individual TIME cell populations, which typically takes several hours depending on tissue quantity and further downstream processing. We also describe integrated modules for immunofluorescent staining of sectioned tissue, bulk tissue genomic analysis and fluorescence- or magnetic-activated cell sorting of digested tissue for subsequent culture or transcriptomic analysis by RNA sequencing. Applying this pipeline, we have previously described the overall TIME landscape across different human brain malignancies, and were able to delineate disease-specific alterations of tissue-resident versus recruited macrophage populations. This protocol will enable researchers to use this pipeline to address further research questions regarding the tumor microenvironment.

Introduction

Brain malignancies comprise tumors of intracranial origin, including low-grade gliomas and glioblastomas, and brain metastases (BrMs) originating from extracranial tumors. Lung cancers, breast cancers and melanoma are the most frequent primary tumor types giving rise to BrM[1]. Overall, patients diagnosed with these brain malignancies share a poor clinical prognosis, with a median overall survival ranging from 2 to 14 months, depending on the tumor type[1,2]. This poor prognosis is due partly to the fact that our knowledge of the complex interactions within the unique tumor microenvironment of the brain is still incomplete[3], especially in comparison with extracranial cancers[4]. In particular, the involvement of the noncancerous tumor immune microenvironment (TIME) in modulating brain cancer progression and therapeutic response is increasingly being appreciated. Recent studies have provided important insights into the cellular composition of the brain TIME and demonstrated both cell- and disease-specific phenotypic alterations[5,6]. Given the expanding success of immunotherapies for multiple extracranial cancers, it is critical to deepen our understanding of the TIME, as it may reveal promising targets to overcome the currently bleak prognosis for many brain cancer patients. To date, TIME-targeting immune checkpoint blockade strategies have only conferred

[1]Department of Oncology, University of Lausanne, Lausanne, Switzerland. [2]Ludwig Institute for Cancer Research, University of Lausanne, Lausanne, Switzerland. [3]Neuroscience Research Center, Centre Hospitalier Universitaire Vaudois, Lausanne, Switzerland. [4]Department of Neurosurgery, Centre Hospitalier Universitaire Vaudois, Lausanne, Switzerland. [5]Memorial Sloan Kettering Cancer Center, New York, NY, USA. [6]Flow Cytometry Facility, Department of Formation and Research, University of Lausanne, Epalinges, Switzerland. [7]Department of Pathology, Centre Hospitalier Universitaire Vaudois, University of Lausanne, Lausanne, Switzerland. [8]These authors contributed equally: Roeltje R. Maas, Klara Soukup, Florian Klemm.
✉e-mail: johanna.joyce@unil.ch

a clinical benefit in a subset of BrMs[7–9] and have been mostly ineffective in gliomas[10,11]. This underscores the necessity to deeply interrogate the distinct properties of the TIME across all brain malignancies.

While animal models represent an important experimental approach for cancer immunology research, studies on human tissue material are indispensable for any translational research platform. The difficulty in obtaining sufficient material for research from neurosurgically resected brain cancers makes studying the TIME of patient tumors particularly challenging. This is further hindered by the unique mechanical properties of brain tumors[12], their lipid composition, and the remnants of myelinated axons within gliomas that impede downstream analyses[13]. We thus present here a modular protocol for the comprehensive analysis of the TIME in human brain tumors that has been specifically optimized to overcome these challenges. Applying this protocol, we have described the overall TIME landscape across different human brain malignancies, including both brain-intrinsic gliomas and brain-extrinsic metastases originating from different primary tumors[5]. Building upon the protocol's modularity, we were further able to delineate disease-specific alterations of tissue-resident versus recruited macrophage populations by performing orthogonal and complementary analyses[5]. Gaining such detailed knowledge about the unique characteristics of the brain TIME of individual tumor types enabled us to provide novel insights into potential factors influencing these tumors' differential responses to immunotherapy.

Applications of the protocol and comparison with other approaches

This pipeline has been specifically designed for the analysis of freshly resected human brain tissue, including non-tumor tissue, low-grade *isocitrate dehydrogenase* (*IDH*) mutant (mut) gliomas, high-grade *IDH* wildtype (wt) glioblastomas and BrMs arising from different primary tumors. It enables identification of disease-specific TIME composition across this range of brain malignancies, revealing important differences in the abundance of tissue-resident microglia (MG), infiltrating monocyte-derived macrophages (MDMs), neutrophils, $CD4^+$ and $CD8^+$ T cells by flow cytometry (FCM) and whole-slide immunofluorescence (IF) image analyses[5]. Due to the protocol's modular workflow, we were able to augment these analyses with RNAseq of sorted cell populations and bulk tumor tissue proteomics, which uncovered multifaceted immune cell activation across different brain malignancies. We thereby revealed converging transcriptional trajectories of MG and MDMs in brain tissue, while also identifying disease- and cell-type-specific changes[5].

Whereas the protocol we provide here enables both global and granular brain TIME investigations, researchers may wish to perform more in-depth studies for particular TIME populations on the single-cell level. High-dimensional methods, such as cytometry by time-of-flight or single-cell RNAseq (scRNAseq), offer the possibility to more deeply profile individual cell populations and to uncover unique subsets or differentiation states. While several of our tissue processing modules may well be compatible with such techniques, we would like to emphasize that the implementation of specific downstream methods should be assessed for each researcher's individual setting. For cytometry by time-of-flight based human brain TIME studies in particular, we recommend that researchers refer to refs. [6,14]. Moreover, several recent studies have described detailed methods for scRNAseq of human gliomas[15–19], including an in-depth investigation of glioma stem cells[20,21], as well as of BrMs among other metastatic sites[17,22–24].

Experimental design

The pipeline we describe in this protocol should enable researchers to extract a substantial amount of data even from small tissue samples (Figs. 1 and 2). The procedure consists of several modules for both bulk tumor preservation (module 1) and tumor dissociation (modules 2, 3) that enable parallel analyses, resulting in an in-depth characterization of TIME composition, phenotype and functional status. The entire pipeline has been designed to include highly complementary modules, in parallel with routine histopathological studies mainly focused on morphological and molecular characteristics of tumor components, thus allowing for multifaceted analyses from even limited amounts of clinical material.

Following bulk tumor preservation, tissue can be assessed by IF staining, proteomics and genomics. In the protocol, we provide details of the procedure we optimized for IF and the preliminary steps required to prepare material for proteomic and genomic analysis (module 1a, b). Standard proteomic and genomic techniques can be used, so these are not described in detail here beyond recommended initial sample preparation. For in-depth studies of individual TIME cell types,

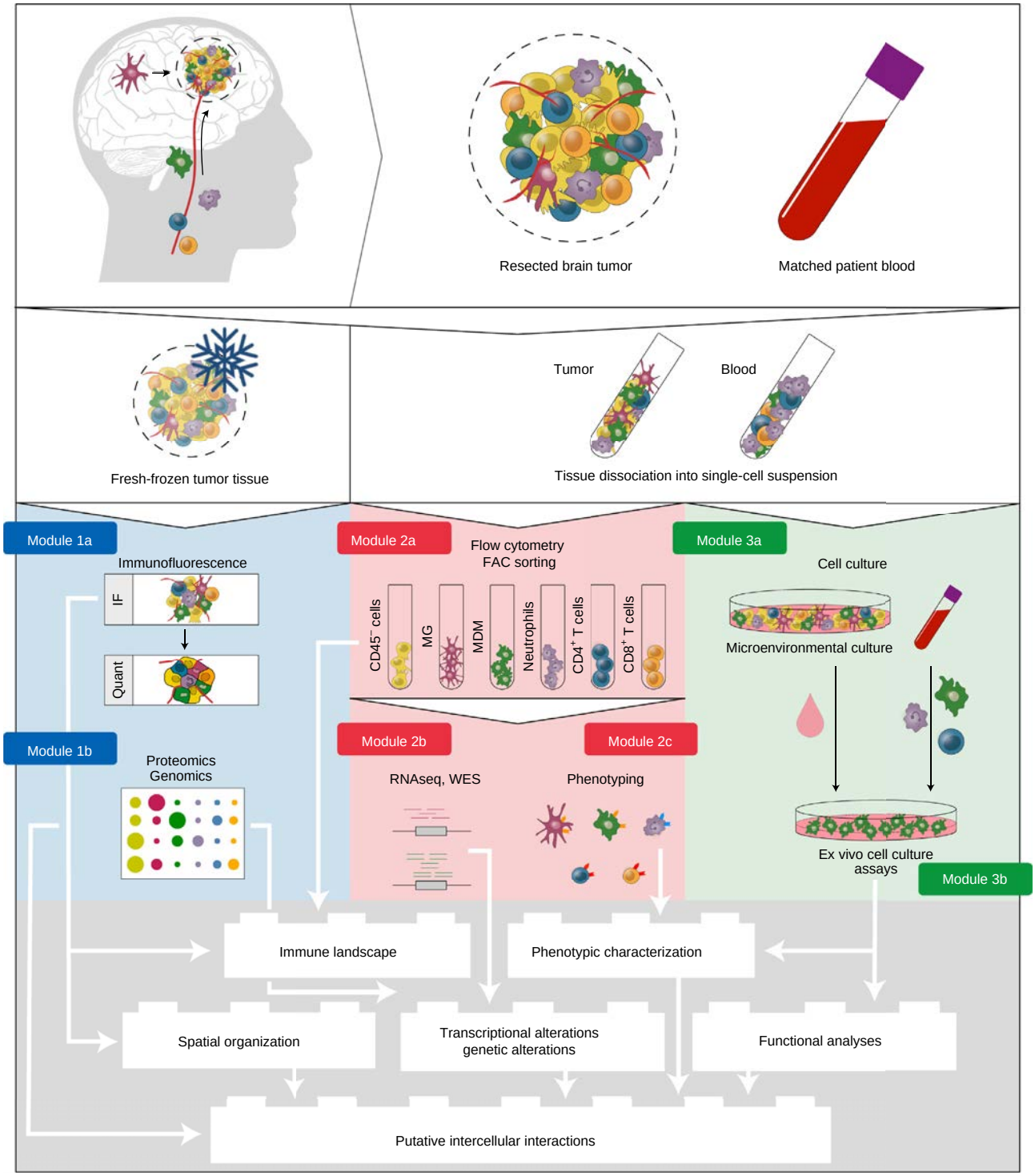

Fig. 1 | Schematic overview of the different modules described in this protocol. Module 1a, Resected human brain (tumor) tissue can be frozen, sectioned and stained with IF antibodies to obtain spatial information of the different cell types of the TIME. **Module 1b**, Fresh snap-frozen brain tumor tissue can be used for bulk tissue proteomic and genomic analysis. **Module 2a**, Single-cell suspension of resected human brain (tumors) after enzymatic digestion and matched blood samples can be analyzed by FCM and immune cells can be sorted via FAC sorting. **Module 2b**, FAC-sorted immune cell populations can be utilized for bulk or scRNAseq analysis and/or WES. **Module 2c**, FCM analysis of immune cells by additional multiparameter panels can serve to characterize their phenotype. **Module 3a**, Single-cell suspension of resected human brain tumors after enzymatic digestion can be used to generate ex vivo MECs. **Module 3b**, Ex vivo cell culture assays can be performed using whole blood–derived immune cells cultured in MEC supernatant, or immune cells isolated from the whole-tumor single-cell suspension.

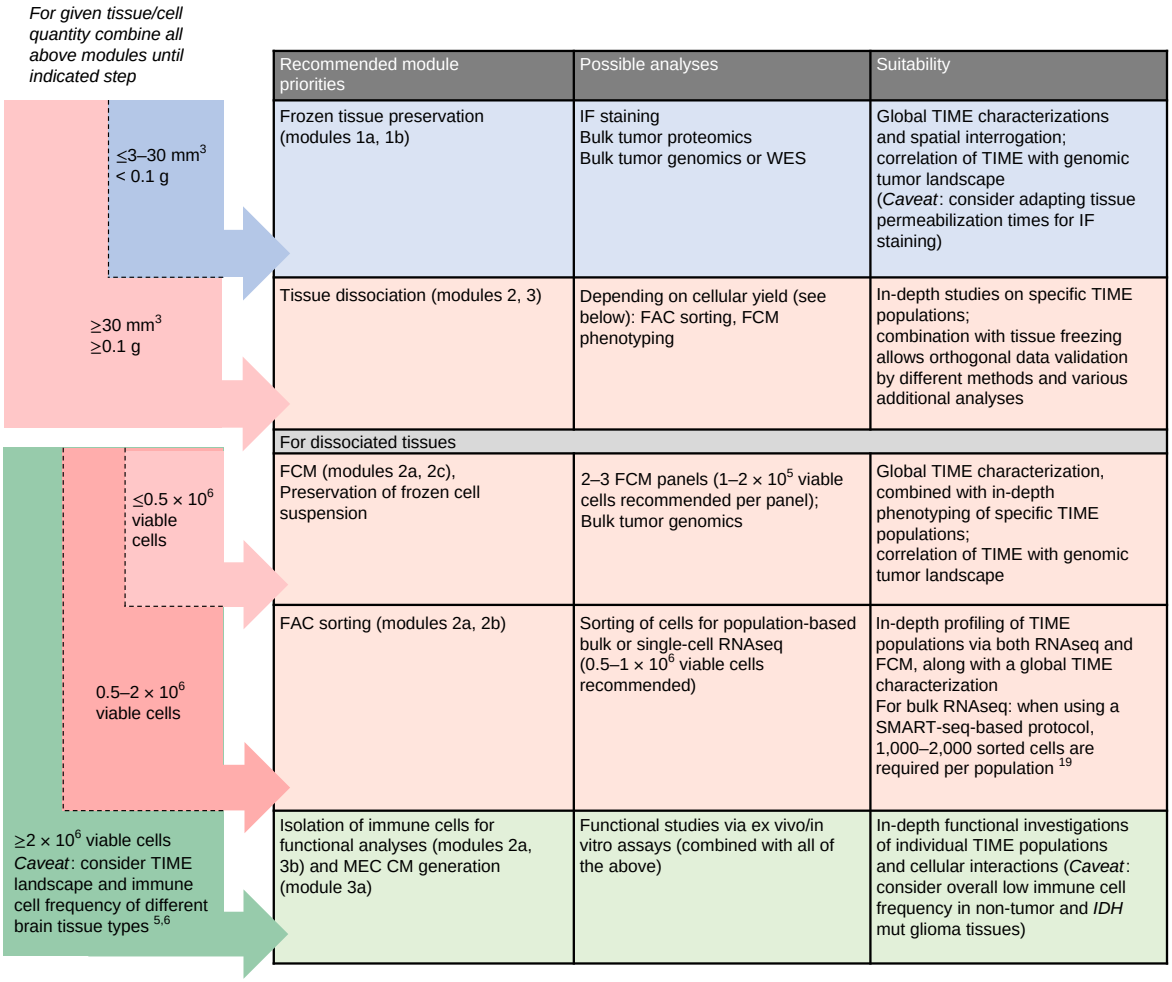

Recommended module priorities	Possible analyses	Suitability
Frozen tissue preservation (modules 1a, 1b)	IF staining Bulk tumor proteomics Bulk tumor genomics or WES	Global TIME characterizations and spatial interrogation; correlation of TIME with genomic tumor landscape (*Caveat*: consider adapting tissue permeabilization times for IF staining)
Tissue dissociation (modules 2, 3)	Depending on cellular yield (see below): FAC sorting, FCM phenotyping	In-depth studies on specific TIME populations; combination with tissue freezing allows orthogonal data validation by different methods and various additional analyses
For dissociated tissues		
FCM (modules 2a, 2c), Preservation of frozen cell suspension	2–3 FCM panels (1–2 × 10^5 viable cells recommended per panel); Bulk tumor genomics	Global TIME characterization, combined with in-depth phenotyping of specific TIME populations; correlation of TIME with genomic tumor landscape
FAC sorting (modules 2a, 2b)	Sorting of cells for population-based bulk or single-cell RNAseq (0.5–1 × 10^6 viable cells recommended)	In-depth profiling of TIME populations via both RNAseq and FCM, along with a global TIME characterization For bulk RNAseq: when using a SMART-seq-based protocol, 1,000–2,000 sorted cells are required per population [19]
Isolation of immune cells for functional analyses (modules 2a, 3b) and MEC CM generation (module 3a)	Functional studies via ex vivo/in vitro assays (combined with all of the above)	In-depth functional investigations of individual TIME populations and cellular interactions (*Caveat*: consider overall low immune cell frequency in non-tumor and *IDH* mut glioma tissues)

Fig. 2 | Recommendations for prioritization of tissue processing modules. Flow chart indicating guidelines for the input material required for the different modules introduced in Fig. 1 (blue, module 1; pink, module 2; green, module 3). The table provides recommendations regarding module prioritization, suggested analyses that can be performed using a given tissue, and their suitability to address specific research questions.

we describe optimized tissue dissociation procedures that allow for the simultaneous isolation of various cell populations. Cells are collected by fluorescence-activated cell sorting (FAC sorting) of immune cell populations (module 2a) for downstream population-based RNAseq or scRNAseq (module 2b). We also describe how to interrogate the phenotype of the different immune cell populations in depth via multiparameter FCM panels (module 2c). These TIME-focused analyses are further augmented by including matched peripheral blood immune cell populations, which enables the researcher to gain insights into local versus systemic immune cell alterations in patients with brain cancer.

In parallel, tumor microenvironment cultures (MECs) can be established (module 3a), providing a unique tool to investigate functional interactions between different TIME populations and tumor cells ex vivo, as well as to analyze the tissue secretome. Additionally, fragile immune cell populations (e.g., neutrophils) can be recovered in higher numbers by alternative isolation methods (such as magnetic bead-based techniques) for cell culture assays (module 3b) depending on the total cell number and tissue type (Fig. 2).

A major strength of this protocol is the modular combination of different methods to study the brain TIME that we have optimized to maximize the information that one can gain from a small piece of freshly resected human brain tumor (or non-tumor) tissue. Each module has been optimized to consider both the unique characteristics of the input material, and also the distinct features of diverse TIME populations.

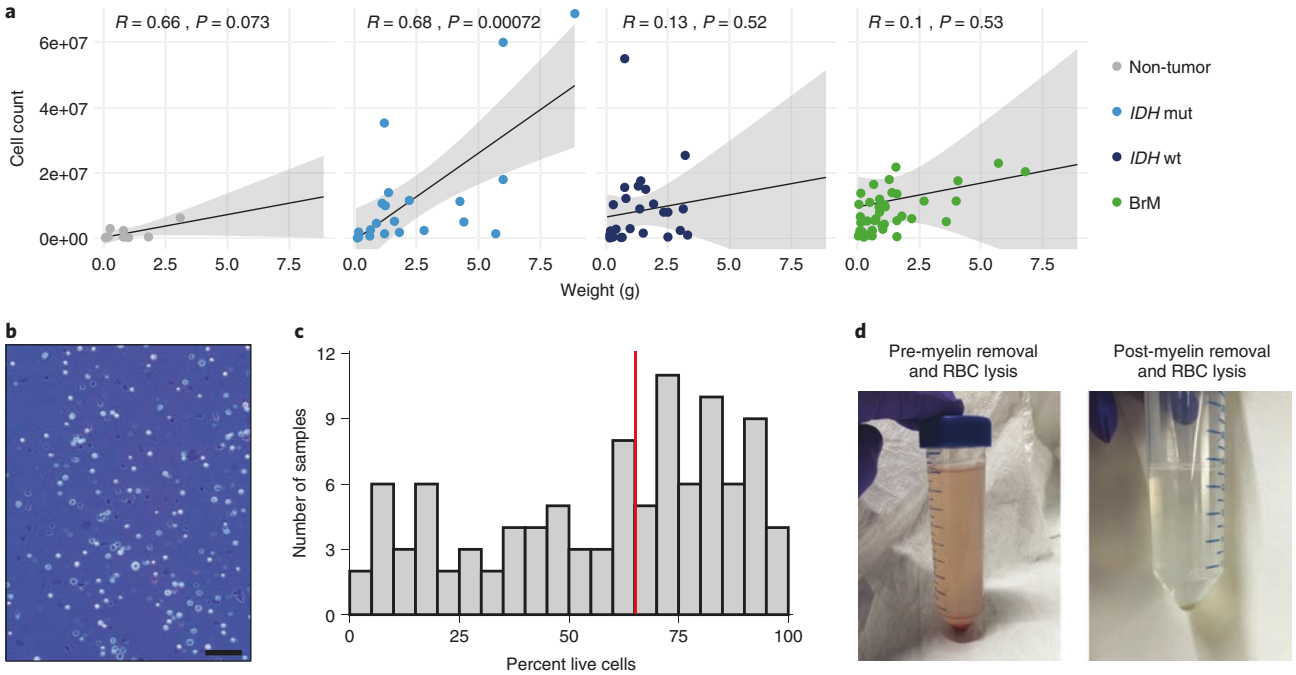

Fig. 3 | Variation in immune cell abundance and cell viability across different brain (tumor) tissue types. a, Weight of input brain (tumor) tissue compared with live cell count retrieved after TDK/BTDK enzymatic digestion for non-tumor brain ($n = 8$) and tumor tissues ($n_{IDHmut} = 21$, $n_{IDHwt} = 27$, $n_{BrM} = 40$). Plot inset: Pearson's correlation coefficient and significance. **b**, Representative image of Trypan Blue staining of an *IDH* wt glioma single cell suspension after TDK enzymatic digestion. FCM analysis revealed a viability of 77% for this representative sample. **c**, Distribution of percent live cells as measured by FCM across non-tumor brain ($n = 12$) and tumor tissues ($n_{IDHmut} = 15$, $n_{IDHwt} = 32$, $n_{BrM} = 43$). The red line represents the median (65.2%) across samples. **d**, Representative images of the single-cell pellet and supernatant pre-myelin removal and RBC lysis, compared with post-myelin removal and RBC lysis.

Module prioritization and feasibility of analyses based on brain (tumor) tissue quality and quantity

The pipeline we describe here offers the researcher the possibility to prioritize different tissue preservation and analysis methods, and to design their individual workflow depending on a specific research question. Based on our experience working with these clinical tissues, we propose the prioritization of distinct pipeline modules depending on the available tissue size and quality (Fig. 2). These recommendations aim to give an overview of the type of results that can be obtained from a defined input material, and to highlight the complementarity of individual modules in order to maximize the information yield. It is important to emphasize, however, that these recommendations should be viewed as guidelines and are based on our own unique tissue collection and processing needs. We would like to specifically point out that the high intersample variability one generally encounters when working with human (brain) tissue samples is also a critical factor. This makes it somewhat challenging to define absolute tissue quantity cutoff criteria for the different downstream methods. We provide more detailed recommendations for the amount of tissue required for each module of the pipeline based on our experience using four different types of human brain tissue: (i) non-tumor brain tissue from epilepsy lobectomies, (ii) low-grade gliomas (*IDH* mut), (iii) high-grade gliomas (glioblastomas, *IDH* wt), and (iv) BrMs.

Several key factors must be considered when selecting specific tissue processing modules: (1) the terms of tissue handling before arrival in the laboratory (e.g., lag time, storage temperature and transport conditions); (2) the overall tissue morphology and condition, in particular the extent of cauterized areas and coagulated blood (which should be removed before further processing), as well as the degree of tissue hydration (we do not recommend processing tissues that have been kept dry for an extended period of time due to their rapid degradation); (3) the tissue volume and weight, which together may be indicative of tissue density and cellularity (Fig. 3a); furthermore, for dissociated tissues (4) the overall cell yield and cellular viability post-dissociation (Fig. 3b,c); and (5) the cell suspension purity versus debris/myelin content (Fig. 3b,d).

For a broad investigation of the overall TIME landscape, we recommend prioritizing the preservation of frozen whole-tissue material for both multiplex IF staining (module 1a) and bulk tissue proteomic and/or genomic analyses such as whole-exome sequencing (WES, module 1b), which is

possible from tissue pieces as small as 3–30 mm^3 or <0.1 g. This allows one to quantify the abundance of various immune cell populations, and to also assess their spatial organization within the tumor tissue. In parallel, large-scale analyses of the tumor protein content and the tumor genomic landscape can be performed. Integrating such diverse data yields an abundance of information and may serve to generate and validate hypotheses about the functions of immune cells in brain tumors.

Initial processing of tissue

Due to the limited amount of these tissues and the modular style of the pipeline, it is essential to store tissue in a form in which it can serve several different applications. As shown in Fig. 1, we optimized a freezing method for the downstream use of human brain tumor tissue for both spatial analysis by IF (module 1a) as well as proteomic and genomic analyses (module 1b). Tissue fixation with formalin followed by paraffin embedding (FFPE) is routinely used during pathological review and is considered the gold standard tissue conservation method, as it allows for excellent tissue morphology preservation as well as for the application of several well-established and validated techniques (e.g., immunohistochemistry (IHC), fluorescence in situ hybridization, targeted sequencing, methylation profiling, *IDH* pyrosequencing). In parallel to FFPE, we explored several methods for the frozen preservation of tissue that would allow one to overcome some of the limitations of FFPE, such as the masking of certain antigens in multiplexed IF staining and limited possibilities for high-quality RNA extraction for transcriptomic analysis. When freezing human brain tissue directly in optimal cutting temperature (OCT) compound, the spatial integrity is of a similar quality to FFPE tissue, without the need for antigen retrieval for IF staining and allowing for straightforward RNA extraction. To validate this freezing strategy, we stained a partitioned glioma tissue for the chromatin remodelling protein ATRX by IHC (see Supplementary Methods for details), which revealed that fresh frozen tissue embedded in OCT and post- or prefixed with paraformaldehyde (PFA) showed a similar staining pattern to FFPE tissue (Fig. 4a, see Table 1 for an overview of the antibodies used). Moreover, both unfixed OCT-frozen tissue as well as PFA fixation prior to OCT embedding and freezing allowed for the assessment of *IDH1* (Fig. 4b) mutational status via *IDH* pyrosequencing (see Supplementary Methods for details), which was comparable to results from FFPE tissue. In sum, if there is a need to economize tissue and simultaneously maximize the potential use of this tissue for parallel techniques (especially considering IF staining and RNA extraction), we have found that direct freezing in OCT compound is a well-suited method that offers the flexibility to perform postfixation as needed.

Furthermore, we extensively optimized a tissue-specific protocol for reliable IF-based quantification of immune cells in frozen tissue of the different brain (tumor) types introduced above (module 1a). Due to considerable differences in tissue structure between these various samples, leading to altered susceptibility to permeabilization, rather long permeabilization times are required when analyzing immune cells across these distinct tissue types in parallel. To obtain high-quality IF staining of high-grade *IDH* wt glioma and BrM tissues, a permeabilization step of 10 min suffices. However, non-tumor brain and low-grade *IDH* mut glioma tissues require a substantially longer permeabilization of 3 h for adequate IF staining. Importantly, a 3 h permeabilization of both high-grade *IDH* wt glioma and BrM tissue does not impair the staining or tissue quality, thus allowing for an unbiased and side-by-side comparison of the immune landscape via IF between the four different tissue types (Fig. 4c; Table 1).

For researchers who do not have access to freshly resected human brain tumor samples, FFPE-preserved tissue may provide an alternative resource for studies on the global brain TIME[25–28], its tumor cell genomic landscape[28–31] and the tissue's spatial organization[32]. Although FFPE tissue poses some challenges to certain methods as discussed above, such tissue may nevertheless be of great value for larger patient cohort studies and the validation of specific findings across research sites, as it allows for the inclusion of older preserved samples.

Considerations for IF analyses

Several important points should be considered for IF-based tissue section staining:

- Antibodies must be carefully selected and titrated to ensure target specificity and an optimal signal-to-background fluorescence ratio. For target specificity evaluation, it is recommended to use positive control tissues, such as tonsil tissue for T-cell detection. In the case of poor signal detection, alternative fixation methods should be compared to achieve optimal staining results
- Antibody specificity and concentration must be carefully evaluated for each tissue type to be analyzed, as binding properties may differ depending on the overall tissue properties (e.g., increased lipid content in non-tumor brain versus tumor tissue). Several steps in the IF staining protocol may need to be

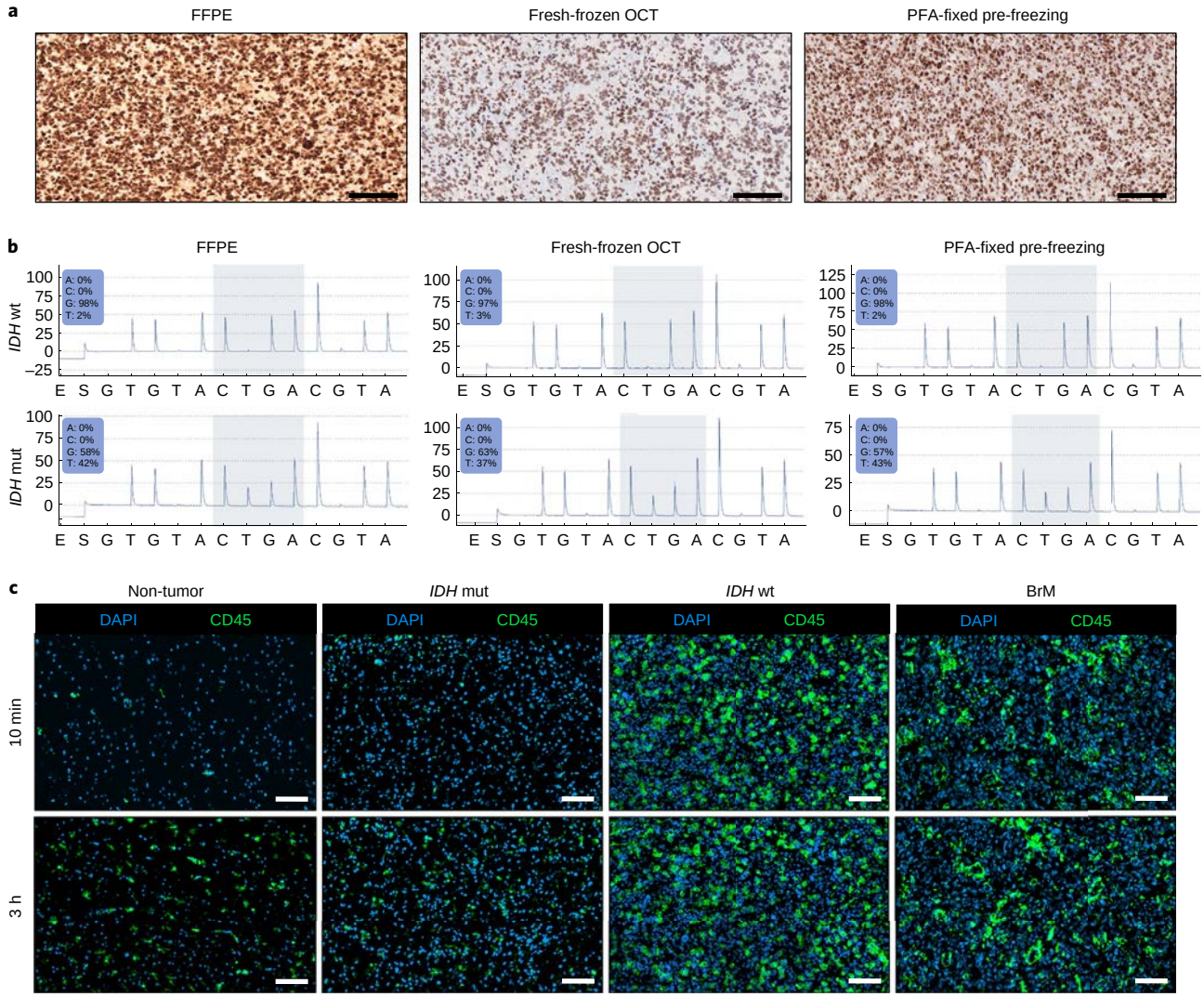

Fig. 4 | Examples of IF staining across different brain (tumor) tissues. a, Representative image of an IHC staining of the ATRX transcription regulator in FFPE tissue, tissue freshly frozen directly in OCT compound and postfixed with PFA, and tissue PFA-fixed prior to OCT embedding, in a partitioned *IDH* wt glioma sample. Scale bars, 100 µm. **b**, *IDH1* pyrosequencing pyrograms depicting the TGACNACCTATGATGAT sequence, from partitioned *IDH* wt and *IDH* mut glioma tissue after either FFPE, fresh freezing in OCT, or pre-fixing with PFA prior to OCT embedding. The shaded region highlights codon 132. Control cutoff values for *IDH1* wt diagnosis were CGA ≥97% and CTA ≤3%. **c**, Representative IF images of non-tumor brain, *IDH* mut and *IDH* wt gliomas and BrM (from lung primary tumor), stained with mouse anti-human CD45 polyclonal antibody after 10 min or 3 h permeabilization with PBS + 0.2% Triton. Scale bars, 100 µm.

adapted to ensure consistent results across different tissues, e.g., time of permeabilization, as discussed in the section above regarding the initial processing of tissue (see also Fig. 4c)

- Secondary antibody-alone staining controls should be performed in parallel with each tissue staining to exclude artifacts resulting from unspecific secondary antibody binding. These controls are also critical to determine the background autofluorescence of the stained tissue. To minimize technical variability, we advise performing such control stainings on a consecutive tissue section, ideally mounted on the same slide
- An isotype control staining should be performed at least once in parallel to a matched antibody-stained tissue to rule out unspecific binding of the antibody. Again, this control staining should ideally be performed on a consecutive tissue section mounted on the same slide

Tissue dissociation

For more detailed studies of specific immune cell populations, tissue dissociation is required (modules 2, 3). A critical consideration here is the obtained yield of viable cells before deciding on the most suitable downstream analysis modules (Fig. 2). Based on our experience, tissues of ≥30 mm^3

Table 1 | Antibodies we have successfully used in our studies using this protocol

Name	Species	Clone	RRID	Vendor	Cat. no.	Use	Dilution
ATRX	Rabbit	Polyclonal	RRID: AB_1078249	Sigma-Aldrich	HPA001906	IHC	1:100
CCR5 AF647	Rat	HEK/1/85a	RRID: AB_528760	BioLegend	313712	FCM	1:320
CD3 AF488	Mouse	UCHT1	RRID: AB_314060	BioLegend	300406	IF	1:100
CD3 PerCP/Cy5.5	Mouse	HIT3a	RRID: AB_1575008	BioLegend	300328	FCM	1:80
CD4 BV650	Mouse	OKT4	RRID: AB_11149170	BioLegend	317436	FCM	1:200
CD8 PE/Cy7	Mouse	HIT8a	RRID: AB_314118	BioLegend	300914	FCM	1:320
CD11B BV421	Rat	M1/70	RRID: AB_10897942	BioLegend	101251	FCM	1:1,280
CD11B BUV661	Rat	M1/70	RRID: AB_2870249	BD	612977	FCM	1:1,280
CD11C BV605	Mouse	3.9	RRID: AB_2562191	BioLegend	301636	FCM	1:320
CD14 FITC	Mouse	HCD14	RRID: AB_830676	BioLegend	325603	FCM	1:640
CD15	Mouse	MY-1	RRID: AB_305962	Abcam	Ab754	IF	1:100
CD16 BUV737	Mouse	3G8	RRID: AB_2869578	BD	564434	FCM	1:640
CD19 BUV563	Mouse	SJ25C1	RRID: AB_2870201	BD	612916	FCM	1:320
CD25 PE	Mouse	BC96	RRID: AB_314276	BioLegend	302606	FCM	1:80
CD31	Sheep	Polyclonal	RRID: AB_355617	R&D Systems	AF806	IF	1:200
CD45	Goat	Polyclonal	RRID:AB_2889893	LSBio	LS-B14248-300	IF	1:100
CD45 AF647	Mouse	HI30	RRID: AB_389336	BioLegend	304018	IF	1:100
CD45 AF700	Mouse	HI30	RRID: AB_493761	BioLegend	304024	FCM	1:640
CD49D	Rat	PS/2	RRID: AB_1107657	BioXCell	BE0071	IF	1:100
CD49D APC	Mouse	9F10	RRID: AB_2130041	BioLegend	304308	FCM	1:320
CD56 PE/Dazzle	Mouse	HCD56	RRID: AB_2563564	BioLegend	318348	FCM	1:640
CD62L PerCP/Cy5.5	Mouse	DREG-56	RRID: AB_2239105	BioLegend	304824	FCM	1:500
CD66B PE	Mouse	6/40c	RRID: AB_2750202	BioLegend	392904	FCM	1:200
CD66B PE/Cy7	Mouse	G10F5	RRID: AB_2566605	BioLegend	305116	FCM	1:640
CD68	Mouse	KP1	RRID: AB_307338	Abcam	ab955	IF	1:100
CD127 BV510	Mouse	A019D5	RRID: AB_2562304	BioLegend	351332	FCM	1:160
CXCR1 BV711	Mouse	5A12	RRID: AB_2741496	BD	743423	FCM	1:80
CXCR2 AF488	Mouse	5E8/CXCR2	RRID: AB_492938	BioLegend	320712	FCM	1:80
CXCR4 PE	Mouse	12G5	RRID: AB_357076	R&D Systems	FAB170P	FCM	1:25
HLA-DR BV711	Mouse	L243	RRID: AB_2562913	BioLegend	307644	FCM	1:320
Zombie NIR APC-Cy7	NA	NA	NA	BioLegend	423105	FCM	1:500
P2RY12	Rabbit	Polyclonal	RRID: AB_2669027	Sigma-Aldrich	HPA014518	IF	1:600
OmniMAP anti-rabbit HRP	NA	NA	RRID: AB_2811043	Roche	1760-4311	IHC	-
Anti-rat IgG H&L AF647	Donkey	Polyclonal	RRID: AB_2813835	Abcam	ab150155	IF	1:500
Anti-mouse IgG (H+L) AF555	Donkey	Polyclonal	RRID: AB_2762848	Invitrogen	A-32773	IF	1:500
Anti-rabbit IgG (H+L) AF555	Donkey	Polyclonal	RRID: AB_2762834	Invitrogen	A-32794	IF	1:500
Anti-goat DyLight 755	Donkey	Polyclonal	RRID: AB_2556671	Invitrogen	SA5-10091	IF	1:500
DAPI	NA	NA	RRID: AB_2629482	Invitrogen	D1306	IF	1:5,000

or 0.1 g will yield sufficient numbers of viable cells for multiple single cell-based analysis methods, including FCM, FAC sorting and functional ex vivo assays[5]. It is, however, critical to consider the overall immune landscape of different human brain tissue types[5,6]: whereas non-tumor brain tissue is largely devoid of immune cells recruited from the peripheral circulation, it is rich in brain-resident MG; this is also the case for low-grade *IDH* mut gliomas, which additionally exhibit slightly increased numbers of MDMs. Recovering peripherally derived immune cells in sufficient numbers for functional studies or RNAseq from those tissue types may thus be challenging. For such purposes, we recommend anticipating processing a two to three times higher number of samples than what will be required for a statistically meaningful final analysis, considering a substantial degree of sample-to-sample variation and a potentially high number of samples that have to be excluded due to insufficient cell yields. High-grade *IDH* wt gliomas and BrMs, by contrast, contain a more diverse landscape of peripherally recruited immune cells, with elevated numbers of tumor-associated neutrophils (TANs) and T cells particularly in BrMs[5,6]. Generally, viable cell yield will vary depending on the

overall tissue quality and condition as discussed above. Whenever possible, we therefore recommend combining tissue dissociation with the preservation of frozen tissue in parallel as this substantially increases the possibilities for orthogonal TIME investigations and critical cross-method validation studies.

When optimizing the protocol, we compared the recovery of immune cells following different enzymatic and nonenzymatic (mechanical) tissue dissociation protocols to optimize digestion of brain (tumor) tissue into a single-cell suspension (modules 2, 3). This comparison was specifically performed using BrM tissue, in order to assess the recovery of all major immune cell populations from brain tumors that contain the most diverse immune landscape[5,6]. This revealed that mechanical dissociation leads to an overall poor cellular yield (Fig. 5a), emphasizing the importance of the use of enzymatic dissociation methods for these complex tissues. Comparing different enzymatic approaches, i.e., the Miltenyi 'Tumor dissociation kit, human' (TDK), a cold protease[33]- and a liberase TL (Roche)-mediated digestion (adapted from ref. [34]), showed that cold protease treatment is also not optimal for the analysis of immune populations from human brain (tumor) tissue, as relatively few immune cells can be recovered (Fig. 5a). By contrast, both TDK- and liberase TL-based digestion methods yielded comparable amounts of immune cells, and also showed a similar overall brain tumor immune landscape (Fig. 5a,b, Table 2). The manufacturer recommends the digestion of primary brain tumors (i.e., gliomas) be performed with a brain-specific TDK (Miltenyi 'Brain tumor dissociation kit (P)', BTDK), containing the additional enzyme papain. We therefore compared the immune cell landscape in *IDH* wt gliomas processed with either TDK or BTDK, which revealed no significant differences in the recovery of major TIME populations (Fig. 5c). This is particularly important considering that the postsurgery diagnosis of a brain tumor (following the pathologist's review) may occasionally differ from the presurgery diagnosis, i.e., a sample might be processed with the 'opposite' tissue dissociation kit. Our results (Fig. 5c) showed that, even in such cases, samples can be pooled into a global analysis without substantial bias occurring.

As neutrophils are widely considered one of the most fragile immune cell populations, susceptible to mechanical stimulation and subsequent activation, and prone to undergo apoptosis or other forms of cell death during isolation from complex tissues[35], we carefully evaluated TAN recovery and activation phenotype across the different tissue dissociation protocols discussed above. In addition to the overall low cellular yield obtained upon mechanical tissue disruption, this method also recovered relatively fewer TANs (Fig. 5a,b). This was similar for liberase TL-mediated digestion, albeit to a lesser extent (Fig. 5b). Comparing the enzymatic methods further revealed that the cold protease treatment appears to cleave off several TAN surface molecules (including CD66B, CD62L, CXCR1 and CXCR2), which is not the case for liberase TL- or TDK-based protocols (Fig. 5d). Importantly, TANs isolated from TDK-digested brain tumors remain functionally intact, and respond to activation stimuli such as phorbol-12-myristate-13-acetate and complement component 5a (data not shown). In sum, we conclude that the TDK-based tissue dissociation represents the optimal method to investigate TANs in parallel with many other brain TIME populations for further in-depth phenotypic characterization. As described in detail in the 'Procedures' section below, we have thus optimized our specific pipeline in accordance with the manufacturer's recommendations, using the human TDK for BrM tissues and the BTDK for glioma and non-tumor brain dissociation. The orthogonal structure of the pipeline further allowed us to verify the accurate recapitulation of the TIME in brain malignancies obtained by the TDK/BTDK dissociation method, as demonstrated by a high degree of overlap between FCM and IF staining of tissue sections for cell enumeration of the three major myeloid cell populations: MG, MDMs and TANs (Fig. 6a). The gating strategy we employed here to delineate MDMs by FCM (Fig. 8d) yields a continuum of MDM subpopulations at different stages of differentiation from monocyte precursors. For researchers aiming to perform a more in-depth characterization of this specific cell population, we recommend incorporating additional markers that enable a further delineation of specific MDM subsets. For a comprehensive resource of brain TIME MDM subsets and their unique cell surface marker expression, we recommend researchers refer to ref. [6].

FAC sorting and FCM analyses

FAC sorting (modules 2a, 2b) is required for transcriptomic characterization of the different immune populations either by bulk or scRNAseq. We thus assessed sorting purity for the three major myeloid cell populations present in brain tumors: MG, MDMs and TANs. This assessment was performed via reacquisition of the sorted populations by FCM (Fig. 6b), whereby we consistently observed a

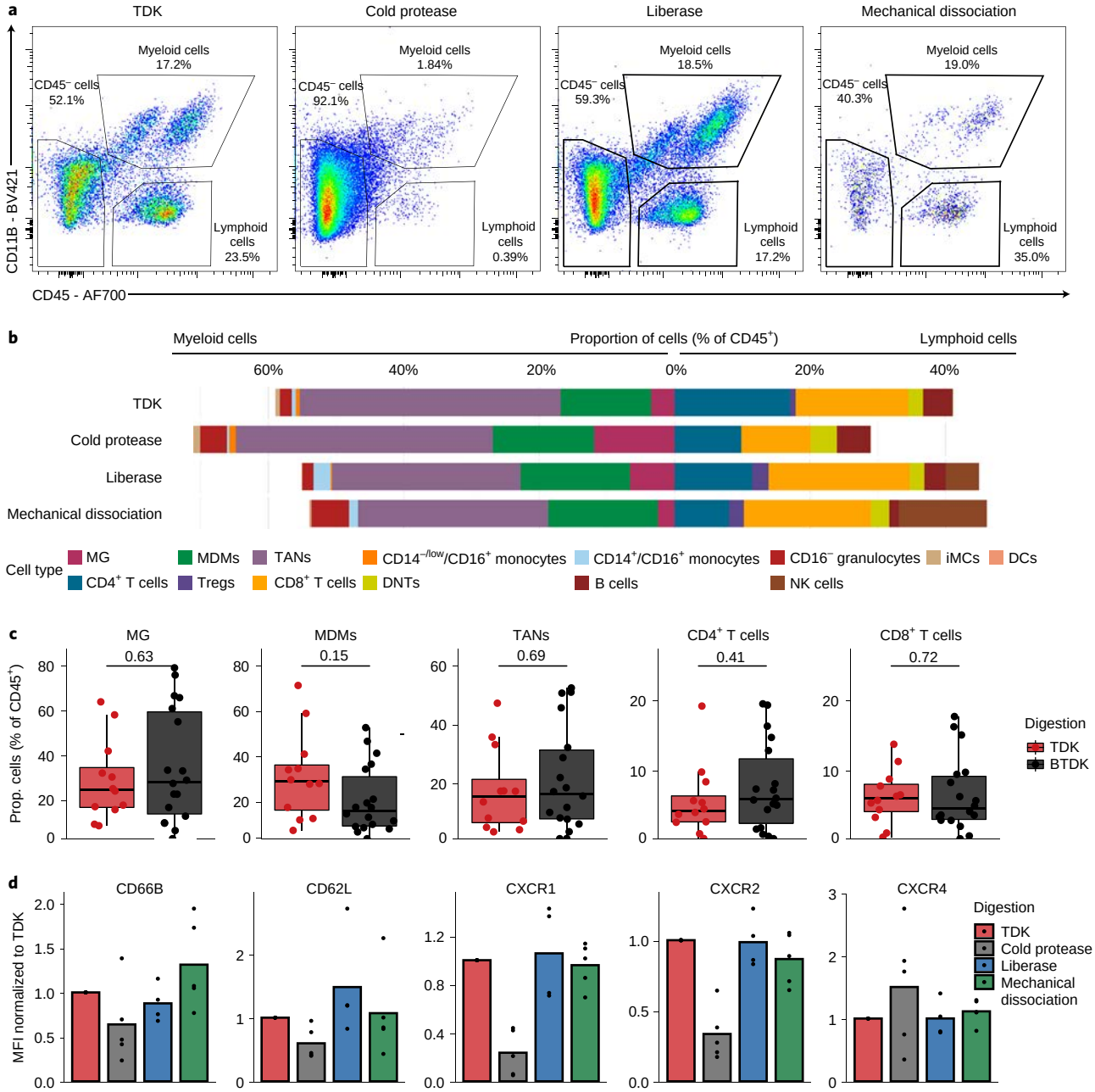

Fig. 5 | Immune cell yield and activation in brain (tumor) tissues differs across tissue dissociation methods. a, Representative FCM plots showing the proportion of non-immune cell ($CD45^-$ cells), myeloid and lymphoid cells after Miltenyi 'Tumor Dissociation Kit, human' (TDK)-, cold protease-, liberase TL (Roche)-mediated digestion or mechanical dissociation within a partitioned BrM tissue sample. Raw FCM data have been deposited at the flow cytometry repository (http://flowrepository.org/): FR-FCM-Z3MF. **b**, Mean of immune cell populations as percent of $CD45^+$ cells in BrM tissues ($n = 4$) after TDK-, cold protease- and liberase TL-mediated digestion and mechanical dissociation. DCs, dendritic cells; DNTs, double-negative T cells; iMCs, immature myeloid cells; Tregs, regulatory T cells. **c**, Proportion of MG, MDMs, TANs, $CD4^+$ and $CD8^+$ T cells of total $CD45^+$ cells by FCM in *IDH* wt gliomas processed by enzymatic dissociation using either TDK ($n = 12$) or brain TDK (BTDK) kits ($n = 18$ independent samples). Plot inset: *P*-value as measured by Wilcoxon rank sum test. **d**, Phenotypic characterization of TANs from different tumor tissues by FCM following TDK ($n_{IDHwt} = 1$, $n_{BrM} = 4$), cold protease ($n_{IDHwt} = 1$, $n_{BrM} = 4$), liberase TL-mediated digestion ($n_{BrM} = 4$) or mechanical dissociation ($n_{IDHwt} = 1$, $n_{BrM} = 4$). Median fluorescence intensity (MFI) normalized to TDK-digested matched samples.

>97% sort purity. The downstream use of cells that were directly FAC-sorted in Trizol LS for RNAseq can therefore be considered reliable in terms of cellular purity.

FAC sorting may also be considered as a means to isolate distinct brain TIME populations at higher numbers for subsequent functional cell culture assays (module 3b). It is critical, however, to evaluate its potential effects on cell viability and activation, if sorted cells are to be further cultured or

Table 2 | Gating strategy for typical results shown in Fig. 8d

Population	Markers	Gate name	Proportion of parent
–	–	Cells	40.1%
–	–	Single Cells FSC	97.7%
–	–	Single Cells SSC	92.7%
–	Zombie NIR$^-$	Live	19.9%
CD45$^-$ cells	Zombie NIR$^-$, CD45$^-$	CD45$^-$	85.5%
Myeloid cells	Zombie NIR$^-$, CD45$^+$, CD11B$^+$	CD45$^+$/CD11B$^+$	8.3%
Lymphoid cells	Zombie NIR$^-$, CD45$^+$, CD11B$^-$	CD45$^+$/CD11B$^-$	5.2%
–	Zombie NIR$^-$, CD45$^+$, CD11B$^+$, CD66B$^+$	CD66B$^+$	44.4%
–	Zombie NIR$^-$, CD45$^+$, CD11B$^+$, CD66B$^-$	CD66B$^-$	53.9%
Neutrophils	Zombie NIR$^-$, CD45$^+$, CD11B$^+$, CD66B$^+$, CD16$^+$	CD16$^+$	98.4%
CD16$^-$ granulocytes	Zombie NIR$^-$, CD45$^+$, CD11B$^+$, CD66B$^+$, CD16$^-$	CD16$^-$	1.0%
CD14$^{-/low}$/CD16$^+$ monocytes	Zombie NIR$^-$, CD45$^+$, CD11B$^+$, CD66B$^-$, CD14$^{-/low}$, CD16$^+$	CD14$^{-/low}$/CD16$^+$	4.0%
CD14$^+$/CD16$^+$ monocytes	Zombie NIR$^-$, CD45$^+$, CD11B$^+$, CD66B$^-$, CD14$^+$, CD16$^+$	CD14$^+$/CD16$^+$	11.6%
–	Zombie NIR$^-$, CD45$^+$, CD11B$^+$, CD66B$^-$, CD14$^{low/+}$, CD16$^-$	CD14$^{low/+}$/CD16$^-$	80.5%
–	Zombie NIR$^-$, CD45$^+$, CD11B$^+$, CD66B$^-$, CD14^{low}, CD16$^-$, CD49D^{med}	CD14$^-$/CD49D^{med}	7.9%
Monocyte-derived macrophages (MDMs)	Zombie NIR$^-$, CD45$^+$, CD11B$^+$, CD66B$^-$, CD14$^+$, CD16$^-$, CD49D^{high}	CD49D^{high}	60.0%
Microglia (MG)	Zombie NIR$^-$, CD45$^+$, CD11B$^+$, CD66B$^-$, CD14$^+$, CD16$^-$, CD49D^{low}	CD49D^{low}	22.9%
Immature myeloid cells (iMCs)	Zombie NIR$^-$, CD45$^+$, CD11B$^+$, CD66B$^-$, CD14^{low}, CD16$^-$, CD49D^{med}, HLA-DR$^-$, CD11C$^-$	HLA-DR$^-$/CD11C$^-$	50.8%
Dendritic cells (DCs)	Zombie NIR$^-$, CD45$^+$, CD11B$^+$, CD66B$^-$, CD14^{low}, CD16$^-$, CD49D^{med}, HLA-DR$^+$, CD11C$^+$	HLA-DR$^+$/CD11C$^+$	42.7%
B cells	Zombie NIR$^-$, CD45$^+$, CD11B$^-$, CD19$^+$, CD3$^-$	CD19$^+$/CD3$^-$	2.2%
–	Zombie NIR$^-$, CD45$^+$, CD11B$^-$, CD19$^-$, CD3$^-$	CD19$^-$/CD3$^-$	20.3%
CD3+ T cells	Zombie NIR$^-$, CD45$^+$, CD11B$^-$, CD19$^-$, CD3$^+$	CD19$^-$/CD3$^+$	71.2%
NK cells	Zombie NIR$^-$, CD45$^+$, CD11B$^-$, CD19$^-$, CD3$^-$, CD56$^+$	CD56$^+$	61.6%
–	Zombie NIR$^-$, CD45$^+$, CD11B$^-$, CD19$^-$, CD3$^+$, CD4$^+$, CD8$^-$	CD4$^+$/CD8$^-$	67.2%
Double-negative T cells (DNTs)	Zombie NIR$^-$, CD45$^+$, CD11B$^-$, CD19$^-$, CD3$^+$, CD4$^-$, CD8$^-$	CD4$^-$/CD8$^-$	4.6%
CD8$^+$ T cells	Zombie NIR$^-$, CD45$^+$, CD11B$^-$, CD19$^-$, CD3$^+$, CD4$^-$, CD8$^+$	CD4$^-$/CD8$^+$	24.6%
CD4$^+$ T cells	Zombie NIR$^-$, CD45$^+$, CD11B$^-$, CD19$^-$, CD3$^+$, CD4$^+$, CD8$^-$, CD25$^-$	CD25$^-$	89.0%
Regulatory T cells (Tregs)	Zombie NIR$^-$, CD45$^+$, CD11B$^-$, CD19$^-$, CD3$^+$, CD4$^+$, CD8$^-$, CD127^{low}, CD25$^+$	CD127^{low}/CD25$^+$	10.0%

used for ex vivo functional assays. Given the above-mentioned fragility of neutrophils, we thus also assessed their activation phenotype post–FAC sorting. Importantly, we observed a substantial induction of CD11B and CD66B, as well as decreased expression of CXCR1 and CXCR2 (canonical neutrophil activation markers), which was not observed to the same extent in TANs isolated via a magnetic bead-based approach (Fig. 6c). Compared with magnetic-activated cell sorting (MACS), FAC sorting thus represents an unfavorable isolation method for this specific cell type for downstream culture assays. We therefore recommend carefully assessing whether similar effects are seen for other brain TIME populations prior to the implementation of this protocol.

Single-cell suspensions of ≤0.5 × 10^6 viable cells can be utilized for FCM analyses of both the overall TIME landscape (using broad panels of immune cell lineage markers) as well as the in-depth phenotypic characterization of individual populations (by designing cell-type specific panels of functional molecules; modules 2a, 2c, Fig. 2)[5]. We generally recommend using 1–2 × 10^5 viable cells per FCM panel, depending on the research question and TIME composition as outlined above. Additionally, aliquots of the single-cell suspension can be frozen for subsequent analyses (e.g., genomic profiling, FCM of thawed cells).

For FAC sorting of individual TIME populations (modules 2a, 2b), we advise using cell suspensions containing ≥0.5 × 10^6 viable cells—again depending on the tissue type, immune cell population of interest, and desired downstream analysis (Fig. 2). As an example, we have successfully employed

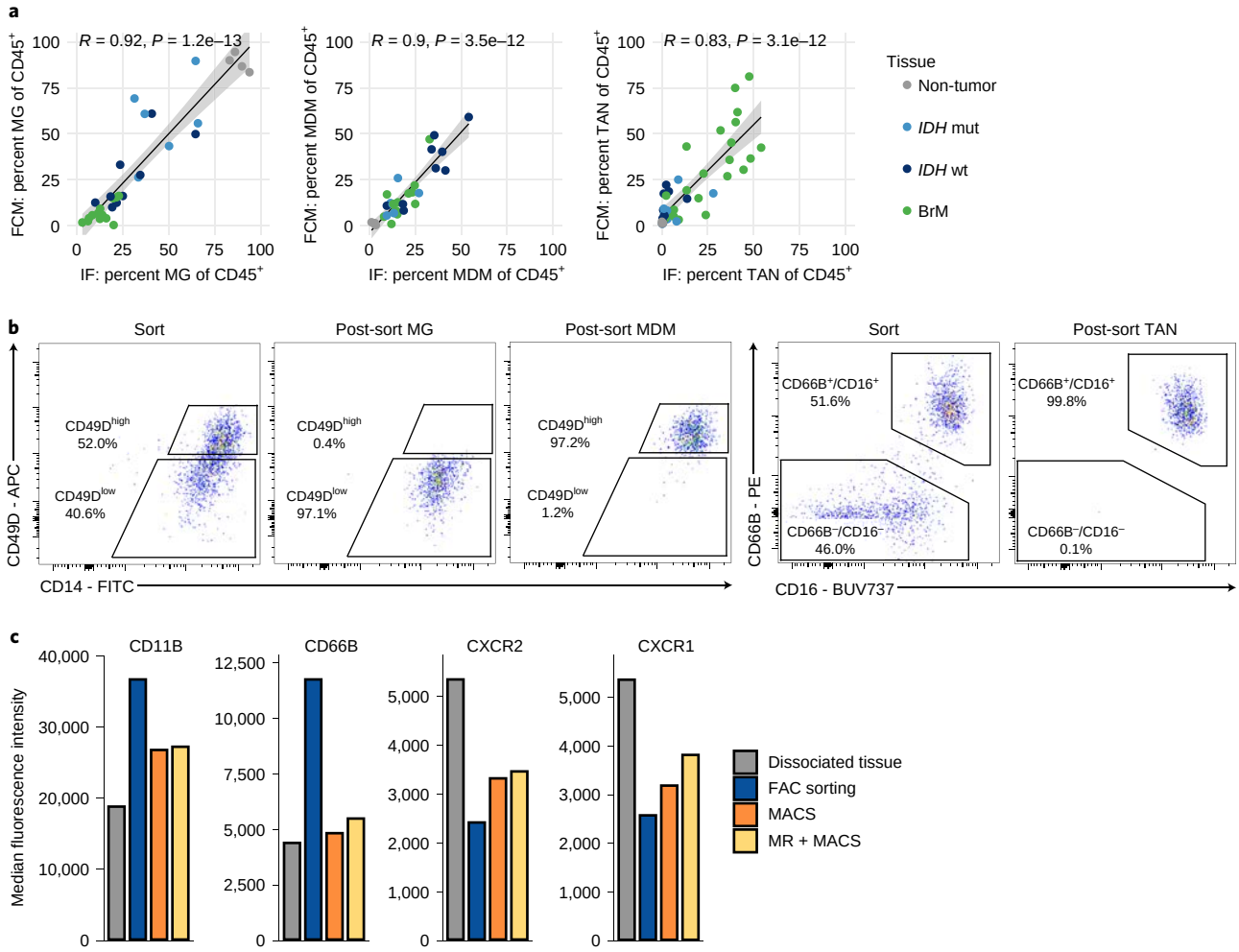

Fig. 6 | Cross-method validation of brain TIME and different isolation methods provide distinct advantages for the extraction of immune cells from brain tumor tissue. a, Scatter plot depicting the abundance of MG, MDMs and TANs (here indicating brain tissue- and tumor-associated neutrophils) as proportion of the CD45$^+$ immune compartment measured by IF versus FCM. MG (CD45$^+$, P2RY12/CD68$^+$, CD49D$^-$), MDMs (CD45$^+$, P2RY12/CD68$^+$, CD49D$^+$) and TANs (CD45$^+$, CD15$^+$, CD31$^-$) can be identified by IF using the mentioned markers (see also Fig. 8a and Table 1). For FCM, MG, MDMs and TANs were identified using the gating strategy as shown in Fig. 8d (see also Tables 1 and 2). Tissue was derived from the same sample and processed independently. For MG and MDM abundance, non-tumor ($n = 4$) and tumor tissues ($n_{IDHmut} = 6$, $n_{IDHwt} = 9$, $n_{BrM} = 13$); for TAN abundance, non-tumor ($n = 4$) and tumor tissues ($n_{IDHmut} = 9$, $n_{IDHwt} = 10$, $n_{BrM} = 22$). Plot inset: Pearson's correlation coefficient and significance. **b**, Representative FCM plots showing TANs (CD66B$^+$/CD16$^+$ as subset of the CD45$^+$/CD11B$^+$ myeloid population), MG (CD49D^{low} as subset of the CD45$^+$/CD11B$^+$/CD66B$^-$/CD16$^-$ population) and MDMs (CD49D^{high} as subset of the CD45$^+$/CD11B$^+$/CD66B$^-$/CD16$^-$ population) during the initial sort and after reacquisition of the sorted populations in an *IDH* wt glioma sample. Percentages shown are indicative of the sort purity. **c**, Representative results of phenotypic characterization of TANs by FCM in dissociated tumor tissue (*IDH* wt glioma) without isolation, FAC-sorted TAN isolation, MACS of TANs and MACS TAN isolation combined with myelin removal (MR).

SMART-seq cDNA library preparation to perform population-based RNAseq of multiple brain TIME populations from 1,000 to 2,000 cells per population, sorted into Trizol LS from a total of 0.5–1 × 10^6 viable cells[5]. A similar cell number can be successfully used to sort live cells or subpopulations for subsequent scRNAseq. If cell numbers permit, FAC sorting can be complemented by additional FCM panel acquisition (module 2c), as well as the freezing of single-cell suspension aliquots.

The amount of input material and cell/tissue type required for a specific downstream functional assay is assay dependent. While FAC sorting may be suitable to obtain sufficient cells for robust and highly abundant TIME populations, alternative methods such as magnetic bead-based isolation protocols should be considered for more fragile populations, e.g., neutrophils (as discussed above, Fig. 6b). In our experience, cell suspensions of ≥2 × 10^6 viable cells from different brain tumors usually yield sufficient numbers of TANs for functional ex vivo assays (module 3b) upon isolation by magnetic beads; however, a substantial amount of biological variability can occur depending on the tumor type (Fig. 2). Additionally, whole-tumor MEC (module 3a) can be established by plating cells

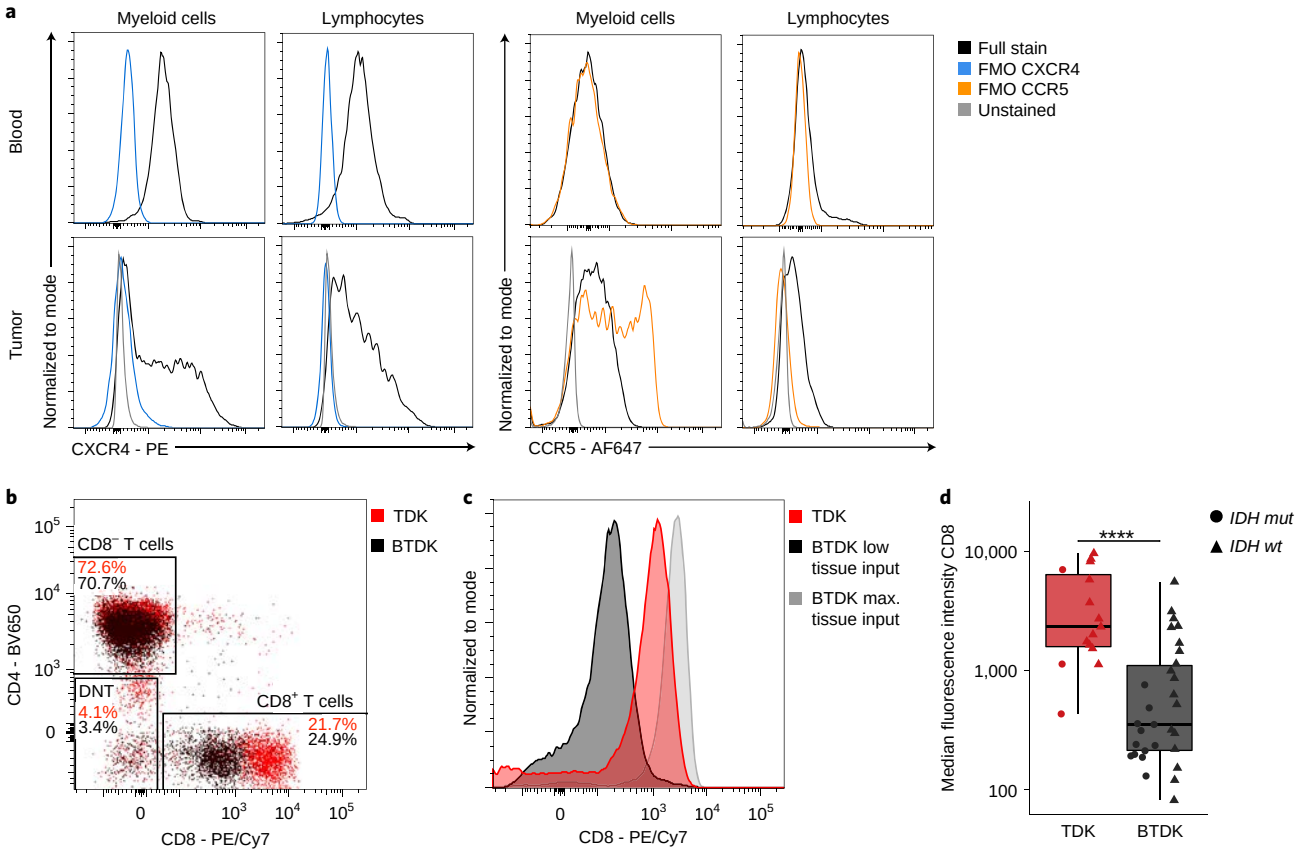

Fig. 7 | FCM controls to be considered for pipeline implementation. a, MFI of CXCR4–PE and CCR5–AF647 in both myeloid cells and lymphocytes in blood versus brain tumor cell suspension in a complete FCM staining panel compared with FMO controls and unstained cells (see Table 1 for antibodies used). **b**, Representative FCM plot of $CD3^+$ T cells from a partitioned lung-BrM sample after digestion with either TDK or BTDK, stained for CD4 and CD8 (see Table 1 for antibodies used). **c**, Representative FCM histogram of the expression of CD8 in $CD3^+$, $CD4^-$ T cells from a partitioned lung-BrM sample after digestion with TDK, BTDK with low tissue input (0.18 g), or BTDK with maximum tissue input (0.8 g, see Table 1 for antibodies used). **d**, MFI of CD8–PE/Cy7, as measured by FCM, across nonmatched glioma samples either treated by TDK ($n_{IDHmut} = 3$, $n_{IDHwt} = 12$) or BTDK ($n_{IDHmut} = 12$, $n_{IDHwt} = 18$) digestion. Wilcoxon rank-sum test; $^{****}P < 0.0001$.

at a density of 2×10^6 cells/ml (Fig. 2)[5]. These cultures can be used to harvest conditioned medium (CM) for ex vivo education assays[5] (module 3b). Such assays enable the in vitro recapitulation of the altered phenotypes observed in certain TIME populations, such as MDMs[5]. We provide here a protocol for the generation of microenvironment culture-conditioned media (MEC-CM); however, we do not include a detailed protocol for the setup of such education assays. For details on how these assays can be performed, we refer researchers to ref. [5].

Controls for FCM analyses and FAC sorting

As for other tissue types, several important controls must be included when performing FCM or FAC sorting on human brain (tumor) samples:

- All antibodies should be titrated for an optimal separation of positive and negative cell populations. For complex multicolor panels, we advise first consulting with a specialist in FCM for optimal panel design
- For multicolor panels, fluorescence minus one (FMO) controls should be performed at least once for each tissue type analyzed (i.e., blood and brain (tumor) tissue), and carefully evaluated for each population of interest, to ensure correct interpretation in the context of data spread due to multiple fluorochromes. Figure 7a illustrates the importance of this point: while the signal for CXCR4-PE in both the myeloid and lymphoid population is substantially higher than the FMO control, this is not the case for CCR5-AlexaFluor 647 in myeloid cells within the brain tumor tissue (Fig. 7a, see Table 1 for the antibodies used). We thus advise carefully evaluating each marker and fluorophore channel across all measured tissues and cell populations

Box 1 | Processing of matched peripheral patient blood

Additional materials required
- Ficoll Paque Plus (GE Healthcare, cat. no. 17-1440-02)
- 7.5 ml EDTA tubes (Sarstedt, cat. no. 01.1605.001)

Procedure

● Timing Steps 1–2A: 1 h 30 min; Step 2B: 1 h 30 min

1 Collect 10 ml whole patient blood in EDTA tubes prior to brain surgery.

2 For plasma and PBMC isolation, follow option A; for FCM analysis and FACS, follow option B. These two options can be carried out in parallel if both are required for a specific experiment.

(A) **PBMC isolation**

(i) Transfer 4 ml of whole blood into a 15 ml conical tube.

(ii) Centrifuge at 680*g* without brakes for 5 min at RT.

(iii) Collect the supernatant/plasma in a cryovial, without disturbing the pellet; retain the pellet for the next step.

■ **PAUSE POINT** The plasma can be frozen at −80 °C for several months.

(iv) Pipet a volume of Ficoll equal to the blood pellet into a 15 ml conical tube.

(v) Dilute the blood pellet with an equal volume of PBS, and carefully layer it on top of the Ficoll.

(vi) Centrifuge at 540*g* without brakes for 20 min at RT.

(vii) Collect the white interphase containing PBMCs, and wash with PBS.

(viii) Centrifuge the PBMCs at 400*g* for 5 min at 4 °C.

(ix) Resuspend the cell pellet in precooled cell freezing medium, transfer to cryovial and freeze down to −80 °C in a controlled rate container.

■ **PAUSE POINT** Frozen PBMCs can be stored at −80 °C for several weeks or in liquid nitrogen for several months. If PBMCs are to be used for DNA extraction, WES library preparation and sequencing, refer to Steps 46C–49 of the main procedure.

(B) **FCM analysis and FAC sorting of whole blood**

(i) Transfer 500 µl whole blood into a 50 ml conical tube, add 10 ml of RBC lysis buffer and incubate at RT for 10 min.

(ii) Centrifuge lysed whole blood at 400*g* for 10 min at 4 °C.

(iii) If RBC lysis is not complete (indicated by cell pellet having a red tinge), repeat RBC lysis.

(iv) Wash cells once with PBS, and start the FCM staining as described in Step 19A of the main procedure.

- Single-color compensation controls have to be performed each time a sample is acquired. Due to the limited amount of available tissue, compensation beads can be utilized instead of the cell suspension. When working with violet or ultraviolet fluorophores, the use of UltraComp beads (Thermo Fisher) is particularly recommended to reduce bead autofluorescence
- It is critical to ensure technical consistency of the flow cytometer setup when comparing data acquired at different time points. One possibility is the regular acquisition of CS&T or Rainbow Beads to ensure consistent read-out across the detection channels. Recent publications further suggest additional controls that can be implemented for longitudinal comparative FCM studies[36]. We advise consulting with a specialist before initial sample acquisition
- For any enzymatic tissue dissociation, antigens may be cleaved by digestion enzymes as an off-target effect. In our experience, this is the case for the T-cell surface protein CD8 when small tissue amounts are dissociated using an enzyme mix containing the peptidase papain, such as the Miltenyi 'Brain Tumor Dissociation Kit (P)' used in this protocol for non-tumor brain and glioma tissue digestion. Importantly, this was more pronounced when small tissue amounts were processed (well below the recommended maximum quantity per digestion reaction), as the ratio of enzymes to tissue input material is higher. While this did not impede $CD8^+$ T-cell identification, the observed mean fluorescence intensity was lower than in samples digested using other enzymes (Fig. 7b–d; Table 2). Thus, a careful validation of all antigens of interest following enzymatic digestion is strongly advised

Recommendations for the parallel processing of matched patient blood

All of the above analyses can be augmented by the parallel processing of matched blood from the same patient (Box 1), which allows the researcher to interrogate local (TIME) versus systemic (blood) immune cell alterations in brain tumor patients. Moreover, matched healthy tissue is critical for genomic profiling of tumors as it allows one to correct for germline variations. Given that numerous protocols have described the functional isolation of different immune cell populations from human whole blood in extensive detail[37–41], we provide here only a few specific recommendations that are based on our own experience and research questions.

Depending on the amount available, whole blood can be utilized for FCM/FAC sorting, the separation of plasma or serum from the cellular compartment, the extraction of peripheral blood mononuclear cells (PBMCs), and/or the isolation of distinct immune cell subsets by other methods (e.g., magnetic beads). While the amount used for each method will inevitably depend on the overall research question, we have found that 0.5 ml of whole blood is sufficient for successful

population-based RNAseq analysis of all major blood immune cell populations (from 2,000 sorted cells, as discussed above)[5]. Similarly, 1–2 ml of blood yields sufficient numbers of neutrophils and T cells, which can be used for multiple downstream functional assays. Plasma, serum and/or PBMCs can be isolated from any given whole-blood volume and frozen for subsequent analyses.

Expertise needed to implement the protocol

As this protocol is focused on the processing of fresh human tissue, it is crucial to establish a close collaboration between the neurosurgeons and operating room staff, the pathology department and the researchers. Any delays in this tissue-handling chain can negatively impact tissue quality and research findings.

Due to the parallel nature of several steps during sample processing, this pipeline requires at least two laboratory researchers working in tandem. This ensures that handling times of fresh clinical samples are kept as short as possible. Given the modularity of our protocol, however, steps can easily be prioritized (as described above) and certain modules omitted if necessary.

Because some modules of the procedure are carried out on frozen material (Steps 20–49), these steps can be performed at a later time point after completion of the steps that must be carried out immediately on fresh tissue (Steps 1–3 and 4–19, see Timing). While intrinsically linked to module 1, we have placed the deferred steps at the end of this protocol to increase its readability at the lab bench. Whereas Steps 20–49 can be undertaken on most samples, Steps 4–19 require larger tissue amounts and are not always feasible in every study.

While most steps of the protocol can be performed by a scientist or technician with standard tissue culture expertise, specific experience is required for the cryosectioning of OCT-embedded tissue, and experience in multiparametric FCM is required to perform FAC sorting. Furthermore, access to core facilities such as a next-generation sequencing facility is required for several downstream modules (e.g., population-based RNAseq, scRNAseq and WES). To review samples for tumor content, collaboration with a pathologist is critical.

Limitations

The main limitation of this protocol is the size of the tissue used as a starting material. This will determine which modules of the pipeline can be performed. Recommendations on tissue quantities required to achieve an expected yield in terms of cell numbers are included throughout the protocol (see also Fig. 2). However, the complementary nature of this modular pipeline allows the researcher to easily prioritize certain modules over others. A priori knowledge of the anticipated TIME in a given tumor sample, e.g., TAN or T-cell abundance in low-grade glioma versus BrM[5,6], will further guide this prioritization.

The tissue dissociation part of the pipeline is tailored to the isolation of immune cells from nonmalignant brain tissue and brain tumors, but has not been specifically optimized for the investigation of non-immune cell populations such as oligodendrocytes, neurons, endothelial cells or pericytes. This is further complicated by our use of a myelin-removal step in non-tumor brain and glioma samples, which potentially depletes myelin-associated cells, e.g., oligodendrocytes from the cell suspension. As a possible alternative, the myelin-bound fraction could be subjected to a Percoll density gradient to recover these cells[42].

Materials

Biological materials

- Human brain tissue samples ▲ **CRITICAL** The specific procedure described here has been optimized for use on non-tumor brain tissue, *IDH* mut and *IDH* wt gliomas and BrMs as shown in ref. [5] and examples provided in the 'Anticipated results' section.
- Matched human peripheral blood. As discussed in the introduction, the use of matched human peripheral blood might be required for certain studies such as WES (Box 1) ▲ **CRITICAL** All work involving human tissue must be approved by the local or institutional ethics committee prior to sample collection, and researchers need to abide by the local rules for the handling of biohazardous materials. Informed consent must be obtained for the use of all samples prior to handling, as well as for the publication of results thereof. Informed consent was obtained prior to surgery from all whose brain tissue and peripheral blood were used to provide the results shown in this protocol. All experiments undertaken to provide the results shown here were approved by the respective institutional and national research committees (at CHUV Lausanne: Commission cantonale d'éthique de la recherche sur l'être humain (CER-VD) protocol PB 2017-00240, F25/99; at MSKCC New York: protocols #06-107, #14-230).

Reagents

- Deionized water
- Liquid nitrogen **! CAUTION** Contains refrigerated gas, may cause cryogenic burns or injuries. May cause frostbites, can displace oxygen and cause rapid suffocation. Handle only with face shield and cryogenic gloves. Do not handle in closed spaces.
- Dry ice **! CAUTION** When thawing, dry ice may displace oxygen and cause rapid suffocation. Do not use in small confined spaces. Contact with dry ice may cause cold burns or frostbite. Wear cold-insulating gloves and eye protection.
- 2-Methylbutane (Sigma-Aldrich, cat. no. 59070) **! CAUTION** Extremely flammable liquid and vapor, may be fatal when swallowed or inhaled, may cause drowsiness or dizziness, harmful to aquatic life with long lasting effects if discarded inappropriately. Handle only in a chemical fume hood, and store at 4 °C in an explosion-proof fridge.
- OCT compound (Tissue-Tek, Sakura Finetek, cat. no. 4583)
- Paraformaldehyde (PFA) 32% solution, EM grade (Electron Microscopy Sciences, cat. no. 15714-S) **! CAUTION** May cause cancer. Harmful if swallowed or inhaled. Causes skin irritation and serious eye damage. May cause an allergic skin reaction and respiratory irritation. Suspected of causing genetic defects. Handle only in a chemical fume hood and wear gloves and eye protection.
- D(+)-sucrose for molecular biology (PanReac AppliChem, cat.no. A2211,1000)
- Methanol (Acros Organics, Fisher Scientific, cat. no. 10317360) **! CAUTION** Highly flammable liquid and vapor, toxic if swallowed, toxic in contact with skin, toxic if inhaled, causes damage to organs. Handle inside a chemical fume hood.
- PBS (Gibco, ThermoFisher, cat. no. 20012027)
- Tween 20 (PanReac AppliChem cat. no. A4974)
- Triton X-100 (PanReac AppliChem, cat. no. A4975) **! CAUTION** Harmful if swallowed, causes serious eye damage. Handle with gloves and safety goggles.
- Blocking reagent (Perkin Elmer, cat. no. FP1012), 'PNB'
- Normal donkey serum (Sigma Aldrich, cat. no. S30-M)
- BSA (Jackson ImmunoResearch, cat. no. 001-000-162)
- Fluorescence mounting medium (Dako, cat. no. S3023) **▲ CRITICAL STEP** Use of a different mounting medium can result in a change of staining quality, especially concerning cell nuclear markers e.g., DAPI.
- RIPA (Pierce, ThemoFisher, cat. no. 89900) **! CAUTION** Causes serious eye irritation. When handling this compound, wear safety goggles.
- cOmplete EDTA-free protease inhibitor (Roche, cat. no. 11836170001) **! CAUTION** Causes skin irritation, causes serious eye damage. Wear gloves, laboratory coat and safety goggles when using this compound.
- BCA protein assay (Pierce, ThermoFisher, cat. no. 23225)
- Hanks' Balanced Salt Solution (HBSS; Gibco, ThermoFisher, cat. no. 14175129)
- Brain Tumor Dissociation Kit (P) (Miltenyi, cat. no. 130-095-942)
- Tumor Dissociation Kit, human (Miltenyi, cat. no. 130-095-929)
- 10× red blood cell (RBC) lysis buffer (BioLegend, cat. no. 420301) **! CAUTION** Very toxic to aquatic life with long-lasting effects if discarded inappropriately. Avoid release into the environment.
- Myelin Removal Beads II (Miltenyi, cat. no. 130-096-433)
- Trypan Blue solution, 0.04% (Gibco, ThermoFisher, cat. no. 15250061) **! CAUTION** May cause cancer, suspected of damaging fertility or the unborn child. Handle with gloves and inside a tissue culture hood.
- FBS (Gibco, ThermoFisher, cat. no. 10270106)
- Dimethylsulfoxide (PanReac AppliChem, cat. no. A3672)
- DMEM/F12 + GlutaMAX (Gibco, ThermoFisher, cat. no. 31331028)
- Penicillin–streptomycin (Gibco, ThermoFisher, cat. no. 15140122)
- UltraPure DNase/RNAse-free distilled H_2O (Invitrogen, Thermo Fisher, cat. no. 10977035)
- Zombie NIR fixable viability dye (BioLegend, cat. no. 423105)
- Human TruStain FcX Fc receptor blocking solution (BioLegend, cat. no. 422301)
- Brilliant Stain buffer (BD; cat. no. 563794)
- 0.5 M EDTA (Invitrogen, ThermoFisher, cat. no. 15575020)
- Foxp3/Transcription Factor Staining Buffer Set (eBioscience, Thermo Fisher, cat. no. 00-5523-00) **! CAUTION** May cause an allergic skin reaction, suspected of causing genetic defects, may cause cancer. When handling this compound, wear gloves and a laboratory coat.

- Trizol LS (Sigma-Aldrich, cat. no. T3934) **! CAUTION** Toxic if swallowed, toxic in contact with skin, toxic if inhaled, causes severe skin burns and eye damage, suspected of causing genetic defects, may cause damage to organs through prolonged or repeated exposure, toxic to aquatic life with long-lasting effects if discarded inappropriately. Use in a chemical fume hood only, and handle with gloves. **▲ CRITICAL STEP** For RNAseq of FAC-sorted populations, it is critical to use Trizol LS instead of regular Trizol, as FAC sorting of cells will yield an aqueous droplet (Trizol LS enables lysis of one volume biological liquid per three volumes of Trizol LS).
- Anti-human CD66B-Biotin (Miltenyi, cat. no. 130-118-983)
- Anti-Biotin MicroBeads UltraPure (Miltenyi, cat. no. 130-105-637)
- Trypsin-EDTA (0.05%) (Gibco, ThermoFisher, cat. no. 25300062)
- DNAeasy Blood & Tissue kit (Qiagen, cat. no. 69504).
- SureSelect Human All Exon V7 exome kit (Agilent, cat. no. 16-rxn 5191-4004, 96-rxn 5191-4005)
- Qubit dsDNA HS Assay Kit (ThermoFisher, cat. no. Q32851)

Reagent setup

▲ CRITICAL Prepare all reagents under sterile conditions in a laminar flow biosafety cabinet.

PBS 0.2% (vol/vol) Tween 20 (PBS-T)
Add 2 ml Tween 20 to 998 ml of PBS, and mix to dissolve. Can be stored at room temperature (RT, 21–26 °C) for up to 3 months.

PBS 0.2% (vol/vol) Triton X-100
Add 2 ml Triton-X to 998 ml of PBS, and mix to dissolve. Can be stored at RT for up to 3 months.

1× (0.5% wt/vol) PNB (1×)
Slowly add 0.2 g blocking reagent to 40 ml of PBS in a 50 ml conical tube, place in water bath on laboratory hotplate, heat to 55 °C and periodically agitate tube to completely dissolve blocking reagent. Prepare aliquots as needed, and store at −20 °C; once thawed, use within 24 h.

PNB + 0.5% (vol/vol) Tween 20 (PNB-T)
Add 200 µl Tween 20 to 39.8 ml of 1× PNB, filter using a 0.4 µm syringe filter. Prepare aliquots as needed, and store at −20 °C; once thawed, use within 24 h.

IF blocking buffer
Add 2 ml (10% vol/vol) donkey serum and 0.4 g (2% wt/vol) BSA to 18 ml of PNB-T; filter using a 0.4 µm syringe filter. Prepare aliquots as needed, and store at −20 °C; once thawed, use within 24 h.

Cell lysis buffer for protein extraction
Dissolve one cOmplete EDTA-free protease inhibitor tablet in 10 ml of RIPA buffer. Can be stored at 4 °C for up to 1 week.

1× RBC lysis buffer
Dilute 1 ml of 10× RBC lysis buffer concentrate with 9 ml of deionized water. Can be stored at 4 °C for up to 3 months.

MACS buffer
Dissolve 2.5 g BSA (0.5% wt/vol) in 500 ml of PBS, pass solution through a vacuum filtration flask and de-gas by applying negative pressure for 30 min; avoid agitation of degassed buffer to prevent reintroduction of gas into solution. Can be stored at 4 °C for up to 4 weeks.

Cell freezing medium
Add 1 ml dimethylsulfoxide to 9 ml FBS. Prepare fresh before use.

Complete medium
Add 50 ml of FBS and 5 ml of penicillin–streptomycin to 445 ml of DMEM/F12. Can be stored at 4 °C for up to 4 weeks.

FAC-sorting buffer

Dissolve 2.5 g BSA (0.5% wt/vol) in 498 ml of PBS, add 2 ml of 0.5 M EDTA (2 mM final concentration), pass solution through vacuum filtration flask and de-gas by applying negative pressure for 30 min; avoid agitation of degassed buffer to prevent reintroduction of gas into solution. Can be stored at 4 °C for up to 4 weeks.

Equipment

- Laboratory balance (Ohaus, cat. no. PA2102)
- Dewar flask (Nalgene, Fisher Scientific, cat. no. 4150-2000)
- Polypropylene measurement cup, 100 ml (Fisher Scientific, cat. no. 10717732)
- Polypropylene tray, ~10 × 12.5 ml (use pipette tip box or rack lid)
- Cryostat (Thermo Scientific, CryoStar NX70)
- Staining dish (Tissue Tek, Sakura Finetek, cat. no. 4457)
- Slide holder (Tissue Tek, Sakura Finetek, cat. no. 4465)
- Laboratory shaker (Labnet, cat. no. S100-A-B-230)
- Humified chamber (line slide box with moist paper tissue) or commercial ten-slide tray (StatLab, cat. no. LWS10BK)
- Table top microcentifuge (Eppendorf, cat. no. 5427 R)
- Slide scanner (Zeiss, Axio Scan.Z1)
- Rotor/stator tissue homogenizer with a ⌀ 5–7 × 115 mm saw tooth stainless steel probe (Omni International, cat. no. TH220)
- gentleMACS Octo dissociator with heaters (Miltenyi, cat. no. 130-096-427)
- Table top centrifuge (Eppendorf, cat. no. 5810 R)
- MACS MultiStand magnet separator stand (Miltenyi, cat. no. 130-042-303)
- MiniMACS separator (Miltenyi, cat. no. 130-042-102)
- MidiMACS separator (Miltenyi, cat. no. 130-042-302)
- Cell freezing container (CoolCell, cat. no. BCS-405)
- Multicolor flow cytometer (BD LSR II/Fortessa)
- Multicolor fluorescence-activated cell sorter (BD FACSAria)
- NanoDrop One spectrophotometer (ThermoFisher, cat. no. ND-ONEC-W)
- Qubit fluorometer (Invitrogen, ThermoFisher cat. no. Q33238)
- General laboratory equipment, e.g., micropipettes, pipetting aids, CO_2 cell culture incubators

Consumables

- 60 mm diameter Petri dish (Corning, cat. no. 353002)
- N°10 blade single-use scalpel (Swann-Morton, cat. no. 0501)
- Single-use tweezers (PharmaPlast, cat. no. 84011022)
- Cryovial (Sarstedt, cat. no. 72.380)
- Cryomold (Tissue-Tek, Sakura Finetek, cat. no. 4557)
- Household aluminum foil
- Superfrost Plus microscope slides (Fisher Scientific, cat. no. 12-550-15)
- 24 × 60 mm #1 cover slips (ThermoFisher, cat. no. BB02400500A113FST0)
- Hydrophobic barrier pen (Daido Sangyo, Plano, cat. no. 22304)
- PVDF 0.4 µm syringe filter (ThermoFisher, cat. no. CH4525-PV)
- 50 ml conical tube (Greiner Bio-One, cat. no. 227261)
- gentleMACS C-tubes (Miltenyi, cat. no. 130-093-237)
- 40 µm cell strainer (Corning, cat. no. 352340)
- Vacuum filter system with 500 ml flask (Merck Millipore, cat. no. S2GPU05RE)
- LS and/or MS MACS columns (Miltenyi, cat. no. 130-042-401 and/or 130-042-201)
- Neubauer disposable hemocytometer (INCYTO, cat. no. DHC-N01-5)
- 15 ml conical tube (Greiner Bio-One, cat. no. 188271)
- 5 ml FAC-sorting tubes (Corning, cat. no. 352052)
- Tissue culture flask 25 ml (Corning, cat.no. 353136)
- Six-well plates (Corning, cat. no. 3506)
- 3 ml syringes (B. Braun, cat. no. 4616025V)
- General laboratory consumables, e.g., pipette tips, serological pipettes

Procedure

Initial processing, freezing and tissue embedding of freshly resected human brain (tumor) tissue (modules 1a,b) ● Timing 30 min

1 Place the resected human brain (tumor) tissue in a Petri dish, resect any cauterized tissue with a scalpel and weigh the remaining pieces.
▲ CRITICAL STEP Perform all steps under sterile conditions in a laminar flow biosafety cabinet.

2 With a scalpel, cut the brain (tumor) tissue into pieces of ~3–8 mm^3.
▲ CRITICAL STEP Ensure that the tissue pieces selected for freezing and/or embedding are representative of the intrasample heterogeneity.

3 For direct freezing in OCT compound, follow option A; for snap-freezing of brain (tumor) tissue, follow option B; or for freezing of PFA-fixed tissue, follow option C. See Box 1 for details of how to undertake parallel processing of matched patient blood (isolation of plasma and PBMCs).

(A) **Direct freezing in OCT of brain (tumor) tissue**
▲ CRITICAL STEP A minimum tissue size of 8 mm^3 is required to ensure tissue integrity for downstream spatial analysis by IF staining.

(i) Fill a small plastic tray with 2-methylbutane, and place on dry ice inside the ice pan.
! CAUTION 2-Methylbutane is toxic and explosive and needs to be used in a chemical fume hood. 2-Methylbutane must be stored at 4 °C in an explosion-proof fridge.

(ii) Place a small amount of OCT into a Cryomold, add the brain (tumor) tissue piece and slowly pour OCT on top of the tissue until mold is filled, without introducing any air bubbles.

(iii) Place two or three dry ice pellets inside the 2-methylbutane container, and wait for bubbling to stop, which indicates a temperature of −80 °C of the 2-methylbutane liquid.

(iv) Dip the Cryomold into the 2-methylbutane container using tweezers while holding it horizontally, and wait for the OCT to freeze and turn solid white (~2–3 min).

(v) Store frozen OCT block at −80 °C till further use in Step 20.
■ PAUSE POINT Frozen OCT tissue blocks can be kept at −80 °C for up to 2–3 years.

(B) **Snap-freezing of brain (tumor) tissue**
▲ CRITICAL STEP A minimum tissue size of 3 mm^3 is required for downstream WES analysis.

(i) Fill a plastic 100 ml measurement cup with 70 ml 2-methylbutane, pour liquid nitrogen into a small laboratory ice pan, place measurement cup in liquid nitrogen and wait for crystals to form on the inside of the plastic cup indicating that 2-methylbutane is sufficiently cooled.
! CAUTION 2-Methylbutane is toxic and explosive and needs to be used in a chemical fume hood. 2-Methylbutane must be stored at 4 °C in an explosion-proof fridge.

(ii) Place a brain (tumor) tissue piece on aluminum foil, and submerge in cold 2-methylbutane for 2–3 min. The tissue color will change to a paler shade when completely frozen.
▲ CRITICAL STEP Depending on downstream assays being undertaken, pieces might be needed for proteomics (further preparation described in Step 38) and/or for tissue disruption, homogenization and digestion for WES (detailed in Step 46). If such assays are performed, keep an adjacent part of the tissue for tissue integrity and composition analysis (IHC, IF).

(iii) Transfer frozen brain (tumor) tissue piece into a cryovial and store at −80 °C till further use in Step 38 for downstream proteomic analysis and/or Step 46 for WES.
■ PAUSE POINT Snap-frozen tissue can be kept at −80 °C for up to 2–3 years.

(C) **Freezing of PFA-fixed brain (tumor) tissue**

(i) Prepare a 4% PFA solution diluted in PBS, and fill up a 15 ml conical tube.

(ii) Place a brain (tumor) tissue piece in the 4% PFA solution at 4 °C overnight.

(iii) Decant the 4% PFA solution, and replace with sucrose 30% and place at 4 °C overnight.

(iv) Wait till the tissue floats in the sucrose solution, then collect the tissue.

(v) Place a small amount of OCT into a Cryomold, add the brain (tumor) tissue and slowly pour OCT on top of tissue until mold is filled, without introducing any air bubbles.

(vi) Place the Cryomold on dry ice, and wait for the OCT to freeze and turn solid white (~2–3 min).

(vii) Store frozen PFA fixed OCT block at −80 °C till further use.
■ PAUSE POINT Frozen OCT tissue blocks can be kept at −80 °C for up to 2–3 years

Enzymatic dissociation of fresh non-tumor brain tissue, gliomas and BrMs (modules 2a–c, 3a,b) ● Timing Steps 4–8: 25 min; Steps 9–12: 35 min for gliomas, 1 h 15 min for BrMs; Steps 13–18: 1 h 30 min for gliomas, 50 min for BrMs

▲ **CRITICAL** If FAC-sorting cells from matched patient blood, see Box 1 for details of the required parallel processing required for the matched patient blood.

4 Remove any cauterized areas of the brain (tumor) tissue from Step 3 that is being used in this section for enzymatic digestion.
▲ **CRITICAL STEP** Enzymatic tissue dissociation must be performed on fresh tissue (not frozen).

5 Weigh the tissue so cell count normalization calculations can be made later.
▲ **CRITICAL STEP** Aim for 300 mg of tissue; however, amounts as low as 100 mg can also yield sufficient cell numbers depending on the cellularity of the tissue piece.

6 In a Petri dish and using a scalpel, cut the tissue into small pieces (<1 mm^3).
▲ **CRITICAL STEP** While cutting tissue, determine the tissue consistency to subsequently select the appropriate dissociation program.

7 Transfer tissue pieces to a 50 ml conical tube. Rinse Petri dish thoroughly with HBSS, and add HBSS to the tissue in the tube to a total volume of 20 ml.

8 Spin at 300*g* for 10 min at RT. Aspirate supernatant completely.
▲ **CRITICAL STEP** To avoid exposing tumor tissue to repeated temperature changes, perform centrifugation steps before dissociation at RT.

9 Perform enzymatic tissue dissociation using the following kits depending on the tumor type:
- For non-tumor brain tissue and gliomas: 'Brain Tumor Dissociation Kit (P)' (BTDK, Miltenyi), based on papain
- For BrMs: 'Tumor Dissociation Kit, human' (TDK, Miltenyi)

10 Resuspend the tissue in dissociation buffer mixed with enzymes in a C-tube (Miltenyi) according to the manufacturer's instructions.
▲ **CRITICAL STEP** These dissociation kits have been selected based on extensive optimization to ensure the highest efficiency of tissue dissociation and a maximum recovery of different immune cell populations (see 'Tissue dissociation' section).
▲ **CRITICAL STEP** Adapt the amounts of enzymes and the number of C-tubes required depending on the amount of processed tissue according to the manufacturer's instructions.
▲ **CRITICAL STEP** Examine the effect of the enzymatic digestion on any antigens of interest used in any of the downstream steps, i.e., cell sorting.

11 Using a gentleMACS Octo Dissociator with heaters (Miltenyi), select the appropriate tissue dissociation program. For non-tumor brain tissues and gliomas, use '37C_BTDK_1'. For BrMs, use one of the following depending on the tissue characteristics:
- '37C_h_TDK_1' for soft tissue
- '37C_h_TDK_2' for medium tissue (this is appropriate in most cases)
- '37C_h_TDK_3' for tough tissue

■ **PAUSE POINT** Dissociation program '37C_BTDK_1' for non-tumor brain tissues and gliomas takes 21 min 48 s, while dissociation programs '37C_h_TDK_1-3' for BrMs require 1 h 1 min. Take this into consideration when processing different tissue types.

12 Invert C-tube making sure that tissue pieces are close to the blades, and insert into dissociator, attach heating sleeve and start program.

13 When the dissociation program has finished, filter the obtained cell suspension through a 40 μm cell strainer into a fresh 50 ml conical tube, and rinse the C-tube and strainer well with HBSS (~20 ml); add to cell suspension for maximum recovery.

14 Spin at 300*g* for 10 min at 4 °C. Aspirate supernatant, leaving 1 ml behind.

15 Perform RBC lysis by adding 20 ml RBC lysis buffer and incubating for 10 min at RT. Stop lysis by adding 20 ml of HBSS.

16 Spin at 400*g* for 10 min at 4 °C. Aspirate supernatant completely.

17 If required, remove myelin using Miltenyi Myelin Removal Beads II according to the manufacturer's instructions. Myelin removal is required for non-tumor brain tissue and gliomas. Usually no myelin removal is required for BrMs.
▲ **CRITICAL STEP** If processing more than 500 mg brain (tumor) tissue, scale up the required volume of myelin removal beads and columns according to the manufacturer's instructions.
? TROUBLESHOOTING

18 Resuspend cells in HBSS, and manually count the number of viable cells via Trypan Blue exclusion using a hemocytometer before further downstream applications (e.g., FCM, FAC sorting, tissue culture, scRNAseq, immune cell isolation for functional assays). Keep cells on ice until further processing.

Processing of the single-cell suspension for further downstream analyses (modules 2a–c and 3a,b)

19 For FCM and FAC sorting, follow option A; for MACS of TANs, follow option B; or for generation of whole-tumor MEC-conditioned medium (CM), follow option C.

(A) **FCM analysis and FAC sorting (modules 2a–c)** ● **Timing 1 h 15 min**

(i) Transfer cell suspension (see Step 18) for FCM or FAC sorting into a 5 ml FAC-sorting tube. Wash with 2 ml of PBS, and spin at 400*g* for 5 min at 4 °C.
▲ **CRITICAL STEP** Aim for 1×10^5 cells as input for FCM analysis (if only data acquisition is desired; module 2c), and 1×10^6 cells for FAC sorting of immune populations for RNAseq (modules 2a,b).

(ii) Resuspend up to 1×10^6 cells in 100 µl of fixable viability dye staining solution (Biolegend; dilute the dye according to manufacturer's instructions, typically 1:500 in PBS).

(iii) Stain for 20 min at RT in the dark.

(iv) Add 5 µl of Fc receptor blocking solution, and incubate for another 10 min at RT in the dark.

(v) For staining of surface molecules, add 105 µl of 2× antibody staining mix in Brilliant Stain Buffer.
▲ **CRITICAL STEP** Prepare the staining mix at a 2× concentration of each desired antibody dilution. While it is recommended to prepare the staining mix fresh just before use, this step can also be performed the previous day if needed and stored at 4 °C in the dark.

(vi) Stain for 15 min at 4 °C in the dark.

(vii) Wash stained cells with FAC-sorting buffer, and spin at 400*g* for 5 min at 4 °C.

(viii) If only FCM acquisition is required (module 2c) and you do not wish to proceed immediate to FAC-sorting analysis, fix cells (e.g., using eBioscience Fixation/Permeabilization solution, FoxP3 staining kit) and store at 4 °C overnight after surface molecule staining. Similarly, staining for intracellular markers can be performed the next day. Otherwise, immediately proceed to the next step.

(ix) Resuspend cells in appropriate amount of FAC-sorting buffer (typically 500 µl to 1 ml) and then filter through a 40 µm cell strainer immediately before sorting.

(x) Proceed to FAC sorting (Box 2). For population-based RNAseq (module 2b), follow step A. For scRNAseq (alternative to module 2b), follow step B.

(B) **MACS of TANs (modules 3a,b)** ● **Timing 1 h 15 min**

(i) Resuspend the single cell suspension obtained following enzymatic tissue digestion (see Step 18) at a concentration of 10×10^6 cells/ml in FAC-sorting buffer in a 15 ml conical tube.
▲ **CRITICAL STEP** The required cell number used as input is highly dependent on the brain (tumor) tissue type and the associated abundance of TANs. Aim for a minimum of 3×10^6 cells.

(ii) Add 1 µl anti-human CD66B-Biotin antibody to 100 µl of the single cell suspension, and mix well.

(iii) Incubate for 10 min at 4 °C.

(iv) Add 1–2 ml FAC-sorting buffer, and centrifuge at 300*g* for 10 min.

(v) Aspirate the supernatant completely, and place the cells on ice for the next steps.

(vi) Resuspend the cell pellet in FAC-sorting buffer. Up to 1×10^8 cells can be suspended in 80 µl FAC-sorting buffer.

(vii) Add 20 µl Anti-Biotin UltraPure beads per 1×10^7 cells, and mix well.

(viii) Incubate for 15 min at 4 °C.

(ix) Add 1–2 ml FAC-sorting buffer, and centrifuge at 300*g* for 10 min.

(x) Aspirate the supernatant, and resuspend in FAC-sorting buffer. Up to 1×10^8 cells can be resuspended in 500 µl FAC-sorting buffer.

(xi) Proceed to MACS of $CD66B^+$ cells with MS or LS columns depending on the total number of cells according to manufacturer's instructions.

Box 2 | FAC sorting of single-cell suspension

Procedure

● Timing A: FAC sorting depending on the tissue input, quality and cell type of interest 30 min to 2 h; B: sample preparation for scRNAseq 20 min

After completion of Step 19 A, follow option A if sorting for subsequent population-based RNAseq and option B if sorting for microfluidic-based scRNAseq.

(A) **For population-based RNAseq (module 2b)**

(i) Sort the desired cell populations directly into 750 µl Trizol LS (Sigma) in 1.5 ml tubes.

(ii) Snap-freeze cells in Trizol LS immediately thereafter by submerging in liquid nitrogen, and transfer to −80 °C for storage until further use (RNAseq).

▲ CRITICAL STEP If FAC sorting is into lysis buffer or Trizol LS, then a 70 µm nozzle can be used to reduce sorting time and volume and increase sorting efficiency. A 100 µm nozzle can be used for sorting live cells, as it causes less mechanical stress to cells.

▲ CRITICAL STEP Aim for 2,000 sorted cells for subsequent RNAseq analysis using a SMART-seq-based cDNA library generation protocol[44]; however, cell numbers <1,000 may also yield sufficient material for analysis.

▲ CRITICAL STEP If sorting large numbers of cells into Trizol LS, ensure that the total volume of sorted cells does not exceed 250 µl to maintain a ratio of 1:3 between Trizol LS and the sorted aqueous droplets.

? TROUBLESHOOTING

(B) **For microfluidic-based scRNAseq (alternative to module 2b)**

(i) Precoat collection tubes (recommended to use polypropylene tubes for minimal cell adherence) by filling with FAC-sorting buffer, and invert for at least 30 min. Discard coating solution, and replace with collection medium.

(ii) Sort the cell populations of interest while maintaining a temperature of 4 °C in the sample chamber.

(iii) Recount single-cell suspension of the dissociated bulk tumor tissue or sorted cell populations using Trypan Blue exclusion method to verify sufficient cell viability.

▲ CRITICAL STEP A high percentage of viable cells (>70%) is essential for successful scRNAseq. Avoid the use of frozen cells as certain immune cell populations such as neutrophils are highly sensitive to freeze–thaw cycles.

▲ CRITICAL STEP When removing dead cells or debris using commercial kits, verify in pilot experiments that these do not deplete immune cell populations based on their intrinsic phosphatidylserine surface exposure[45] or density.

? TROUBLESHOOTING

(iv) Pellet cells by centrifugation at 300*g*, 4 °C for 5 min, remove supernatant and resuspend at the required concentration (e.g., for DropSeq 1×10^5 cells/ml) in PBS + 0.04% (wt/vol) BSA, and proceed to scRNAseq, i.e., DropSeq[46] or 10x Genomics Chromium platform.

(C) **Generation of whole-tumor MEC-CM (modules 3a,b)** ● Timing **24 h (30 min per CM collection)**

(i) Resuspend the single cell suspension obtained following enzymatic tissue digestion (see Step 18) in complete medium at a concentration of 2×10^6 cells/ml.

(ii) Culture the cell suspension in an appropriately sized flask or tissue culture plate at 37 °C, 5% CO_2 and 95% humidity.

(iii) Collect the MEC-CM after 24 h, and replace with fresh complete medium.

(iv) Spin the MEC-CM for 10 min at 300*g*, store at 4 °C before immediate use, or prepare into aliquots and store at −80 °C until further use at a later timepoint.

Fixation and multiplex IF protocol (module 1a) ● Timing Steps 20–30: 5 h 30 min; Steps 31–37: 2 h 45 min

20 Section the frozen OCT-embedded human non-tumor and tumor brain tissues following Step 3A at a thickness of 10 µm using a cryostat, and store in slide boxes at −80 °C.

▲ CRITICAL STEP Two consecutive pieces of tissue need to be sectioned and should ideally be placed on the same slide to ensure proper quality control for IF stainings with isotype and/or secondary-only control staining.

■ PAUSE POINT Tissue sections can be stored at −80 °C for several months.

? TROUBLESHOOTING

21 Take the tissue section slides out of the freezer, and allow to air-dry for 20–30 min. This step can be performed in a laminar flow hood to increase air flow and reduce time if needed.

22 Place slides in a multislide holder, fill a staining dish with 100% methanol prechilled to −20 °C and submerge for 10 min.

! CAUTION 100% methanol is highly flammable liquid and vapor and toxic if swallowed, inhaled or in contact with skin. Handle inside a chemical fume hood.

▲ CRITICAL STEP From this step on, ensure the tissue section does not dry out, by continuously submerging the tissue in liquid.

23 Transfer the slide holder to a staining dish containing nonsterile PBS, and rehydrate by washing three times for 5 min each, using gentle agitation on a laboratory rocker. Perform all subsequent washing steps in a similar fashion.

24 Take slides out of the slide holder, and draw a circle around the tissue using a hydrophobic pen. After adding a drop of PBS onto the tissue to avoid drying out of the tissue section, leave the hydrophobic marking to dry for 5 min.

25 Return slides to the slide holder and wash twice in PBS containing 0.2% Tween (PBS-T) for 5 min each.

26 Take out slides from the slide holder, place the slides horizontally in a humidified chamber and permeabilize the tissue by adding 100 µl of PBS with 0.2% Triton for 3 h.

▲ CRITICAL STEP Permeabilization for 3 h is required to adequately stain non-tumor and low-grade glioma tissue. For high-grade glioma and BrM tissue, shorter permeabilization times (10 min) are sufficient.

? TROUBLESHOOTING

27 Discard permeabilization solution by gently tilting slides. Return slides to slide holder, and wash twice in PBS-T for 5 min each.

28 Place slides in a humidified chamber, add 100 µl blocking buffer to tissue section and incubate for 1 h at RT.

29 Prepare the primary antibody solution by diluting the required antibodies in PNB-T at the appropriate concentrations. Table 1 contains details of antibodies we have successfully used.

30 Decant the blocking buffer, and directly add 100 µl of the primary antibody solution to the first tissue. Add 100 µl PNB-T to the second tissue on the slide to prevent it from drying out. Incubate overnight in a humidified chamber at 4 °C.

31 Prepare the secondary antibody solution by diluting antibodies in filtered PNB-T. Spin secondary antibody mix for 15 min at 10,000*g* at 4 °C to remove antibody precipitates that can cause imaging artifacts. Table 1 contains details of antibodies we have successfully used.

32 Return slides to the slide holder, and wash the slides three times in PBS-T for 5 min each.

33 Take out slides from the slide holder, add 100 µl secondary antibody mix to both tissue sections and incubate for 1 h in the humidified chamber at RT.

▲ CRITICAL STEP After this step, there is the option to add an additional staining round with directly fluorophore-conjugated antibodies: wash the tissue three times in PBS-T for 5 min each, followed by incubation with the directly fluorophore-conjugated antibodies for 1 h in the humidified chamber at RT.

34 Wash the slides six times in PBS-T for 10 min each.

35 Remove excess liquid by gently tapping sections, add two drops of fluorescence mounting medium onto the slide and gently place a cover glass on the slide, avoiding the introduction of air bubbles.

▲ CRITICAL STEP Change in mounting medium can result in a change of staining patterns with nuclear markers e.g., DAPI.

36 Let the mounting medium solidify by placing the slide in the dark for 1 h at RT.

■ PAUSE POINT Store slides at 4 °C in the dark until scanning. Staining intensity can slowly diminish over time; we recommend scanning of the slides within 1 week of staining.

37 Scan the slide.

Bulk tumor protein extraction (module 1b) ● Timing 30 min

38 Place a snap-frozen tumor tissue piece from Step 3B in a 2 ml microcentrifuge tube on dry ice.

39 Determine tissue weight using an analytical scale.

40 Add 10 µl cell lysis buffer per mg of frozen tissue, and let the tissue thaw on ice. This typically yields ~20–60 µg of protein per mg of tissue.

41 Submerge tissue rotor/stator homogenizer 5–7 mm tip, and homogenize the tissue on ice with three or four short bursts to avoid excessive foaming.

42 Agitate the homogenate on ice for 10 min using a laboratory shaker.

43 Centrifuge the suspension at 10,000*g* for 5 min at 4 °C, and collect the supernatant.

44 Determine the protein concentration with a commercial BCA assay, and adjust to 1 µg/µl.

■ PAUSE POINT Prepare aliquots and store protein extracts at −80 °C for a maximum of 1 year.

45 Proceed to ELISA or more extensive proteomic analysis. See our research paper for further details on analyses we used previously[5].

WES of snap-frozen and OCT-embedded frozen tumor tissue (module 1b)

● Timing Steps 46–48: 2 h (depending on number of samples); Step 49: 8 h

▲ CRITICAL STEP Matched normal tissue must be processed in parallel to be used as a reference for WES analyses. For brain malignancies, the use of PBMCs isolated from matched patient blood is recommended (as described in Box 1).

46 For tissue disruption, homogenization and digestion of OCT-embedded tumor tissue, follow option A after completing Step 3A; for snap-frozen tissue, follow option B after completing 3B; for frozen PBMCs, follow option C. If starting with the isolation of matched PBMCs from whole blood, undertake Step 1 and Step 2A of Box 1 prior to embarking on option C.

(A) **Tissue disruption, homogenization and digestion of OCT-embedded tissue:**

(i) Section the frozen OCT-embedded tumor tissue at a thickness of 500 µm using a cryostat (four sections per tumor). Store tissue sections at −80 °C.

PAUSE POINT Tissue sections can be stored at −80 °C for several months.

(ii) Place tissue sections into a 1.5 ml microcentrifuge tube, and warm them at 36 °C in a heat block until OCT melts.

(iii) Remove melted OCT using a pipette and place tissue sections into a new 1.5 ml microcentrifuge tube.

(iv) Add 600 µl RLT buffer (Qiagen DNAeasy Blood & Tissue kit), and incubate at 55 °C in a heat block for 1 h. Incubation time can be extended if tissue sections are not completely digested.

(B) **Tissue disruption, homogenization and digestion of snap-frozen tissue**

(i) Place frozen tissue (optimal size sections ~1–3 mm^3 each) into a 2 ml round-bottomed microcentrifuge tube containing 600 µl RLT buffer (Qiagen DNAeasy Blood & Tissue kit) for DNA extraction.

(ii) Disrupt and homogenize tissue using a rotor/stator homogenizer with a 5–7 mm probe for 1–3 min. Try to avoid generating foam by keeping the tip of the probe submerged and holding it to one side of the tube.

CRITICAL STEP Longer homogenization times can result in genomic DNA fragmentation and negatively impact library preparation. Homogenization times should be kept as short as possible.

(iii) Incubate the homogenized lysate at 55 °C in a heat block for 1 h.

(C) **Tissue disruption, homogenization and digestion of frozen PBMCs**

(i) Thaw 1 ml of frozen PBMCs into 9 ml of complete medium and spin at 400*g* for 5 min at 4 °C.

(ii) Remove supernatant, wash pellet with 5 ml PBS 1× and spin at 400*g* for 5 min at 4 °C.

(iii) Resuspend pellet in 600 µl RLT buffer (Qiagen DNAeasy Blood&Tissue kit), and incubate at 55 °C in a heat block for 1 h.

47 Perform genomic DNA extraction following manufacturer instructions (Qiagen DNAeasy Blood & Tissue kit).

PAUSE POINT Genomic DNA can be safely kept at 4 °C for short-term storage (up to 1 month) or at −80 °C for long-term storage (up to several years in solution, such as the elution buffer provided by QIAGEN).

48 Quantify genomic DNA concentration, and estimate sample contamination in a NanoDrop spectrophotometer.

CRITICAL STEP An absorbance 260/280 ratio of ~1.8 and a 260/230 ratio of ~2 are generally accepted as indicators of sufficient DNA purity for downstream analyses. It is recommended to complement this with DNA quantification by Qubit fluorometer for increased accuracy. Aim for a total of 3 µg DNA per sample in 130 µl of buffer EB (Qiagen DNAeasy Blood & Tissue kit). DNA input for library preparation can be scaled down to 200 ng in 50 µl volume if necessary (see Agilent SureSelect Human All Exon v7 manufacturer protocol).

49 Proceed with WES library preparation and sequencing following manufacturer instructions (we use an Agilent SureSelect Human All Exon v7).

Troubleshooting

Troubleshooting advice can be found in Table 3.

Table 3 | Troubleshooting table

Step	Problem	Possible reason	Solution
17	FAC sorting hampered by debris in single-cell suspension	Excessive myelin present after sample dissociation	Consider myelin removal using Miltenyi myelin removal beads II
		High level of necrosis in (tumor) tissue	Discuss with neurosurgeons and pathologist to reduce the lag time between resection of the tissue and the start of tissue processing in the laboratory
			Test the effect of debris or dead cell removal kits (bear in mind that cell removal kits can remove populations from the single-cell suspension)

Table continued

Table 3 (continued)

Step	Problem	Possible reason	Solution
Box 2A(ii)	Difficulties in delineating populations during FCM/FAC sorting	Compensation matrix is not set up adequately	Carefully check if the single-color compensation matrix was designed correctly
		Data spread due to multiple fluorophores in FCM panel	Identify gating boundaries using FMO controls in cell suspensions from both tumor samples and peripheral blood
		FCM antibody is not titrated properly on (tumor) tissue	Titrate FCM antibodies on both whole blood and dissociated (tumor) tissue
	Cell surface antigen is not detected by FCM/FAC sorting	Enzymatic cleavage of antigen during tissue dissociation	Test antigen preservation by comparing an undigested versus digested peripheral blood sample; compare different dissociation methods (e.g., mechanical versus enzyme-based) on your tissue of interest; titrate the ratio of enzymatic digestion mix to tissue: switch to alternative digestion protocol if maintenance of specific antigen expression is crucial
		The cell surface antigen is not expressed in the tissue	Use IF to determine if marker is expressed/cell population is present in the tissue
	Low RNA yield from sorted populations	Volume of sorted cell suspension does not correspond to prepared Trizol LS volume	While RNA amounts obtained from sorted cells can be below the detection limit, ensure a ratio of 1:3 between the aqueous solution and Trizol LS
Box 2B(iii)	Population missing from single-cell data	Enzymatic cleavage of antigen during tissue dissociation	Compare composition of single cell suspension using different digestion methods
		The cell surface antigen is not expressed in the tissue	Use IF to determine if marker is expressed/cell population is present in the tissue
		Inadvertent removal of cell population during sample preparation when using debris or dead cell removal kits	Investigate the effects of debris or dead cell removal kits on the presence of the missing population
20	Poor tissue quality with freezing artifacts	High level of necrosis in brain (tumor) tissue	Discuss with neurosurgeons and pathologist reducing the lag time between resection of the tissue and the start of tissue processing in the laboratory
		Freezing occurred too slowly	Ensure that the 2-methylbutane is at a temperature of −80 °C
		OCT blocks thawed before sectioning of the block	Ensure that OCT tissue blocks do not thaw after freezing
26	Antigen only weakly or not detected in some tissues	Primary and secondary antibodies do not match	Verify that secondary antibodies react to the correct species used in the primary antibodies. Do not use secondary antibodies against sheep and goat primary antibodies in one staining panel as they can cross-react
		Antigen is masked	Titrate permeabilization time for antigen of interest, test alternative fixation methods
		The antigen is not expressed in the tissue	Test by FCM if marker is expressed/population is present in tissue

Timing

Steps that need to be performed on the day of tissue reception, as soon as possible post-resection

Steps 1–3, freezing and tissue embedding: 30 min (modules 1a,b). *In parallel (if no FCM/FAC sorting is performed)*: Box 1, processing of peripheral blood: 1 h 30 min to 3 h

Steps 4–18, enzymatic dissociation of tissue: 2 h 30 min (modules 2a–c, 3a,b). *In parallel (if FCM/FAC sorting is performed)*: Box 1, processing of peripheral blood: 1 h 30 min to 3 h (modules 2a–c)

Step 19: depending on the downstream use of the single-cell suspension:

Option A: FCM staining: 1 h 15 min (modules 2a–c); FAC sorting of tissue (Box 2): 30 min to 2 h (depending on tissue size, quality and cell type of interest, modules 2a,b)

If scRNAseq is performed (Box 2): sample preparation for scRNAseq: 20 min (modules 2a,b)

Option B: MACS isolation of TANs: 1 h 15 min (modules 3a,b)

Option C: plating of tumor cell suspension for MEC-CM generation: 10 min (modules 3a,b)

Steps that can be performed at a later time point

Step 19, option C: collection of MEC-CM after 24 h: 30 min (modules 3a,b)

Steps 20–30, IF staining day 1: 5 h 30 min (module 1a)

Steps 31–37, IF staining day 2: 2 h 45 min additional slide scanning time depending on tissue size and slide scanner (module 1a)
Steps 38–45, bulk tumor protein extraction: 30 min (module 1b)
Steps 46–48, DNA extraction from tumor tissue/PBMCs for WES: 2 h (depending on number of samples, module 1b)
Step 49, WES of tumor tissue/PBMC DNA: 8 h (module 1b)

Anticipated results

The strength of this protocol is that it maximizes the use of limited tissue for several complementary techniques, which multiplies the possible analytical insights and enables cross-method validation of findings. Processed tissue needs to surpass certain quality control assessments within each of the individual processing modules before cross-method validation can be implemented. In this section, we discuss these quality control checks.

When planning to use tissue for IF, the first quality control step is the assessment of OCT-frozen tissue section integrity following H&E staining. We usually perform H&E staining using Gill's hematoxylin solution II with eosin counterstain following a standard protocol[43]. Although our freezing protocol has been optimized to preserve tissue quality, a loss of ~5% of processed samples due to artifacts should be anticipated. Tissues surpassing this quality control can then be stained by IF. The specific antibodies and their dilutions, which we have employed in our studies, can be found in Table 1.

As an example, a breast cancer-BrM sample was stained for CD45, CD68 and P2RY12, CD49D, CD3 and DAPI (Fig. 8a, Table 1). Because of the fixed number of fluorochromes that can be analyzed on a conventional slide scanner, both anti-CD68 and anti-P2RY12 antibodies, detecting complementary macrophage markers[5], were placed into one channel, allowing the addition of another antibody/fluorochrome combination. A directly conjugated CD3 antibody was used in this staining panel, due to its superior staining quality and the possibility to combine this antibody with the four other markers while circumventing cross-species reactivity. An adjacent tissue section mounted onto the same slide was simultaneously stained with the secondary antibodies only, serving as a control for background and nonspecific antibody binding (Fig. 8b). This permits the setting of valid signal cutoffs to detect only true signal, which is crucial for any downstream analysis such as performed here with Visiopharm's VIS image analysis software, allowing one to label non-immune cells ($CD45^-$), MG ($CD45^+$, P2RY12/$CD68^+$, $CD49D^-$), MDMs ($CD45^+$, P2RY12/$CD68^+$, $CD49D^+$), $CD3^+$ T cells ($CD45^+$, $P2RY12^-$/$CD68^-$, $CD3^+$) and other immune cells ($CD45^+$, $P2RY12^-$/$CD68^-$, $CD49D^{-/+}$, $CD3^-$) (Fig. 8c).

Tissue that is not used for snap- or OCT-freezing can be dissociated using the TDK or BTDK digestion protocol. After digestion, the majority of the tissue will be in a single-cell suspension, with only few undigested tissue pieces remaining. These are removed by filtration through a 40 µm cell

Fig. 8 | Representative data from human brain tumor tissue. a, Representative IF images of a BrM (from primary breast tumor) tissue sample fresh frozen in OCT. The sample was stained with a nuclear marker (DAPI), and antibodies against CD45, CD68 and P2RY12, CD49D and CD3. IF signal for CD68 and P2RY12 was acquired in the same channel. Scale bars, 100 µm (see Table 1 for antibodies used). **b**, IF secondary antibody-only staining for the panel shown in **a**. Exposure time and signal intensity values are equal to the matched tissue in **a**. Scale bar, 100 µm. **c**, Cell type identification of non-immune cells ($CD45^-$), MG ($CD45^+$, P2RY12/$CD68^+$, $CD49D^-$), MDMs ($CD45^+$, P2RY12/$CD68^+$, $CD49D^+$), $CD3^+$ T cells ($CD45^+$, $P2RY12^-$/$CD68^-$, $CD3^+$) and other immune cells ($CD45^+$, $P2RY12^-$/$CD68^-$, $CD49D^{-/+}$, $CD3^-$) of the IF image shown in Fig. 8a. Tissue sections were scanned on a AxioScan.Z1 slide scanner (Zeiss) using a 20× objective resulting in a scale of 0.325 × 0.325 µm per pixel. Analysis performed with VIS software. Regions of interest (ROI) were generated within the software using a 21-pixel mean filter in the DAPI channel. The edges of the ROI were smoothened using the 'close' command. Any holes in the ROI were filled with the software's 'fill holes' function, and any mounting artifacts such as dust specks or air bubbles were manually removed from the ROI. Nuclear classification was obtained by converting a median DAPI signal (filtersize = 3) into a watershed signal using VIS' polynomial blob filter function (order = 4, filtersize = 41) and cleaned up by removal of nuclear remnants based on a nuclear size filter of 5 – 500 µm^2. Nuclei were expanded by five pixels to capture both cytoplasmic and nuclear fluorescent signals. To identify different brain TIME cell types, a hierarchical decision tree was generated with manually set thresholds to determine marker positivity. Scale bar, 100 µm. **d**, FCM plots of the same breast-BrM sample showing the FAC-sorting strategy of the indicated immune cell populations. Populations that can be distinguished include $CD45^-$ cells, MG, MDMs, TANs, $CD14^{-/low}$/$CD16^+$ monocytes, $CD14^+$/$CD16^+$ monocytes, $CD16^-$ granulocytes, iMCs, DCs, $CD4^+$ T cells, Tregs, $CD8^+$ T cells, DNTs, B cells and NK cells. See Table 2 for the marker overview and proportion of each gated population, see Table 1 for the antibodies used. **e**, Scatter plot depicting the abundance of $CD3^+$ T cells as measured by IF versus FCM in non-tumor brain ($n = 4$) and tumor tissues ($n_{IDHmut} = 6$, $n_{IDHwt} = 8$, $n_{BrM} = 13$). Encircled in red is the breast-BrM sample described in **a**–**d**. Tissue pieces were derived from the same sample and processed independently. Plot inset: Pearson's correlation coefficient and significance. **f**, Representative images of the single-cell suspension of a brain tumor tissue (*IDH* wt glioma) after being plated at a cellular density of 2 × 10^6 viable cells/ml. Images were obtained at the timepoints and culture passages indicated.

strainer. For samples containing an abundance of myelin (especially non-tumor brain tissue and low-grade gliomas), the resulting cell suspension will appear whitish and rich in lipids. When washing these samples postdigestion, the supernatant will continue to appear turbid (Fig. 3d). These are indications that a myelin removal step is required to clean up the sample and allow for higher FAC sorting and/or magnetic bead-based cell isolation purity.

Once the digestion protocol has been completed, the single-cell suspension can be stained for FCM and/or FAC sorting. Unlike blood samples, brain (tumor) samples can still contain substantial amounts of debris making clean gating difficult. Thus, it is crucial to be stringent when excluding

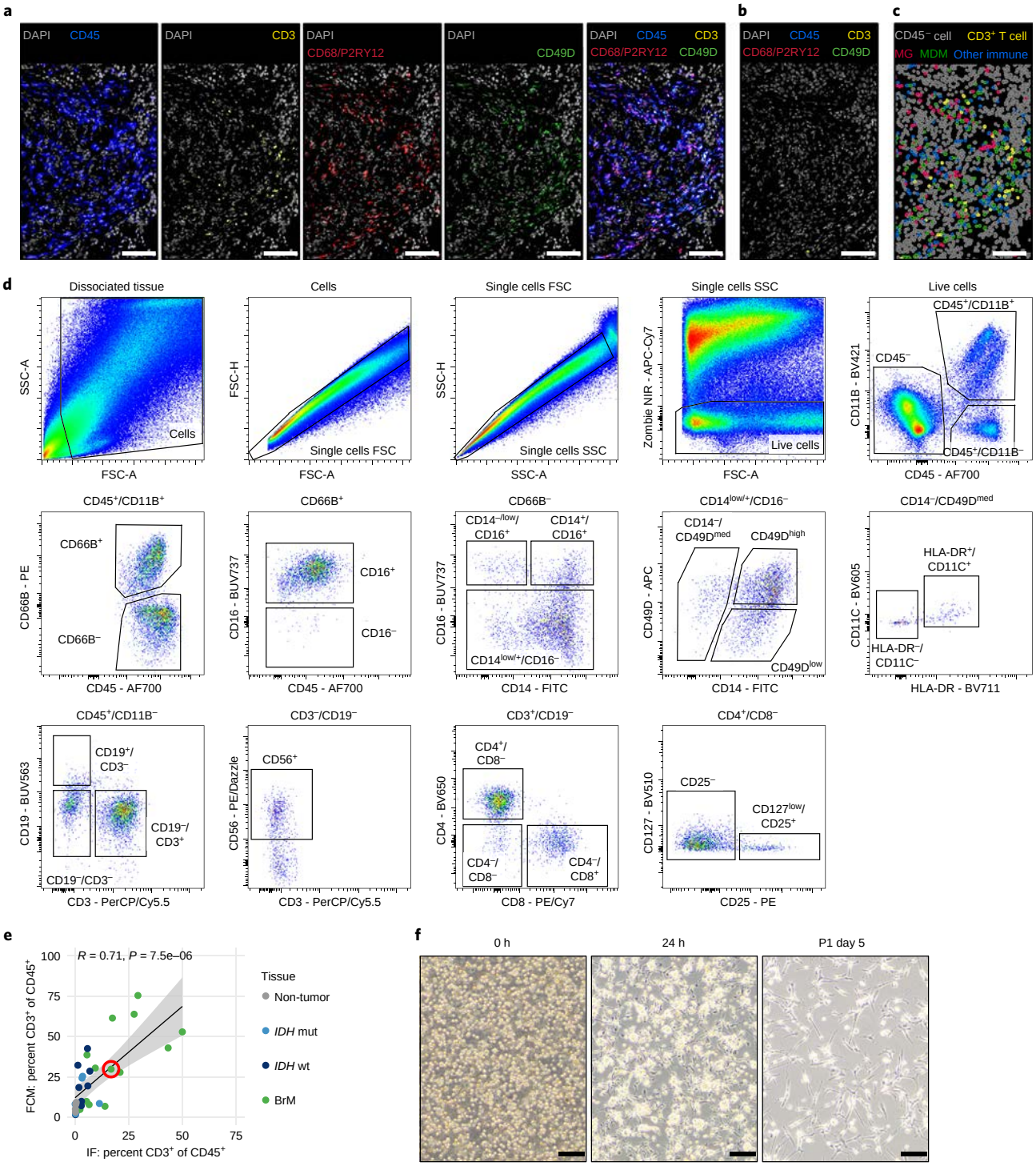

debris, doublets and dead cells (Fig. 8d, Table 2). Tumor samples can include a wide range of viability of cells (5–95%, median 65.2%, Fig. 3c). When setting up scRNAseq experiments with these samples, it is advised to only proceed with this module when the sample has a cell viability >70%, which was the case for ~46% of samples in our experience to date (Fig. 3c). Based on cell lineage markers, our current gating strategy allows us to sort $CD45^-$ cells, TANs, $CD14^{-/low}/CD16^+$ monocytes, $CD14^+/CD16^+$ monocytes, MG, MDMs, B cells, NK cells, $CD4^+$ T cells, $CD8^+$ T cells, $CD4^-/CD8^-$ T cells and T-regulatory cells (Tregs, Fig. 8d, Tables 1 and 2). The frequencies of these different cell populations can be compared with the abundance obtained from cell type-specific quantifications based on IF (Fig. 8c) for internal cross-validation as described for $CD3^+$ T cells (Fig. 8e). Analyses of 34 samples ($n_{\text{non-tumor}} = 4$, $n_{IDH\text{mut}} = 6$, $n_{IDH\text{wt}} = 8$, $n_{\text{BrM}} = 13$) using this strategy revealed that the abundance of $CD3^+$ T cells detected by IF shows a significant correlation with FCM quantitation (Fig. 8e), similar to MG, MDMs and TANs (Fig. 6a). Such cross-method validation thus enables the researcher to carefully evaluate the reliability and accuracy of brain TIME population quantification.

Single-cell suspensions obtained from tumor tissue, if not used for FCM/FAC sorting or downstream sequencing, can be used for MEC-CM collection (Fig. 8f). After 24 h in culture, both adherent and nonadherent cells can be observed in the tissue culture flask, indicative of a complete TIME culture. Over time, with a medium change after 24 h and passaging, a reduction in the numbers of nonadherent cells can be observed. However, it is important to be aware that CM collected at such later time points no longer fully represents the secretome of the complete TIME.

Data availability

All data generated or analyzed during this study are included in either this paper or our original research study[5]. Transcriptomic data generated using this pipeline are available at https://joycelab.shinyapps.io/braintime/. FCM data of the comparison of various brain tumor dissociation methods (included in Fig. 5a,b) have been deposited at the flow cytometry repository (http://flowrepository.org/): FR-FCM-Z3MF. Data not included in the aforementioned sources can be obtained from the corresponding author upon request due to patient privacy protection.

References

1. Achrol, A. S. et al. Brain metastases. *Nat. Rev. Dis. Prim.* **5**, 5 (2019).
2. Stupp, R. et al. Radiotherapy plus concomitant and adjuvant temozolomide for glioblastoma. *N. Engl. J. Med.* **352**, 987–996 (2005).
3. Quail, D. F. & Joyce, J. A. The microenvironmental landscape of brain tumors. *Cancer Cell* **31**, 326–341 (2017).
4. Bejarano, L., Jordao, M. J. C. & Joyce, J. A. Therapeutic targeting of the tumor microenvironment. *Cancer Discov.* **11**, 933–959 (2021).
5. Klemm, F. et al. Interrogation of the microenvironmental landscape in brain tumors reveals disease-specific alterations of immune cells. *Cell* **181**, 1643–1660 e1617 (2020).
6. Friebel, E. et al. Single-cell mapping of human brain cancer reveals tumor-specific instruction of tissue-invading leukocytes. *Cell* **181**, 1626–1642 e1620 (2020).
7. Long, G. V. et al. Combination nivolumab and ipilimumab or nivolumab alone in melanoma brain metastases: a multicentre randomised phase 2 study. *Lancet Oncol.* **19**, 672–681 (2018).
8. Tawbi, H. A. et al. Combined nivolumab and ipilimumab in melanoma metastatic to the brain. *N. Engl. J. Med.* **379**, 722–730 (2018).
9. Hendriks, L. E. L. et al. Outcome of patients with non-small cell lung cancer and brain metastases treated with checkpoint inhibitors. *J. Thorac. Oncol.* **14**, 1244–1254 (2019).
10. Lim, M., Xia, Y., Bettegowda, C. & Weller, M. Current state of immunotherapy for glioblastoma. *Nat. Rev. Clin. Oncol.* **15**, 422–442 (2018).
11. Schalper, K. A. et al. Neoadjuvant nivolumab modifies the tumor immune microenvironment in resectable glioblastoma. *Nat. Med.* **25**, 470–476 (2019).
12. Bunevicius, A., Schregel, K., Sinkus, R., Golby, A. & Patz, S. REVIEW: MR elastography of brain tumors. *Neuroimage Clin.* **25**, 102109 (2020).
13. Gritsenko, P. G. et al. p120-catenin-dependent collective brain infiltration by glioma cell networks. *Nat. Cell Biol.* **22**, 97–107 (2020).
14. Leelatian, N. et al. Unsupervised machine learning reveals risk stratifying glioblastoma tumor cells. *eLife* https://doi.org/10.7554/eLife.56879 (2020).
15. Garofano, L. et al. Pathway-based classification of glioblastoma uncovers a mitochondrial subtype with therapeutic vulnerabilities. *Nat. Cancer* **2**, 141–156 (2021).
16. Yuan, J. et al. Single-cell transcriptome analysis of lineage diversity in high-grade glioma. *Genome Med.* **10**, 57 (2018).

17. Sankowski, R. et al. Mapping microglia states in the human brain through the integration of high-dimensional techniques. *Nat. Neurosci.* **22**, 2098–2110 (2019).
18. Pombo Antunes, A. R. et al. Single-cell profiling of myeloid cells in glioblastoma across species and disease stage reveals macrophage competition and specialization. *Nat. Neurosci.* https://doi.org/10.1038/s41593-020-00789-y (2021).
19. Chen, A. X. et al. Single-cell characterization of macrophages in glioblastoma reveals MARCO as a mesenchymal pro-tumor marker. *Genome Med.* **13**, 88 (2021).
20. Castellan, M. et al. Single-cell analyses reveal YAP/TAZ as regulators of stemness and cell plasticity in glioblastoma. *Nat. Cancer* **2**, 174–188 (2021).
21. Richards, L. M. et al. Gradient of developmental and injury response transcriptional states defines functional vulnerabilities underpinning glioblastoma heterogeneity. *Nat. Cancer* **2**, 157–173 (2021).
22. Kim, N. et al. Single-cell RNA sequencing demonstrates the molecular and cellular reprogramming of metastatic lung adenocarcinoma. *Nat. Commun.* **11**, 2285 (2020).
23. Laughney, A. M. et al. Regenerative lineages and immune-mediated pruning in lung cancer metastasis. *Nat. Med.* **26**, 259–269 (2020).
24. Rubio-Perez, C. et al. Immune cell profiling of the cerebrospinal fluid enables the characterization of the brain metastasis microenvironment. *Nat. Commun.* **12**, 1503 (2021).
25. Berghoff, A. S. et al. Density of tumor-infiltrating lymphocytes correlates with extent of brain edema and overall survival time in patients with brain metastases. *Oncoimmunology* **5**, e1057388 (2016).
26. Berghoff, A. S. et al. Correlation of immune phenotype with IDH mutation in diffuse glioma. *Neuro Oncol.* **19**, 1460–1468 (2017).
27. Kohanbash, G. et al. Isocitrate dehydrogenase mutations suppress STAT1 and CD8+ T cell accumulation in gliomas. *J. Clin. Invest.* **127**, 1425–1437 (2017).
28. Hodges, T. R. et al. Mutational burden, immune checkpoint expression, and mismatch repair in glioma: implications for immune checkpoint immunotherapy. *Neuro Oncol.* **19**, 1047–1057 (2017).
29. Shih, D. J. H. et al. Genomic characterization of human brain metastases identifies drivers of metastatic lung adenocarcinoma. *Nat. Genet.* **52**, 371–377 (2020).
30. Brastianos, P. K. et al. Genomic characterization of brain metastases reveals branched evolution and potential therapeutic targets. *Cancer Discov.* **5**, 1164–1177 (2015).
31. Gromeier, M. et al. Very low mutation burden is a feature of inflamed recurrent glioblastomas responsive to cancer immunotherapy. *Nat. Commun.* **12**, 352 (2021).
32. Berghoff, A. S. et al. Invasion patterns in brain metastases of solid cancers. *Neuro Oncol.* **15**, 1664–1672 (2013).
33. O'Flanagan, C. H. et al. Dissociation of solid tumor tissues with cold active protease for single-cell RNA-seq minimizes conserved collagenase-associated stress responses. *Genome Biol.* **20**, 210 (2019).
34. Hansen, D. M. et al. A holistic analysis of the intestinal stem cell niche network. Preprint at *bioRxiv* https://doi.org/10.1101/2019.12.12.871756 (2019).
35. Wenisch, C., Fladerer, P., Patruta, S., Krause, R. & Horl, W. Assessment of neutrophil function in patients with septic shock: comparison of methods. *Clin. Diagn. Lab. Immunol.* **8**, 178–180 (2001).
36. Van Gassen, S., Gaudilliere, B., Angst, M. S., Saeys, Y. & Aghaeepour, N. CytoNorm: a normalization algorithm for cytometry data. *Cytom. Part A* **97**, 268–278 (2020).
37. Plouffe, B. D., Murthy, S. K. & Lewis, L. H. Fundamentals and application of magnetic particles in cell isolation and enrichment: a review. *Rep. Prog. Phys.* **78**, 016601 (2015).
38. Son, K. et al. Improved recovery of functionally active eosinophils and neutrophils using novel immunomagnetic technology. *J. Immunol. Methods* **449**, 44–55 (2017).
39. Lozano-Ojalvo, D., et al. PBMC-derived T cells. in *The Impact of Food Bioactives on Health: In Vitro and Ex Vivo Models* (eds Verhoeckx, K. et al.) 169–180 (Springer, 2015).
40. Chometon, T. Q. et al. A protocol for rapid monocyte isolation and generation of singular human monocyte-derived dendritic cells. *PLoS One* **15**, e0231132 (2020).
41. Ferrara, F. et al. Rapid purification of billions of circulating CD19+ B cells directly from leukophoresis samples. *N. Biotechnol.* **46**, 14–21 (2018).
42. Swartzlander, D. B. et al. Concurrent cell type-specific isolation and profiling of mouse brains in inflammation and Alzheimer's disease. *JCI Insight* https://doi.org/10.1172/jci.insight.121109 (2018).
43. National Society for Histotechnology (NSH). *Guidelines for Hematoxylin & Eosin Staining.* http://nsh.org/sites/default/files/Guidelines_For_Hematoxylin_and_Eosin_Staining.pdf (reviewed July 2001).
44. Picelli, S. et al. Full-length RNA-seq from single cells using Smart-seq2. *Nat. Protoc.* **9**, 171–181 (2014).
45. Callahan, M. K., Williamson, P. & Schlegel, R. A. Surface expression of phosphatidylserine on macrophages is required for phagocytosis of apoptotic thymocytes. *Cell Death Differ.* **7**, 645–653 (2000).
46. Macosko, E. Z. et al. Highly parallel genome-wide expression profiling of individual cells using nanoliter droplets. *Cell* **161**, 1202–1214 (2015).

Acknowledgements

We express our gratitude to all patients who kindly agreed to donate tissue under protocol PB 2017-00240, F25/99. We thank the neurosurgery operating room staff and the technicians at the Pathology department of the Centre Hospitalier Universitaire Vaudois (CHUV) for their support in providing human patient samples; L. Bejarano Bosque, V. Wischnewski, A. Zomer and S. Watson in the Joyce lab for their technical assistance during sample processing; N. Piazzon for coordinating ATRX staining and *IDH* pyrosequencing

performed at the Pathology department; the team of the UNIL Mouse Pathology Facility for cryosectioning of patient tissues; and K. Blackney and F. Sala de Oyanguren of the UNIL Flow Cytometry Facility for assistance with FAC sorting. Research in the Joyce lab is funded by the Carigest Foundation, ISREC Foundation, the Swiss Bridge Award, Breast Cancer Research Foundation, Cancer Research UK, Ludwig Institute for Cancer Research and the University of Lausanne. K.S. is supported in part by an Erwin-Schrödinger Fellowship from the Austrian Science Fund (FWF, J4343-B28). F.K. was supported in part by the German Research Foundation (DFG, KL2491/1-1) and Fondation Medic. A.A-P. is supported by an EMBO Long-term Postdoctoral Fellowship (EMBO ALTF 654-2019).

Author contributions

F.K., R.L.B. and J.A.J. conceived the initial project; R.R.M., K.S., F.K., M.K. and R.L.B. designed and optimized pipeline modules; R.R.M., K.S., F.K., M.K., D.N.M. and A.A-P. performed experiments; R.R.M and K.S. analyzed data; R.B., D.L. and A.W. provided technical expertise for FCM experiments; R.B. and D.L. performed FAC sorting; J-P.B., R.D. and M.H. provided clinical material; J-P.B. performed histopathological review; R.R.M. and K.S. prepared the figures; R.R.M., K.S., F.K. and J.A.J. wrote the manuscript; J.A.J. supervised the project. All authors reviewed and edited the manuscript and approved the final draft.

Competing interests

The authors declare no competing interests.

Additional information

Supplementary information The online version contains supplementary material available at https://doi.org/10.1038/s41596-021-00594-2.

Correspondence and requests for materials should be addressed to J.A.J.

Peer review information *Nature Protocols* thanks Burkhard Becher and the other, anonymous reviewer(s) for their contribution to the peer review of this work.

Reprints and permissions information is available at www.nature.com/reprints.

Publisher's note Springer Nature remains neutral with regard to jurisdictional claims in published maps and institutional affiliations.

Received: 22 January 2021; Accepted: 21 June 2021;
Published online: 30 August 2021

Related links
Key reference using this protocol
Klemm, F. et al. *Cell* **181**, 1643–1660.e17 (2020): https://doi.org/10.1016/j.cell.2020.05.007

Supplementary Methods

Isocitrate dehydrogenase (IDH) pyrosequencing

IDH pyrosequencing of the relevant mutational hotspots of *IDH1* and *IDH2* genes was performed at the Service of Clinical Pathology of the Centre Hospitalier Universitaire Vaudois (CHUV), Lausanne. Representative tissue blocks used for pyrosequencing were either from (i) fresh-frozen OCT Compound (Sakura TissueTek; #4583) embedded tissues, (ii) tissues fixed with 4% paraformaldehyde (PFA, E.M.S.; #15714-S) for 24 hours at 4°C before OCT- embedding and freezing at -80°C, or (iii) formalin-fixed paraffin-embedded (FFPE) tissue. Blocks were selected based on hematoxylin and eosin (H&E)-stained slides. For FFPE tissue blocks, if tumor cell content was <80%, the regions of interest were marked on the H&E section and subsequently reported on corresponding FFPE sections stained with toluidine blue. Manual microdissection of the regions of interest was performed under a microscope, by scraping the tissue sections off the slides, followed by genomic DNA extraction (Maxwell 16 FFPE Plus LEV DNA Purification Kit, Promega). For all cases the estimated tumor cell content in the analyzed DNA was ≥80%.

Prior to sequencing, exons 4 of *IDH1* and *IDH2*, including codon 132 and 172 respectively, were amplified by polymerase chain reaction (PCR) using primers with the following sequences: *IDH1* biotinylated forward primer 5'-TGATGAGAAGAGGGTTGAGGAGTT-3' and reverse primer 5'- TTGCCAACATGACTTACTTGATCC-3' (198 bp amplicon); *IDH2* forward primer 5'-ATCCCACGCCTAGTCCCTG-3' and biotinylated reverse primer 5'-CTCCACCCTGGCCTACCT-3' (82 bp amplicon). PCR reactions were performed in duplicate, each in a total volume of 20 µl, containing : 5.9 µl nuclease-free water (Promega; #P119C), 1 µl dNTPs (5 mM; Illustra, dNTP mix set; #28-4065-57), 0.1 µl Platinum Taq DNA Polymerase (2U/ reaction; Invitrogen; #10-966-026), 10 µl of a 2X mix of the appropriate primers (for each *IDH* gene, a primer mix was prepared at 0.5 µM: nuclease-free water + 10X PCR Rnx Buffer (Invitrogen) + 50 mM MgCl2 (Invitrogen) + Forward/Reverse primers as indicated above), and 3 µl of genomic DNA (3 ng/µl) per reaction. Thermal cycling consisted of 38 cycles with denaturing (95°C, 15 s), annealing (57°C, 30 s), and elongation (72°C, 15 s) steps, preceded by an initial denaturation step (95°C, 5 min) and completed with a final elongation step (72°C, 5 min).

Pyrosequencing was performed utilizing a PyroMark Q24 Advanced pyrosequencer (Qiagen). 70 µl of Sepharose bead mix (comprised of 2 µl of Streptavidin Sepharose High Performance beads (GE Healthcare, Piscataway, NJ; #17511301), 40 µl PyroMark Binding Buffer (Qiagen; #979006), and 28 µl of Ultra Pure MilliQ water) were added to a 96-well PCR plate per run. 10 µl of PCR product were added to the wells, and then shaken at room temperature for 8 minutes (1500 rpm) to bind the biotinylated amplicons to the sepharose beads. Biotinylated PCR amplicons captured on the beads were then processed through washes of 70% ethanol (5 to 10 s), 0.2 M NaOH for denaturation (5 to 10 s), and PyroMark Wash Buffer to remove nonbiotinylated DNA strands (10 to 20 s) using the PyroMark Q24 Advanced Vacuum Prep Workstation. Biotinylated DNA strands were then released into the sequencing primer solution (25 µl at 0.3 µM of primer) in a PyroMark Q24 Plate. The sequencing primers were as follows: for *IDH1* codon 132: 5'-TGATCCCCATAAGCA-3' (annealing to the reverse strand) and for *IDH2* codon 172: 5'-AAGCCCATCACCAT-3'. The solution was then heated at 80°C for 2 minutes, and then cooled at room temperature (5 min). PyroMark Q24 Gold Reagents (enzymes, substrates, dNTPs; Qiagen; #971802) were used in the pyrosequencing reactions. Each assay was performed in duplicate, in parallel with a wild-type DNA control and a no template control.

The technical sensitivity (limit of detection) of the method is of approximately 10% mutant allele content.

Sequence to analyze (S2A) and dispensation order (DO) using PyroMark Q24 software were designed in order to optimize non-synonymous variant detection at codon 132 of *IDH1* and codon 172 of *IDH2*. *IDH1* codon 132 was interrogated using DO GTGTACTGACGTA and S2A TGAC*N*ACCTATGATGAT (*N,* any base; sequence to be read on the reverse strand). *IDH2* codon 172 was assessed using DO CGTCTACTGTCACG and S2A GGCA*N*GCACGCCCATGGCGACC.

Automated immunohistochemistry (IHC) staining for ATRX

ATRX IHC staining was performed at the Service of Clinical Pathology of the Centre Hospitalier Universitaire Vaudois (CHUV), Lausanne, using a DISCOVERY Ultra automated stainer (Roche Ventana). Sections used for staining were either from (i) fresh-frozen OCT Compound embedded tissues, (ii) tissues fixed with 4% PFA for 24 hours at 4°C before OCT- embedding and freezing at -80°C (both cryosectioned at 10 µm), or (iii) FFPE tissue sections (4 µm). FFPE slides were heated for 4 minutes at 72°C and placed in EZ Prep solution (Roche Ventana; #950-102) for deparaffinization. Frozen slides were thawed and air-dried for 5 min, followed by fixation using 4% PFA for 3 min at room temperature (RT; only performed for frozen slides that had not been pre-fixed before OCT-embedding). Slides were then hydrated using Reaction Buffer (Roche Ventana; #950-300). Slides were placed in the DISCOVERY Ultra automated stainer. In the selected staining program, slides were washed 1x with Ultra Liquid Coverslip (LCS) solution (Roche Ventana; #650-210), followed by Reaction Buffer. Antigen retrieval was performed using Cell Conditioning 1 antigen retrieval solution (Roche Ventana; #950-500) for 32 min at 95 °C, followed by a wash with Reaction Buffer. ATRX was detected using a polyclonal rabbit anti-human ATRX antibody (Sigma; #HPA001906, at 1:100 dilution) for 60 min at 37°C, followed by 2 washes of 5 min each with Reaction Buffer. Primary antibody detection was performed using an OmniMap anti-rabbit HRP-conjugated secondary antibody (Roche Ventana; #760-4310) for 16 min at RT. The DISCOVERY ChromoMap DAB detection kit (Roche Ventana; #760-159) was used for detection. Tissue counterstaining was performed using Hematoxylin II solution (Roche Ventana; #790-2208). The stained slides were rinsed with distilled water and dehydrated using an alcohol bath sequence (3 x 5 s per step: ethanol 95% - ethanol absolute (Reactolab SA; #99570) - xylol (VWR Chemicals, #28973.363). Finally, slides were mounted using Glas Mounting Medium (Sakura TissueTek; #1408) and covered (24x50 mm coverslips, VWR, ECN 631-1574) using a TissueTek Glas g2-E2 coverslipper (Sakura Finetek; #6502). Slides were scanned using a digital slide scanner (NanoZoomer S60, Hamamatsu; #C13210-01) with 20x objective lens magnification, 0.75 numerical aperture, and a scanning resolution of 0.46 µm/pixel. Images were acquired in a jpeg compressed file format and analyzed using Leica Biosystems Version 4.0.7 (Leica Biosystems).

7.2 Interrogation of the microenvironmental landscape in brain tumors reveals disease-specific alterations of immune cells

Cell

Interrogation of the Microenvironmental Landscape in Brain Tumors Reveals Disease-Specific Alterations of Immune Cells

Graphical Abstract

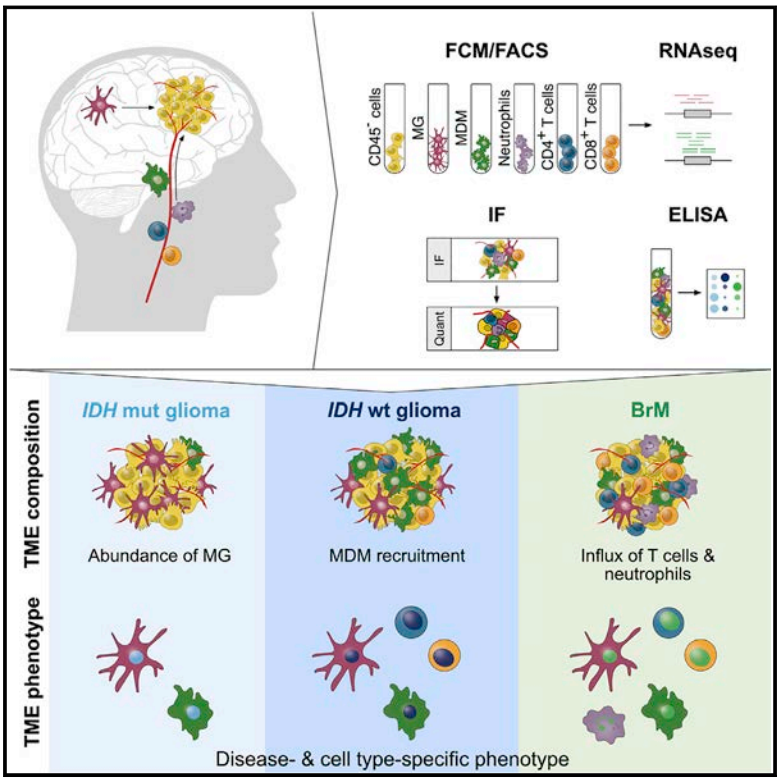

Highlights

- Flow cytometry, RNA-seq, and protein and image analyses reveal brain TME complexity
- Glioma *IDH* mutation status and brain metastasis primary tumors shape the brain TME
- Microglia and monocyte-derived macrophages exhibit multifaceted activation
- TME immune cells show disease- and cell-type-specific expression patterns

Authors

Florian Klemm, Roeltje R. Maas, Robert L. Bowman, ..., Roy T. Daniel, Monika E. Hegi, Johanna A. Joyce

Correspondence

johanna.joyce@unil.ch

In Brief

High-dimensional, multi-omics characterization of the brain tumor microenvironment, including comparisons of gliomas and brain metastases, suggests that education of immune cell types in the TME depends on tumor origin and *IDH* mutational status.

Klemm et al., 2020, Cell *181*, 1643–1660
June 25, 2020
https://doi.org/10.1016/j.cell.2020.05.007

Cell

CellPress

Resource

Interrogation of the Microenvironmental Landscape in Brain Tumors Reveals Disease-Specific Alterations of Immune Cells

Florian Klemm,[1,2] Roeltje R. Maas,[1,2,3,4] Robert L. Bowman,[5] Mara Kornete,[1,2] Klara Soukup,[1,2] Sina Nassiri,[1,2,6] Jean-Philippe Brouland,[7] Christine A. Iacobuzio-Donahue,[8] Cameron Brennan,[9] Viviane Tabar,[9] Philip H. Gutin,[9] Roy T. Daniel,[4] Monika E. Hegi,[3,4] and Johanna A. Joyce[1,2,10,*]

[1]Department of Oncology, University of Lausanne, Lausanne, Switzerland
[2]Ludwig Institute for Cancer Research, University of Lausanne, Lausanne, Switzerland
[3]Neuroscience Research Center, Centre Hospitalier Universitaire Vaudois, Lausanne, Switzerland
[4]Department of Neurosurgery, Centre Hospitalier Universitaire Vaudois, Lausanne, Switzerland
[5]Memorial Sloan Kettering Cancer Center, New York, NY, USA
[6]Bioinformatics Core Facility, SIB Swiss Institute of Bioinformatics, Lausanne, Switzerland
[7]Department of Pathology, Centre Hospitalier Universitaire Vaudois, Lausanne, Switzerland
[8]Department of Pathology, Memorial Sloan Kettering Cancer Center, New York, NY, USA
[9]Department of Neurosurgery, Memorial Sloan Kettering Cancer Center, New York, NY, USA
[10]Lead Contact
*Correspondence: johanna.joyce@unil.ch
https://doi.org/10.1016/j.cell.2020.05.007

SUMMARY

Brain malignancies encompass a range of primary and metastatic cancers, including low-grade and high-grade gliomas and brain metastases (BrMs) originating from diverse extracranial tumors. Our understanding of the brain tumor microenvironment (TME) remains limited, and it is unknown whether it is sculpted differentially by primary versus metastatic disease. We therefore comprehensively analyzed the brain TME landscape via flow cytometry, RNA sequencing, protein arrays, culture assays, and spatial tissue characterization. This revealed disease-specific enrichment of immune cells with pronounced differences in proportional abundance of tissue-resident microglia, infiltrating monocyte-derived macrophages, neutrophils, and T cells. These integrated analyses also uncovered multifaceted immune cell activation within brain malignancies entailing converging transcriptional trajectories while maintaining disease- and cell-type-specific programs. Given the interest in developing TME-targeted therapies for brain malignancies, this comprehensive resource of the immune landscape offers insights into possible strategies to overcome tumor-supporting TME properties and instead harness the TME to fight cancer.

INTRODUCTION

Brain malignancies include tumors that arise within the brain, such as low-grade gliomas and glioblastomas, and brain metastases (BrMs), which originate from extracranial primary tumors, including melanoma, breast, and lung cancers (Cagney et al., 2017). Gliomas mutant for the metabolic enzymes isocitrate dehydrogenase 1 and 2 (*IDH* mut) are generally low grade (II or III) and have a significantly better prognosis than *IDH* wild-type (WT) tumors, which are typically grade IV glioblastomas. Despite standard of care treatment comprising surgery followed by radiation and temozolomide (Stupp et al., 2005), median survival rates for glioblastoma patients remain stubbornly low (Aldape et al., 2019). Patient survival following BrM diagnosis can be even lower, with rates typically measured in months (Cagney et al., 2017; Ceccarelli et al., 2016), and among all adult brain tumors, the incidence of BrMs significantly exceeds that of gliomas.

Given the current limited treatment options for these patients, a key question to address is whether a deep comprehensive understanding of how primary and metastatic cancers develop within the brain tumor microenvironment (TME) could reveal promising new targets for therapeutic intervention. Although diverse TME cell types can critically regulate cancer progression and response to therapy across a broad range of extracranial tumors (Klemm and Joyce, 2015), we cannot simply extrapolate findings from these cancers to the singular brain TME, given its unique cell types, including astrocytes, neurons, and microglia (MG); the immune-suppressive environment of this organ; and the challenges presented for cells and drugs to cross the blood-brain barrier (BBB) (Quail and Joyce, 2017).

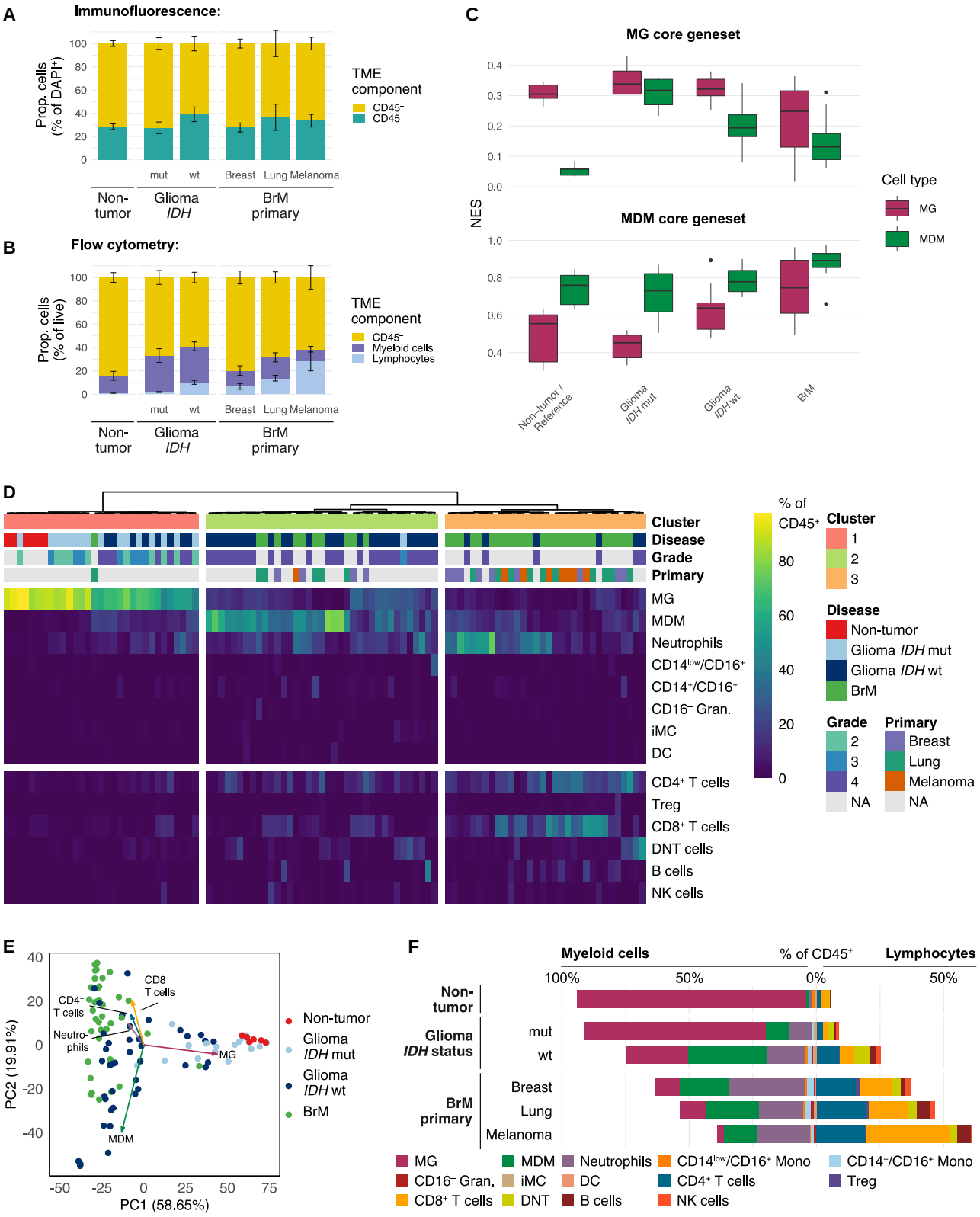

(legend on next page)

Immune checkpoint blockade (ICB), adoptive cell therapy, and vaccines represent treatments targeted against immune cells within the TME and systemically. The success of immunotherapies in certain extracranial cancers has led to clear motivation for their evaluation in brain malignancies. However, although they show some clinical efficacy in a subset of BrM patients (Hendriks et al., 2019; Long et al., 2018; Tawbi et al., 2018), ICB has only resulted in responses in isolated cases of primary gliomas to date (Lim et al., 2018; Schalper et al., 2019). Beyond tumor cell-intrinsic effects, this may be attributed in part to immune-suppressive components of the brain TME, including tumor-associated macrophages (TAMs), which have emerged as prominent players in brain cancers (Gutmann and Kettenmann, 2019; Quail and Joyce, 2017).

Lineage-tracing experiments in mice revealed that brain TAMs can originate from tissue-resident MG or monocyte-derived macrophages (MDMs) recruited from the peripheral circulation (Bowman et al., 2016; Chen et al., 2017). TAMs are highly plastic cells that integrate input from cytokines, growth factors, and other stimuli, resulting in diverse activation states and cellular phenotypes, including promotion of invasion, angiogenesis, metastasis, and immune suppression (Mantovani et al., 2017; Noy and Pollard, 2014). This plasticity and their position at the nexus between malignant cells and tumor-infiltrating T cells makes TAMs a promising target of TME-directed therapies in different cancers. Indeed, studies in mice showed that phenotypic alteration of TAMs results in anti-tumor efficacy in glioblastoma (Pyonteck et al., 2013; Quail et al., 2016; Yan et al., 2017), whereas TAM depletion prevents BrM outgrowth (Qiao et al., 2019).

Despite these preclinical studies, the precise contribution of the two ontogenetically distinct TAM cell types in human brain malignancies is unclear, which hinders clinical translation. For example, previous studies interrogating the role of TAMs in patient brain tumors did not distinguish between MG and MDMs based on use of lineage tracing-derived markers (Gabrusiewicz et al., 2016; Sankowski et al., 2019; Szulzewsky et al., 2016) or focused solely on gliomas (Müller et al., 2017; Venteicher et al., 2017). We therefore interrogated the TME landscape in gliomas and BrMs, with an emphasis on exploring TAMs, while also investigating their relation to other immune cells and structures in the TME. We leveraged this multimodal resource to address a number of questions. Do tumors arising within the brain shape their TME differently than cancers that metastasize from extracranial sites? Does *IDH* mutation status affect the TME? How do distinct TME compositions potentially modulate the activation states of immune cells? By integrating the answers to these questions, we provide insights into potential strategies to harness the brain TME in the fight against these deadly diseases.

RESULTS

Tumor Origin and *IDH* Mutational Status Influence the Immune Composition of Brain Malignancies

We first determined the broad immune cell abundance in the brain TME by analyzing the pan-leukocyte marker CD45 through immunofluorescence (IF) staining of whole-tissue sections and flow cytometry (FCM) analyses of non-tumor brain tissue, *IDH* mut low-grade and *IDH* WT high-grade gliomas, and BrMs originating from different primaries, including breast cancer, lung cancer, and melanoma (Figures 1A, 1B, and S1A). This showed a leukocyte abundance from ~20%–40% across the cancer samples. Stratification of $CD45^+$ cells into myeloid and lymphoid lineages revealed a significant increase in myeloid cells in *IDH* mut and *IDH* WT gliomas and of lymphocytes in *IDH* WT tumors and BrMs compared with non-tumor tissue (Figure 1B; $p < 0.05$, one-sided Student's t test). We used multicolor fluorescence-activated cell sorting (FACS) to analyze 14 major immune cell populations across 100 clinical samples (Figure S1A; Tables S1 and S2) and collected cells for RNA sequencing (RNA-seq) from 48 patients (Table S3; full clinical annotation).

By incorporating cell lineage tracing and mouse models of high-grade gliomas and BrM, we previously identified the cell surface marker integrin alpha 4, *ITGA4/CD49D*, as a means to discriminate tumor-associated MG (T-MG) from tumor-associated MDMs (T-MDMs) (Bowman et al., 2016), which we integrated here into clinical sample analyses. This enabled sorting of $CD45^-$ non-immune cells, $CD49D^{low}$ MG, $CD49D^{high}$ MDMs, neutrophils, and $CD4^+$ and $CD8^+$ T cells (Figure S1A; Tables S2 and S3A) for transcriptome analysis by RNA-seq. We assessed sorting fidelity by FCM re-analysis of the sorted $CD49D^{low}$ and $CD49D^{high}$ TAM populations (purity, 98.4%–99.8%) and by investigating the frequency of the canonical *IDH* codon 132 missense mutation in the RNA-seq reads from $CD45^-$ cells and $CD49D^{low}$ and $CD49D^{high}$ TAM populations. Although we

Figure 1. The Immune Cell Composition of Brain Malignancies

(A) Quantification of immunofluorescence (IF) staining of non-immune ($CD45^-$) and immune cells ($CD45^+$) in sections of non-tumor brain tissue (n = 6), gliomas ($n_{IDH\ mut} = 16$, $n_{IDH\ WT} = 16$), and brain metastases (BrMs, $n_{breast} = 12$, $n_{lung} = 5$, $n_{melanoma} = 7$). Data are represented as mean ± SEM.

(B) Flow cytometry (FCM) quantification of non-immune cells ($CD45^-$), myeloid cells ($CD45^+$, $CD11B^+$), and lymphocytes ($CD45^+$, $CD11B^-$) in non-tumor tissue (n = 6), gliomas ($n_{IDH\ mut} = 17$, $n_{IDH\ WT} = 40$), and BrMs ($n_{breast} = 13$, $n_{lung} = 16$, $n_{melanoma} = 8$). Data are represented as mean ± SEM.

(C) Gene set variation analysis (GSVA) normalized enrichment score (NES) of MG and MDM ontogeny-specific core gene signatures in $CD49D^{low}$ MG and $CD49D^{high}$ MDMs from non-tumor and tumor tissues.

(D) Heatmap of immune cell proportions in relation to all $CD45^+$ cells (MG, microglia; MDM, monocyte-derived macrophage; $CD14^{low}/CD16^+$, $CD14^{low}/CD16^+$ monocyte; $CD14^+/CD16^+$, $CD14^+/CD16^+$ monocyte; $CD16^-$ Gran., $CD16^-$ granulocyte; iMC, immature myeloid cell; DC, dendritic cell; Treg, regulatory T cell; DNT, double-negative T cell) across the cohort ($n_{non\text{-}tumor} = 6$, $n_{glioma} = 57$, $n_{BrM} = 37$). Cluster assignment, disease type, *IDH* mutation status, and BrM primary tumor are annotated per column (for clinical information, see Table S1).

(E) Principal component (PC) biplot of FCM data with sample scores and top 5 loadings of the first two PCs (n = 100 clinical samples, proportion of variance shown on PC axes).

(F) Mean of immune cell populations in non-tumor tissue (n = 6), gliomas ($n_{IDH\ mut} = 17$, $n_{IDH\ WT} = 40$), and BrMs ($n_{breast} = 13$, $n_{lung} = 16$, $n_{melanoma} = 8$) as percentage of $CD45^+$ cells.

See also Figure S1 and Tables S1 and S2.

observed a mean mutated allele frequency of 0.43 in CD45$^-$ cells from *IDH* mut gliomas (range, 0.3–0.61), this was very rare in TAMs (mean, 0.01; range, 0.0–0.09), indicating reliable separation of cell populations. In a t-distributed stochastic neighbor embedding (t-SNE) visualization of sorted populations, samples clustered mostly by cell type (Figure S1B), with gliomas and BrMs discernible as separate groups in the CD45$^-$ population.

In this global expression analysis in the context of the other major brain TME components, CD49D^{low} and CD49D^{high} TAM populations clustered closely, suggesting broad transcriptomic similarity. We thus further interrogated the utility of CD49D to differentiate between TAM populations by analyzing association of MG- and MDM-specific ontogeny core gene sets, identified previously from lineage-tracing studies (Bowman et al., 2016), in human CD49D^{low} and CD49D^{high} cells sorted from non-malignant and brain cancer tissues. This revealed enrichment of ontogeny core gene sets in the corresponding cell type (Figure 1C), demonstrating our ability to accurately distinguish MG and MDMs in human samples across different disease entities. Interestingly, these core signatures were influenced within certain tumor types, with T-MDMs showing an increased MG core gene set signal in *IDH* mut gliomas and T-MG acquiring MDM features in BrMs, suggesting tissue-dependent transcriptional programming of these cells, as further interrogated below.

We next assessed the landscape of intratumoral immune cell populations (Figure S1A; Table S2) using clustering analysis to identify patterns of cellular abundance (Figure 1D; chi-square test for independence, $p < 0.0001$). This revealed three major clusters: (1) non-tumor samples and *IDH* mut gliomas characterized by dominance of MG with low numbers of other immune cells; (2) *IDH* WT gliomas and several BrMs with an influx of MDMs and, to some extent, neutrophils into the tumor while mostly excluding lymphocytes; and (3) predominantly BrMs and few *IDH* WT gliomas exhibiting the most diverse immune cell landscape with substantial infiltration of T cells and neutrophils. Certain tumors contained CD14^{low}/CD16$^+$ non-classical monocytes, CD14$^+$/CD16$^+$ intermediate monocytes, CD16$^-$ granulocytes, dendritic cells (DCs), or immature myeloid cells. Across all samples, the lymphocyte compartment was mostly composed of T cells with fewer natural killer (NK) cells and B cells.

Principal-component analysis (PCA) of the relative abundance of all investigated populations confirmed that MG, MDMs, neutrophils, and CD4$^+$ and CD8$^+$ T cells are the major immune cell determinants of the brain TME landscape (Figure 1E). Principal component 1 (PC1) separated non-tumor tissue and *IDH* mut gliomas from *IDH* WT gliomas and BrMs, whereas PC2 distinguished *IDH* WT gliomas and BrMs. Further analysis stratifying for *IDH* status in gliomas and the primary tumor site in BrMs verified a substantially higher proportion of lymphocytes in BrMs (Figure 1F; $mean_{lymphocytes\ \%CD45^+} = 46.23\%$, SEM = 4.15, t test, $p < 0.0001$). Melanoma BrMs exhibited the most abundant lymphocyte infiltrate with a sizeable CD8$^+$ T cell fraction ($mean_{CD8^+\ \%CD45^+} = 33.01\%$, SEM = 5.82, one-way ANOVA, $p < 0.01$). Regulatory T cells (Tregs) were detected in certain BrMs ($mean_{Treg\ \%CD45^+} = 1.2\%$, SEM = 0.36) but were rare in gliomas ($mean_{Treg\ \%CD45^+} = 0.25\ \%$, SEM = 0.05, t test, $p < 0.05$).

Because of the prominence of T-MG and T-MDMs in the myeloid compartment of brain malignancies, we used IF staining and deconvolution analyses to independently validate their presence. Commonly employed MG markers, such as *P2RY12*, *TMEM119*, and *SALL1*, and MDM-associated genes, such as *AHR* and *VDR*, showed varying RNA expression levels across different brain malignancies while maintaining their cell type specificity (Figure S2A) in a similar manner as observed for the ontogeny core gene sets (Figure 1C). An equivalent pattern was observed at the protein level (Figure S2B), where P2RY12 showed the highest expression in non-tumor tissue, and CD68 was most abundant in BrM-TAM populations. This necessitated use of both markers complemented by CD49D to reliably identify MG and MDMs in IF analyses (Figure S2C). We used this strategy to interrogate a cohort of non-tumor, glioma, and BrM samples by whole-section quantification, confirming MDM accumulation in *IDH* WT gliomas and BrMs (Figures 2A–2C). Furthermore, comparison of tissue processed independently for IF and FCM from the same individual samples demonstrated significant concordance (Figure S2D).

We queried the sorted cell populations for T-MG- and T-MDM-specific differentially expressed genes (DEGs) that separate these two populations from the most abundant other cell types; i.e., CD45$^-$ cells, neutrophils, and T cells (Figure S2E). Several of the genes highly expressed in T-MG are well-established MG markers (*P2RY12*, *TMEM119*, and *TAL1*), whereas genes highly expressed in T-MDMs include markers of alternative macrophage polarization (*FCGR2B* and *CLEC10A*) and DC-like phenotypes (*CD1C*, *CD1B*, and *CD207*) with increased phagocytic and antigen cross-presentation ability (*CD209*). These gene sets also allowed us to utilize a publicly available integrated dataset (Vivian et al., 2017) containing bulk expression data of healthy cortical brain tissue from the Genotype-Tissue Expression project (GTEx; GTEx Consortium, 2013) and low- and high-grade glioma samples from The Cancer Genome Atlas (TCGA; Ceccarelli et al., 2016) in a bulk tissue transcriptome deconvolution approach (Racle et al., 2017). The estimates obtained of MG and MDM proportions in this external dataset (n = 711 samples) verified the prevalence of MG in *IDH* mut gliomas and MDM enrichment in *IDH* WT gliomas (Figure 2D).

MG and MDMs Exhibit a Multifaceted Polarization Phenotype in Brain Malignancies

We next employed PCA to specifically focus on TAMs and analyze genes whose expression was influenced by tissue type (i.e., reference MDMs, non-tumor brain, gliomas, and BrMs) and cell type (i.e., MG and MDMs) (Figure 3A). Within the first two PCs, MG and MDMs projected into different spaces, with *in vitro* differentiated MDMs distinct from tissue-derived samples. We observed a gradient across PC1 with non-tumor brain tissue at one end, traversing *IDH* mut and *IDH* WT gliomas, and ending with BrMs. Thus, TAM transcriptomic changes are influenced by the brain TME per se and also by the specific type of malignancy.

We contrasted T-MG and T-MDMs from BrMs or gliomas (regardless of *IDH* mutation status) with MG from non-tumor brain or *in vitro* differentiated MDMs from healthy donors, respectively (Figure S3A; Tables S3A and S4). This revealed profound expression changes in both populations, with T-MDMs exhibiting a higher magnitude in their transcriptional response

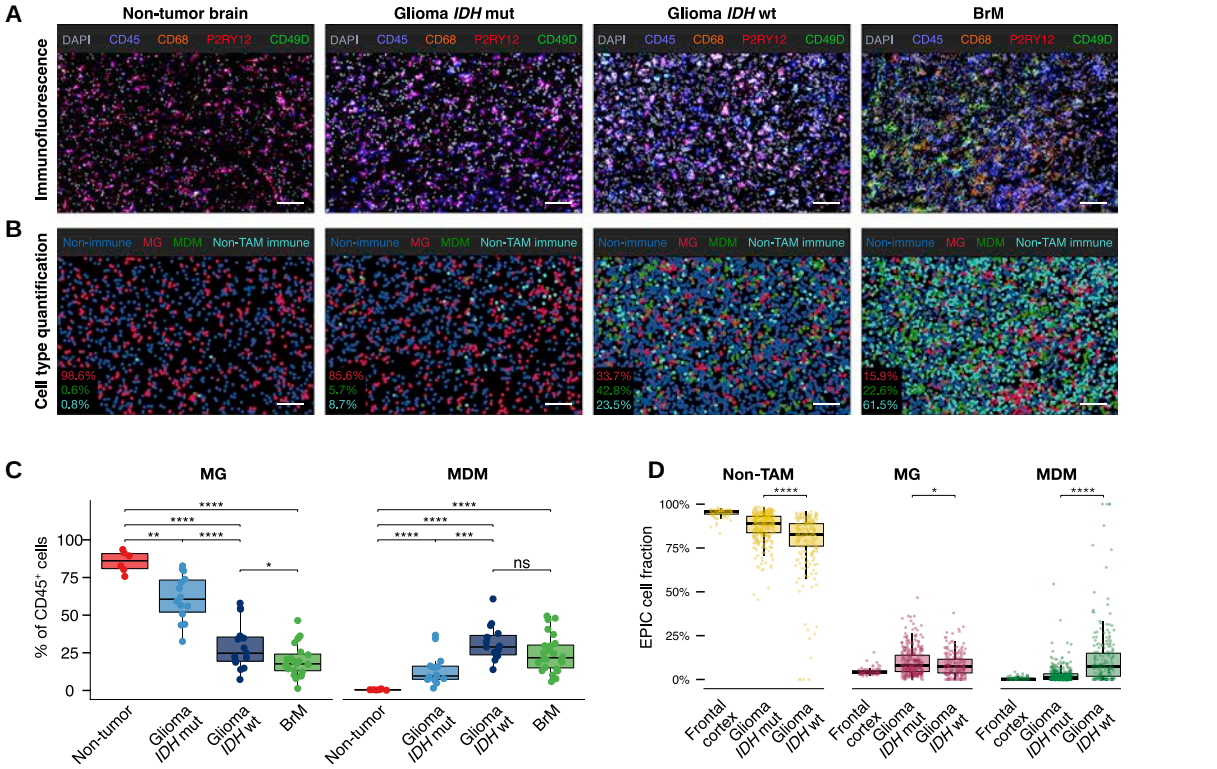

Figure 2. Analysis of MG and MDM Abundance

(A and B) Representative IF images (A) and corresponding cell type identification (B) of MG (CD45$^+$, P2RY12$^+$/CD68$^+$, CD49D$^-$), MDMs (CD45$^+$, P2RY12$^+$/CD68$^+$, CD49D$^+$), and non-immune (CD45$^-$) and non-TAM immune cells (CD45$^+$, P2RY12$^-$/CD68$^-$, CD49D$^{-/+}$) in non-tumor brain tissue, *IDH* mut and *IDH* WT gliomas, and BrMs. Scale bars, 100 μm. Insets show quantification per field of view (FOV).

(C) IF quantification of MG and MDM abundance in non-tumor brain tissue (n = 6), *IDH* mut (n = 16) and *IDH* WT (n = 16) gliomas, and BrMs (n = 24).

(D) Deconvolution of merged GTEx and TCGA glioma datasets, showing relative abundance of MG, MDMs, and non-TAMs ("other cells") in healthy frontal cortex and *IDH* mut and *IDH* WT gliomas.

Wilcoxon rank-sum test was used for statistical analysis: *p < 0.05, **p < 0.01, ***p < 0.001, ****p < 0.0001. See also Figure S2.

compared with T-MG (Figure S3A). The intersect of DEGs in gliomas and BrMs was highest in T-MDMs (Figure S3B), potentially reflecting the greater changes experienced by these cells upon entering the completely foreign environment of a brain tumor. This was also evident when focusing on genes upregulated in gliomas and BrMs that are exclusive to T-MG or T-MDMs (Figure 3B). In T-MG and T-MDMs, the number of shared genes was higher across different diseases than between these two cell populations within the same tumor type. Consequently, only a small number of genes (n = 137) showed concordant upregulation across a comparison of all diseases and TAM types (Figure 3B).

To explore the underlying biological processes conserved in gliomas and BrMs, we examined the intersect of upregulated genes (Figure S3B) in T-MG or T-MDMs using gene set overrepresentation analysis (ORA). In the Molecular Signature Database (MSigDB; Liberzon et al., 2015) "hallmark" collection of major biological categories, T-MG and T-MDMs showed pathway enrichment in (1) modeling of the TME ("Angiogenesis," "Hypoxia"), (2) inflammation ("Inflammatory Response," "Allograft Rejection"), and (3) immune cell activation states ("TNFα Signaling via NFκB," "Interferon α Response," "Interferon γ Response," "IL2 STAT5 Signaling," and "IL6 JAK STAT3 Signaling") (Figure S3C).

We also assessed the M1 and M2 polarization status of T-MG and T-MDMs using a panel of marker genes (Murray et al., 2014). However, no evident pattern emerged of a defined M1 versus M2 phenotype in glioma or BrM T-MG or T-MDMs (Figure S3D). To further explore the activation state of T-MG and T-MDMs, we subjected their respective upregulated genes to ORA of macrophage stimulus-specific programs (Xue et al., 2014). This revealed a multifaceted response (Figure 3C) incorporating canonical M1 (interferon γ [IFNγ]) and M2 polarization (interleukin-4 [IL-4]), including expression changes associated with chronic inflammatory stimuli (tumor necrosis factor alpha [TNF-α] + prostaglandin E [PGE_2] and TNFα + PGE_2 + Pam3CysSerLys4 [TPP]) and exposure to free fatty acids (oleic acid [OA] and palmitic acid [PA]), which have been implicated in modulating myeloid cell function (Thapa and Lee, 2019). This indicates diverse transcriptional programming of T-MG and T-MDMs in gliomas and BrMs extending beyond simple M1 versus M2 polarization.

To understand which processes are linked to and potentially driving these responses, we identified the gene set enrichment

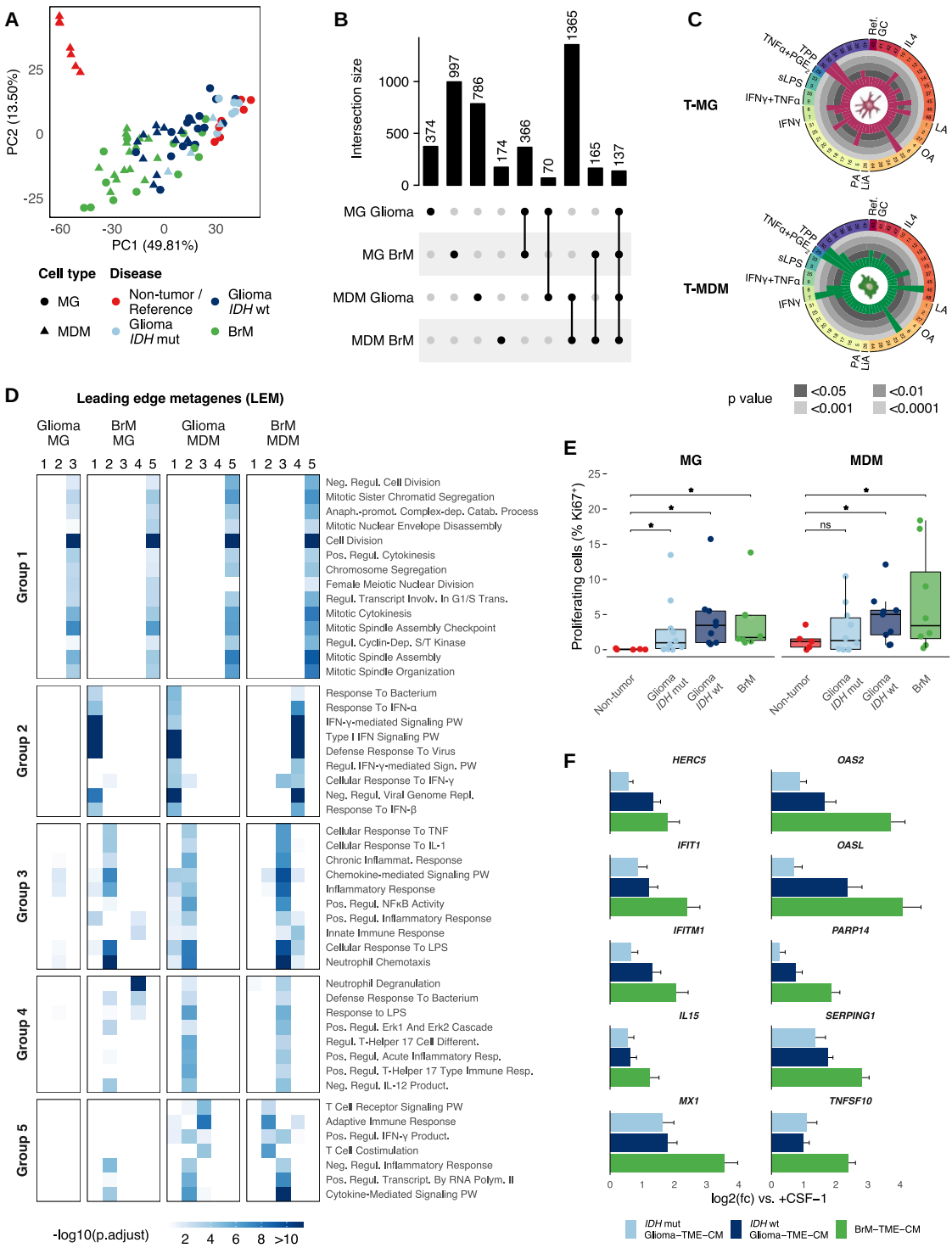

Figure 3. MG and MDMs Exhibit a Multifaceted Polarization Phenotype in Brain Malignancies

(A) PC biplot of MG and MDM transcriptome data from non-tumor brain tissue, *IDH* mut and *IDH* WT gliomas, and BrMs (for clinical information, see Table S3A; reference = *in-vitro*-generated MDMs; proportion of variance shown on PC axes).

(B) Visualization of intersects of the conserved sets of significantly upregulated genes in MG and MDMs. Intersects between sets are shown in the combination matrix. n_{genes} found uniquely in a gene set or intersect is indicated above individual bars.

(C) Stimulus-specific macrophage gene expression modules overrepresented (within conserved differentially expressed genes [DEGs] versus respective references) in tumor associated MG (T-MG) and tumor-associated MDMs (T-MDMs). Bar heights and color indicate significance level. GC, glucocorticoid; IFNγ,

(legend continued on next page)

analysis (GSEA; Subramanian et al., 2005) leading-edge genes in T-MG and T-MDMs in gliomas and BrMs and clustered them into leading-edge metagenes (LEMs) with non-negative matrix factorization (Godec et al., 2016). This identified up to 5 distinct LEMs per cell type and comparison that were tested for significant overlap in a pairwise fashion (Figure S3E) and annotated using Gene Ontology (GO) terms (Figure 3D). LEMs associated with mitosis and cell proliferation were present in T-MG and T-MDMs in gliomas and BrMs (Figure 3D, group 1). The biological validity of these LEMs were verified by staining for Ki-67, a marker of cell proliferation, in non-tumor, glioma, and BrM tissue sections (Figure 3E), showing increased proliferation in T-MG and T-MDMs in *IDH* WT gliomas and BrMs and in T-MG in *IDH* mut gliomas.

Interestingly, LEMs enriched for type I IFN signaling were detected in glioma and BrM T-MDMs and in BrM T-MG but not in glioma T-MG (Figure 3D, group 2). Sustained type I IFN signaling has been implicated in mediating immune suppression and ICB resistance (Benci et al., 2016). The stringency of these group 2 LEMs was validated by building a protein-protein interaction (PPI) network of the shared LEM genes (Figure S3F). Beyond their role in antiviral responses, the genes highlighted at the center of the PPI network (Figure S3F, red nodes) have been implicated in a variety of tumor-promoting and -suppressing roles (Benci et al., 2016). Similarly, the more peripheral network nodes *IL15* and *TNFSF10* are potentially able to modulate an effective immunological anti-tumor response or induce apoptosis in cancer cells, respectively (Bouralexis et al., 2005; Santana Carrero et al., 2019). We asked whether these genes were directly induced by secreted factors in the brain TME and established cell-based assays to expose MDMs to TME conditioned medium (CM) generated from single-cell suspensions of freshly isolated glioma or BrM samples in culture. All genes analyzed were upregulated by BrM-TME-CM and to a lesser extent by glioma TME-CM (Figure 3F). We also detected induction of inflammation- and nuclear factor κB (NFκB) signaling-associated LEMs in BrM-MG, glioma MDMs, and BrM-MDMs (Figure 3D, group 3). LEMs that point toward a Th17 response (group 4) and recruitment of immune cells and interactions between different immune cell compartments were exclusively detected in MDMs (group 5). Collectively, these analyses reveal acquisition of a multifaceted activation state of MG and MDMs upon their integration into the TME of brain malignancies.

IDH Mutation Status Associated with Changes in Glioma TAM Activation

We next asked whether MG and MDMs occupy distinct regions within the TME of *IDH* WT gliomas. Spatial analysis of tissue sections showed significant enrichment of both populations in the perivascular niche (Figures 4A and S4A). Analysis of their distribution relative to $CD31^+$ vascular structures showed a closer proximity of T-MDMs compared with T-MG (Figures 4B and S4A). Interrogation of anatomical transcriptome data from the Ivy Glioblastoma Atlas Project (Ivy GAP) study (Puchalski et al., 2018) also demonstrated enrichment of T-MDMs in the microvascular compartment (Figure S4B). This enrichment coincided with $CD4^+$ and $CD8^+$ T cells, indicating further spatial TME organization in *IDH* WT gliomas.

We assessed whether the distinct T-MG and T-MDM distributions and cell numbers are paralleled by their activation state. In the LEM analysis, we had detected a type I IFN response in glioma MDMs but not MG (Figure 3D); we therefore queried the FCM data to analyze levels of major histocompatibility complex (MHC) class II human leukocyte antigen-DR isotype (HLA-DR) expression. This showed significantly increased HLA-DR in T-MDMs compared with T-MG in *IDH* mut and *IDH* WT tumors (Figure 4C). We screened the associated RNA-seq data for antigen processing and presentation pathway gene sets using GSEA and gene set variation analysis (GSVA) (Figure 4D). Interestingly, we found evidence of increased expression of MHC class II antigen presentation gene sets in *IDH* WT glioma MDMs and also antigen processing-associated pathways (Figure S4C) and MHC class I presentation gene sets (Figure 4D). Although these findings suggest the potential of TAMs, particularly T-MDMs, to initiate an immune response, this potential is generally not realized in the glioma TME, based on the current status of ICB trials in this disease, and we thus asked whether there was also evidence of pro-tumor states in these cell populations.

We compared T-MG and T-MDMs from *IDH* WT gliomas with T-MG from *IDH* mut gliomas because they constitute the most abundant TME cell types in these tumors, respectively (Figures 1F and 2C; Table S5). This revealed 489 DEGs in T-MG (Figure 4E; Table S5; 406 up- and 83 downregulated), and 1,478 DEGs in T-MDMs (Figure 4F; Table S5; 903 up- and 575 downregulated). Although these gene lists were generated by comparing T-MDMs from *IDH* WT gliomas with T-MG from *IDH* mut gliomas, they similarly separated T-MDMs in *IDH* mut versus *IDH* WT disease in a clustering analysis (Figure 4F), indicating that they indeed reflect T-MDM alterations based on the *IDH* status of the tumor. 421 genes exhibit a similar pattern across both TAM cell types (343 up- and 78 downregulated), suggesting that T-MG and T-MDMs can also acquire a common transcriptional pattern in *IDH* WT tumors. Among the shared genes were several encoding extracellular matrix (ECM) proteins (Figure 4G, *FN1* and *VCAN*) and ECM-associated matricellular proteins (*THBS1*, *TGFBI*, *LGALS3*, and *ANGPTL4*) that regulate the availability of ECM-sequestered ligands, angiogenesis, and tumor

interferon gamma; LA, lauric acid; LiA, linoleic acid; OA, oleic acid; PA, palmitic acid; PGE_2, prostaglandin E_2; sLPS, standard lipopolysaccharide; TNF-α = tumor necrosis factor alpha; TPP, TNFα + PGE_2 + Pam3CysSerLys4; IL-10, interleukin 10.

(D) Heatmap of GO overrepresentation analysis of leading-edge metagenes (LEMs) in MG and MDMs from gliomas and BrMs. Tile fill indicates significance (hypergeometric test, -log10 (adjusted p value), terms were filtered by significance).

(E) IF quantification of the proportion of proliferating $Ki67^+$ MG and MDMs in non-tumor tissue (n = 5), *IDH* mut (n = 10) and *IDH* WT gliomas (n = 9), and BrMs (n = 8). Means were compared with one-tailed t test: *$p < 0.05$.

(F) qRT-PCR of type I IFN LEM marker genes from group 2 (Figure S3F) in *in-vitro*-generated MDMs stimulated with the indicated TME culture-conditioned medium (TME CM). Fold changes were calculated relative to colony-stimulating factor-1 (CSF-1)-treated MDM baseline (one-way ANOVA, $p < 0.1$, $n_{MDM} = 4–11$). Data are represented as mean ± SEM.

See also Figure S3 and Table S4.

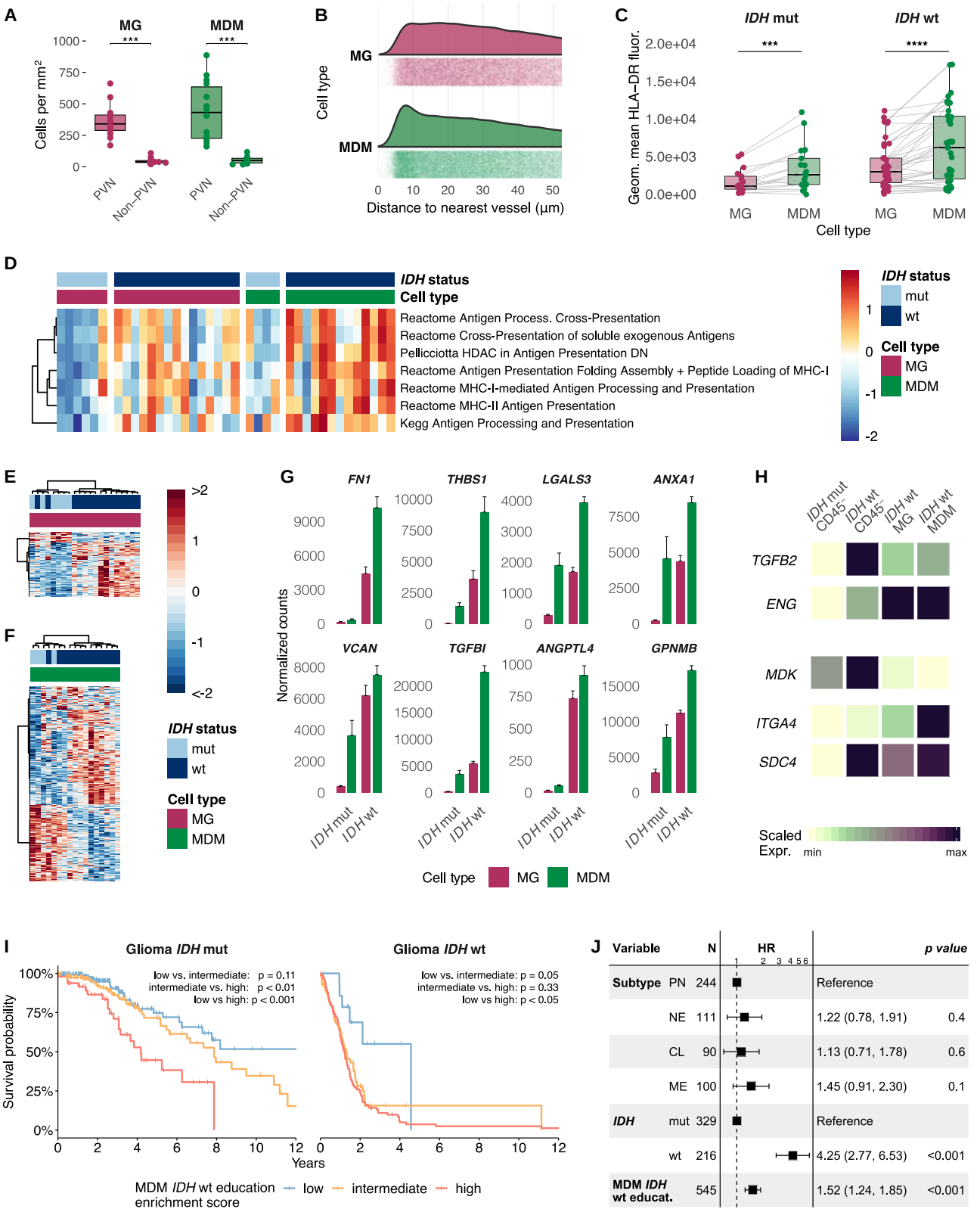

(legend on next page)

immunity (Mushtaq et al., 2018). This suggests that TAMs help shape the composition and effector functions of ECM proteins in *IDH* WT tumors. We also found the anti-inflammatory molecules *ANXA1* and *GPNMB* (Figure 4G), previously implicated in pro-tumorigenic macrophage polarization and inhibition of T cell activation (Kobayashi et al., 2019; Ripoll et al., 2007), to be upregulated in T-MG and T-MDMs.

We next investigated inflammation mediators within the CD45$^-$ population of *IDH* WT tumors in parallel with their corresponding receptors in TAMs. *TGFB2* expression was elevated compared with *IDH* mut CD45$^-$ cells, and the accessory transforming growth factor β (TGF-β) receptor *ENG* was highly expressed in *IDH* WT TAMs (Figure 4H). TGFB2 has pleiotropic effects in inflammation and tissue remodeling during wound healing and has been implicated in an autocrine signaling loop in glioblastoma cells (Rodón et al., 2014). The neuroinflammatory cytokine *MDK*, which modulates TAM polarization to a M2-like phenotype in glioma (Meng et al., 2019), was upregulated in CD45$^-$ cells from *IDH* WT tumors, and its receptors *SDC4* and *ITGA4*/*CD49D* were differentially expressed in T-MDMs versus T-MG (Figure 4H), suggesting cell-type-specific effects of this inferred signaling loop.

We asked whether a T-MDM-specific gene set generated from *IDH* WT gliomas was associated with a survival difference in patients. By logistic regression, we derived a representative signature consisting of 36 genes (Figure S4D) from the total number of genes upregulated in TAMs in brain malignancies (Figure 3B). This included the macrophage marker *RUNX3*; the atypical chemokine receptor *ACKR3*, which can regulate CXCL12-CXCR4 signaling; the endoplasmic reticulum (ER) stress protein *HERPUD1* and the inhibitory Fc receptor *FCGR2B*, which can modulate macrophage activation (Bournazos et al., 2016; Li et al., 2018); and the cytokine *IL19*, which affects angiogenesis and macrophage polarization (Richards et al., 2015). The signature was used to classify patients in a merged TCGA dataset of low- and high-grade gliomas (Figures 4I and S4E). In *IDH* mut patients, a decrease in median overall survival was associated with enrichment of the T-MDM *IDH* WT signature, whereas *IDH* WT patients with a low enrichment score showed increased survival. This was confirmed in a multivariate Cox proportional hazard model that included the transcriptomic glioma subtypes (as annotated in the TCGA dataset) and *IDH* status (Figure 4J). To verify that this effect did not simply reflect changes in T-MDM number, we classified the TCGA cohort based on enrichment of the T-MDM-specific gene set used for deconvolution, which showed a low effect on survival (Figure S4F).

In light of disappointing outcomes from PD1 or PDL1 ICB trials in glioblastoma to date, we queried whether the abundant T-MG and T-MDMs could contribute to the limited therapeutic efficacy. We performed ORA of a panel of 20 gene sets previously associated with innate anti-PD1 resistance (IPRES; Hugo et al., 2016) in the TAM DEGs of *IDH* WT gliomas and found a sizeable fraction to be upregulated in T-MG and T-MDMs (Figure S4G). We then included the CD45$^-$ population and interrogated enrichment of IPRES gene sets on the single-sample level by GSVA (Figure S4H). This yielded a diverse picture with tumor cells and TAMs enriched for IPRES gene sets to varying degrees. Therefore, TAMs and CD45$^-$ cells from *IDH* WT gliomas may contribute to mediating innate ICB resistance.

The Immune Contexture Influences the TME on a Global Level

Through integrated analysis of protein and gene expression data, we next explored the effect of immune cell infiltration. Of 200 inflammation-associated proteins assessed, 55 were differentially detected in our sample cohort (for clinical information, see Table S3B). Unsupervised clustering analysis revealed distinct clusters with abundant inflammatory proteins in tumors (Figure 5A). The profile of *IDH* WT gliomas and BrMs showed a sizeable overlap (protein cluster 1), encompassing angiogenic factors (VEGFA and ANG), growth factors (PDGFA, TGFB1, SPP1, and GDF15), several proteases and protease inhibitors (SERPINE1, CTSS, and TIMP1), the proteolysis cascade regulator PLAUR, and the cytokines CCL2 and CCL5 (Figures 5A and S5A). However, we also found distinct protein patterns between gliomas and BrMs. The neurotrophic growth factor FGF2 and neuronal cell adhesion molecules, including ALCAM, which regulates immune cell infiltration during

Figure 4. *IDH* Mutation Status Shapes TAM Activation in Gliomas

(A) Number of MG and MDMs per square millimeter in the perivascular niche (PVN) or distant from the PVN (non-PVN) in *IDH* WT gliomas by IF staining. Means were compared with Wilcoxon signed-rank test: ***p < 0.001.

(B) Distance of MG and MDMs to the nearest vessel in *IDH* WT gliomas ($n_{samples}$ = 14, n_{MG} = 88,781, and n_{MDM} = 92,969 cells counted).

(C) Boxplot of HLA-DR geometric mean fluorescence intensity measured by FCM in MG and MDMs in *IDH* mut and *IDH* WT gliomas. MG and MDMs from the same samples are connected by lines ($n_{IDH\ mut}$ = 17, $n_{IDH\ WT}$ = 39; Wilcoxon signed-rank test: ***p < 0.001, ****p < 0.0001).

(D) GSVA of antigen processing and presentation pathways from the Molecular Signatures Database (MSigDB) "Canonical Pathways" collection with significant differential enrichment between MG and MDMs in *IDH* WT tumors and in MG and MDMs across *IDH* mut and *IDH* WT samples. Columns are ordered by *IDH* mutation status and cell type, and rows (*Z* score) are hierarchically clustered.

(E and F) Expression heatmap of T-MG (E) and T-MDM (F) DEGs (compared with T-MG in *IDH* mut gliomas) in *IDH* mut and *IDH* WT glioma samples. Columns and rows (*Z* score) are hierarchically clustered.

(G) Normalized counts of selected genes in MG and MDMs in gliomas stratified by *IDH* status. Data are represented as mean ± SEM.

(H) Relative expression in CD45$^-$ MG and MDM cells of ligands and receptors upregulated in CD45$^-$ cells in *IDH* WT versus *IDH* mut samples and their matching counterparts. Variance-stabilized expression values were scaled to the expression range.

(I) Kaplan-Meier estimator of survival in the TCGA glioma cohort based on enrichment for the MDM *IDH* WT signature, assessed by GSVA in *IDH* mut and *IDH* WT gliomas from the combined TCGA cohort. GSVA scores were separated into tertiles across the combined *IDH* mut and *IDH* WT sample set. Pairwise p values were calculated using a log rank test.

(J) Hazard ratios of a multivariate Cox proportional hazards model with transcriptomic subtype (TCGA annotation), *IDH* status (TCGA annotation), and T-MDM *IDH* WT GSVA score as covariates for overall survival within the TCGA glioma cohort (PN, proneural; NE, neural; CL, classical; ME, mesenchymal subtype).

See also Figure S4 and Table S5.

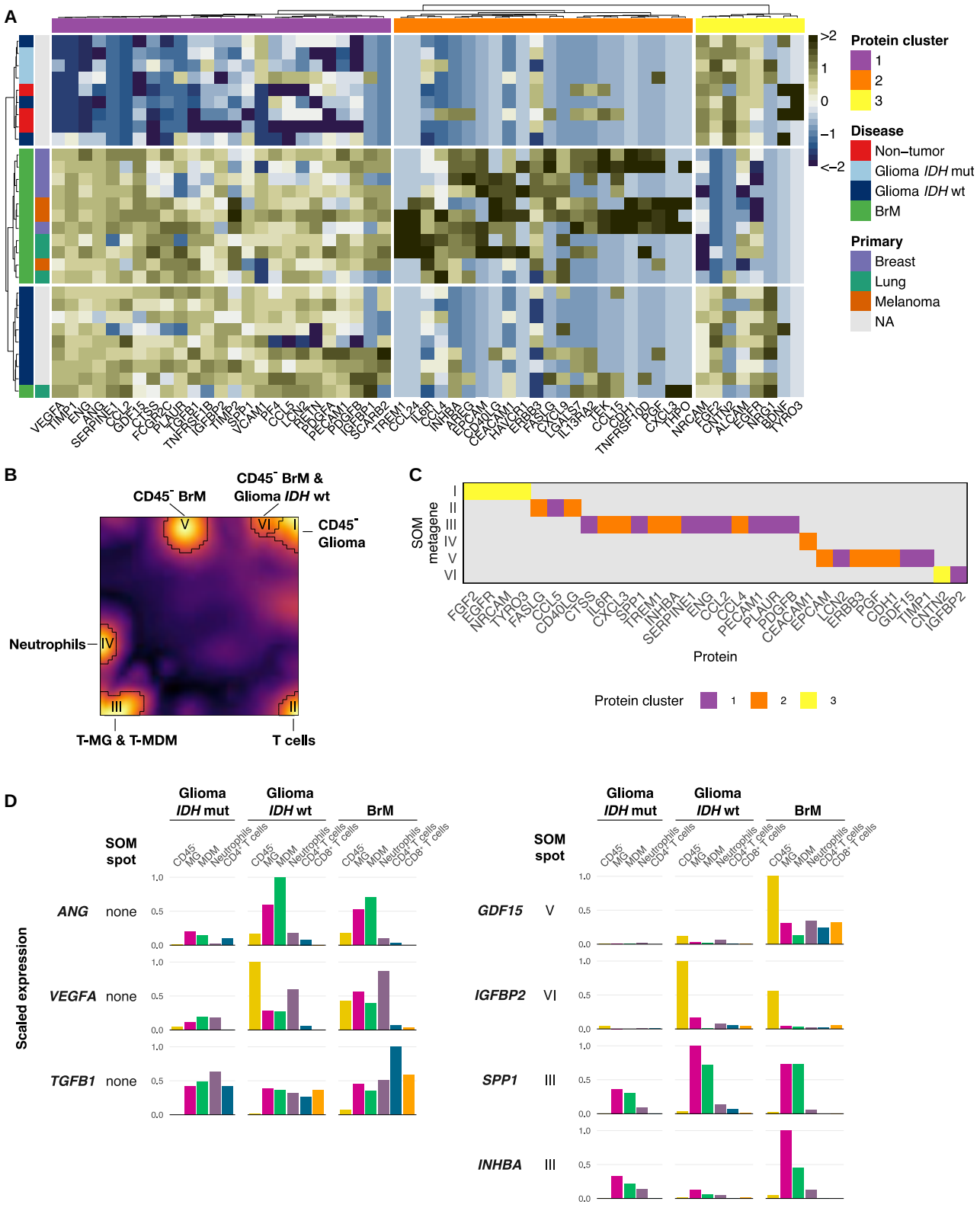

Figure 5. The Immune Contexture Influences the TME on a Global Level

(A) Inflammation-associated bulk tissue protein concentration heatmap subset on 55 proteins with significantly different concentrations between non-tumor brain, gliomas, and BrMs in an ANOVA ($p < 0.1$, $n_{non\text{-}tumor} = 3$, $n_{glioma} = 14$, $n_{BrM} = 12$; concentrations were log10-transformed and *Z* scored). Rows and columns

(legend continued on next page)

neuroinflammation (Lécuyer et al., 2017), were highly expressed in non-tumor brain, *IDH* mut, and *IDH* WT samples (protein cluster 3; Figure S5A). Conversely, BrM samples had abundant immune-regulatory molecules affecting myeloid and lymphocytic cells and their heterotypic signaling (protein cluster 2; Figure S5A), such as CD40L, IL6R, INHBA, and AREG (Morianos et al., 2019; Zaiss et al., 2015), possibly reflecting the greater immune cell diversity in BrMs. This orthogonal dataset reinforces the RNA-seq analyses showing that inflammatory signaling pathways are highly enriched in brain tumors.

We integrated the cell-type-specific RNA-seq data and bulk protein data to distinguish proteins with more restricted expression versus those that are expressed across a range of cell types. Transcriptome data from $CD45^-$ cells, TAMs, neutrophils, and $CD4^+$ and $CD8^+$ T cells from all tumor samples were clustered using a self-organizing map (SOM). This yielded 6 SOM spots (i.e., metagenes of co-expressed genes; Figure 5B) that recapitulated the respective cell lineages (Figure S5B). The $CD45^-$ populations were assigned to three distinct spots that were associated with more aggressive *IDH* WT gliomas and BrMs (spot VI) or reflected the brain-intrinsic or -extrinsic tumor origin (spots I and V). These cell-type-associated SOM spots overlapped considerably with the protein data (30 of 55 proteins, Fisher's exact test, $p < 0.0001$; Figure 5C). Although *VEGFA*, *ANG*, and *TGFB1* were expressed by diverse cell types in gliomas and BrMs, other genes, such as *GDF15* and *IGFBP2*, showed more $CD45^-$ cell-restricted expression (Figure 5D). The significant contribution of TAMs to production of key inflammatory proteins, including *SPP1* and *IHNBA*, is reflected by TAM SOM spot III, constituting the largest group of proteins with cell type-specific expression (Figures 5C and 5D).

Myeloid Cells Show a Distinct Phenotype in BrMs

Our global analysis juxtaposing the expression patterns of TAMs in gliomas (regardless of *IDH* status) with BrMs showed disease- and cell-type-specific transcriptomic changes. We thus explored BrM-specific alterations by focusing on genes upregulated only in relation to the corresponding reference and to *IDH* WT gliomas (Figures S6A and S6B; Table S6). Various cytokines, chemokines, and pro-inflammatory molecules were elevated in BrM-MG and BrM-MDMs (Figure 6A), including the potent mediators of autoimmune neuroinflammation *CSF2* and *IL23A* (Zhao et al., 2017) and the pattern recognition receptor *MARCO*. Intriguingly, antibody-mediated MARCO targeting in extracranial tumors increases M1-like polarization of TAMs and enhances ICB efficacy (Georgoudaki et al., 2016). These effects relied on interaction of the antibody with *FCGR2B*, which is also part of the T-MDM *IDH* WT signature (Figures S2E and S4C). Finally, *RETN*, which is involved in systemic inflammatory disorders (Filková et al., 2009), was upregulated in BrM-TAMs (Figure 6A).

Analysis of individual BrM-TAM populations uncovered distinct expression patterns. BrM-MG showed restricted upregulation of *IL6* (Figure 6A), which exerts immunosuppressive effects on T cell function in cancer and mediates ICB resistance (Tsukamoto et al., 2018), and the receptor *TREM1*, which modulates pro-inflammatory responses in MG and systemically in myeloid cells during neuroinflammation (Liu et al., 2019; Xu et al., 2019). Among the upregulated chemokines, we found increases in both TAM cell types (*CCL23*) and BrM-MG-restricted (*CXCL5* and *CXCL8*) or BrM-MDM-restricted increases (*CCL8*, *CCL13*, *CCL17*, and *CCL18*) (Figure 6A). These results reveal distinct contributions of TAM populations to the inflammatory TME milieu in a disease-specific manner.

GSEA identified additional cell-type-specific enrichment patterns. BrM-MG showed evidence of IL-6 pathway activity (Figure S6C), and in BrM-MDMs, the "Naba core matrisome" gene set was significantly enriched (Figure S6D). This prompted us to assess expression of genes encoding ECM and matricellular proteins in BrM-MDMs versus BrM-MG, which revealed genes encoding matrix proteins, including type III and IV collagens, *FN1*, the proteoglycans *LUM* and *OGN*, and the matricellular proteins *ECM1*, *SPARC*, and *SPARCL1* as highly expressed in BrM-MDMs (Figure 6B). Although ECM remodeling has been implicated in tumor progression, *LUM*, *OGN, SPARCL*, and *SPARCL1* exhibit pro- and anti-metastatic properties, which underscores the complex context-dependent role of the ECM (Kai et al., 2019). We also found high expression of the cathepsin proteases *CTSB* and *CTSW* in BrM-MDMs (Figure 6B), which participate in multiple tumor-promoting processes, including invasion and metastasis (Olson and Joyce, 2015). The hyaluronan receptor *HMMR*, involved in macrophage chemotaxis and fibrosis in lung injury (Cui et al., 2019), was also higher in BrM-MDMs (Figure 6B). Together, these data suggest that the ECM is not only shaped by macrophages at the primary site (Afik et al., 2016) but that T-MDMs may also play a pivotal role in ECM niche construction in BrM that is distinct from *IDH* WT gliomas (Figure 4G).

Given the upregulation of *CXCL8*, a key neutrophil chemoattractant, by BrM-MG (Figure 6A), we explored the TME contribution to recruitment of neutrophils, which were highly abundant in BrM (Figure 1F). Analysis of major neutrophil-recruiting chemokines and their receptors showed broad expression across all interrogated myeloid cells (Figure S6E). To explore the phenotype of BrM-associated neutrophils, we queried the RNA-seq data, which revealed BrM-specific upregulation of *ITGA3* (Figure 6C), which is involved in neutrophil tissue infiltration in sepsis, and *CXCL17*, previously implicated in neutrophil and macrophage recruitment in cancer (Li et al., 2014). We also observed upregulation of the

are hierarchically clustered. Clinical data are annotated per row; column annotation reflects the major protein clusters (further information can be found in Table S3B).

(B) Self-organizing map (SOM) of RNA expression data of major cell populations in glioma and BrM samples. SOM spots are highlighted, numbered with Roman numerals, and annotated with their cell type association.

(C) Overlap of individual proteins and SOM spot metagenes; tile color fill reflects protein cluster membership from (A).

(D) RNA-seq counts (normalized, scaled to expression range) of proteins from (A) across major cell types in *IDH* mut and *IDH* WT gliomas and BrMs. SOM spot membership of individual genes is indicated per row.

See also Figure S5.

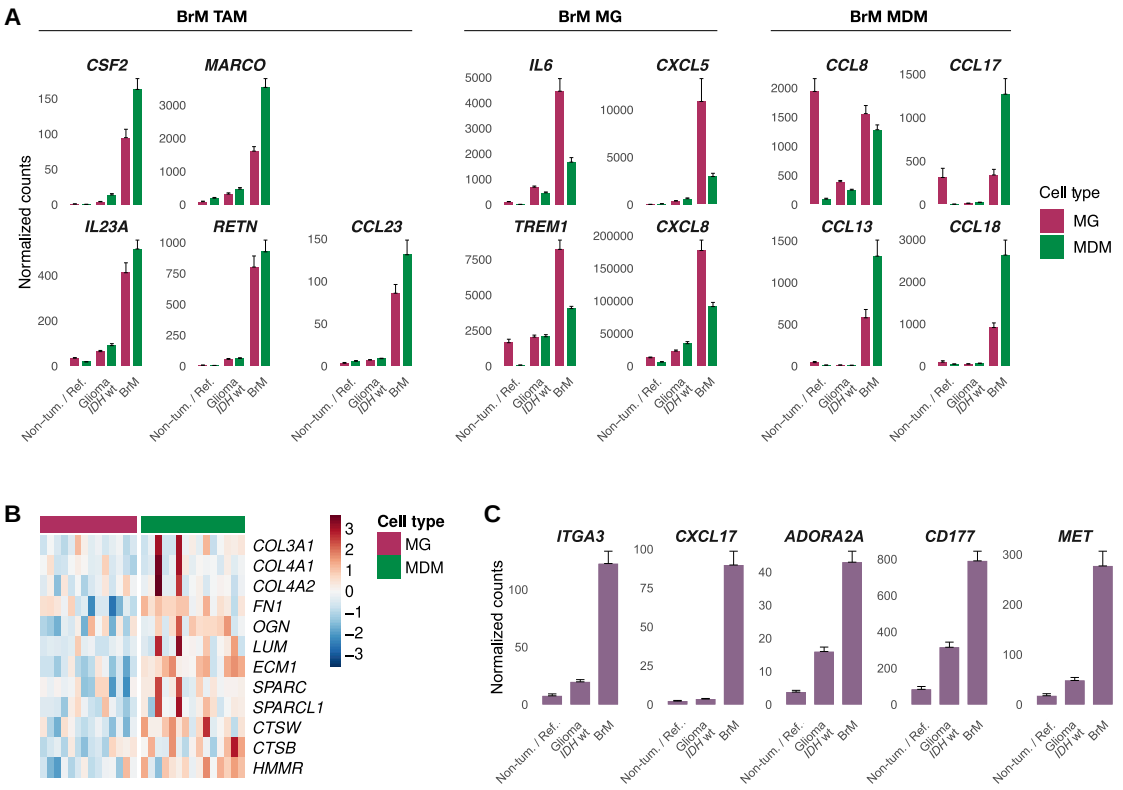

Figure 6. Myeloid Cells Show Distinct Transcriptional Changes in BrMs

(A) Normalized counts of the indicated genes in MG and MDMs in non-tumor or reference, *IDH* WT gliomas, and BrMs. Data are represented as mean ± SEM.

(B) Expression heatmap of Extracellular matrix-associated genes differentially expressed between MG and MDMs in BrMs. Rows are *Z*-scored and manually sorted, and columns are ordered by cell type.

(C) Expression of the indicated BrM-specific genes in neutrophils from unmatched healthy blood, *IDH* WT gliomas, and BrMs. Data are represented as mean ± SEM.

See also Figure S6 and Table S6.

adenosine receptor *ADORA2A* (Figure 6C), which attenuates the phenotype of pro-inflammatory neutrophils (Barletta et al., 2012). Furthermore, we found increased expression of *CD177* (Figure 6C), a cell surface receptor that modulates neutrophil migration and activation and serves as a marker for PR3-positive neutrophils, which, in turn, negatively affect T cell proliferation (Yang et al., 2018). Notably, *MET*, which has been linked to recruitment of immunosuppressive neutrophils in cancer (Glodde et al., 2017), was upregulated in neutrophils in a BrM-specific manner (Figure 6C). In sum, we have uncovered multiple disease-specific alterations of myeloid cells extending beyond BrM-TAMs to neutrophils, which has potential implications for the recruitment and activation of other cell types within the TME, including T cells.

TAMs Are Poised toward an Immunomodulatory Phenotype in BrMs

Although we found a significant accumulation of $CD4^+$ and $CD8^+$ T cells in BrMs versus *IDH* WT gliomas by FCM, this analysis of dissociated tissue samples lacks structural information. We thus performed neighborhood analysis of IF-phenotyped *IDH* WT and BrM tissue sections to elucidate whether there is a spatial relationship between TAMs and $CD3^+$ T cells in BrMs. In *IDH* WT gliomas, T-MG and T-MDMs mostly neighbored homotypic cells while lacking T cells in their close vicinity (Figures 7A, 7B, and S7A), possibly reflecting the general T cell sparseness in these tumors. In contrast, both TAM populations neighbored T cells far more frequently in BrMs, indicating the potential for interaction (Figures 7A, 7B, and S7A).

We thus investigated the T cell activation state in BrMs in relation to unmatched healthy donor blood and also juxtaposed them to the corresponding populations from *IDH* WT gliomas. Compared with controls, $CD4^+$ T cells from BrM showed evidence of a hyporesponsive, anergic phenotype (Figure 7C), whereas $CD8^+$ T cells exhibited an exhaustion signature (Figure 7D), which usually occurs upon chronic activation, resulting in upregulation of inhibitory receptors. These defective T cell states can be caused by aberrant activation or T cell inhibition by tumor cells and antigen-presenting cells in the TME and are a major obstacle in treating cancers.

To delineate putative mechanisms in the BrM TME that may drive these alterations, we probed the RNA-seq data from $CD45^-$ cells, TAMs, and T cells (Figure 7E) for expression of activating and inhibitory immunomodulatory signals (Wei et al., 2018). This revealed upregulation of various canonical T cell

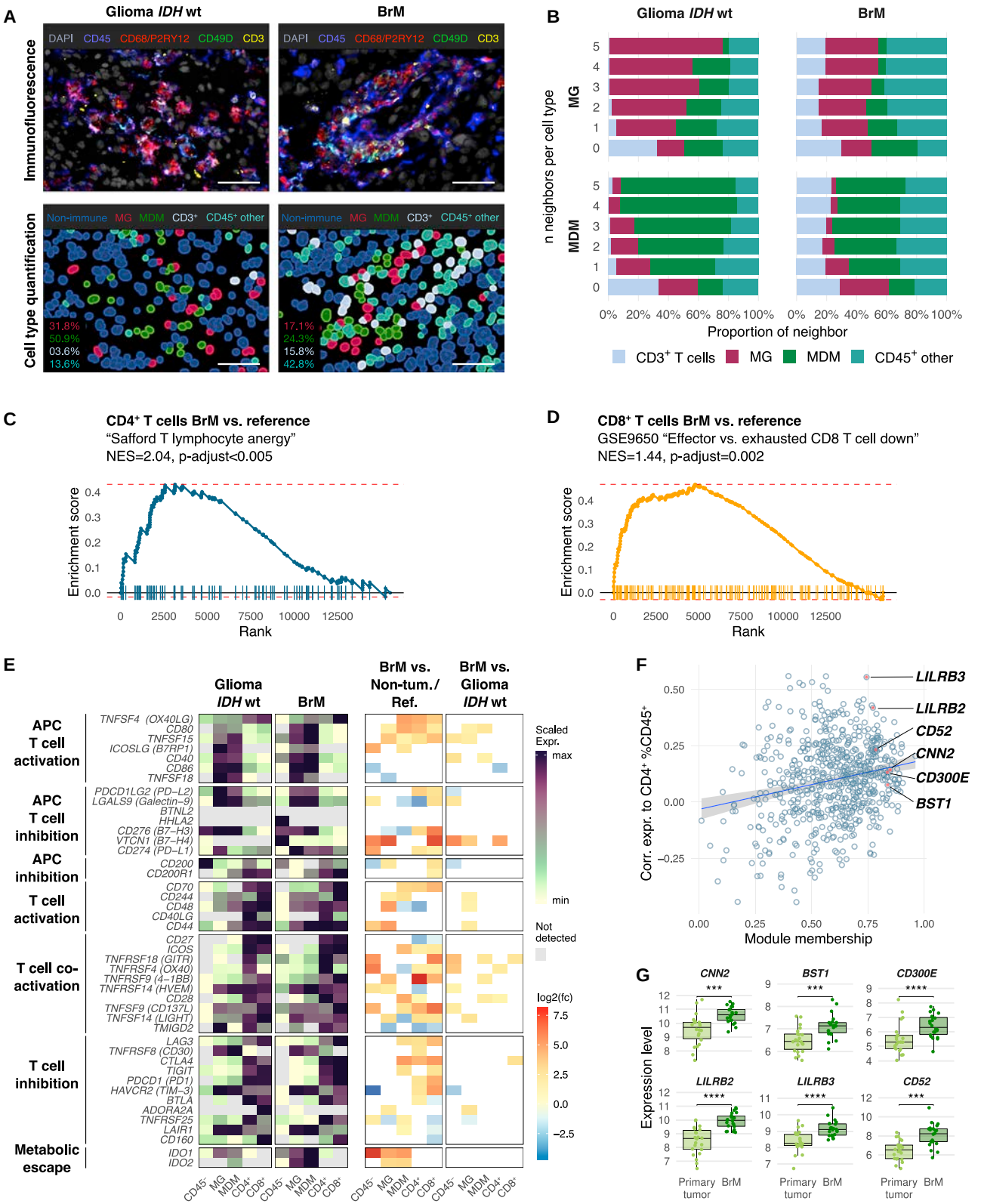

(legend on next page)

activators and co-activators but also mediators of inhibition in T cells (*PDCD1*/*PD1*, *CD28*, and *CTLA4*), whereas T cell-inhibiting and activating signals were detected in both TAM populations (*CD274*/*PD-L1* and *PDCD1LG2*/*PD-L2*). Notably, we found an upregulation of *CD80*, which has diverse roles in T cell activation because it heterodimerizes with CD274, provides co-stimulatory signals to T cells via CD28 and exerts inhibitory effects via interaction with CTLA4 (Zhao et al., 2019), in both TAM populations compared with their normal references and *IDH* WT tumor populations (Figure 7E). The potential contribution of TAMs to metabolic immune evasion is also suggested by high expression of *IDO1* and *IDO2* (Zhai et al., 2018) in BrM (Figure 7E).

We investigated additional immunomodulatory mediators using weighted gene correlation network analysis (WGCNA; Langfelder and Horvath, 2008) and correlated the resulting expression patterns with paired FCM abundance of $CD4^+$ and $CD8^+$ cells in a disease- and cell-type-specific manner. We identified 15 unique co-expression modules showing significant correlation ($p < 0.05$) of their eigengenes (i.e., the first PC of the module expression data) with any of the provided sample traits (Figure S7B). Among these, the ''brown'' WGCNA module correlated with a specific BrM-MDM annotation and $CD4^+$ T cell abundance. ORA of this module revealed signals for pathways such as coagulation and ECM modulation (Figure S7C) that affect the availability and activity of growth factors and cytokines within the TME (Mohan et al., 2020). We ranked genes by module membership strength and correlation with $CD4^+$ T cell abundance, which identified several factors with opposing immunomodulatory functions (Figure 7F). Although the receptors *CD300E* and *BST1* promote monocyte motility and survival (Isobe et al., 2018; Ortolan et al., 2019), we also detected effectors of immunosuppression, such as the actin-associated regulatory protein *CNN2*, which negatively regulates macrophage motility and phagocytic activity (Huang et al., 2008). The leukocyte immunoglobulin-like receptor subfamily B members LILRB2 and LILRB3, which attenuate myeloid cell activation (van der Touw et al., 2017), are also highly ranked genes within this module. Interestingly, *LILRB2* has been identified as a novel myeloid immune checkpoint that limits antitumor immunity (Chen et al., 2018). We also found evidence of effects on T cells; *CD52*, which, in its soluble form, inhibits T cell function, was among the BrM-MDM module genes. The notion that BrM-MDMs undergo disease-specific alterations distinct from the primary extracranial tumor is supported by upregulation of these genes (Figure 7G) in our analysis of an external cohort of BrM samples compared with their matched primary tumor tissue (Varešlija et al., 2019).

DISCUSSION

Brain tumors, including glioblastoma and BrMs, confer some of the poorest prognoses for patients with cancer, with survival rates often measured in just months. Given the current dearth of effective therapeutic options for these patients and the modest effects of the various immunotherapies evaluated to date, it is of critical urgency to identify novel targets for future clinical evaluation. One potentially rich source of therapeutic targets is the TME. However, even though the TME is now widely accepted as an important regulator of cancer progression and therapeutic response, our knowledge of the brain TME is restricted to individual brain tumor types or cellular compartments and lacks comprehensive and integrative analysis.

In this study, we leveraged a diverse panel of analyses to deeply interrogate the immune landscape of primary and metastatic brain cancers. Through integration of multiparameter FCM analyses, RNA-seq data, TME cell culture assays, protein arrays, and spatial tissue characterization, we uncovered critical insights into the composition and transcriptomes of the most abundant immune cell populations in patient samples from *IDH* mut and WT gliomas and BrMs originating from distinct extracranial primary tumors.

By exploring the broad immune landscape, we uncovered several pronounced differences between gliomas and BrMs when directly compared side by side. In brain tumors, TAMs are composed of tissue-resident MG and recruited MDMs, and we found a significant shift in the ratio of MG to MDMs between *IDH* mut and *IDH* WT gliomas. Additionally, gliomas contain an abundance of TAMs, whereas T cells were much fewer, particularly in *IDH* mut tumors. This confirms the notion that gliomas are immunologically cold tumors (Jackson et al., 2019). Although T cell sequestration in the bone marrow has been observed in glioma mouse models and following intracranial implantation of brain-extrinsic tumors (Chongsathidkiet et al., 2018), our clinical

Figure 7. TAMs Have a Wide Range of Immunomodulatory Functions in BrMs

(A) Representative IF images and corresponding cell type identification of non-immune cells ($CD45^-$), MG ($CD45^+$, $P2RY12/CD68^+$, $CD49D^-$), MDMs ($CD45^+$, $P2RY12/CD68^+$, $CD49D^+$), $CD3^+$ ($CD45^+$, $P2RY12/CD68^-$, $CD49D^{-/+}$, $CD3^+$) and $CD45^+$ other cells ($CD45^+$, $P2RY12/CD68^-$, $CD49D^{-/+}$, $CD3^-$) in *IDH* WT gliomas and BrMs. Scale bars, 50 μm. Insets show quantifications per FOV.

(B) Neighborhood analyses of *IDH* WT glioma and BrM IF tissue sections. Rows show the mean proportion of each neighboring cell type per frequency of observed $n_{neighbors}$ in the vicinity of MG or MDMs ($n_{IDH\ WT} = 9$, $n_{BrMs} = 13$).

(C and D) Gene set enrichment analysis (GSEA) of a T cell anergy gene set in $CD4^+$ T cells (C) and a T cell exhaustion gene set in $CD8^+$ T cells (D) from the MSigDB C2 collection.

(E) Gene expression heatmap of antigen-presenting cell (APC) and T cell activating and inhibitory signaling mediators (left panels, scaled to the expression range of variance-stabilized counts across all cell types in *IDH* WT glioma and BrMs) and corresponding fold changes (right panels, BrMs versus non-tumor/reference and *IDH* WT glioma versus BrMs, absolute log2(fold change) > 1, adjusted p value < 0.05) in $CD45^-$ MG and MDMs and $CD4^+$ and $CD8^+$ T cells in *IDH* WT gliomas and BrMs. Gray tiles indicate expression below the threshold (normalized counts < 10); white tiles correspond to a non-significant fold change.

(F) Scatterplot of module membership (correlation of expression to the module eigengene) and gene significance (correlation of expression to $CD4^+$ T cell abundance) of genes from the BrM-MDM-related gene co-expression network. Highly connected genes with immunomodulatory functions are annotated.

(G) Expression of the indicated genes in matched bulk primary breast cancer and BrM tissues using the Varešlija et al. (2019) dataset (Wilcoxon signed-rank test: ***$p < 0.001$, ****$p < 0.0001$).

See also Figure S7.

BrM samples showed pronounced accumulation of lymphocytes and neutrophils. This indicates that tumors that arise within the brain indeed shape their TME differently than cancers that metastasize from extracranial sites. Moreover, when exploring BrMs that originate from distinct primary tumors, there were additional differences; for example, in melanoma BrM samples, the combined abundance of $CD4^+$ and $CD8^+$ T cells represented the major immune compartment, whereas breast BrM samples showed the highest neutrophil infiltration. These key differences in the TME landscape, which are evident only when directly juxtaposing different brain malignancies, mirror the efficacy of immunotherapies that show promising efficacy in melanoma patients for controlling BrMs but with very modest effects to date in treating T cell-excluded glioblastoma (Schalper et al., 2019).

We also uncovered complex multifaceted phenotypes for TAMs across different brain tumors that extend beyond their numerical abundance. T-MG and T-MDMs showed distinct transcriptomic profiles and shared expression signatures, which are additionally influenced by the underlying disease type (*IDH* mut versus *IDH* WT glioma versus BrMs). A T-MDM signature derived from *IDH* WT gliomas, consisting of macrophage activation markers, chemokine receptors, and cytokines, proved to also be a predictor of patient survival in *IDH* mut gliomas. Moreover, analyses of T-MDMs indicated that even though these recruited cells have the potential to process and present antigens, and can be located proximally to T cells in BrMs, this potential is evidently not sufficiently utilized within the brain TME. Orthogonal analyses from the diverse panel of experimental assays used in this study reveal additional insights into potential mechanisms of immune suppression. These included our findings that different TAM populations produced pro-inflammatory molecules, negative regulators of myeloid cell activation, factors associated with IPRES, IDO1 and IDO2 immune checkpoint inhibitors, and specific ECM components and proteases that may collectively help sculpt an immune-suppressive niche. Therefore, therapeutic strategies that alter the multifaceted phenotypes of TAMs (Kowal et al., 2019), rather than aiming to simply deplete all of these cells with potentially opposing functions, should be considerably more effective.

Looking beyond TAMs, it will also be critical to assess the roles of neutrophils, particularly in BrMs, where we found them to be highly abundant, because they can act as potent immune-suppressive cells, as indicated by studies of other organs (Coffelt et al., 2016). Given the highly complex and multifaceted immune landscape of brain cancers revealed in this study, it is clear that rational combinations of TME-targeted agents will be critical to avoid the emergence of adaptive resistance, incorporating preclinical studies to help determine optimal combinations (Quail et al., 2016). In sum, this rich resource is available for further interrogation by the research community so that we can work collectively to uncover novel therapeutic strategies that unleash the potential of diverse cells in the TME to combat different brain malignancies.

STAR★METHODS

Detailed methods are provided in the online version of this paper and include the following:

- KEY RESOURCES TABLE
- RESOURCE AVAILABILITY
  - Lead Contact
  - Materials Availability
  - Data and Code Availability
- EXPERIMENTAL MODEL AND SUBJECT DETAILS
- METHOD DETAILS
  - Clinical sample processing, flow cytometry (FCM) and fluorescence activated cell sorting (FACS)
  - Tumor microenvironment-conditioned medium (TME-CM) generation
  - *In vitro* generation of monocyte-derived macrophages (MDM) and TME-CM stimulation
  - RNA isolation, cDNA synthesis and quantitative real-time PCR
  - Immunofluorescence staining and microscopy image acquisition
  - Image analysis and cell type identification
  - Protein isolation and enzyme-linked immunosorbent assay (ELISA)
  - RNA sequencing (RNA-seq)
  - Bioinformatic analysis environment
  - Gene set-centered analyses
  - Deconvolution of Toil-RNA sequencing data
  - Leading edge metagene (LEM) analysis
  - Protein-Protein-Interaction network building
  - Nearest neighbor distance measurements and neighborhood analysis of IF data
  - Cell type abundance estimation in spatial Ivy Glioblastoma Atlas Project (GAP) data
  - Survival analysis of the IDH wt MDM-specific gene signature in gliomas
  - Self-organizing map (SOM) clustering
  - Weighted gene correlation network analysis (WGCNA)
  - Expression analysis of external dataset of matched primary breast cancer and BrMs
  - Plotting and graph generation
- QUANTIFICATION AND STATISTICAL ANALYSIS

SUPPLEMENTAL INFORMATION

Supplemental Information can be found online at https://doi.org/10.1016/j.cell.2020.05.007.

ACKNOWLEDGMENTS

We thank Prof. Ron Stoop, Dr. Nathalie Piazzon, and the Neurosurgery/Neuro-oncology clinical and nursing teams at CHUV and MSKCC for excellent infrastructural support; the Joyce lab members for insightful discussions; the Hegi lab members for technical help during sample processing; and Vladimir Wischnewski for critical manuscript review. We thank the UNIL and MSKCC Flow Cytometry Core Facilities for exceptional technical assistance, especially Romain Bedel. Finally, we convey our immense gratitude to all patients who volunteered to participate in this study. Research in the Joyce lab is supported by the Swiss Cancer League, a Swiss Bridge award, the Ludwig Institute for Cancer Research, the University of Lausanne, the Breast Cancer Research Foundation, and Cancer Research UK. F.K. was supported in part by the German Research Foundation (DFG, KL2491/1-1) and Fondation Medic and K.S. by the Austrian Science Fund (FWF, J4343-B28). The results shown here are in part based on data generated by the TCGA Research Network (https://www.cancer.gov/tcga).

AUTHOR CONTRIBUTIONS

F.K., R.L.B., and J.A.J. designed the study. F.K., R.R.M., R.L.B., M.K., and K.S. performed experiments and analyzed data. F.K., R.R.M., R.L.B., and S.N. performed computational analyses. C.A.I.-D., C.B., V.T., P.H.G., R.T.D., and M.E.H. provided clinical material. J.-P.B. provided histopathological reviews. F.K. and R.R.M. prepared the figures. F.K. and J.A.J. wrote the manuscript. All authors edited or commented on the manuscript.

DECLARATION OF INTERESTS

The authors declare no competing interests.

Received: November 29, 2019
Revised: April 1, 2020
Accepted: May 1, 2020
Published: May 28, 2020

REFERENCES

Afik, R., Zigmond, E., Vugman, M., Klepfish, M., Shimshoni, E., Pasmanik-Chor, M., Shenoy, A., Bassat, E., Halpern, Z., Geiger, T., et al. (2016). Tumor macrophages are pivotal constructors of tumor collagenous matrix. J. Exp. Med. *213*, 2315–2331.

Aldape, K., Brindle, K.M., Chesler, L., Chopra, R., Gajjar, A., Gilbert, M.R., Gottardo, N., Gutmann, D.H., Hargrave, D., Holland, E.C., et al. (2019). Challenges to curing primary brain tumours. Nat. Rev. Clin. Oncol. *16*, 509–520.

Baddeley, A.D., Eysenck, M.W., and Anderson, M.C. (2015). Spatial Point Patterns: Methodology and Applications with R (London: Chapman and Hall/CRC Press).

Barletta, K.E., Ley, K., and Mehrad, B. (2012). Regulation of neutrophil function by adenosine. Arterioscler. Thromb. Vasc. Biol. *32*, 856–864.

Bates, D., Machler, M., Bolker, B.M., and Walker, S.C. (2015). Fitting Linear Mixed-Effects Models Using lme4. J. Stat. Softw. *67*, 1–48.

Benci, J.L., Xu, B., Qiu, Y., Wu, T.J., Dada, H., Twyman-Saint Victor, C., Cucolo, L., Lee, D.S.M., Pauken, K.E., Huang, A.C., et al. (2016). Tumor Interferon Signaling Regulates a Multigenic Resistance Program to Immune Checkpoint Blockade. Cell *167*, 1540–1554.e12.

Bouralexis, S., Findlay, D.M., and Evdokiou, A. (2005). Death to the bad guys: targeting cancer via Apo2L/TRAIL. Apoptosis *10*, 35–51.

Bournazos, S., Wang, T.T., and Ravetch, J.V. (2016). The Role and Function of Fcγ Receptors on Myeloid Cells. Microbiol. Spectr. *4* https://doi.org/10.1128/microbiolspec.MCHD-0045-2016.

Bowman, R.L., Klemm, F., Akkari, L., Pyonteck, S.M., Sevenich, L., Quail, D.F., Dhara, S., Simpson, K., Gardner, E.E., Iacobuzio-Donahue, C.A., et al. (2016). Macrophage Ontogeny Underlies Differences in Tumor-Specific Education in Brain Malignancies. Cell Rep. *17*, 2445–2459.

Cagney, D.N., Martin, A.M., Catalano, P.J., Redig, A.J., Lin, N.U., Lee, E.Q., Wen, P.Y., Dunn, I.F., Bi, W.L., Weiss, S.E., et al. (2017). Incidence and prognosis of patients with brain metastases at diagnosis of systemic malignancy: a population-based study. Neuro-oncol. *19*, 1511–1521.

Ceccarelli, M., Barthel, F.P., Malta, T.M., Sabedot, T.S., Salama, S.R., Murray, B.A., Morozova, O., Newton, Y., Radenbaugh, A., Pagnotta, S.M., et al.; TCGA Research Network (2016). Molecular Profiling Reveals Biologically Discrete Subsets and Pathways of Progression in Diffuse Glioma. Cell *164*, 550–563.

Chen, Z., Feng, X., Herting, C.J., Garcia, V.A., Nie, K., Pong, W.W., Rasmussen, R., Dwivedi, B., Seby, S., Wolf, S.A., et al. (2017). Cellular and Molecular Identity of Tumor-Associated Macrophages in Glioblastoma. Cancer Res. *77*, 2266–2278.

Chen, H.M., van der Touw, W., Wang, Y.S., Kang, K., Mai, S., Zhang, J., Alsina-Beauchamp, D., Duty, J.A., Mungamuri, S.K., Zhang, B., et al. (2018). Blocking immunoinhibitory receptor LILRB2 reprograms tumor-associated myeloid cells and promotes antitumor immunity. J. Clin. Invest. *128*, 5647–5662.

Chongsathidkiet, P., Jackson, C., Koyama, S., Loebel, F., Cui, X., Farber, S.H., Woroniecka, K., Elsamadicy, A.A., Dechant, C.A., Kemeny, H.R., et al. (2018). Sequestration of T cells in bone marrow in the setting of glioblastoma and other intracranial tumors. Nat. Med. *24*, 1459–1468.

Coffelt, S.B., Wellenstein, M.D., and de Visser, K.E. (2016). Neutrophils in cancer: neutral no more. Nat. Rev. Cancer *16*, 431–446.

Colaprico, A., Silva, T.C., Olsen, C., Garofano, L., Cava, C., Garolini, D., Sabedot, T.S., Malta, T.M., Pagnotta, S.M., Castiglioni, I., et al. (2016). TCGAbiolinks: an R/Bioconductor package for integrative analysis of TCGA data. Nucleic Acids Res. *44*, e71.

Cui, Z., Liao, J., Cheong, N., Longoria, C., Cao, G., DeLisser, H.M., and Savani, R.C. (2019). The Receptor for Hyaluronan-Mediated Motility (CD168) promotes inflammation and fibrosis after acute lung injury. Matrix Biol. *78-79*, 255–271.

Dobin, A., Davis, C.A., Schlesinger, F., Drenkow, J., Zaleski, C., Jha, S., Batut, P., Chaisson, M., and Gingeras, T.R. (2013). STAR: ultrafast universal RNA-seq aligner. Bioinformatics *29*, 15–21.

Filková, M., Haluzík, M., Gay, S., and Senolt, L. (2009). The role of resistin as a regulator of inflammation: Implications for various human pathologies. Clin. Immunol. *133*, 157–170.

Friedman, J., Hastie, T., and Tibshirani, R. (2010). Regularization Paths for Generalized Linear Models via Coordinate Descent. J. Stat. Softw. *33*, 1–22.

Gabrusiewicz, K., Rodriguez, B., Wei, J., Hashimoto, Y., Healy, L.M., Maiti, S.N., Thomas, G., Zhou, S., Wang, Q., Elakkad, A., et al. (2016). Glioblastoma-infiltrated innate immune cells resemble M0 macrophage phenotype. JCI Insight *1*, e85841.

Gaujoux, R., and Seoighe, C. (2010). A flexible R package for nonnegative matrix factorization. BMC Bioinformatics *11*, 367.

Georgoudaki, A.M., Prokopec, K.E., Boura, V.F., Hellqvist, E., Sohn, S., Östling, J., Dahan, R., Harris, R.A., Rantalainen, M., Klevebring, D., et al. (2016). Reprogramming Tumor-Associated Macrophages by Antibody Targeting Inhibits Cancer Progression and Metastasis. Cell Rep. *15*, 2000–2011.

Glodde, N., Bald, T., van den Boorn-Konijnenberg, D., Nakamura, K., O'Donnell, J.S., Szczepanski, S., Brandes, M., Eickhoff, S., Das, I., Shridhar, N., et al. (2017). Reactive Neutrophil Responses Dependent on the Receptor Tyrosine Kinase c-MET Limit Cancer Immunotherapy. Immunity *47*, 789–802.e9.

Godec, J., Tan, Y., Liberzon, A., Tamayo, P., Bhattacharya, S., Butte, A.J., Mesirov, J.P., and Haining, W.N. (2016). Compendium of Immune Signatures Identifies Conserved and Species-Specific Biology in Response to Inflammation. Immunity *44*, 194–206.

GTEx Consortium (2013). The Genotype-Tissue Expression (GTEx) project. Nat. Genet. *45*, 580–585.

Gutmann, D.H., and Kettenmann, H. (2019). Microglia/Brain Macrophages as Central Drivers of Brain Tumor Pathobiology. Neuron *104*, 442–449.

Hänzelmann, S., Castelo, R., and Guinney, J. (2013). GSVA: gene set variation analysis for microarray and RNA-seq data. BMC Bioinformatics *14*, 7.

Hendriks, L.E.L., Henon, C., Auclin, E., Mezquita, L., Ferrara, R., Audigier-Valette, C., Mazieres, J., Lefebvre, C., Rabeau, A., Le Moulec, S., et al. (2019). Outcome of Patients with Non-Small Cell Lung Cancer and Brain Metastases Treated with Checkpoint Inhibitors. J. Thorac. Oncol. *14*, 1244–1254.

Huang, Q.Q., Hossain, M.M., Wu, K., Parai, K., Pope, R.M., and Jin, J.P. (2008). Role of H2-calponin in regulating macrophage motility and phagocytosis. J. Biol. Chem. *283*, 25887–25899.

Hugo, W., Zaretsky, J.M., Sun, L., Song, C., Moreno, B.H., Hu-Lieskovan, S., Berent-Maoz, B., Pang, J., Chmielowski, B., Cherry, G., et al. (2016). Genomic and Transcriptomic Features of Response to Anti-PD-1 Therapy in Metastatic Melanoma. Cell *165*, 35–44.

Isobe, M., Izawa, K., Sugiuchi, M., Sakanishi, T., Kaitani, A., Takamori, A., Maehara, A., Matsukawa, T., Takahashi, M., Yamanishi, Y., et al. (2018). The CD300e molecule in mice is an immune-activating receptor. J. Biol. Chem. *293*, 3793–3805.

Jackson, C.M., Choi, J., and Lim, M. (2019). Mechanisms of immunotherapy resistance: lessons from glioblastoma. Nat. Immunol. *20*, 1100–1109.

Kai, F., Drain, A.P., and Weaver, V.M. (2019). The Extracellular Matrix Modulates the Metastatic Journey. Dev. Cell *49*, 332–346.

Klemm, F., and Joyce, J.A. (2015). Microenvironmental regulation of therapeutic response in cancer. Trends Cell Biol. *25*, 198–213.

Kobayashi, M., Chung, J.S., Beg, M., Arriaga, Y., Verma, U., Courtney, K., Mansour, J., Haley, B., Khan, S., Horiuchi, Y., et al. (2019). Blocking Monocytic Myeloid-Derived Suppressor Cell Function via Anti-DC-HIL/GPNMB Antibody Restores the *In Vitro* Integrity of T Cells from Cancer Patients. Clin. Cancer Res. *25*, 828–838.

Kowal, J., Kornete, M., and Joyce, J.A. (2019). Re-education of macrophages as a therapeutic strategy in cancer. Immunotherapy *11*, 677–689.

Langfelder, P., and Horvath, S. (2008). WGCNA: an R package for weighted correlation network analysis. BMC Bioinformatics *9*, 559.

Lécuyer, M.A., Saint-Laurent, O., Bourbonnière, L., Larouche, S., Larochelle, C., Michel, L., Charabati, M., Abadier, M., Zandee, S., Haghayegh Jahromi, N., et al. (2017). Dual role of ALCAM in neuroinflammation and blood-brain barrier homeostasis. Proc. Natl. Acad. Sci. USA *114*, E524–E533.

Li, L., Yan, J., Xu, J., Liu, C.Q., Zhen, Z.J., Chen, H.W., Ji, Y., Wu, Z.P., Hu, J.Y., Zheng, L., and Lau, W.Y. (2014). CXCL17 expression predicts poor prognosis and correlates with adverse immune infiltration in hepatocellular carcinoma. PLoS ONE *9*, e110064.

Li, Y., Xie, Y., Hao, J., Liu, J., Ning, Y., Tang, Q., Ma, M., Zhou, H., Guan, S., Zhou, Q., and Lv, X. (2018). ER-localized protein-Herpud1 is a new mediator of IL-4-induced macrophage polarization and migration. Exp. Cell Res. *368*, 167–173.

Liberzon, A., Birger, C., Thorvaldsdóttir, H., Ghandi, M., Mesirov, J.P., and Tamayo, P. (2015). The Molecular Signatures Database (MSigDB) hallmark gene set collection. Cell Syst. *1*, 417–425.

Lim, M., Xia, Y., Bettegowda, C., and Weller, M. (2018). Current state of immunotherapy for glioblastoma. Nat. Rev. Clin. Oncol. *15*, 422–442.

Liu, Q., Johnson, E.M., Lam, R.K., Wang, Q., Ye, B.H., Wilson, E.N., Minhas, P.S., Liu, L., Swarovski, M.S., Tran, S., et al. (2019). Peripheral TREM1 responses to brain and intestinal immunogens amplify stroke severity. Nat. Immunol. *20*, 1023–1034.

Löffler-Wirth, H., Kalcher, M., and Binder, H. (2015). oposSOM: R-package for high-dimensional portraying of genome-wide expression landscapes on bioconductor. Bioinformatics *31*, 3225–3227.

Long, G.V., Atkinson, V., Lo, S., Sandhu, S., Guminski, A.D., Brown, M.P., Wilmott, J.S., Edwards, J., Gonzalez, M., Scolyer, R.A., et al. (2018). Combination nivolumab and ipilimumab or nivolumab alone in melanoma brain metastases: a multicentre randomised phase 2 study. Lancet Oncol. *19*, 672–681.

Love, M.I., Huber, W., and Anders, S. (2014). Moderated estimation of fold change and dispersion for RNA-seq data with DESeq2. Genome Biol. *15*, 550.

Mantovani, A., Marchesi, F., Malesci, A., Laghi, L., and Allavena, P. (2017). Tumour-associated macrophages as treatment targets in oncology. Nat. Rev. Clin. Oncol. *14*, 399–416.

Meng, X., Duan, C., Pang, H., Chen, Q., Han, B., Zha, C., Dinislam, M., Wu, P., Li, Z., Zhao, S., et al. (2019). DNA damage repair alterations modulate M2 polarization of microglia to remodel the tumor microenvironment via the p53-mediated MDK expression in glioma. EBioMedicine *41*, 185–199.

Mohan, V., Das, A., and Sagi, I. (2020). Emerging roles of ECM remodeling processes in cancer. Semin. Cancer Biol. *62*, 192–200.

Morianos, I., Papadopoulou, G., Semitekolou, M., and Xanthou, G. (2019). Activin-A in the regulation of immunity in health and disease. J. Autoimmun. *104*, 102314.

Müller, S., Kohanbash, G., Liu, S.J., Alvarado, B., Carrera, D., Bhaduri, A., Watchmaker, P.B., Yagnik, G., Di Lullo, E., Malatesta, M., et al. (2017). Single-cell profiling of human gliomas reveals macrophage ontogeny as a basis for regional differences in macrophage activation in the tumor microenvironment. Genome Biol. *18*, 234.

Murray, P.J., Allen, J.E., Biswas, S.K., Fisher, E.A., Gilroy, D.W., Goerdt, S., Gordon, S., Hamilton, J.A., Ivashkiv, L.B., Lawrence, T., et al. (2014). Macrophage activation and polarization: nomenclature and experimental guidelines. Immunity *41*, 14–20.

Mushtaq, M.U., Papadas, A., Pagenkopf, A., Flietner, E., Morrow, Z., Chaudhary, S.G., and Asimakopoulos, F. (2018). Tumor matrix remodeling and novel immunotherapies: the promise of matrix-derived immune biomarkers. J. Immunother. Cancer *6*, 65.

Noy, R., and Pollard, J.W. (2014). Tumor-associated macrophages: from mechanisms to therapy. Immunity *41*, 49–61.

Olson, O.C., and Joyce, J.A. (2015). Cysteine cathepsin proteases: regulators of cancer progression and therapeutic response. Nat. Rev. Cancer *15*, 712–729.

Ortolan, E., Augeri, S., Fissolo, G., Musso, I., and Funaro, A. (2019). CD157: From immunoregulatory protein to potential therapeutic target. Immunol. Lett. *205*, 59–64.

Puchalski, R.B., Shah, N., Miller, J., Dalley, R., Nomura, S.R., Yoon, J.G., Smith, K.A., Lankerovich, M., Bertagnolli, D., Bickley, K., et al. (2018). An anatomic transcriptional atlas of human glioblastoma. Science *360*, 660–663.

Pyonteck, S.M., Akkari, L., Schuhmacher, A.J., Bowman, R.L., Sevenich, L., Quail, D.F., Olson, O.C., Quick, M.L., Huse, J.T., Teijeiro, V., et al. (2013). CSF-1R inhibition alters macrophage polarization and blocks glioma progression. Nat. Med. *19*, 1264–1272.

Qiao, S., Qian, Y., Xu, G., Luo, Q., and Zhang, Z. (2019). Long-term characterization of activated microglia/macrophages facilitating the development of experimental brain metastasis through intravital microscopic imaging. J. Neuroinflammation *16*, 4.

Quail, D.F., and Joyce, J.A. (2017). The Microenvironmental Landscape of Brain Tumors. Cancer Cell *31*, 326–341.

Quail, D.F., Bowman, R.L., Akkari, L., Quick, M.L., Schuhmacher, A.J., Huse, J.T., Holland, E.C., Sutton, J.C., and Joyce, J.A. (2016). The tumor microenvironment underlies acquired resistance to CSF-1R inhibition in gliomas. Science *352*, aad3018.

R Core Team (2018). R: A Language and Environment for Statistical Computing (R Foundation for Statistical Computing).

Racle, J., de Jonge, K., Baumgaertner, P., Speiser, D.E., and Gfeller, D. (2017). Simultaneous enumeration of cancer and immune cell types from bulk tumor gene expression data. eLife *6*, e26476.

Rau, A., Gallopin, M., Celeux, G., and Jaffrézic, F. (2013). Data-based filtering for replicated high-throughput transcriptome sequencing experiments. Bioinformatics *29*, 2146–2152.

Richards, J., Gabunia, K., Kelemen, S.E., Kako, F., Choi, E.T., and Autieri, M.V. (2015). Interleukin-19 increases angiogenesis in ischemic hind limbs by direct effects on both endothelial cells and macrophage polarization. J. Mol. Cell. Cardiol. *79*, 21–31.

Ripoll, V.M., Irvine, K.M., Ravasi, T., Sweet, M.J., and Hume, D.A. (2007). Gpnmb is induced in macrophages by IFN-gamma and lipopolysaccharide and acts as a feedback regulator of proinflammatory responses. J. Immunol. *178*, 6557–6566.

Robinson, J.T., Thorvaldsdóttir, H., Wenger, A.M., Zehir, A., and Mesirov, J.P. (2017). Variant Review with the Integrative Genomics Viewer. Cancer Res. *77*, e31–e34.

Rodón, L., Gonzàlez-Juncà, A., Inda, Mdel.M., Sala-Hojman, A., Martínez-Sáez, E., and Seoane, J. (2014). Active CREB1 promotes a malignant TGFβ2 autocrine loop in glioblastoma. Cancer Discov. *4*, 1230–1241.

Sankowski, R., Böttcher, C., Masuda, T., Geirsdottir, L., Sagar, Sindram, E., Seredenina, T., Muhs, A., Scheiwe, C., Shah, M.J., et al. (2019). Mapping microglia states in the human brain through the integration of high-dimensional techniques. Nat. Neurosci. *22*, 2098–2110.

Santana Carrero, R.M., Beceren-Braun, F., Rivas, S.C., Hegde, S.M., Gangadharan, A., Plote, D., Pham, G., Anthony, S.M., and Schluns, K.S. (2019). IL-15 is a component of the inflammatory milieu in the tumor microenvironment promoting antitumor responses. Proc. Natl. Acad. Sci. USA *116*, 599–608.

Schalper, K.A., Rodriguez-Ruiz, M.E., Diez-Valle, R., López-Janeiro, A., Porciuncula, A., Idoate, M.A., Inogés, S., de Andrea, C., López-Diaz de Cerio,

A., Tejada, S., et al. (2019). Neoadjuvant nivolumab modifies the tumor immune microenvironment in resectable glioblastoma. Nat. Med. *25*, 470–476.

Stupp, R., Mason, W.P., van den Bent, M.J., Weller, M., Fisher, B., Taphoorn, M.J., Belanger, K., Brandes, A.A., Marosi, C., Bogdahn, U., et al.; European Organisation for Research and Treatment of Cancer Brain Tumor and Radiotherapy Groups; National Cancer Institute of Canada Clinical Trials Group (2005). Radiotherapy plus concomitant and adjuvant temozolomide for glioblastoma. N. Engl. J. Med. *352*, 987–996.

Subramanian, A., Tamayo, P., Mootha, V.K., Mukherjee, S., Ebert, B.L., Gillette, M.A., Paulovich, A., Pomeroy, S.L., Golub, T.R., Lander, E.S., and Mesirov, J.P. (2005). Gene set enrichment analysis: a knowledge-based approach for interpreting genome-wide expression profiles. Proc. Natl. Acad. Sci. USA *102*, 15545–15550.

Szklarczyk, D., Morris, J.H., Cook, H., Kuhn, M., Wyder, S., Simonovic, M., Santos, A., Doncheva, N.T., Roth, A., Bork, P., et al. (2017). The STRING database in 2017: quality-controlled protein-protein association networks, made broadly accessible. Nucleic Acids Res. *45* (D1), D362–D368.

Szulzewsky, F., Arora, S., de Witte, L., Ulas, T., Markovic, D., Schultze, J.L., Holland, E.C., Synowitz, M., Wolf, S.A., and Kettenmann, H. (2016). Human glioblastoma-associated microglia/monocytes express a distinct RNA profile compared to human control and murine samples. Glia *64*, 1416–1436.

Tawbi, H.A., Forsyth, P.A., Algazi, A., Hamid, O., Hodi, F.S., Moschos, S.J., Khushalani, N.I., Lewis, K., Lao, C.D., Postow, M.A., et al. (2018). Combined Nivolumab and Ipilimumab in Melanoma Metastatic to the Brain. N. Engl. J. Med. *379*, 722–730.

Thapa, B., and Lee, K. (2019). Metabolic influence on macrophage polarization and pathogenesis. BMB Rep. *52*, 360–372.

Tsukamoto, H., Fujieda, K., Miyashita, A., Fukushima, S., Ikeda, T., Kubo, Y., Senju, S., Ihn, H., Nishimura, Y., and Oshiumi, H. (2018). Combined Blockade of IL6 and PD-1/PD-L1 Signaling Abrogates Mutual Regulation of Their Immunosuppressive Effects in the Tumor Microenvironment. Cancer Res. *78*, 5011–5022.

Van, P., Jiang, W., Gottardo, R., and Finak, G. (2018). ggCyto: next generation open-source visualization software for cytometry. Bioinformatics *34*, 3951–3953.

van der Touw, W., Chen, H.M., Pan, P.Y., and Chen, S.H. (2017). LILRB receptor-mediated regulation of myeloid cell maturation and function. Cancer Immunol. Immunother. *66*, 1079–1087.

Vareslija, D., Priedigkeit, N., Fagan, A., Purcell, S., Cosgrove, N., O'Halloran, P.J., Ward, E., Cocchiglia, S., Hartmaier, R., Castro, C.A., et al. (2019). Transcriptome Characterization of Matched Primary Breast and Brain Metastatic Tumors to Detect Novel Actionable Targets. J. Natl. Cancer Inst. *111*, 388–398.

Venteicher, A.S., Tirosh, I., Hebert, C., Yizhak, K., Neftel, C., Filbin, M.G., Hovestadt, V., Escalante, L.E., Shaw, M.L., Rodman, C., et al. (2017). Decoupling genetics, lineages, and microenvironment in IDH-mutant gliomas by single-cell RNA-seq. Science *355*, eaai8478.

Vivian, J., Rao, A.A., Nothaft, F.A., Ketchum, C., Armstrong, J., Novak, A., Pfeil, J., Narkizian, J., Deran, A.D., Musselman-Brown, A., et al. (2017). Toil enables reproducible, open source, big biomedical data analyses. Nat. Biotechnol. *35*, 314–316.

Wei, S.C., Duffy, C.R., and Allison, J.P. (2018). Fundamental Mechanisms of Immune Checkpoint Blockade Therapy. Cancer Discov. *8*, 1069–1086.

Wickham, H. (2016). ggplot2: Elegant Graphics for Data Analysis (Springer).

Xu, P., Zhang, X., Liu, Q., Xie, Y., Shi, X., Chen, J., Li, Y., Guo, H., Sun, R., Hong, Y., et al. (2019). Microglial TREM-1 receptor mediates neuroinflammatory injury via interaction with SYK in experimental ischemic stroke. Cell Death Dis. *10*, 555.

Xue, J., Schmidt, S.V., Sander, J., Draffehn, A., Krebs, W., Quester, I., De Nardo, D., Gohel, T.D., Emde, M., Schmidleithner, L., et al. (2014). Transcriptome-based network analysis reveals a spectrum model of human macrophage activation. Immunity *40*, 274–288.

Yan, D., Kowal, J., Akkari, L., Schuhmacher, A.J., Huse, J.T., West, B.L., and Joyce, J.A. (2017). Inhibition of colony stimulating factor-1 receptor abrogates microenvironment-mediated therapeutic resistance in gliomas. Oncogene *36*, 6049–6058.

Yang, T.H., St John, L.S., Garber, H.R., Kerros, C., Ruisaard, K.E., Clise-Dwyer, K., Alatrash, G., Ma, Q., and Molldrem, J.J. (2018). Membrane-Associated Proteinase 3 on Granulocytes and Acute Myeloid Leukemia Inhibits T Cell Proliferation. J. Immunol. *201*, 1389–1399.

Young, M.D., Wakefield, M.J., Smyth, G.K., and Oshlack, A. (2010). Gene ontology analysis for RNA-seq: accounting for selection bias. Genome Biol. *11*, R14.

Zaiss, D.M.W., Gause, W.C., Osborne, L.C., and Artis, D. (2015). Emerging functions of amphiregulin in orchestrating immunity, inflammation, and tissue repair. Immunity *42*, 216–226.

Zhai, L., Ladomersky, E., Lenzen, A., Nguyen, B., Patel, R., Lauing, K.L., Wu, M., and Wainwright, D.A. (2018). IDO1 in cancer: a Gemini of immune checkpoints. Cell. Mol. Immunol. *15*, 447–457.

Zhao, J., Sun, L., and Li, X. (2017). Commanding CNS Invasion: GM-CSF. Immunity *46*, 165–167.

Zhao, Y., Lee, C.K., Lin, C.H., Gassen, R.B., Xu, X., Huang, Z., Xiao, C., Bonorino, C., Lu, L.F., Bui, J.D., et al. (2019). PD-L1:CD80 Cis-Heterodimer Triggers the Co-stimulatory Receptor CD28 While Repressing the Inhibitory PD-1 and CTLA-4 Pathways. Immunity *51*, 1059–1073.e9.

STAR★METHODS

KEY RESOURCES TABLE

REAGENT or RESOURCE	SOURCE	IDENTIFIER
Antibodies		
FCM: AF700 mouse monoclonal anti-human CD45 (clone HI30)	BioLegend	Cat#304024; RRID:AB_493761
FCM: BV421 rat monoclonal anti-mouse/human CD11B (clone M1/70)	BioLegend	Cat#101251; RRID:AB_2562904
FCM: PE mouse monoclonal anti-human CD66B (clone G10F5)	BioLegend	Cat#305106; RRID:AB_2077857
FCM: AF488 mouse monoclonal anti-human CD14 (clone HCD14)	BioLegend	Cat#325610; RRID:AB_830683
FCM: BUV737 mouse monoclonal anti-human CD16 (clone 3G8)	BD	Cat#612786; RRID:AB_2833077
FCM: APC mouse monoclonal anti-human CD49D (clone 9F10)	BioLegend	Cat#304308; RRID:AB_2130041
FCM: BV605 mouse monoclonal anti-human CD11C (clone 3.9)	BioLegend	Cat#301636; RRID:AB_2563796
FCM: BV711 mouse monoclonal anti-human anti HLA-DR (clone L243)	BioLegend	Cat#307644; RRID:AB_2562913
FCM: PerCP/Cy5.5 mouse monoclonal anti-human CD3 (clone HIT3a)	BioLegend	Cat#300328; RRID:AB_1575008
FCM: BV 650 mouse monoclonal anti-human anti CD4 (clone OKT4)	BioLegend	Cat#317436; RRID:AB_2563050
FCM: PE mouse monoclonal anti-human CD25 (clone BC96)	BioLegend	Cat#302606; RRID:AB_314276
FCM: BV510 mouse monoclonal anti-human CD127 (clone A019D5)	BioLegend	Cat#351332; RRID:AB_2562304
FCM: PE/Cy7 mouse monoclonal anti-human CD8A (clone HIT8a)	BioLegend	Cat#300914; RRID:AB_314118
FCM: BUV563 mouse monoclonal anti-human CD20 (clone 2H7)	BD	Cat#748456
FCM: BUV563 mouse monoclonal anti-human CD19 (clone SJ25C1)	BD	Cat#612916
FCM: PE/Dazzle mouse monoclonal anti-human CD56 (clone HDC56)	BioLegend	Cat#318348; RRID:AB_2563564
FCM: PE mouse monoclonal anti-human P2RY12 (clone S16001E)	BioLegend	Cat#392103; RRID:AB_2716006
FCM: PE/Cy7 Mouse monoclonal anti-human CD68 (clone Y1/82A)	BioLegend	Cat#333816; RRID:AB_2562936
IF: Mouse monoclonal anti-human CD68 (clone KP1), 1:100 dilution	Abcam	Cat#ab955; RRID:AB_307338
IF: Rat monoclonal anti-human CD49D (clone PS/2), 1:100 dilution	Abcam	Cat#ab25247
IF: Rabbit polyclonal anti-human P2RY12, 1:600 dilution	Sigma-Aldrich	Cat#HPA014518; RRID:AB_2669027
IF: Goat polyclonal anti-human CD45, 1:100 dilution	LSBio	Cat#LS-B14248-300
IF: AF488 mouse monoclonal anti-human CD45 (clone HI30), 1:100 dilution	BioLegend	Cat#304019; RRID:AB_493033
IF: AF488 mouse monoclonal anti-human CD3 (clone UCHT1), 1:100 dilution	BioLegend	Cat#300406; RRID:AB_314060
IF: Sheep polyclonal anti-human CD31, 1:200 dilution	R&D	Cat#AF806; RRID:AB_355617
IF: APC rat monoclonal anti Ki-67 (clone SolA15), 1:100 dilution	Thermo Fisher Scientific	Cat#17-5698-82

(*Continued on next page*)

Continued

REAGENT or RESOURCE	SOURCE	IDENTIFIER
IF: AF555 donkey anti-rabbit IgG 1:1000 dilution	Thermo Fisher Scientific	Cat#A31572, RRID:AB_162543
IF: AF555 donkey anti-mouse IgG, 1:500 dilution	Thermo Fisher Scientific	Cat#A32773; RRID:AB_2762848
IF: AF488 donkey anti-rat IgG, 1:500 dilution	Thermo Fisher Scientific	Cat#A21208; RRID:AB_141709
IF: AF647 donkey anti-rat IgG, 1:500 dilution	abcam	Cat#ab150155; RRID:AB_2813835
IF: DyLight755 donkey anti-goat IgG, 1:500 dilution	Thermo Fisher Scientific	Cat# SA5-10091; RRID:AB_2556671
IF: AF555 donkey anti-sheep IgG, 1:500 dilution	Thermo Fisher Scientific	Cat#A21436; RRID:AB_2535857
Biological Samples		
Non-tumor, glioma and brain metastasis tissue	Centre Hospitalier Universitaire Vaudois, Lausanne, Switzerland	N/A
Non-tumor, glioma and brain metastasis tissue	Memorial Sloan Kettering Cancer Center, New York, NY, USA	N/A
Healthy donor blood	Transfusion Interrégionale Croix-Rouge Suisse, Epalinges, Switzerland	N/A
Healthy donor blood	New York Blood Bank, New York, NY, USA	N/A
Chemicals, Peptides, and Recombinant Proteins		
DMEM-F12 (1:1), GlutaMAX	GIBCO	Cat#31331028
DMEM, high glucose, GlutaMAX, pyruvate	GIBCO	Cat#31966021
Penicillin/Streptomycin	GIBCO	Cat#15140122
Human recombinant CSF-1	R&D Systems	Cat#216-MC-025
Ficoll-Paque Premium	GE	Cat#17-5442-02
Trizol	Thermo Fisher Scientific	Cat#15596018
Trizol LS	Thermo Fisher Scientific	Cat#10296028
Tween 20	Applied Chemicals	Cat#A4974
Triton X-100	Applied Chemicals	Cat#A4975
TNB Blocking Reagent	Perkin Elmer	Cat#FP1020
Fluorescence Mounting Medium	Dako	Cat#S302380
Critical Commercial Assays		
Brain Tumor Dissociation Kit (P)	Miltenyi	Cat#130-095-942
Tumor Dissociation Kit, human	Miltenyi	Cat#130-095-929
Myelin Removal Beads	Miltenyi	Cat#130-096-733
CD14 MicroBeads, human	Miltenyi	Cat#130-050-201
Human TruStain FcX	BioLegend	Cat#422302
ZombieNIR Fixable Viability Kit	BioLegend	Cat#423106
High Capacity cDNA Reverse Transcription Kit	Applied Biosystems	Cat#4368814
TaqMan Universal PCR Master Mix	Applied Biosystems	Cat#4304437
Quantibody Array Q4000 ELISA	Raybiotech	Cat#QAH-CAA-4000-1
Deposited Data		
RNAseq count data	This paper	https://joycelab.shinyapps.io/braintime/
Human reference genome, hg38	Genomics Data Common	https://gdc.cancer.gov/about-data/data-harmonization-and-generation/gdc-reference-files
TCGA LGG and GBM datasets	Genomics Data Common	https://portal.gdc.cancer.gov/
TOIL TGCA TARGET GTEx datasets	Vivian et al., 2017	https://xenabrowser.net/datapages/
Ivy Glioblastoma Atlas Project RNA sequencing fata	Puchalski et al., 2018	https://glioblastoma.alleninstitute.org/static/download.html

(*Continued on next page*)

Continued

REAGENT or RESOURCE	SOURCE	IDENTIFIER
STRING Protein-Protein-Interaction database, version 10.5	Szklarczyk et al., 2017	https://version-10-5.string-db.org/cgi/download.pl
Molecular Signatures Database gene set collection	Liberzon et al., 2015; Subramanian et al., 2005	https://www.gsea-msigdb.org/gsea/msigdb/
RNA sequencing count matrix from matched breast cancer primaries and brain metastases	Varešlija et al., 2019	https://github.com/npriedig
Oligonucleotides		
See Table S7		N/A
Software and Algorithms		
FlowJo, version 10.4	BD	https://www.flowjo.com/
BBDuk, version 38.12	Joint Genome Institute	https://jgi.doe.gov/data-and-tools/bbtools/
STAR aligner, version 2.5.2b	Dobin et al., 2013	https://github.com/alexdobin/STAR
R environment, version 3.5.0	R Core Team, 2018	https://www.r-project.org/
VIS Image Analysis, version 2019.7	Visiopharm	https://www.visiopharm.com/
Other		
gentleMACS Octo Dissociator	Miltenyi	Cat#130-095-937
gentleMACS C Tubes	Miltenyi	Cat#130-096-334
LS Columns	Miltenyi	Cat#130-042-401
SepMate-50	StemCell	Cat#85450
PermaLife Cell Culture Bags	OriGen Biomedical	Cat#PL30-2G
LSR II flow cytometer	BD	N/A
Fortessa flow cytometer	BD	N/A
FACSAria III, flow cytometer & cell sorter	BD	N/A
Axio Scan.Z1 slide scanner	Zeiss	N/A
QuantStudio 6 Flex	Applied Biosystems	N/A
Omni Tissue Homogenizer (TH)	Omni International	Cat#TH220

RESOURCE AVAILABILITY

Lead Contact

Further information and requests for resources should be directed to the Lead Contact, Johanna Joyce (johanna.joyce@unil.ch).

Materials Availability

This study did not generate new unique reagents.

Data and Code Availability

RNA-seq count expression data generated during this study can be visualized and downloaded at https://joycelab.shinyapps.io/braintime/. Due to patient privacy protection, the raw RNA-seq data will be made available upon request.

EXPERIMENTAL MODEL AND SUBJECT DETAILS

All procedures performed in studies involving human participants were in accordance with the ethical standards of the institutional and/or national research committee and with the 1964 Helsinki declaration and its later amendments or comparable ethical standards.

Informed consent was obtained from all individual participants included in this study. The collection of non-tumor and tumor tissue samples at the Centre Hospitalier Universitaire Vaudois (CHUV, Lausanne, Switzerland) was approved by the Commission cantonale d'éthique de la recherche sur l'être humain (CER-VD, protocol PB 2017-00240, F25 / 99). Sample collection at Memorial Sloan Kettering Cancer Center (MSKCC, New York, NY, USA) was approved by the institutional review board (IRB, protocols #IRB #06-107, #14-230). Non-tumor samples of cerebral cortex tissues were collected at CHUV during medically indicated surgical treatment of

refractory epilepsy patients, and at MSKCC in normal brain distant from the tumor in patients with low-grade glioma or from post-mortem samples collected through the rapid autopsy program with no history of brain malignancy.

Tissue specimens were immediately collected from the operating room and processed as described below. All patient-related data and unique identifiers were removed so that human samples were anonymized before any further processing.

Pathological review and molecular analysis of tumor samples was performed as part of standard clinical care at the respective locations (CHUV or MSKCC). In all glioma samples subjected to RNA sequencing, the *IDH1 and IDH2* mutation status was verified by inspection of the reads from the $CD45^-$ population aligning to the *IDH1* and *IDH2* loci with the Integrative Genomics Viewer (IGV; Robinson et al., 2017). For immunofluorescence sections the tumor diagnosis was confirmed independently, for all non-tumor samples, the absence of malignancy was equally confirmed by a pathologist.

Peripheral blood and buffy coats were obtained from the Transfusion Interrégionale, Croix-Rouge Suisse (Epalinges/Lausanne, Switzerland), the New York Blood Center (New York, NY, USA), and healthy donors.

METHOD DETAILS

Clinical sample processing, flow cytometry (FCM) and fluorescence activated cell sorting (FACS)

Tissue specimens were washed in HBSS and macro-dissected under sterile conditions. Parts of the tissue were either immediately frozen by submerging the sample in liquid nitrogen-cooled 2-methyl butane (Sigma-Aldrich) or OCT-embedded (Tissue-Tek) before freezing for subsequent sectioning and immunofluorescence staining. OCT embedding was performed by placing the sample in a freezing mold filled with OCT and then submerging the mold in 2-methyl butane cooled with dry ice.

The remaining tissue was further processed with either the Brain Tumor Dissociation Kit (Miltenyi) for non-tumor tissue and gliomas, or the Tumor Dissociation Kit for BrMs (Miltenyi) using the gentleMACS Octo Dissociator (Miltenyi). Myelin debris in cell suspensions from non-tumor and glioma tissues was removed by incubating the cells with Myelin Removal Beads (Miltenyi) and magnetic-activated cell sorting (MACS) using LS columns (Miltenyi) according to the manufacturer's instructions. All tissue suspensions were filtered through a 40 μm filter and underwent red blood cell lysis (BioLegend). Single cell suspensions were stained with a fixable live-dead stain (Zombie NIR, BioLegend), FC-blocked for 10 min (Human TruStain FcX, BioLegend) and then incubated with direct fluorophore-conjugated antibodies for 20 min at 4°C. All FCM antibodies were titrated in a lot-specific manner. Antibody details are listed in the Key Resources Table. Cells were washed with PBS +2% fetal bovine serum (FBS) +0.5 mM EDTA and stored at 4°C in the dark until FAC-sorting.

All FCM acquisition was completed on either a BD Fortessa or a BD LSR II device (BD), and cell sorting was performed on a FACSAria III (BD) using FACSDiva (BD). Cells were sorted directly into Trizol LS (Thermo Fisher Scientific) and immediately snap frozen with liquid nitrogen. Analysis of FCM data was performed with FlowJo (BD).

Tumor microenvironment-conditioned medium (TME-CM) generation

Single cell suspensions from whole tumor samples were resuspended in DMEM-F12 (1:1) +Glutamax (GIBCO) +10% FBS +1% penicillin/streptomycin (P/S, GIBCO) and adjusted to a concentration of 2×10^6 cells/ml with 2 ml plated into each well of a 6-well plate (TPP). The supernatant of these tissue cultures, containing cancer cells, immune cells etc. from the complex brain TME, was harvested at 24 hours after initial seeding, spun down to remove debris (300 g, 10 min) and stored at −80°C until further use.

In vitro generation of monocyte-derived macrophages (MDM) and TME-CM stimulation

Peripheral blood mononuclear cells were isolated from buffy coats of healthy donors with a Ficoll (GE) gradient using SepMate tubes (StemCell) and monocytes selected by MACsorting with CD14 MicroBeads (Miltenyi). Monocytes were differentiated into macrophages by culture in Teflon-coated bags (OriGen) for 7 days in DMEM +GlutaMAX (GIBCO) +10% FBS +1% P/S with the addition of 10 ng/ml recombinant human CSF-1 (R&D Systems).

Differentiated MDMs were plated at a density of 1×10^6 cells/well of a 6-well plate in DMEM +10% FBS +1% P/S +10 ng/ml CSF-1. After cell attachment, MDMs were cultured in serum free medium for 6 hours before stimulation with TME-CM for 24 hours.

RNA isolation, cDNA synthesis and quantitative real-time PCR

TME-CM-stimulated MDMs were lysed with Trizol (Thermo Fisher Scientific), RNA was purified with Direct-zol columns (Zymo Research), DNase treated and 1.0 μg of RNA was used for cDNA synthesis using the High Capacity cDNA Reverse Transcription Kit (Applied Biosystems). An amount of cDNA equivalent to 5 ng total RNA was used for real-time PCR. For primer and probe details see Table S6. Assays were run in triplicate on a QuantStudio 6 Flex instrument (Applied Biosystems) using the TaqMan Universal PCR Master Mix (Applied Biosystems) and expression was normalized to the average expression of *Ubiquitin C* (*UBC*) and *Ribosomal Protein L19* (*RPL19*) for each sample.

Immunofluorescence staining and microscopy image acquisition

10 μm cryostat sections were thawed, air-dried and fixed with ice-cold 100% methanol for 5 minutes. After rehydration with PBS, sections were washed twice in PBS +0.2% Tween 20 (Applied Chemicals), permeabilized with PBS +0.2% Triton X-100 (Applied Chemicals) for 3 hours and washed again with PBS +0.2% Tween 20. Blocking was performed with PBS +0.5% Tween 20 +1%

TNB Blocking Reagent (Perkin Elmer), followed by incubation with primary antibody in the same buffer overnight at 4°C. Primary antibody information and dilutions are listed in the Key Resources table. Sections were washed with PBS +0.2% Tween 20 before incubation with fluorophore-conjugated secondary antibodies at a dilution of 1:500 in PBS +0.5% Tween 20 +1% TNB Blocking Reagent +1 μg/ml DAPI at room temperature. Directly-conjugated primary antibodies were employed where indicated after an initial round of primary and secondary antibody staining, to avoid potential for cross reactivity. Finally, sections were washed with PBS +0.2% Tween and mounted with Fluorescence Mounting Medium (Dako).

Stained tissue sections were imaged with an Axio Scan.Z1 slide scanner (Zeiss) equipped with a Colibri 7 LED light source (Zeiss) using a Plan-Apochromat 20x/0.8 DIC M27 coverslip-corrected objective (Zeiss). All slides from the same staining panel were digitalized using identical acquisition settings.

Image analysis and cell type identification

Image quantification was performed using the VIS Image Analysis software (Visiopharm). For each staining panel a specific application was created using the software's authoring module. The tissue outline was detected after applying a 21 pixel mean filter. The edges of the derived regions of interest were smoothened with the built-in function "close" and holes in the mask were filled using the "fill holes" command. Aberrant signals resulting from e.g., dust particles, tissue folds or air bubbles were manually excluded from these regions of interest. Nuclear classification was based on the watershed signal of the DAPI staining and filtered by area to exclude incomplete nuclei. The obtained nuclear label was expanded by 5 pixels to capture both nuclear and adjacent cytoplasmic fluorescent signal. Cell types were identified using a hierarchical decision tree with manually set thresholds. Finally, a representation of the cytoplasm was created using the inbuilt growth algorithm with a maximum distance of 15 pixels from the nucleus. Vessel segmentation was performed by creating a separate classifier based on pixel intensity of the CD31 signal. Nuclear classifiers were excluded *a priori* and incorporated in the vessel label only when exceeding the threshold for CD31. Perivascular niches (PVNs) were established by generating an ROI around vessels at a distance of 20 μm. All object-based phenotyping result tables were exported as csv files for further analysis within the R environment.

Protein isolation and enzyme-linked immunosorbent assay (ELISA)

Frozen tissues were weighed and homogenized on ice with an Omni Tissue Homogenizer (Omni International) in 10 μL of RIPA lysis buffer (Thermo Fisher Scientific) +cOmplete Protease Inhibitor (Roche Diagnostics) per mg of tissue. The homogenate was gently agitated on ice for 10 minutes, centrifuged at 10.000 g for 5 minutes at 4°C and the supernatant collected. The protein concentration was determined using a Bradford assay (Bio-Rad) and adjusted to 1 μg/μl. Samples were shipped to Raybiotech (Peachtree Corners) for quantitative analysis with the multiplexed Quantibody Array Q4000 ELISA.

RNA sequencing (RNA-seq)

RNA was isolated by chloroform extraction and isopropanol precipitation. RNA sequencing libraries were generated with the SMART-Seq preparation kit (CloneTech) and fragmented with the Nextera XT kit (Illumina). Paired end, 100 or 150 base pair, and single end, 100 base pair, sequencing was performed by Genewiz (South Plainfield, New Jersey, USA) on an Illumina HiSeq 2500 (Illumina).

Reads were adaptor trimmed and quality clipped using BBDuk (version 38.12; https://sourceforge.net/projects/bbmap/). Trimmed reads were mapped to the Genomic Data Commons (GDC) GRCh38.d1.vd1 reference sequence using the STAR aligner (version 2.5.2b, Dobin et al., 2013) in two-pass mode with parameters corresponding to the GDC RNA-seq alignment workflow. Transcript abundance was estimated using the corresponding GDC reference gtf file. A raw count matrix was produced and differential gene expression was assessed with DESeq2 using an absolute log2 fold change of 1 and a false discovery rate of 0.01 when contrasting to reference samples, and 0.05 for within tumor contrasts (Love et al., 2014).

Bioinformatic analysis environment

All bioinformatic analyses were performed within the R environment (version 3.5.0, R Core Team 2018).

Gene set-centered analyses

The Molecular Signatures Database (MSigDB, version 6.1, Liberzon et al., 2015; Subramanian et al., 2005) was used as the main source for gene set-based analyses.

Over-representation was assessed with the goseq R package (Young et al., 2010) for differentially expressed genes to correct for gene length bias, otherwise the hypergeometric test was employed. For individual samples, gene set enrichment was estimated with the Gene Set Variation Analysis R package (GSVA, Hänzelmann et al., 2013) using the "gsva" function. Gene set enrichment analysis (GSEA) was evaluated with the R package fgsea (https://github.com/ctlab/fgsea) using the maximum likelihood log fold changes determined by DESeq2 as the ranking metric.

Deconvolution of Toil-RNA sequencing data

Toil-processed (Vivian et al., 2017), DESeq2-standardized gene expression data and matching phenotype data from the TCGA and Genotype-Tissue Expression Project (GTEx) databases were downloaded from the UCSC Xena platform and filtered to include only

low-grade glioma "TCGA-LGG" and high-grade "TCGA-GBM" and "frontal cortex" GTEx samples to integrate bulk glioma expression data with unmatched non-tumor samples. MG- and MDM-specific marker genes were derived by identifying differentially expressed genes in these two populations versus all other sorted populations in a pairwise fashion, determining the intersect and ranking the resulting genes by their fold change versus the $CD45^-$ population. The 20 highest ranked genes were then used as cell type-specific marker genes. Deconvolution of MG- and MDM-proportions in tumor and non-tumor sample expression data was done with the EPIC R package (Racle et al., 2017) using these marker genes and providing the expression data from the sorted populations as reference profiles. As the exact amount of RNA within the estimated cell types is not known, this parameter was set to 1 when running the deconvolution.

Leading edge metagene (LEM) analysis

To capture biologically meaningful patterns of gene expression within the differentially expressed genes the LEM approach (Godec et al., 2016) was employed: (a) GSEA was performed using the MSigDB C7 collection as described above, (b) the leading edge genes of the significant gene sets were arranged into a genes by gene sets matrix with the shrunken fold changes as the entries, (c) this matrix was clustered using non-negative matrix factorization with the R package NMF (Gaujoux and Seoighe, 2010), (d) genes with a small coefficient in each metagene were filtered based on the 95^{th} quantile of a fitted exponential distribution of the coefficients and (e) each gene with a coefficient above the threshold was assigned to the metagene where it had the highest coefficient.

Protein-Protein-Interaction network building

Version 11.0 of the STRING database (Szklarczyk et al., 2017) was downloaded from the consortium's website and gene identifiers from RNA-seq were mapped to Ensembl Protein IDs using the provided accessory data. The resulting interaction data was filtered to contain only interactions with a high confidence STRING combined score (i.e., > 700). For network layout calculation the combined score was used as an edge weight.

Nearest neighbor distance measurements and neighborhood analysis of IF data

Nearest neighbor distances from MG and MDM to vessels in *IDH* wt glioma samples were calculated using the spatstat R package (Baddeley et al., 2015). Statistical significance was assessed by fitting a mixed effects model with the cell type as the fixed effect, and the clinical sample ID as the random effect using the R package lme4 (Bates et al., 2015).

Neighbors for each individual cell were determined based on their occurrence within a range of 5 μm outside of the radius of the cell (calculated based on the area). This was used to tabulate the number of neighbors and their cell type for each cell within the tissue section.

Cell type abundance estimation in spatial Ivy Glioblastoma Atlas Project (GAP) data

The micro-dissected Ivy GAP (Puchalski et al., 2018) RNA-seq RSEM count data and sample annotation containing anatomical location were downloaded from the Ivy GAP website (https://glioblastoma.alleninstitute.org/static/download.html) and normalized using DESeq2. The relative abundance of cell types was estimated by deriving marker genes through a multinomial logistic regression model on the normalized expression data of the FAC-sorted cell types of interest in *IDH* WT tumors and then computing the GSVA enrichment scores in the Ivy GAP samples.

Survival analysis of the IDH wt MDM-specific gene signature in gliomas

The harmonized TCGA low-grade and high-grade HTSeq hg38 count data and clinical data was accessed from the GDC repository using the TCGAbiolinks R package (Colaprico et al., 2016). Datasets were pre-processed to remove outliers and normalized using the functions provided by TCGAbiolink before merging. Subsequent analyses were performed including only samples where an annotation of the *IDH* mutation status was available. Cell type-specific gene signatures were derived by training a multinomial logistic regression model with an elastic-net penalty to separate between MG and MDMs along *IDH* status with the "glmnet" R package (Friedman et al., 2010). A mean-centered expression matrix of all MG and MDMs expression data in gliomas and BrMs, subset by genes that were upregulated in tumors versus non-tumor tissue or healthy controls, served as the input matrix. The strength of the penalty was determined by a 10-fold cross-validation of the λ parameter. For survival analysis, GSVA enrichment scores of these cell type-specific gene signatures were estimated and used to divide samples into tertiles. Kaplan-Meier survival curves were computed using the "survfit" function. Survival curves were compared with a log-rank test between the individual levels and multivariate Cox regression analysis was performed with the "coxph" function.

Self-organizing map (SOM) clustering

Variance stabilized counts from sorted populations of interest from *IDH* mut, *IDH* WT glioma and BrM samples were filtered with the R package HTSFilter (Rau et al., 2013) to ensure removal of genes with a low, constant expression. The resulting matrix of genes and samples was used as input for the SOM neural network building, which was performed with the oposSOM R package (Löffler-Wirth et al., 2015) with a map space of 50 × 50. To investigate associations between the sample phenotype and the SOM metagenes, the tumor type and cell type were provided as group labels.

Weighted gene correlation network analysis (WGCNA)

The WGCNA (Langfelder and Horvath, 2008) R package was used to identify co-regulated genes associated with a MG- or MDM-BrM phenotype. A variance stabilized, batch-corrected count matrix of MG and MDM samples was filtered with the R package HTSFilter (Rau et al., 2013) yielding input expression data with 15826 genes and 56 samples. WGCNA standard parameters were changed as follows: the soft-thresholding power was raised to 7, the minModuleSize was increased to 50, "bicor" was used to calculate the correlation, the network type was set to "signed hybrid" and a dendrogram cut height of 0.25 was used for module merging. This yielded 20 modules whose eigengene, i.e., the first principal component, was tested for correlation to the provided sample information, i.e., tumor- and cell-type and abundance as determined by FCM.

Expression analysis of external dataset of matched primary breast cancer and BrMs

RNA-seq raw count data from patient-matched primary breast tumors and corresponding BrMs (Varešlija et al., 2019) were downloaded (https://github.com/npriedig/jnci_2018) and transformed using DESeq2. The statistical significance of gene expression changes between primary tumors and BrMs was assessed with a two-tailed Wilcoxon signed-rank test on the variance-stabilized counts.

Plotting and graph generation

Plots were created using the ggplot2 R package (Wickham, 2016) and the ggpubr (https://cran.r-project.org/web/packages/ggpubr/), survminer (https://cran.r-project.org/web/packages/survminer/), ggraph (https://cran.r-project.org/web/packages/ggraph/) and ggcyto extensions (Van et al., 2018). Annotated heatmaps were drawn with the pheatmap R package (https://cran.r-project.org/web/packages/pheatmap/).

QUANTIFICATION AND STATISTICAL ANALYSIS

Summary data are presented as mean ± standard error of the mean (SEM) or Tukey boxplots using "ggplot2." Numerical data was analyzed using the statistical tests noted within the corresponding sections of the article. Hierarchical clustering was performed using Ward's method with 1-Pearson correlation coefficient as the distance metric unless noted otherwise. P values were annotated as follows: * < 0.05, ** < 0.01, *** < 0.001, **** < 0.0001, ns > 0.05.

Supplemental Figures

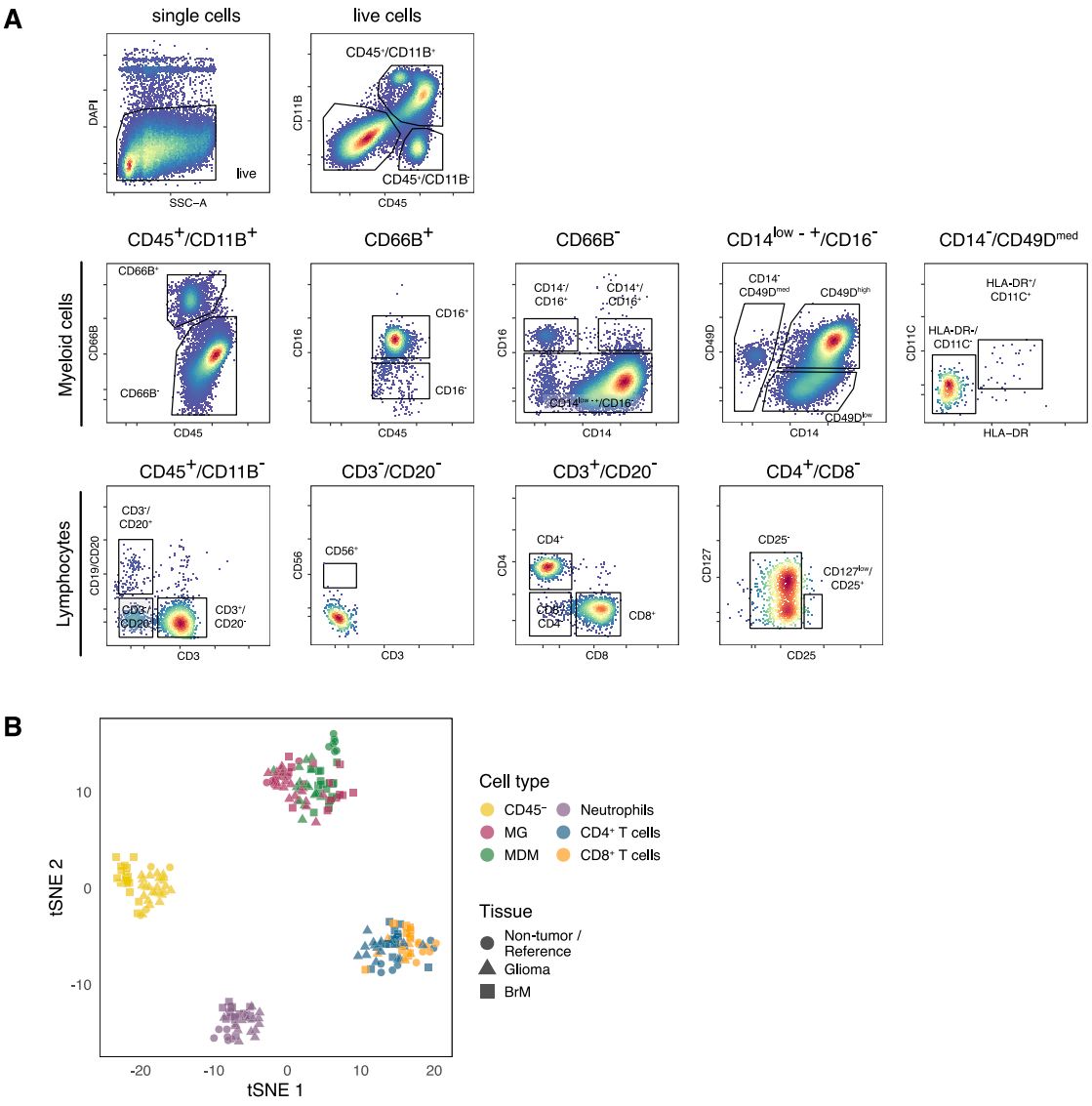

Figure S1. FACS of Cell Populations and RNA-Seq, Related to Figure 1

(A) Flow cytometry (FCM) plots illustrating the gating strategy employed during FAC-sorting of immune cell populations in non-tumor and tumor tissue (for cell type markers, see Table S2). (B) tSNE plot of gene expression data (500 most variable genes) from all sorted cell populations (n = 226) across the complete clinical cohort (MG = microglia, MDM = monocyte-derived macrophages, reference = unmatched healthy blood and *in vitro* generated MDMs).
See also Table S2.

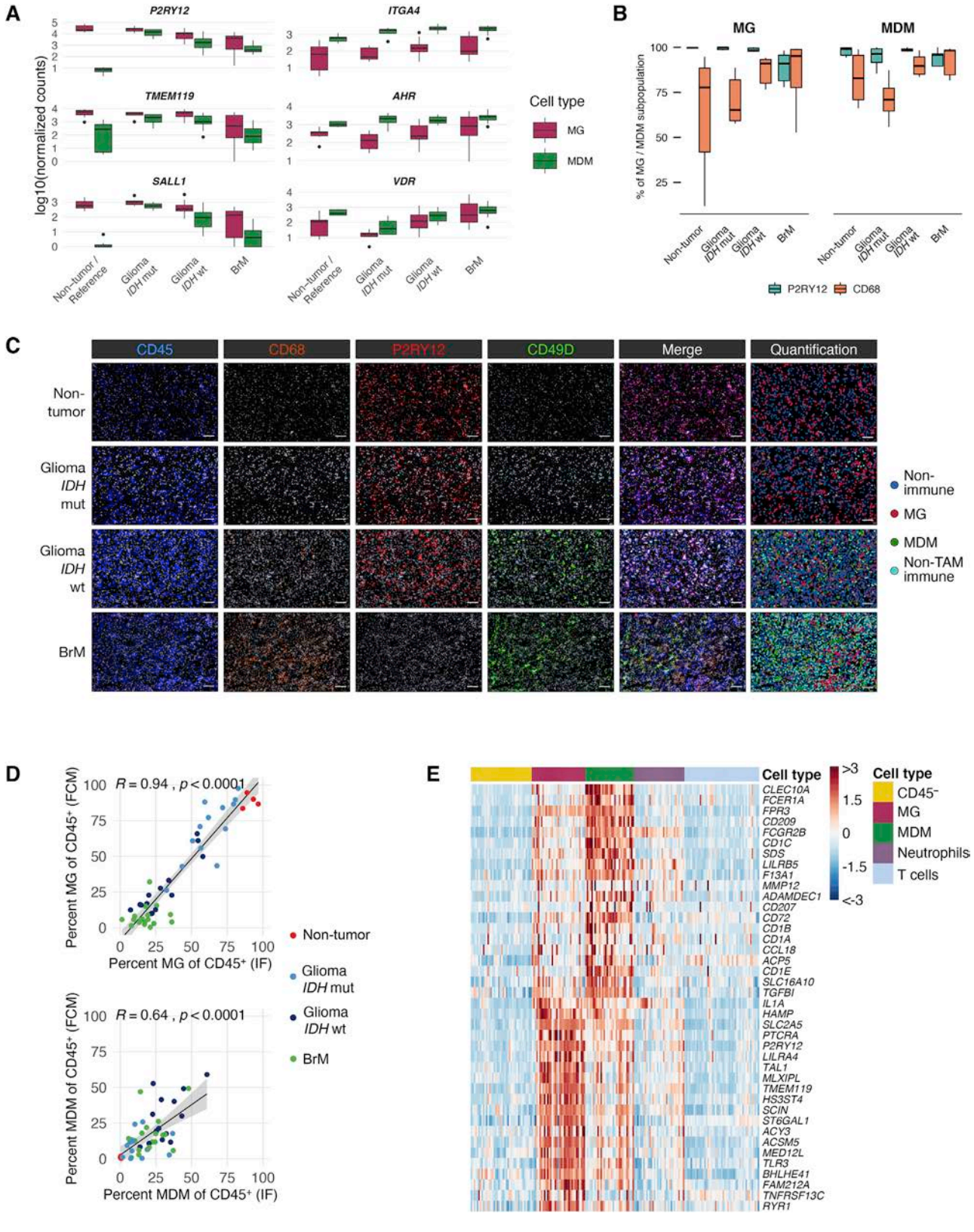

(legend on next page)

Figure S2. MG and MDM Marker Expression, Related to Figure 2

(A) Normalized counts (log10 transformed) of MG and MDM marker genes in sorted CD49D^{low} MG and CD49D^{high} MDM populations across both non-tumor and tumor tissues (reference = healthy donor *in vitro* generated MDMs). (B) Percentage of CD49D^{low} MG and CD49D^{high} MDMs positive for P2RY12 and CD68 as determined by FCM in relation to the total number of MG/MDMs in non-tumor (n = 8) and tumor tissue ($n_{IDH\ mut}$ = 6, $n_{IDH\ WT}$ = 6, n_{BrM} = 9). (C) Single channel and merged immunofluorescence (IF) images of CD45, CD68, P2RY12 and CD49D stainings which were employed to delineate MG and MDMs. The last column shows the resulting Visiopharm cell type assignments for quantitative analyses (MG (CD45$^+$, P2RY12$^+$/CD68$^+$, CD49D$^-$), MDM (CD45$^+$, P2RY12$^+$/CD68$^+$, CD49D$^+$), non-immune cells (CD45$^-$) and non-TAM-immune cells (CD45$^+$, P2RY12$^-$/CD68$^-$, CD49D$^{-/+}$). Scale bars represent 100μm. (D) Scatterplots of the abundance of MG and MDMs as determined by IF versus FCM in non-tumor (n = 4) and tumor tissues ($n_{IDH\ mut}$ = 13, $n_{IDH\ WT}$ = 14, n_{BrM} = 18) processed independently from the same individual samples. Pearson's correlation coefficient and significance are indicated at the top of each plot. (E) Heatmap of human MG- and MDM-specific gene set expression used for deconvolution across FAC-sorted population samples from all disease types.

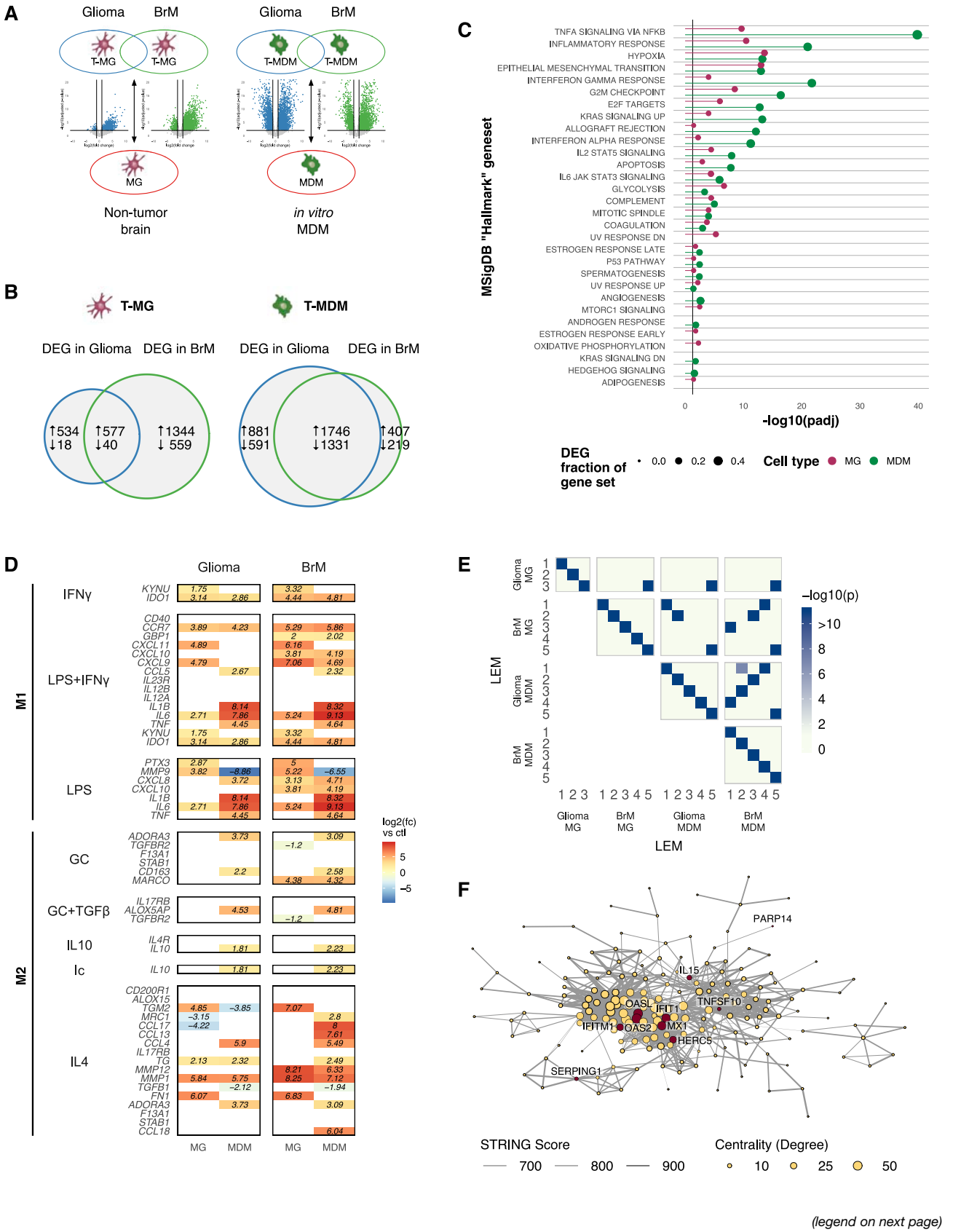

(legend on next page)

Figure S3. Analysis of DEGs and TAM Activation Patterns, Related to Figure 3

(A) Summary of contrasts applied when performing differential gene expression (DEG) analysis in MG and MDMs in gliomas (regardless of *IDH* status) and BrMs (from all primaries) in comparison to normal controls (non-tumor brain MG and *in vitro* differentiated MDMs respectively) with the corresponding log2(fold-change) versus -log10(adjusted p value) volcano plots. (B) Euler plot of the number of differentially expressed genes (DEG, log2(fc) > 1, p.adj < 0.01) that overlap in MG and MDMs as shown in (A). (C) Molecular Signatures Database (MSigDB) "Hallmark" gene set collection overrepresentation analysis (ORA) in genes upregulated in both gliomas and BrMs versus non-tumor brain tissue or healthy donors in MDMs and MG in MDMs and MG. Dot sizes reflect the fraction of gene set members found within the analyzed DEGs, and dot color indicates cell type. (D) Heatmap of fold changes of macrophage M1 and M2 polarization marker genes (absolute log2(fc) > 1, p.adj < 0.05) in MDMs and MG in gliomas and BrMs. Blank tiles indicate the lack of significant fold change. Genes are annotated with their canonical stimuli and the associated polarization phenotype. (GC = glucocorticoid, Ic = immune complexes, IFNγ = Interferon gamma, IL10 = interleukin 10, IL4 = interleukin 4, LPS = lipopolysaccharide, TGFβ = transforming growth factor beta). (E) Overlap between leading edge metagenes (LEMs) in MG and MDMs in gliomas and BrMs. Tile fill color indicates significance of overlap determined by hypergeometric testing (-log10(p.adj)). (F) String-DB protein-protein-interaction network of the intersect from IFN Type-1 group 2 modules from LEMs "BrM-MG 1," "Glioma MDM 1" and "BrM-MDM 4." Genes selected for validation through qRT-PCR are highlighted in red (corresponding data shown in Figure 3E). Node size indicates the centrality, while edge width corresponds to the String-DB interaction score (only scores > 700, i.e., with a high degree of confidence have been included).

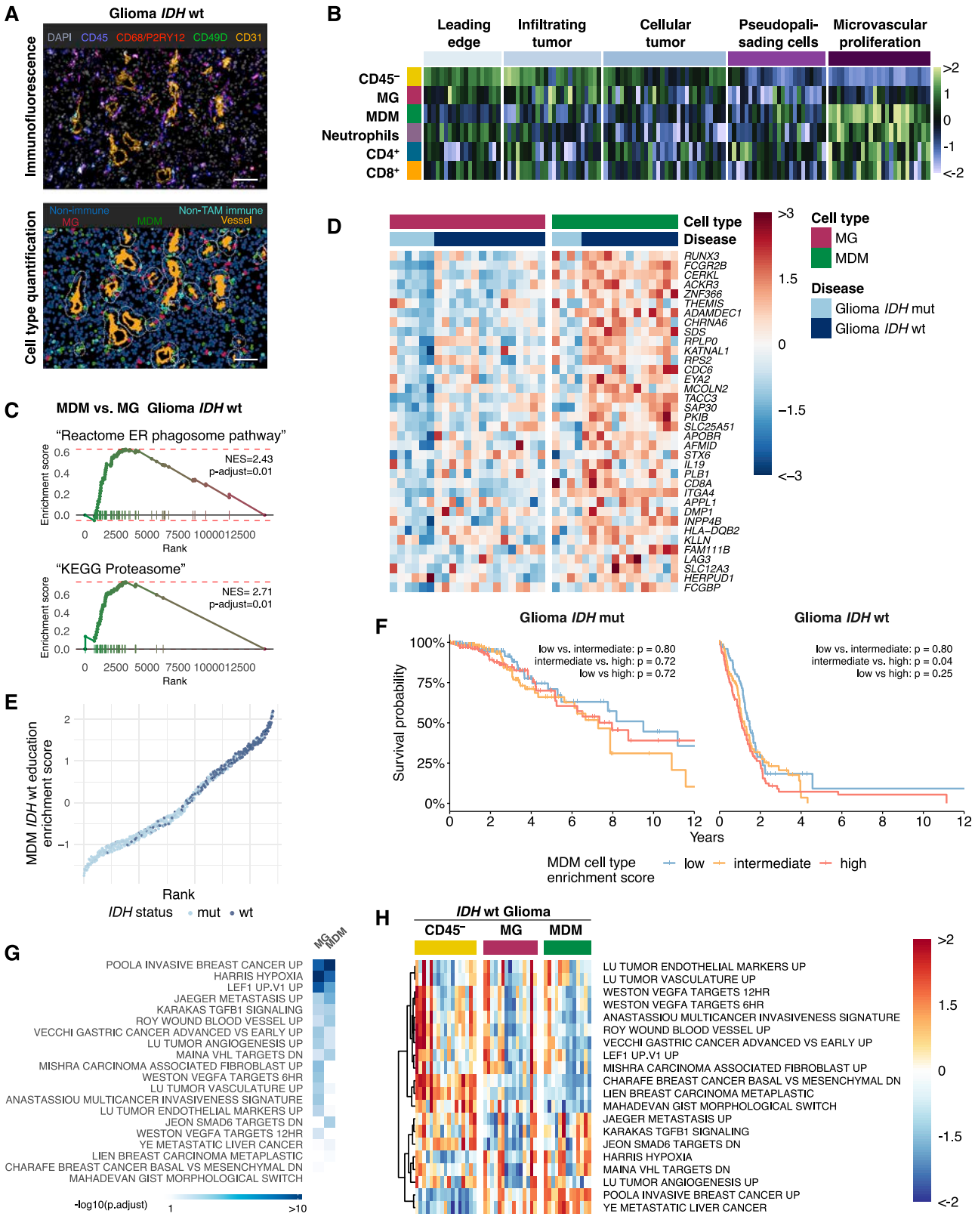

(legend on next page)

Figure S4. *IDH* WT-Specific Alterations in TAMs, Related to Figure 4

(A) Representative IF image and cell type quantification below of non-immune cells ($CD45^-$), non-TAM immune cells ($CD45^+$, $P2RY12/CD68^-$, $CD49D^{+/-}$), MG ($CD45^+$, $P2RY12/CD68^+$, CD49D) and MDM ($CD45^+$, $P2RY12/CD68^+$, $CD49D^+$) and vessels ($CD31^+$) in *IDH* WT glioma. Dashed line indicates the border of the perivascular niche (PVN), scale bar represents 100μm. (B) Heatmap of cell-type gene set variation analysis (GSVA) enrichment scores of micro-dissected Ivy Glioblastoma Atlas Project samples (dataset from Puchalski et al., 2018). Columns are ordered by anatomical location, rows have been z-scored. (C) Gene set enrichment analysis (GSEA) results of MSigDB "C2" antigen processing and cross-presentation associated pathways in T-MDMs versus T-MG in *IDH* WT glioma. (D) Heatmap of MDM *IDH* WT gene set expression in sorted MG and MDMs from *IDH* mut and WT glioma samples. Columns are ordered by *IDH* status and cell type, expression values have been z-scored. (E) Plot of z-scored MDM *IDH* WT signature scores in the TCGA glioma dataset. Subjects are ranked by their enrichment score (small amount of random variation added for readability) and the *IDH* status is indicated by color. (F) Kaplan-Meier estimator of survival in the combined TCGA glioma cohort based on the enrichment for a cell type-specific T-MDM signature (see Figure S2E). (G) ORA of "innate anti-PD-1 resistance" (IPRES) signatures within DEG from MG- and MDMs in *IDH* WT gliomas DEGs (versus MG from *IDH* mut tumors) with tile fill indicating the -log10 of the adjusted p value. (H) GSVA of IPRES signatures in $CD45^-$ cells, MG, and MDMs from *IDH* mut and *IDH* WT gliomas. Columns are ordered by cell type, rows (z-score) have been hierarchically clustered.

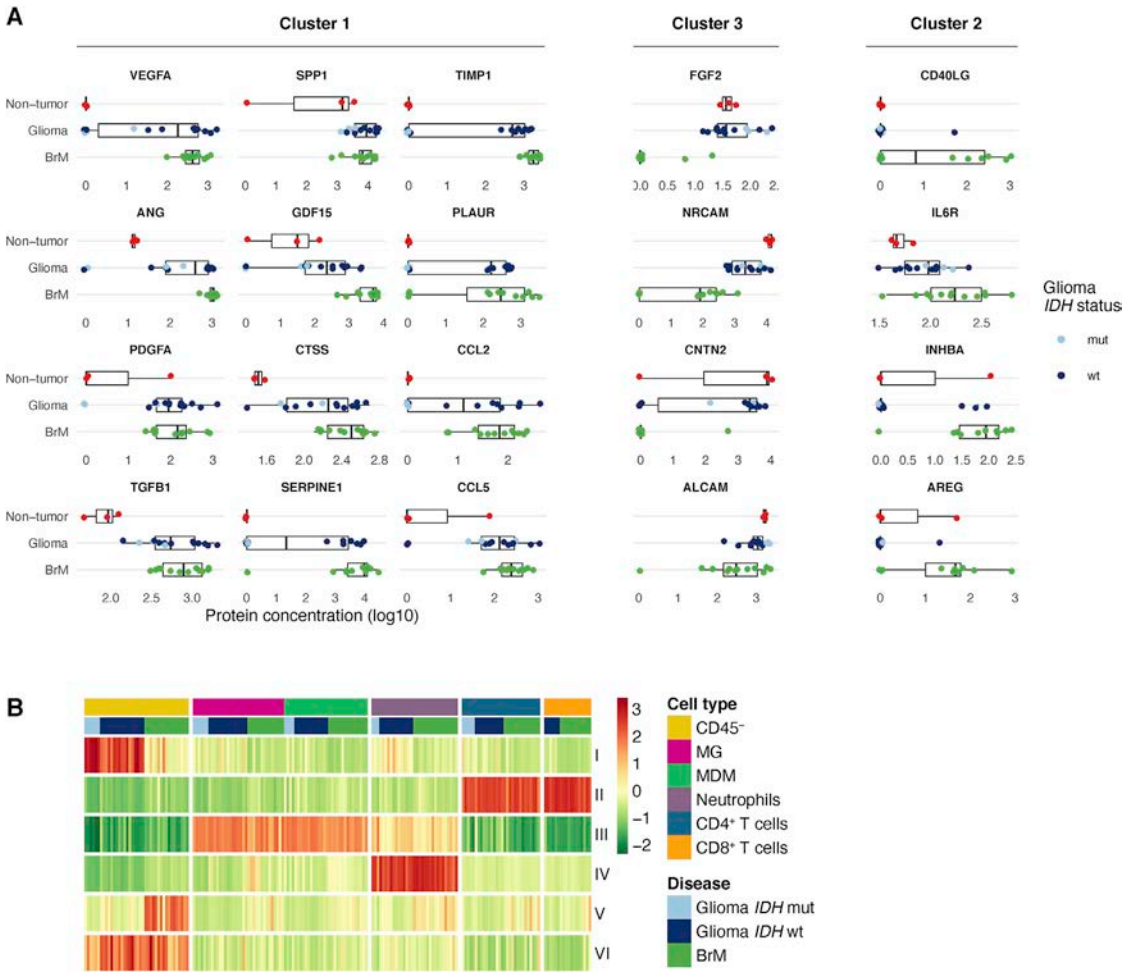

Figure S5. Protein Concentration in Bulk Tumor Tissues and Relation to Cell-Type-Associated SOM Spots, Related to Figure 5

(A) Bulk tissue protein concentrations of indicated proteins in non-tumor brain (n = 3), gliomas (n = 14) and BrMs (n = 12). Color indicates disease type and *IDH* status. (B) Heatmap of self-organizing map (SOM) spot metagene expression across the analyzed samples. Rows were z-scored and have been hierarchically clustered, columns were ordered by cell type, disease type and *IDH* mutation status.

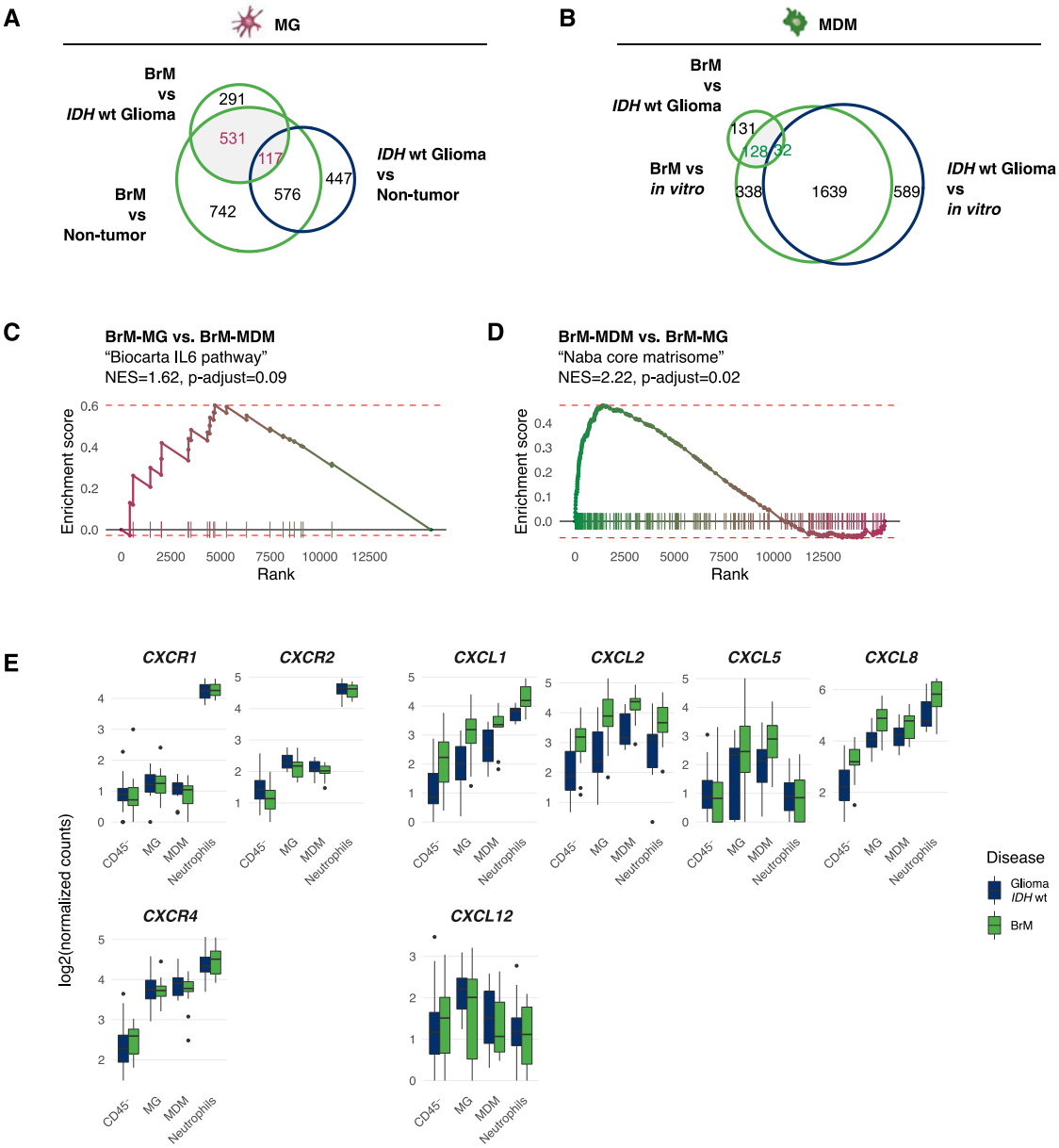

Figure S6. Gene Expression Analysis in BrM-TAMs, Related to Figure 6

(A) Overlap of the number of differentially expressed genes (DEG, log2(fc) > 1, p.adj < 0.05) in MG and (B) MDMs in the indicated comparisons. BrM-specific gene sets are highlighted in gray within each cell type. The intersect of highlighted BrM-MG and BrM-MDM sets contains 87 genes. (C) GSEA of the "Biocarta IL-6 pathway" in BrM-MG versus -MDM and the (D) "Naba core matrisome" gene set from the MSigDB "C2" collection in BrM-MDM versus -MG. (E) Expression (log10-transformed normalized counts) of neutrophil-recruiting chemokines and receptors in sorted MG, MDMs and neutrophil populations from *IDH* WT and BrM samples.

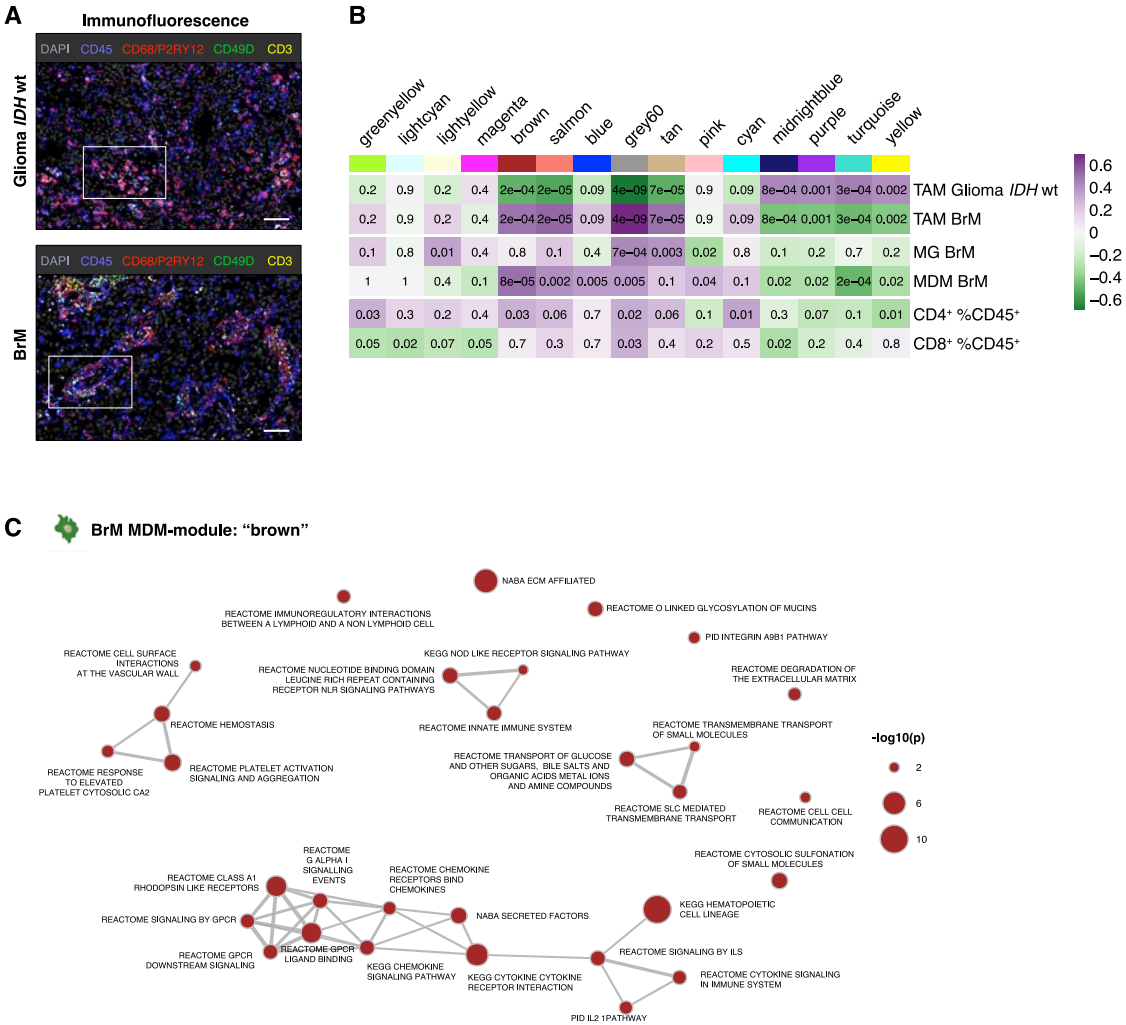

Figure S7. Correlation of WGCNA Modules with External Traits and Module Pathway ORA, Related to Figure 7

(A) Representative immunofluorescence images in *IDH* WT gliomas and BrMs. Scale bars = 100μm, boxed area is shown in higher magnification in Figure 7A. (B) Heatmap of the weighted gene correlation network analysis (WGCNA) module eigengene (= first principal component of expression data, columns, module columns are labeled with a color code) correlation to the traits (rows, cell type and disease, abundance of $CD4^+$ or $CD8^+$ T cells in % of $CD45^+$). Values inside the cells state Pearson's r and the associated p value. (C) "Brown" BrM-MDM module MSigDB "C2CP" ORA results (p value < 0.01) enrichment map network visualization. Node size represents p value, edge thickness reflects overlap of genes between gene sets.

7.3 The local microenvironment drives activation of neutrophils in human brain tumors

Roeltje R. Maas[1,2,3,4,5,13], Klara Soukup[1,2,13], Nadine Fournier[6,7], Sabine Galland[1,2,3,8], Mara Kornete[1,2], Davide Croci[1,2], Matteo Massara[1,2,3], Joao Lourenco[6], Ángel F. Álvarez Prado[1,2,3], Damien N. Marie[1,2], Johanna Lilja[1,2], Vladimir Wischnewski[1,2,3], Rachel Marcone[6], Gabriel F. Calvo[9], Pratyaksha Wirapati[7], Iván Ballesteros[10], Andrés Hidalgo[10,11], Andreas F. Hottinger[1,3,8], Jean-Philippe Brouland[12], Roy T. Daniel[3,5], Monika E. Hegi[3,4,5], and Johanna A. Joyce[1,2,3,14]*

[1] Department of Oncology, University of Lausanne, Lausanne, Switzerland

[2] Ludwig Institute for Cancer Research, University of Lausanne, Lausanne, Switzerland

[3] L. Lundin and Family Brain Tumor Research Center, Departments of Oncology and Clinical Neurosciences, Centre Hospitalier Universitaire Vaudois, Lausanne, Switzerland

[4] Neuroscience Research Center, Centre Hospitalier Universitaire Vaudois, Lausanne, Switzerland

[5] Department of Neurosurgery, Centre Hospitalier Universitaire Vaudois, Lausanne, Switzerland

[6] Translational Data Science Group, Swiss Institute of Bioinformatics, Lausanne, Switzerland

[7] Bioinformatics Core Facility, Swiss Institute of Bioinformatics, Lausanne, Switzerland

[8] Department of Oncology, Centre Hospitalier Universitaire Vaudois, Lausanne, Switzerland

[9] Department of Mathematics & MOLAB-Mathematical Oncology Laboratory, University of Castilla-La Mancha, Ciudad Real, Spain

[10] Program of Cardiovascular Regeneration, Centro Nacional de Investigaciones Cardiovasculares Carlos III, Madrid, Spain

[11] Vascular Biology and Therapeutics Program and Department of Immunobiology, Yale University School of Medicine, New Haven, USA

[12] Department of Pathology, Centre Hospitalier Universitaire Vaudois, University of Lausanne, Lausanne, Switzerland

[13] Equal contribution

[14] Lead Contact

7.3.1 Summary

Neutrophils are among the most abundant immune cells in humans, and frequently infiltrate tumors in substantial numbers. However, their precise functions in different cancer types remain poorly understood, including in the brain microenvironment. We therefore investigated neutrophils in tumor tissue of glioma and brain metastasis patients, along with peripheral blood, and describe herein the first in-depth analysis of their phenotypes and functions in these tissues. A combination of profiling strategies revealed that brain tumor-associated neutrophils (TANs) differ significantly from circulating blood neutrophils and have immune suppressive capacity. TANs exhibit a distinct inflammatory signature, which is driven by a combination of soluble inflammatory mediators centered on TNF-α, and is more pronounced in brain metastasis than glioma TANs. Myeloid cells, including tumor-associated macrophages, emerge at the core of this inflammatory network – supporting the concept of a critical myeloid niche regulating overall immune suppression in human brain tumors.

Keywords

tumor microenvironment, tumor immune microenvironment, glioma, glioblastoma, brain metastasis, tumor immunology, neutrophil-to-lymphocyte ratio, immune suppression, angiogenesis, myeloid niche

7.3.2 Introduction

Central nervous system tumors comprise primary and metastatic malignancies, and unfortunately often confer a poor prognosis. Among primary brain tumors, diffuse gliomas represent the most aggressive types and are classified based on the occurrence of isocitrate dehydrogenase 1 and 2 (*IDH*) mutations (20). *IDH* mutant (mut) tumors are generally low-grade gliomas, whereas *IDH* wildtype (wt) tumors represent high-grade aggressive glioblastomas (GBM). Secondary tumors (brain metastases, BrMs) are more frequent and originate predominantly from primary lung, breast, melanoma, and kidney tumors (25). Prognosis following the current standard of care therapy remains poor (163, 164), and ongoing trials to identify new treatment

strategies mostly focus on immuno- and targeted therapies, which have shown some efficacy in a subset of BrMs but only very limited effects in gliomas (136, 140, 141, 165). The suboptimal efficacy of these treatments is likely driven in part by immune-suppressive mechanisms operating in the brain (166).

The brain tumor microenvironment (TME) is a critical regulator of cancer progression and metastasis (167), with unique cell types (e.g., microglia, astrocytes, and neurons), a specialized immune composition (49, 50), and physiological regulation by the blood-brain barrier (BBB) (168). The overall tumor immune landscape of human gliomas and BrMs has been recently reported (49, 50), with a particular focus on analyzing microglia (MG) and monocyte-derived macrophages (MDMs). Importantly, among brain-infiltrating immune cells, a substantial proportion of tumor-associated neutrophils (TANs) was reported specifically in human BrMs and *IDH* wt gliomas (49).

However, to date, only a handful of studies have started to explore the roles of TANs in brain tumors, and mostly reported pro-tumoral roles in mouse models of gliomas (110, 126, 130, 131) and BrM (93, 128). Given a number of differences between mouse and human neutrophil biology (129), a comprehensive and multifaceted investigation of TANs in human brain tumors is of critical importance and currently lacking. Moreover, given the diversity of neutrophil functions in distinct organ environments, in both health (79) and disease (169), the emphasis must be placed on understanding the contribution of TANs to each specific tumor type and stage (74).

Here, we present the first in-depth analysis of neutrophils in patients with diverse brain malignancies. We identified commonalities and differences between neutrophils in blood *vs.* tumor tissue and determined how primary *vs.* metastatic brain TMEs coopt these cells. We thereby addressed the following questions: (i) What determines neutrophil abundance in human brain tumors, (ii) where do TANs localize in the brain TME and which cell types do they interact with, and (iii) how do specific tissue *vs.* tumor types dictate neutrophil phenotypes and functionalities.

7.3.3 Results

Neutrophils are more abundant in the TME of human BrMs than primary gliomas and preferentially localize proximal to blood vessels

In this study, we specifically interrogated neutrophils to address if they are altered by distinct brain TMEs in tumors of intracranial *vs.* extracranial origin. We analyzed freshly resected human glioma and BrMs, matched blood samples, and non-tumor brain tissue (epilepsy lobectomies) using a wide range of complementary approaches (including flow cytometry (FCM), immunofluorescence (IF) staining, RNA-sequencing (RNAseq), mixed environmental cultures (MECs), protein arrays and various *ex vivo* functional assays) (Fig. 1A). This allowed us to comprehensively interrogate the phenotype, transcriptome, and functionality of brain TANs and peripheral blood neutrophils (PBNs) for the first time.

Analysis of 192 human samples by FCM, revealed a significant increase in relative TAN abundance in *IDH* wt gliomas and BrMs compared to *IDH* mut gliomas and non-tumor tissue, with the highest TAN proportions in BrMs (Fig. 1B, S1A; Table S1A; detailed sample processing and gating strategy of different immune cell populations described in (162)). Similarly, the blood neutrophil-to-lymphocyte ratio (NLR) was substantially elevated in both *IDH* wt glioma and BrM patients *vs.* healthy donors (HD; Fig. 1C, S1B). High NLR has been associated with poor survival in many cancer types including brain tumors (80-82, 170).

Given the pronounced shift in PBN abundance in *IDH* wt glioma and BrM patients, we asked whether TANs infiltrate into the tumor parenchyma or remain primarily within blood vessels in the brain TME. We analyzed neutrophil ($CD45^+$ $CD15^+$) localization in relation to the vasculature ($CD31^+$) by IF staining of whole tissue sections (Fig. 1D-G). This spatial analysis demonstrated that neutrophils indeed cross the BBB and penetrate the brain (tumor) tissue (Fig. 1E-F). Quantifying the proximity of neutrophils to blood vessels (Fig. 1G), revealed that they localize at higher densities in the perivascular niche (PVN = within 20 µm distance of vessels) in both tumor and non-tumor brain tissue (Fig. 1D, G). Moreover, we found the highest spatial TAN densities

in BrMs, confirming their overall elevated abundance as determined above by FCM (Fig. 1D).

The neutrophil phenotype is altered in the brain tissue environment

Given the differential abundance of TANs in BrMs *vs.* gliomas, and the increased frequency of PBNs in both patient groups, we next asked whether neutrophils were phenotypically altered (i) compared to healthy donors, (ii) in different tissues (blood *vs.* tumors), and (iii) in distinct brain tumor types (gliomas *vs.* BrMs). We first analyzed canonical neutrophil activation markers and functional molecules, previously reported to be differentially expressed by TANs in other tumors (86, 92, 93, 128, 170-173). Using FCM, we found that brain TANs – independent of tumor type – exhibited a pronounced activation profile with increased expression of CD11B, CD15, CD66B and S100A9, and decreased expression of CD62L, in parallel with marked alterations in levels of the chemokine receptors CXCR1, CXCR2 and CXCR4, as compared to matched PBNs (Fig. 2A, S2A). Functionally, we observed lower intracellular levels of matrix metalloproteinase 9 (MMP9) and arginase 1 (Arg1) in TANs, potentially indicating their secretion into the TME, as reported in other contexts (174, 175) (Fig. 2A, S2A). Interestingly, TANs also expressed significantly higher levels of programmed death-ligand 1 (PD-L1) (Fig. 2A), which is not only implicated in T cell inhibition (93), but can also delay neutrophil apoptosis (174, 176). While these alterations exhibited inter-individual variation, there were no pronounced differences in this specific panel of markers between BrMs *vs.* glioma TANs, nor patient PBNs *vs.* HD PBNs (Fig. 2A, S2A).

We therefore took an unsupervised approach and profiled the transcriptome of fluorescence activated cell (FAC)-sorted matched PBNs and TANs from brain tumor patients, PBNs from HD, and neutrophils from non-tumor brain tissue by RNAseq. Principal component analysis (PCA) and unsupervised clustering revealed that TANs have a distinct transcriptional profile from PBNs (Fig. 2B-C; Table S1B), while patient PBNs are highly similar to HDs. In BrM patients only, we found specific alterations in PBNs *vs.* HD PBNs (Fig. S2B-C; Table S2A-B), of which a small subset was also evident in the comparison of BrM TANs *vs*. HD PBNs. (Fig. S2D; Table S2A-C).

Performing over-representation analysis (ORA) to identify shared induced pathways in BrM PBNs and TANs vs. HD PBNs, revealed three significantly different signatures, all broadly related to inflammatory signaling (Fig. 2D; Table S2D).

Although low in abundance, neutrophils in non-tumor brain tissue also showed a substantially different transcriptional profile compared to HD PBNs, and clustered with brain TANs (Fig. 2B-C), with most genes overlapping with either BrM-, glioma- or both TAN types (Fig. 2E, S2E; Table S2C, E-F). Several genes were elevated in non-tumor brain neutrophils *vs.* HD PBNs, including changes consistent with altered metabolism (*OLR1*/*LOX1, ALOX15B*, *CH25H*, *AREG*, *PTN*, *APOC2*) and multiple neurotrophic genes (*NR4A1, NR4A2, NR4A3, RAB3IL1, SYNDIG1, TSPAN7, RASGEF1C*) (Fig. 2F-G; Table S2F-G). Together, these data indicate that neutrophils adapt to the unique molecular composition and nutrient availability in the brain upon extravasation from the blood. These findings, and previous studies investigating the neutrophil phenotype in different tissues under homeostasis in mouse models (79), underscore the contribution of distinct organ environments as a key factor shaping the neutrophil transcriptome; as shown here in brain tissue from epilepsy patients for the first time.

Brain neutrophils are enriched in inflammatory gene signatures, which become more pronounced in BrMs but not in gliomas

Having determined that the brain microenvironment impacts the neutrophil transcriptome even in the absence of tumor growth, we interrogated non-tumor brain neutrophils *vs.* brain TANs more deeply. ORA of the 89 shared genes induced in neutrophils across all brain (tumor) tissues *vs.* HD PBNs (Fig. 2E) identified predominantly inflammatory pathways (Fig. 3A; Table S3A). We then asked what distinguishes brain TANs from non-tumor brain neutrophils and found significantly more differentially expressed genes (DEGs) in BrM TANs *vs.* glioma TANs when compared with non-tumor neutrophils (Fig. 3B; Table S3B-C). While BrM TANs are even further enriched in inflammatory and immune-activation genes and signaling pathways (Fig. 3C; Table S3D), glioma TANs mostly show increased extracellular matrix-related signatures (Fig. S3A; Table S3E). These alterations were only detected in *IDH* wt and absent in *IDH* mut glioma TANs (Table S3F-G). We did not observe any

overlap between BrM and glioma TANs regardless of mutational status (Fig. 3B), which was corroborated by PCA, with glioma TANs clustering with non-tumor brain neutrophils, separate from BrMs (Fig. 3D). We then extracted a core DEG signature distinguishing BrM from glioma TANs by applying a stringent filtering process to intersect DEGs identified when comparing BrM *vs.* glioma TANs (disease-specific alterations), with DEGs in TANs *vs.* matched blood PBNs (tissue-specific alterations). While only 30 genes were higher in glioma TANs, 247 were BrM TAN-specific (Fig. 3E, S3B-C; Table S3H-I), and again substantially enriched in pro-inflammatory signaling pathways, most prominently TNF-α signaling (Fig. 3F; Table S3J).

We next compared our data with publicly available single-cell RNAseq (scRNAseq) datasets of human TANs in primary lung cancer (122) and melanoma-BrM (125). Gene expression signatures of pro-inflammatory and tumor-specific neutrophil clusters N4-5 identified by Zilionis and colleagues were particularly enriched in lung-BrM TANs (Fig. 3G), potentially indicating similarity between lung cancer and lung-BrM TMEs. A comparison with the melanoma-BrM scRNA-seq dataset showed that glioma TANs are enriched in genes associated with interferon responsive clusters (Fig. S3D), whereas BrM TANs associate with more pro-inflammatory IL-8- and calprotectin-high clusters (Fig. S3B). This integration underscores the transcriptional heterogeneity of TANs between, but also within gliomas and BrMs, suggesting the presence of various subsets within each tissue.

Together, these analyses indicate that in addition to the brain tissue environment, the local TME imprints a further layer of alterations onto TANs, which is more pronounced in BrMs compared to gliomas, and predominantly characterized by inflammatory signaling.

Reactive oxygen species (ROS) release is elevated in circulating neutrophils from BrM-bearing patients, and is abrogated in the brain TME milieu

Given the pronounced phenotypic and transcriptional differences between PBNs and TANs, we next queried whether these alterations convey functional consequences. We thus examined the capacity of isolated PBNs and TANs to produce ROS – a

hallmark property of activated neutrophils, associated with tumor cell killing (108, 109, 114) and T-cell suppression (115, 117). Interestingly, in functional assays, we found that BrM PBNs released more ROS compared to glioma and HD PBNs (Fig. 4A-B, S4A). Confirming this result, BrM PBNs (but not glioma PBNs) showed a positive enrichment score for transcriptional pathways associated with augmented ROS production compared to HDs (Fig. S4B, highlighted pathways in dark grey).

By comparison, TANs isolated from both glioma and BrM samples produced substantially less ROS *vs.* matched PBNs (Fig. 4C). Consistently, brain TANs show pronounced dysregulation of genes related to ROS production and oxidative homeostasis (Fig. 4D). Most prominently, expression of *NCF1*, *NCF2* and *NCF4* (NADPH oxidase subunits) was decreased in TANs *vs.* PBNs, while constituents of potent antioxidant response mechanisms were induced (e.g. glutathione pathway members *GCLC*, *GCLM*, *GPX3*, *GPX8*; peroxiredoxins *PRDX1*, *PRDX2*, *PRDX4*; and superoxide dismutase subunits *SOD1*, *SOD2* and *SOD3*). When we separated TANs ($CD66B^+$) from the rest of the TME milieu (i.e. CD66B-neg cells), ROS levels were increased immediately (Fig. 4E), suggesting a partially reversible, transient component to the ROS impairment. Consequently, we found that TAN ROS release significantly increased in response to phorbol 12-myristate 13-acetate (PMA), a potent driver of neutrophil ROS production, and this activation overcame the CD66B-neg TME-driven ROS inhibition (Fig. 4E), albeit not to the same extent as for PBNs. To model PBN entry into the brain TME via *ex vivo* culture, we co-incubated PBNs or TANs with the matched CD66B-neg TME, which confirmed an immediate and cell ratio-dependent inhibition of ROS release (Fig. 4E, S4C). In sum, these functional data show that the brain TME milieu can counteract neutrophil ROS release. Given that ROS acts as a potent cytotoxic agent (108, 109, 114), its neutralization may represent a fast-acting defense mechanism of the brain TME, resulting in pro-tumorigenic effects in both gliomas and BrMs.

TANs associate with regulatory T cells and PD-1^+ $CD8^+$ T cells

We next assessed whether neutrophils from brain tumor patients differentially modulate T-cells by measuring their cytokine production in coculture with PBNs or

TANs. Interestingly, TANs promoted the secretion of cytokines associated with a regulatory T-cell (Treg) phenotype in tumor-infiltrating T-cells (TILs) (Fig. 4F) and matched peripheral T-cells (Fig. 4G), while PBNs did not alter production of the factors analyzed. By contrast, and in parallel with elevated expression of PD-L1 (Fig. 2A), TANs did not induce any secretion of cytotoxic T-cell cytokines (Fig. S4D-E). Therefore, we investigated the spatial relationship of TANs ($CD45^+$ $CD15^+$) and T-cells *in situ* using sequential IF. Interrogating *IDH* wt gliomas and BrMs, we found that T-cells are in closer proximity to TANs compared to the average distance of all cells to this population, as indicated by the red line (Fig. 4H, $p < 0.0001$; Fig. S4F). $CD4^+$ T helper cells ($CD45^+$ $CD3^+$ $CD4^+$ $CD8^-$ $FOXP3^-$), followed by Tregs ($CD45^+$ $CD3^+$ $CD4^+$ $CD8^-$ $FOXP3^+$), reside closest to TANs (Fig. 4H). As proximity between cells is only suggestive of potential interactions, we also assessed the expression of PD-1 and PD-L1 on $CD8^+$ T-cells ($CD45^+$ $CD3^+$ $CD4^-$ $CD8^+$ $FOXP3^-$) and TANs, respectively. This revealed that PD-$L1^+$ TANs (~52% of TANs express PD-L1) are indeed located closest to PD-1^+ $CD8^+$ T-cells (Fig. 4I, S4G-H), and the most abundant PD-L1+ cell type in the PD-1^+ $CD8^+$ T-cell niche are in fact TANs (Fig. 4J). Together, this is consistent with an immunomodulatory activity of TANs via Treg association and PD-1/PD-L1 engagement on $CD8^+$ T-cells in both *IDH* wt gliomas and BrMs.

The brain TME has both transient and permanent effects on neutrophils and extends their lifespan

Given the pronounced phenotypic and transcriptional alterations we observed in brain TANs compared to PBNs, and their potential immunosuppressive functions, we considered it critical to assess their longevity and transit time in the brain TME. While neutrophils are generally considered short-lived cells, a recent study revealed that murine neutrophils in certain organs have a substantially longer half-life/transit time than in blood (79). Here, we analyzed the numbers of live human TANs cultured *ex vivo* in tumor microenvironmental cultures (MECs) over time and observed that up to 80% of TANs survive for 24h, and up to 20% remain alive even after 48h, which is similar across all brain tumor types (Fig. 5A, S5A). As expected, considerably fewer viable PBNs remain at 24h and almost all PBNs die within 48h (Fig. 5A, S5A). Interestingly, however, PBNs cultured within the CD66B-neg TME exhibit significantly

increased survival, reaching a similar level to TANs (Fig. 5A), and indicating that the TME modulates neutrophil longevity. Critically, separating TANs from the TME milieu abrogated this effect (Fig. S5B), underscoring the importance of TME-supplied factors.

Neutrophils are continuously released from the bone marrow in vast numbers (75, 177, 178); thus, programmed cell death and a tightly regulated aging program are critical to maintain homeostasis. We therefore assessed PBN lifecycle stage at 24h, via Annexin V/DAPI staining, which showed that PBNs cultured within TME MECs remain alive/pre-apoptotic for longer compared to PBNs cultured alone (Fig. 5B). Corroborating these *ex vivo* findings, a pronounced number of pro-apoptotic genes were down-regulated in TANs *vs.* PBNs in both BrMs and gliomas, and conversely, several anti-apoptotic genes were induced in BrM-TANs (Fig. 5C).

Considering the limitations of assessing neutrophil lifespan *ex vivo,* we next utilized a neutrophil fate-mapping mouse line (iLy6G^{tdTomato}) (79) to investigate neutrophil decay *in vivo*; the first time this has been addressed using preclinical cancer models. The fully immunocompetent tumor models we analyzed closely reflect the shift in abundance and phenotype of TANs in BrMs and gliomas as observed in humans (Fig. S5C-D). In both murine models of BrM and GBM, we indeed observed a trend towards longer mean lifetimes of brain TANs compared to healthy brain neutrophils (Fig. 5D-E). Interestingly, among BrM and GBM TANs, a subset of neutrophils showed a further prolonged maximum lifespan, indicating that a larger fraction of aged neutrophils may persist within the brain tumor niche (Fig. S5E). Importantly, the presence of a growing tumor did not alter neutrophil lifespan in any of the peripheral organs assessed, including blood, consistent with our results for human neutrophils *ex vivo* (Fig. S5F).

Having confirmed that brain TAN lifespan is prolonged both *in vivo* and *ex vivo,* in mouse and human respectively, we next queried whether human TANs display signs of overall aging (i.e., physiological circadian priming) (172, 179). Indeed, we found that TANs have increased CD62L shedding, low CXCR2, and modestly higher expression of CXCR4 *vs.* PBNs (Fig. 2A, S2A, S5G). Culturing PBNs for 24h within a CD66B-neg TME milieu broadly recapitulated the TAN phenotype (Fig. 5F). However, while some

alterations were age-dependent and induced in 24h-old PBNs in the presence or absence of the TME (e.g. CD62L, CXCR4, CXCR2, S100A9), others were modulated by the TME independent of age (e.g. CD66B, PD-L1) (Fig. 5F). Interestingly, TANs maintain all their phenotypic alterations even when isolated from the TME (Fig. S5H). The partially age-related transition of PBNs to TANs was further confirmed through an unbiased approach: trajectory analysis on single cells analyzed for 10 TAN phenotype markers (by FCM) demonstrated that PBNs cultured for 24h in CD66B-neg TME converge with TANs (black arrow). PBNs alone, by contrast, follow a separate trajectory over time (Fig. 5G, red arrow). Interestingly, both increased longevity and TAN phenotypes were also induced in HD-PBNs when cultured in the presence of conditioned media (CM) from 24h MECs from different brain tumors (Fig. 5H-I). Similarly, BrM MEC-CM suppressed the levels of PBN-released ROS to a similar extent as diphenyleneiodonium (DPI), a ROS production inhibitor. This effect was rescued by the addition of PMA (Fig. 5J). Together this implicates soluble factors as the main mediators of these processes and indicates combined mechanisms of transitory and permanent alterations, which appear partially linked to the persistence of neutrophils in the brain TME.

Secreted factors, mostly produced by myeloid cells, modulate TAN phenotype and lifespan

We next asked which TME populations are the major drivers of these alterations. First, we characterized the cellular composition of *ex vivo* MEC cultures. At 24h, $CD45^-$ cells and all major immune populations were still present (Fig. 6A-B), with a gradual reduction in absolute cell counts that was more pronounced for $CD45^-$ cells, MG and MDMs *vs.* $CD4^+$ and $CD8^+$ T-cells (Fig. S6A) – but overall indicating that all populations can potentially contribute to the effects observed *in situ* and upon exposure of PBNs to MEC-CM *ex vivo*. As $CD45^-$ cells, comprising mostly tumor cells, were the most abundant cells in 24h MECs (Fig. 6A), we considered them a likely driver of neutrophil alterations. We therefore derived cell lines from MECs, which were confirmed by whole exome sequencing analysis to represent tumor cells (Fig. S6B-C). These lines enabled interrogation of the effect of soluble factors released exclusively by tumor cells on neutrophils. Interestingly, when culturing HD PBNs in CM from tumor cell lines

(TCM), we did not detect any lifespan extension, contrasting with the matched MEC-CM (Fig. 6C). We thus next assessed whether CM derived from either tumor-naïve $CD45^-$ cell types (i.e. human brain microvascular endothelial cells (HBMEC), human umbilical vein endothelial cells (HUVECs) and astrocytes (HA)) and *in vitro*-derived unpolarized HD MDMs (non-TCM), confers the capacity to prolong neutrophil survival. Interestingly, only HBMEC-CM induced prolonged lifespan to some extent, indicating that this is in part a brain endothelial-specific effect (Fig. S6D). Furthermore, neither TCM nor non-TCM recapitulated the complete phenotypic transition of neutrophils induced by MEC-CM (Fig. 6D, S6E). However, it is important to note that these tumor naïve $CD45^-$ cell lines, and HD *in vitro*-derived MDMs, can be transcriptionally distinct from their brain tumor-associated counterparts as shown for MDMs (49). Taken together, these results indicate that tumor cells (alone) are not the major sources of factors driving neutrophil alterations, but rather other brain microenvironment-educated populations.

To identify such factors, we performed a 1000-protein array analysis on a panel of 24h MEC-CM ($n_{IDH\ mut}$=2, $n_{IDH\ wt}$=3, n_{BrM}=9), matched TCM ($n_{IDH\ mut}$=1, $n_{IDH\ wt}$=3, n_{BrM}=2), and non-TCM (HBMEC, HA, MDM) compared to media alone (control). Using an unsupervised clustering approach, MEC-CM overall clustered separately from TCM, non-TCM, and control media, except for one outlier (Fig. S6F). Most BrM-MEC clustered closely together, with some distinction from glioma-MEC. Subsetting for upregulated protein expression *vs.* control, and significant differential expression between CM types, revealed 57 MEC-specific proteins (Fig. 6E). Of these, 51 were enriched in MEC-CM compared to both TCM and non-TCM (Fig. S6G; Table S4), thereby representing potential contributors to TAN alterations.

By applying interaction network analysis to MEC-specific upregulated proteins, several clusters were identified, centered on a highly interconnected pro-inflammatory cytokine group (Fig. 6F). TNF-α, a potent recruiter and activator of neutrophils (180, 181), is at the core of this cluster (Fig. 6F-G). Interestingly, when HD PBNs were exposed to TNF-α they showed a more TAN-like phenotype compared to their untreated counterparts, including CD11B/66B upregulation and CD62L shedding (Fig.

6H). Moreover, a TNF-α signaling readout was enriched in the brain neutrophil-specific signature (Fig. 3A), in BrM and glioma TANs *vs.* matched PBNs (Fig. S6H), and even more pronounced in BrM-TANs *vs.* gliomas (Fig. 3F). However, not all phenotypic alterations in the PBN-to-TAN transition were induced by TNF-α treatment alone (e.g. CXCR2, CXCR4; Fig. 6H), indicating that multiple factors combine to sculpt the TAN phenotype. In connection with our findings above (Fig. 5J; 6C), we also detected Ceruloplasmin (CP), GLO-1 and IL-9 at high levels in MEC-CM (Fig. 6G), which are important regulators of reduced ROS production (182-184) and prolonged neutrophil lifespan (185). Additionally, we observed high expression of the major neutrophil chemoattractant CXCL8 in MEC-CM specifically (Fig. 6G).

We next queried the major brain TME populations via bulk RNAseq to identify which cell types produce these factors. This revealed the myeloid compartment, including MDMs, MG, and TANs themselves, as the highest expressers of most MEC-specific pro-inflammatory cytokines (Fig. 6I). Three myeloid-specific clusters emerged: i) Proinflammatory factors produced mainly by TAMs (e.g. *TNF, IL6, IL10*); ii) factors associated with recruitment and myeloid activation produced predominantly by neutrophils (e.g. *CXCR2, IL9, IL11*); and iii) activating/recruitment factors produced by the entire myeloid compartment (e.g. *MMP10, MMP12, CXCL8, S100A8, S100A9, S100A12*) (Fig. 6G, 6I). The TAM-specific inflammatory cluster was of interest as it contains many factors also found at the core of the secreted protein network (Fig. 6F, I), suggesting a key role in shaping the MEC-CM. By contrast, and consistent with our TCM experiments, the $CD45^-$ population does not appear to be an important source of these cytokines specifically; however, it is a major producer of extracellular matrix-associated factors (Fig. 6I). Together, this led us to consider that the myeloid compartment is a predominant source of soluble factors driving brain-TAN alterations.

Neutrophils interact predominantly with the myeloid compartment and the brain vasculature

To next dissect the interactions within the myeloid compartment, we assessed whether TANs have a close spatial relationship with TAMs. Both TANs (Fig. 1D-G) and TAMs (49) are predominantly localized in the PVN, however their spatial orientation in

relation to each other has not been studied to date in brain tumors. In a cohort of *IDH* wt glioma and BrM tissue samples we quantified the cell types present in a radius of 20 µm around TANs, using sequential IF staining. We observed that TANs predominantly interact with other TANs both inside and outside the PVN (Fig. 7A, B). Interactions with tumor cells were mostly observed in the non-PVN area. By contrast, MG and MDMs represent the most abundant non-TAN immune cells close to TANs, particularly in the BrM PVN, where they account for ~20% of the cellular neighborhoods (Fig. 7B). Querying our RNAseq data for factors involved in neutrophil recruitment (Fig. 7C*)*, we found that TANs and TAMs show the highest expression of these chemokines compared to other TME populations, with a progressive increase in more malignant tumor types (*IDH* wt gliomas and BrMs). Taken together, this further corroborates a tightly interactive network within the myeloid cell niche of brain tumors.

Considering the proximity of TANs to the vasculature (Fig. 1D-G), and our finding that HBMECs prolong PBN survival (Fig. S6D), we investigated the relationship between TANs and vessels. We first characterized the phenotype of vessels containing TANs in the PVN compared to those lacking TANs, based on two phenotypic measurements: (i) size, and (ii) form factor, indicating their degree of circularity (Fig. S7A). As described in the literature, larger and more deformed vessels (with a form factor <1) tend to be less functional and more leaky (186, 187). Especially in the brain, where the BBB tightly regulates molecular and cellular transport under homeostatic conditions, the development of leaky vessels can substantially impact the influx of cells (9). Interestingly, we found that vessel form factor decreases in *IDH* wt gliomas and BrMs, with vessels having TANs in their PVN showing an even higher degree of deformity (Fig. 7D, S7B). Additionally, TANs preferentially localized within the PVN of larger vessels (Fig. S7C), and these findings were irrespective of tumor type.

Neutrophils have long been appreciated as important regulators of angiogenesis in tumors (188), as well as healthy (189) and inflammatory brain tissue (190, 191). However, studies investigating their potential role in brain tumor angiogenesis are lacking. Interestingly, we detected significant enrichment of the Hallmark angiogenesis pathway in both glioma and BrM TANs *vs.* matched PBNs (Fig. 7E-F). Expression of

various canonical pro-angiogenic genes (e.g. *VEGFA, THBD*, *ICAM1*) was higher in TANs compared to other TME populations (Fig. S7D). At the protein level, we found that the angiogenesis-associated protein S100A9 (192) was enriched in TANs *vs.* PBNs (Fig. 2A, FCM data). Interestingly, MMP9, an important VEGF-associated pro-angiogenic metalloprotease (193), was detected at lower protein levels (Fig. 2A), potentially indicating its extracellular release. Of note, *MMP9* mRNA levels were highly elevated in TANs compared to other TME populations, designating them as a major MMP9 source in brain tumors (Fig. S7D). Moreover, we detected a significant correlation between the degree of vessel deformity and the expression levels of several of these genes in matched samples in TANs (Fig. 7G), MG, and MDMs (Fig. S7E). Together, these findings support important roles for the myeloid compartment in promoting aberrant angiogenesis in gliomas and BrMs, and potentially via distinct pathways in each specific myeloid cell population.

7.3.4 Discussion

In this study, we have analyzed the phenotypes and functions of neutrophils across diverse human brain tumors, comprising >190 clinical samples in total. By interrogating neutrophils in the periphery (PBNs) and the tumor (TANs), we found that brain TANs are highly abundant in *IDH* wt gliomas and BrMs and have a robust inflammatory phenotype compared to PBNs. Interestingly, independent of tumor type, and even in the absence of a tumor, PBNs which infiltrate into the brain adapt to this unique organ microenvironment. The type of brain tumor confers additional, more pronounced transcriptional alterations, with BrM TANs showing the most notable differences, including enrichment in multiple pro-inflammatory signaling networks. This discovery that the disease-specific TME imprints a unique layer of alterations onto TANs, in addition to brain tissue-driven changes, shows interesting parallels to analyses of other TME populations including MG/MDMs (49, 50, 194) and T-cells (Wischnewski et al., manuscript in preparation; (195)). Our findings thereby underscore the necessity to not only investigate neutrophils within the specific organ of interest, but also by additional stratification into distinct tumor subtypes.

We addressed how the brain TME drives the observed TAN alterations, phenotypes, and functions, through a series of *ex vivo* assays and spatial analyses of patient samples, in parallel with interrogation of neutrophil behavior in mouse models. We found that one notably pronounced effect of the brain TME on neutrophils in direct contact, and via soluble factors, is the increased lifespan of TANs compared to matched PBNs. We also showed that secreted factors in the brain TME milieu can mimic the TAN phenotype and block the production of ROS by PBNs, consistent with suppression of these potentially damaging oxidative species within the brain microenvironment. By interrogating potential soluble drivers of the various brain TAN phenotypes identified, we uncovered predominantly pro-inflammatory mediators, most notably TNF-α. Given that the brain TME is rich in secreted TNF-α, and with TANs (especially in BrM) showing a clear elevation of TNF-α signaling pathways, our data indicate that this cytokine is a critical mediator of the complex multifactorial neutrophil alterations we have revealed. Indeed, in *ex vivo* assays, we found that TNF-α stimulation of healthy donor PBNs can recapitulate a substantial proportion of TAN phenotypes.

Spatial interrogation of the complex brain TME enabled the identification of perivascular and myeloid cell niches, in which TANs interact with these specific cell types. Within the myeloid niche this is predominantly driven by TNF-α signaling, and the active recruitment of neutrophils into the brain. TANs are also enriched in pathways critical for angiogenesis and closely associated with deformed tumor vessels, which likely contributes to the continuous influx of cells from the peripheral circulation. Indeed, extension of these analyses, in combination with interrogation of secreted cytokines, added a further level of complexity - with TANs showing differential interactions between regulatory T-cells and cytotoxic T-cells, indicative of critical immune suppressive mechanisms at play within the brain TME.

In summary, this study reports the first in-depth and multifaceted interrogation of TANs across a large panel of diverse human brain tumors. This has revealed extensive pro-inflammatory alterations of neutrophils within the brain tumor milieu, which is associated with T-cell suppressive and pro-angiogenic phenotypes. Moreover, we also

present the first *in vivo* analyses of neutrophil dynamics in cancer, taking advantage of neutrophil-reporter mice (79) and multiple immune-competent brain cancer models. Together, these findings indicate the potential benefit of targeting soluble mediators that dictate the pro-inflammatory TAN phenotypes in brain cancers. Future studies, including in preclinical models, will be of considerable interest to investigate the efficacy of such therapeutic approaches.

7.3.5 Acknowledgments

We would like to thank the Departments of Neurosurgery, Neuro-oncology, and Pathology at CHUV Lausanne, Drs. Leire Bejarano and Florian Klemm, members of Prof. Hegi's lab, and Prof. Ron Stoop for generous collaboration in obtaining and processing patient samples. We thank Dr. Spencer Watson and Paola Guerrero for insightful advice on QuPath image quantification. We gratefully acknowledge all current and former members of Prof. Joyce's lab, members of the laboratories of Prof. Tacchini-Cottier (UNIL), Prof. Meylan (EPFL/ULB), Prof. De Palma (EPFL), and Prof. Petrova (UNIL), for insightful discussions and advice. We thank V. Noguet Brechbühl (Mouse Pathology Facility) for expert preparation of tissue sections; all members of the Epalinges and Agora animal facilities; P. Baumgartner, A-C. Thierry (Center of Experimental Therapies) for advice and technical support on multiplex cytokine arrays; all members of the UNIL Flow Cytometry Facility for expert guidance designing panels and performing FAC-sorts. This research was supported by the Breast Cancer Research Foundation, Carigest Foundation, Fondation ISREC, Ludwig Institute for Cancer Research, Swiss Bridge Award, and University of Lausanne (to J.A.J.). K.S. was supported in part by an Erwin-Schrödinger Fellowship from the Austrian Science Fund (FWF, J4343-B28); S.G. was supported by Fondation Leenaards and is currently supported in part by a Fondation ISREC fellowship; M.M. was supported by funding from the AIRC and European Union's Horizon 2020 research and innovation programme under the Marie Skłodowska Curie (grant agreement 800924); A.A-P. was supported by an EMBO Long-term Postdoctoral Fellowship (EMBO ALTF 654-2019) and is currently supported in part by a Marie Skłodowska Curie Actions Individual Fellowship (MSCA-IF 890933). G.F.C. is supported by MCIN/ AEI/10.13039/501100011033 (grant PID2019-110895RB-I00) and by Junta de

Comunidades de Castilla-La Mancha (SBPLY/19/180501/000211). A.H. is funded by FET-OPEN (no. 861878) from the European Commission. The CNIC is supported by the MCIN and the Pro CNIC Foundation and is a Severo Ochoa Center of Excellence (CEX2020-001041-S). Our particular gratitude is extended to all patients and healthy volunteers who generously donated tissue for analyses, and without whom this study would not have been possible.

7.3.6 Author Contributions

Conceptualization, R.R.M., K.S., and J.A.J.; Methodology, R.R.M., K.S., S.G., M.K., and G.F.C.; Formal Analysis, R.R.M., N.F., A.F.A.P., J.Lo., R.M., P.W., and G.F.C.; Investigation, R.R.M., K.S., S.G., M.K., D.C., M.M., A.F.A.P., D.N.M., J.Li., and V.W.; Visualization, R.R.M., N.F., S.G., and K.S.; Writing - Original Draft, R.R.M., K.S., S.G., and J.A.J; Writing – Review & Editing, all authors reviewed, edited or commented on the manuscript; Funding acquisition, J.A.J., R.R.M., and K.S.; Resources, A.H., I.B., A.F.H., J.P.B., R.T.D., and M.E.H.; Supervision, J.A.J.

7.3.7 Declaration of Interests

R.R.M., K.S., N.F., S.G., M.K., D.C., M.M., J.Lo., A.F.A.P., D.N.M., J.Li., V.W., R.M., G.F.C., P.W., I.B., A.F.H., J-P.B., R.T.D. none; P.W. has provided consulting for Almax, Bayer, Sanofi and Genentech. A.H. is a paid consultor for Flagship Pioneering, Inc. for matters unrelated to this study; M.E.H. has an advisory role at TME Pharma (formerly NOXXON Pharma AG); J.A.J. has received honoraria for speaking at research symposia organized by Bristol Meyers Squibb and Glenmark Pharmaceuticals, and currently serves on the scientific advisory board of Pionyr Immunotherapeutics.

7.3.8 Methods

Resource availability:

Lead contact

Further information and requests for resources and reagents should be directed to and will be fulfilled by the lead contact, Prof. Johanna Joyce (johanna.joyce@unil.ch).

Data and code availability

Bulk RNA-seq count data generated, and used for this study, can be queried and downloaded at (shinyapp link). Due to protective legislation regarding patient privacy, the raw RNA-seq data can only be shared by the lead contact upon request. This paper does not report original code.

Experimental model and subject details:

Human subjects

All procedures in this study involving the use of tissues derived from human participants were in accordance with the ethical standards of the national research committees and the declaration of Helsinki.

For detailed information related to the cohort of human participants, please see Table S1A-B. Informed consent was obtained for all human subjects participating in this study. The processing of non-tumor and tumor tissue at the Biobank of the Brain and Spine Tumor Center (BB_031_BBLBGT) at the Centre Hospitalier Universitaire Vaudois (CHUV, Lausanne, Switzerland), was approved by the Commission cantonale d'éthique de la recherche sur l'être humain (CER-VD, protocol PB 2017-00240, F25 / 99). Similarly, the processing of tumor tissue at Memorial Sloan Kettering Cancer Center (MSKCC, New York, NY, USA) was approved by the institutional review board (IRB, protocols #IRB #06-107, #14-230). Non-tumor brain surgeries were performed on patients with therapy-resistant focal epilepsy, as part of the clinical management. Brain tumor resections were performed to either aid in diagnosing the origin of the lesion or as part of the therapeutic strategy. Diagnostic identification of the brain (tumor) tissue was performed by a trained pathologist as part of the standard of care at the CHUV or MSKCC.

Matched blood of brain tumor patients was collected at the time of the brain surgery as part of the ethical permit stated above (CER-VD, protocol PB 2017-00240, F25 / 99). Whole blood collection from identified healthy donor volunteers was approved by CER-VD (protocol 2018-00492). Buffy coats from anonymous voluntary donors were

obtained from the Transfusion Interrégionale, Croix-Rouge Suisse (Epalinges/Lausanne, Switzerland).
All tissue specimens used were coded before further handling in this study in accordance with patient privacy regulations.

Primary cell cultures

Human

Brain tumor-derived cell lines were generated by plating single-cell suspensions of dissociated tumors in a cell culture flask at a density of 2 x 10^6 cells per ml in DMEM-F12 (1:1) +Glutamax (Gibco) +10% FCS (Gibco) +1% penicillin/streptomycin (P/S, Gibco) in an incubator at 37°C and 5% CO_2. Cells were passaged using 0.05% Trypsin-EDTA (Gibco) once the cells reached 70% confluency in the cell culture flask. Cell lines were validated using whole exome sequencing (WES) of both snap frozen tumor tissue and matched tumor cell lines.

Primary human astrocytes (HA, Cat.no. #1800) and human brain microvascular endothelial cells (HBMEC; Cat.no. #1000) were purchased from ScienCell and cultured according to the vendor's instructions. Human umbilical vein endothelial cells (HUVECs) were kindly provided by the laboratory of Prof. T. Petrova, and were cultured in DMEM-F12 (1:1) +GlutaMAX +10% FBS +1% P/S. Healthy donor monocyte-derived macrophages (MDMs) were derived from peripheral blood mononuclear cells (PBMCs) from buffy coats, isolated using a Ficoll (GE) gradient and SepMate tubes (StemCell). Monocytes were selected using MACsorting by CD14 MicroBeads (Miltenyi) and differentiated into macrophages by culture in Teflon-coated bags (OriGen) for 7 days in DMEM-F12 (1:1) +GlutaMAX +10% FBS +1% P/S with the addition of 10 ng/ml recombinant human CSF-1 (R&D Systems).

Murine

To generate murine breast-to-brain metastasis (BrM) a brain-homing breast tumor cell line, MMTV-PyMT (murine mammary tumor virus; Polyoma middle T antigen)-BrM3, was used (C57BL/6J background) (Croci et al., *manuscript in revision*). This cell line was initially derived from a murine breast-to-lymph node metastasis and consequently passaged three times *in vivo* for brain-homing capacity via intracardiac injections. The

PyMT-BrM3 cell line was maintained in DMEM-F12 (1:1) +GlutaMAX medium +10% FCS +1% P/S and passaged using 0.05% Trypsin-EDTA once the cells reached 70% confluency.

Transfected DF1 chicken fibroblasts

DF1 chicken fibroblasts (ATCC), which were previously transfected with an RCAS viral vector expressing PDGFB-HA or a short hairpin against murine p53 (shP53) were kindly provided by Dr. Tatsuya Ozawa and Dr. Eric Holland (196, 197). The PDGFB-HA and p53 DF1 cells were cultured in DMEM (Life Technologies) supplemented with 10% fetal bovine serum (Life Technologies) under standard conditions.

Mouse models

All experiments performed in this study were approved by the local Institutional Animal Care and Use Committees of the University of Lausanne and the Canton Vaud, Switzerland (protocol numbers VD3314, VD3444, VD3688). Experiments involving the development of breast-BrM tumors were performed in 6–10-week-old female *Ly6G*^{CreERT2} mice in a C57BL/6J background (79). Experiments involving the development of gliomas were performed in 4.5-7-week-old male and female *Ly6G*^{CreERT} C57BL/6J mice bred to Nestin-Tv-a mice (198) (generously provided by Dr. Eric Holland). All mice were housed in the Agora In Vivo Center (AIVC) animal facility in individually ventilated cages. Mice were held under a 12-hour light/dark schedule at 22°C, in the presence of 2-5 cage mates. Standard autoclaved lab diet and water were provided.

Methods details:

Human brain (tumor) enzymatic digestion

Single cell suspensions of human non-tumor and brain tumor tissue were obtained after enzymatic digestion as described in (162) (Module 2). Single cell suspensions were used for flow cytometric (FCM) analysis, bulk-RNAseq after FAC-sorting, *ex vivo* functional analysis as well as the generation of tumor-derived cell lines.

Flow cytometry and FAC-sorting

FCM and FAC-sorting were performed as described in (162) (Module 2a). Validation of the sorting purity (>97%) was assessed by re-acquisition of FAC-sorted populations by FCM (162). Technical consistency of the flow cytometer setup, allowing for comparison of data across different timepoints, was ensured by saving a baseline measurement on the flow cytometer used on the first day of acquisition. On consecutive dates, the baseline was reloaded and adapted based on the read-out of the acquired CS&T beads in the different channels, maximizing a consistent read-out.

Immunofluorescence staining of tissue sections

Human tissue was frozen in optimal cutting temperature (OCT) compound (Tissue-Tek, Sakura Finetek) as described in (162) (Module 1). 10-um thick frozen sections were used for both standard single round immunofluorescence (IF) staining, as well as sequential IF. Standard single round IF was performed on non-tumor brain tissue, *IDH* mut and wt gliomas, and BrMs, and described in (162) (Module 1). For sequential IF up to 7 rounds, frozen tissue slides from *IDH* wt gliomas and BrMs were used. Slides were air-dried for 20-30 min, prior to fixation in 10% Neutral Buffered Formalin (Fisher Scientific, Epredia^{TM} 5701, Cat. No. 22-050-104) for 40 min at RT. Slides were rehydrated and washed 3x 5 min in PBS (Gibco) while gently rocking. A ring was drawn around the tissue using a hydrophobic pen. Potential autofluorescence signal was quenched by adding 100 ul glycine 10mM (Panreac Applichem ITW reagents, A1067) diluted in PBS for 10 min at RT. Slides were washed 2x 5 min in PBS-0.2%Tween (Applied Chemicals). Tissue was permeabilized with PBS-0.2%Triton (Applied Chemicals) for 10 min at RT and sequentially washed 2x 5 min with PBS-0.2%Tween. The slides were incubated with blocking buffer (1x Blocking Reagent (PerkinElmer, cat. no. FP1012; 'PNB') + 0.5% Tween + 10% normal donkey serum (SigmaAldrich, cat.no. S30-M) + 2% BSA (Jackson ImmunoResearch, cat.no. 001-000-162)) filtered through a 0.22-um filter, for 1 hour in a humidified chamber. Primary antibodies (see Table S5 for the antibodies used) were diluted in antibody dilution buffer (1x PNB + 0.5% Tween + 10% normal donkey serum; 0.22-um filtered before use) for 3 h in a humidified chamber on a shaker at RT. Then slides were washed 3x 5 min, before adding fluorophore-conjugated secondary antibodies and a nuclear detection marker 4', 6- Diamidino-2-Phenylindole, Dihydrochloride (DAPI, Life technologies, D1306) in

antibody dilution buffer to the slides (see Table S5 for the antibodies used). Slides were placed in a humidified chamber for 1 hour at RT. Staining with secondary antibodies alone was used as the control. The slides were washed 6x 10 min with PBS-0.2%Tween, and a final wash was performed with PBS. 20 ul SlowFade Diamond Antifade Mountant media (Invitrogen, S36972) was added to each tissue and a coverslip (Menzel-Gläser) was carefully placed on top. The fluorescent signal was acquired using the Axio Scan.Z1 slide scanner (Zeiss), with a Colibri 7 LED light source (Zeiss) and a Plan-Apochromat 20x/0.8 DIC M27 cover slip-corrected objective (Zeiss). Once acquisition was completed, the coverslip was carefully removed by leaving the slide upright in PBS to let the coverslip slide off. The slides were washed 3x 5 min in PBS, prior to elution in freshly prepared tris(2-carboxyethyl)phosphine (TCEP)-based elution buffer (0.5 M glycine + 3 M guanidium chloride (Carl Roth, 0037.1) + 2 M urea (Panreac Applichem ITW reagents, A1360) + 40 mM TCEP (Sigma, C4706) in ddH_2O) for 5 min on a rocker at RT (199). Finally, slides were washed 3x 5 min in PBS-Tween, before restarting the staining process by returning to adding blocking buffer to the slides, and following all the steps detailed above.

Image analysis and cell type identification

Standard single-round IF: Image quantification was performed using the VIS Image Analysis software (Visiopharm) on preprocessed images applying ZEN software (stitching and z-stacking of the images). Cellular identification as well as perivascular niche (PVN) characterization were performed as described in (49).

Sequential IF: Image preprocessing was performed using ZEN software. The images of different rounds of staining were stitched, and background subtraction was performed using the rolling ball method with a radius of 75 (200). Using the signal obtained from single staining of the tissue with DAPI alone allowed for the subsequent subtraction of autofluorescence signal. Autofluorescence subtraction and alignment of the final image made from the sequential rounds of staining were performed in a Python library script (Watson, Joyce et al., *manuscript in preparation*).

Image quantification was performed using QuPath open-source image analysis software (201). Tumor tissue was detected within each sample using the “Pixel

classifier" command. First, a training image made of single regions of interest (ROIs) drawn in each sample was generated. The "Pixel classifier" was trained on these images, using a positive detection class for tissue detection. Then, the trained pixel classifier was applied to the entire image dataset, followed by cleanup of the resulting binary image by morphological operations. Nucleus detection was performed by StarDist, a deep-learning-based method from Martin Weigert and Uwe Schmidt, using the dsb2018_heavy_augment.pb model (202). A cell expansion value of 3 was used and subsequently, area identification (PVN and vessels) was performed with the "Pixel classifier" command according to the same method described above. Finally, cell identification was performed using QuPath's "Object classifier" command. Training was performed on 40% of the ROIs and validated on the remaining 60%. A classifier was generated from one or several mutually exclusive markers. Training of the classifier was based on annotations (minimum 10 annotations per class). Selected features for training included all marker measurements. Composite classifiers generated from sequentially added classifiers were created to allow final cell identification. These classifiers were applied to the entire project and data export in .csv format for subsequent analysis in R and CytoMAP (203). Filtering of cells using a diameter size of > 4 um and < 12.5 um, detected nuclei probability > 0.65, as well as filtering of the relevant final cell populations, was performed in R.

Image quantification:

Nearest neighbor distance and neighborhood analysis of sequential IF data

Nearest neighbor distance from different T-cell populations and $CD8^+$ T-cells stratified by PD-1 expression to TANs in *IDH* wt gliomas and BrMs, was assessed using the spatstat R package (204). Neighborhood analysis of TANs was performed based on the occurrence of cells within a 20µm radius of the border of the nuclei, calculated using the radius of individual nuclei.

RNAseq analysis

Isolation of RNA was performed using chloroform extraction and isopropanol precipitations as previously described (49, 162). The SMART-Seq preparation kit (CloneTech) was used to generate RNA sequencing (RNAseq) libraries and

fragmented using the Nextera XT kit (Illumina). Sequencing of paired end, 100 or 150 base pair and single end 100 base pair, was performed by Genewiz (South Plainfield, New Jersey, USA) on an Illumina HiSeq 2500 (Illumina).

Alignment of RNAseq reads was performed using STAR v2.7.7a (205) and quantified using RSEM v1.3.3 (206). Human genome version 38 was used with GENCODE v36 annotation. Raw counts of transcripts with the same gene symbol were pooled. All genes were hierarchically clustered using Ward distance, and the expression heatmap was visually examined to identify a major branch containing a non-informative expression pattern. Non-protein coding genes, pseudogenes, predicted genes, genes with less than 1 FPKM in at least one sample in a sample group (tissue/disease group), and genes with low variance were filtered out. A total of 16,052 genes were retained and their expression was normalized between samples using the TMM method (edgeR version 3.32.1) and log2 transformed with voom (limma version 3.46.0). Batch effect was corrected for with ComBat (sva version 3.38.0). Differential expression was computed using limma (version 3.46.0). To reduce the potential bias introduced by any contaminating tumor cells ($CD45^-$ cells), genes with higher expression in the $CD45^-$ cells vs. neutrophils in the leading comparison group were filtered out if they additionally were found to be significantly differentially expressed in $CD45^-$ cells, $CD4^+$ T-cells or $CD8^+$ T-cells within the same comparison. Genes with p.adj value <0.05 and -1>LFC>1 are called significantly differentially expressed in all comparisons except when non-tumor brain (n=5) was one of the comparison groups, then genes with p-value <0.005 and -1>LFC>1 were called significantly differentially expressed. Pathway analyses (ORA and GSEA) were performed using clusterProfiler R package (version 3.18.1).

PBN and TAN isolation

Whole blood from healthy donors (HD) and patients was collected in BD Vacutainer tubes (BD 368861). Peripheral blood neutrophils (PBNs) were isolated using the MACSxpress Whole Blood Neutrophil Isolation Kit (Miltenyi, 130-104-434) according to the manufacturer's instructions, followed by red blood cell lysis for 10 min at RT (Biolegend, 00-4333-57, diluted to 1X in deionized water). Tumor-associated

neutrophils (TANs) were isolated from enzymatically digested human brain tumors using Magnetic-activated cell sorting (MACS) as described in (162) (Module 3). A positive selection method was applied using an anti-human CD66B-Biotin antibody (Miltenyi, cat. no. 130-118-983) combined with Anti-Biotin UltraPure beads (Miltenyi, cat. no. 130-105-637) allowing for magnetic extraction of TANs from the dissociated tumor.

Reactive oxygen species (ROS) detection

Isolated PBNs were resuspended at 5 x 10^6 cells/ml in starved media (DMEM-F12 w/o phenol red, Gibco, 21041-025) and 5 x 10^5 PBNs were plated in 100 ul per well in a white flat bottom 96-well plate (ThermoFisher, 136101). For PBN/TAN co-cultures, 5 x 10^4 neutrophils were plated per well and CD66B-neg TME cells were added at a ratio 5:1 in 100 ul final volume. Luminol (Sigma, A8511-5G) was added to a final concentration of 100 uM. Inhibition of ROS production by PBNs was achieved by adding diphenyleneiodonium chloride (DPI, Sigma, D2926-10mg) at a final concentration of 50 uM; stimulation of ROS production was achieved by adding phorbol-12-myristat-13-acetate (PMA, abcam, abb120297) at a final concentration of 4 uM. The plate was gently shaken prior to read-out by measuring all wavelengths in a luminescence plate-reader (Microplate reader Infinite® 200 PRO Tecan) at an interval of every 5 min for 2 h.

Mixed environmental culture (MEC)-conditioned media (CM) collection and characterization

The generation and collection of whole-tumor microenvironmental culture-conditioned media (MEC-CM) was performed as described in (162) (Module 3a). For the generation of MEC-CM for ROS detection, media without phenol red was used. The immune landscape of the MEC was characterized by FCM at 0h, 24h and 48h after the start of culture. Survival of immune populations over time was assessed by absolute viable cell counts using Trucount Absolute Counting Tubes (BD Biosciences, cat. no. 340334) by FCM.

Conditioned media (CM) generation from cell lines and primary cells

Tumor cell lines were derived from brain tumor MEC by plating 2 x 10^6 cells in a tissue flask as described above. Cells were passaged at least 3 times prior to CM collection and submission for validation by WES.

HBMEC (ScienCell, Cat. no 1000) were cultured in Endothelial Cell Medium (ScienCell, 1001) and HA (ScienCell, Cat. no 1800) were cultured in Astrocyte Medium (ScienCell, 1801) in accordance with vendor's recommendations. HUVECs were cultured in DMEM-F12 (1:1) +GlutaMAX +10% FBS +1% P/S. Cells were passaged when 70% confluency was reached. 0.25% Trypsin was added to the plates and trypsinization was stopped by adding Trypsin Neutralization Solution (ScienCell, 0113) according to manufacturer's instructions.

Differentiated MDMs from healthy donors were generated as described above and harvested from Teflon-coated bags at day 7, followed by plating at a density of 1 × 10^6 cells/well of a 6-well plate in DMEM +10% FBS +1% P/S.

For all cell lines, media was changed to complete media (DMEM +10% FBS + 1% P/S) when 70% confluency was reached. The supernatant was collected after 24h, spun at 300G for 10 min and stored at -80°C until further use.

MEC and CM education experiments

MEC, TCM and primary cell line CM were thawed at RT. Isolated PBNs from HD were resuspended in CM and plated at 1 x 10^6 cells/ml in U-bottom 96 well plates (Costar, Cat no. 3799). Cells were incubated at 37°C and 5% CO_2, until they were collected for phenotypic characterization by FCM (after 5-6 h) and cell survival assessment at 24h and 48h.

T-cell cytokine array

Peripheral $CD3^+$ T-cells were isolated from patient whole blood using the Easy HLA Chimerism Whole Blood CD3 positive selection kit (Stemcell, cat. no 17871) according to the manufacturer's protocol. 1 x 10^5 viable peripheral $CD3^+$ T-cells or 2.5 x 10^5 viable CD66B-neg TME cells were plated in complete media in a flat bottom 96 well-plate (ThermoFisher, Cat#136101), in the presence or absence of 1 x 10^5 PBNs/TANs in a final volume of 100ul. After 96 h, the plate was spun at 300G for 10 min, and the

supernatant collected and frozen at -20°C until further use. Supernatants were thawed at 4°C and diluted 2x in Assay Diluent (MSD, cat. no K151AEL-1). A customized 6-plex cytokine panel assay containing Granzyme B, IFN-y, IL-2, IL-10, IL-12p70 and TNF-α (U-PLEX Immuno-Oncology Group 1 (hu) assay, MSD, Cat. no. K151AEL-1) was performed according to the manufacturer's instructions. Cytokine detection was performed using the MESO QuickPlex SQ120 instrument (Meso Scale Discovery).

Annexin V apoptosis analysis

PBNs were cultured with whole tumor MEC at a ratio of 1:1 in complete media (DMEM-F12 + 10% FBS + 1% P/S) at 37°C and 5% CO_2. Cells were collected after 24h or 48h and incubated in PBS with Human TruStain FcX Fc receptor blocking solution (FC block; 1:100) (BioLegend) for 10 min at RT. The 2x concentrated FCM antibody mix was added to the cells for 15 min at 4°C in the dark (see Table S5 for the antibodies used). Cells were washed with 1x binding buffer (Invitrogen, Cat no. 00-0055-56) and stained with a 1:100 dilution of Annexin V-PE (Invitrogen, 12-8102-69) in binding buffer. The cells were incubated for 15 min at RT in the dark, before washing in binding buffer. Cells were resuspended in binding buffer containing 2 ug/ml DAPI.

Tumor mouse models

Breast-BrM model

For the development of breast-BrMs in immunocompetent mice, *Ly6G*^{CreERT2} mice were anesthetized using isoflurane inhalation (O_2 + 2% isoflurane) and shaved on their chest. Mice were placed with their back down on a heating pad, and 1 x 10^5 PyMT-BrM3 cells were injected in the left cardiac ventricle. Mice were monitored weekly by magnetic resonance imaging (MRI).

Glioma tumor model

4.5 to 7 week-old immunocompetent *Ly6G*^{CreERT};Nestin-Tv-a mice were used to generate primary brain tumors using the RCAS system as previously described (64, 207). In brief, mice were anesthetized using isoflurane inhalation (O_2 + 2% isoflurane), and a mixture of 0.5% bupivacaine (Carbostesin; Aspen Pharma Schweiz) and 2% lidocaïne (Streuli Pharma) was applied as a local analgesic (50 ul per mouse), and 0.3 mg/ml buprenorphine (Temgesic; Indivior Schweiz) was injected subcutaneously as a

systemic analgesic (100 ul per mouse). Using a stereotactic apparatus, transfected DF1 cells were injected into the right frontal cortex (2 mm frontal, 1.5 mm lateral from bregma, 2 mm deep. Mice were injected with a 1:1 mixture of PDGFB-HA and shP53 DF1 cells, for a total of 3 x 10^5 DF1 cells intracranially. The skin of the skull was sealed using Vetbond tissue adhesive (3M). The mouse was placed on a heating pad and monitored until fully recovered from anesthesia. Finally, Bepanthen cream (Bayer) was applied on the site of the incision prior to placing the animal back in the cage. Mice were carefully monitored, and tumor development was assessed by weekly MRI.

Tumor-bearing *Ly6G^{CreERT}* and *Ly6G^{CreERT}*;Nestin-Tv-a mice were injected intraperitoneally with 400 ul of 10 mg/ml Tamoxifen, 8-0 days prior to sacrificing to follow the decay of iLy6G TdTomato$^+$ neutrophils in different organs.

Mouse tissue analysis

Whole blood was collected from mice prior to sacrifice via the submandibular vein. Mice were euthanized by terminal anesthesia by intraperitoneal injection of pentobarbital (150 mg/kg) (CHUV Hospital, Lausanne, Switzerland), followed by transcardial perfusion with PBS. Spleen, femur, lungs and brain were resected from each mouse and placed on ice. Single cell suspensions of the different organs were obtained using the following methods: i) The spleen was smashed through a 70-um cell strainer. ii) The bone marrow was flushed out of the femur by cutting off the crown of the bone on one end, placing the bone upside-down into a pierced 0.2 mL vial inside a 1.5 mL vial and centrifuging for 10s at maximum velocity in an Eppendorf centrifuge. iii) Lung tissue was cut in 1 mm^3 pieces, resuspended in digestion mix (HEPES buffer + 2mg/ml Collagenase D (Roche) + 80U/ml DNase I (Roche)) and transferred to a gentleMACS™ C tube (Miltenyi, Cat no. 130096334). The C tube was placed in the gentleMACS Dissociator (Miltenyi, cat. no. 130-096-427) and following programs were run consecutively: “m_lung_02_01” (165 rounds per run (rpr) for 0.36 s at RT), 1500 rpr for 30 min at 37°C and finally 2079 rpr for 37s at RT. The digested tissue was filtered through a 70-um cell strainer. iv) Brain (tumor) tissue was cut in 1 mm^3 pieces, placed in a C-tube and resuspended in Tumor Dissociation Kit, mouse (TDK, Miltenyi), according to the manufacturer’s instructions. The C tube was placed in the GentleMACS dissociator and the “37C_m_TDK_1” (1081 rpr at 37°C for ~41 min)

digestion program was run. The digested (tumor) tissue was filtered through a 40-um cell strainer. For healthy brain tissue, subsequent myelin removal using the Myelin Removal Beads II kit (Miltenyi, Cat no. 130-096-433) was performed according to the manufacturer's instructions. Apart from healthy brain, all tissues were subjected to red blood cell lysis (Biolegend, 00-4333-57, diluted to 1X in deionized water) prior to FCM staining.

Mathematical modeling of mean neutrophil lifetime

To assess neutrophil mean lifetimes, the proportion of tdTomato$^+$ neutrophils was normalized to the maximum proportion measured 1-8 days post tamoxifen injection. To track neutrophils in each tissue, an age-structured mathematical model was developed that incorporated the phenotypic heterogeneity of neutrophils. Let $u = u(t, a)$ denote the density of neutrophils which, at time t, have an age a . The age varies in the interval $a \in [0,\ a_{\max}]$, where $a_{\max}$ is the maximum age that a neutrophil could have. To describe the temporal dynamics of their age distribution, the following age-structured model, via a linear first-order partial differential equation, was used:

$$\frac{\partial u}{\partial t} + \frac{\partial u}{\partial a} = -\frac{u(t,a)}{\tau(a)} + \phi(t,a). \qquad (1)$$

The left-hand side of (1) represents the temporal change in the number of neutrophils and their age. The first term on the right-hand side accounts for neutrophil death. The death time, $\tau(a)$, generally depends on neutrophil age. The addition of the flux $\phi(t,a)$ addresses the net effect of neutrophils entering and/or leaving the tissue. The total number of neutrophils at time t, irrespective of age, is given by the following integral:

$$n(t) = \int_0^{a_{\max}} u(t,a)\, da. \qquad (2)$$

When calculating the mean lifetime, τ_{LT}, of neutrophils in the context of one synchronous wave of neutrophils after tamoxifen administration, the survival function $S(a)$, with $a \in [0,\ a_{\max}]$, can be applied, yielding the fraction of neutrophils that survive to an exact age *a*:

$$\tau_{\mathrm{LT}} = \int_0^{a_{\max}} S(a)\, da. \qquad (3)$$

As $S(a)$ is not available, an effective probability density function has been introduced here based on (1):

$$\tau_{\mathrm{LT}}(t) = \frac{\int_0^{a_{\max}} a\, u(t,a)\, da}{n(t)}\,. \qquad (4)$$

Since (4) depends on time t, computing a representative mean lifetime requires the temporal average of $\tau_{\mathrm{LT}}(t)$ leading to the following final formula:

$$\langle \tau_{\mathrm{LT}} \rangle = \frac{\int_0^{\infty} \tau_{\mathrm{LT}}(t)\, n(t)\, dt}{\int_0^{\infty} n(t)\, dt}\,. \qquad (5)$$

Assuming that at time $t = 0$ no neutrophils of any age have yet arrived at tissue i, we have the initial condition $u(0,a) = 0$. Thus, the exact solution to (1) is

$$u(t,a) \;=\; e^{-\int_0^t \frac{d\xi}{\tau(a-\xi)}} \int_0^t \phi(\xi, a-t+\xi)\; e^{\int_0^{\xi} \frac{d\eta}{\tau(a-t+\eta)}}\, d\xi. \qquad (6)$$

In the nonlinear regressions shown in Figs. 5D and S5E we used for the neutrophil death time $\tau(a) = \tau_i$. Furthermore, to describe the synchronous wave of neutrophils recruited at tissue i, a bivariate Gaussian profile was assumed for the flux function:

$$\phi(t,a) \;=\; \phi_0 \exp\left[-\frac{1}{2(1-\rho^2)}\left(\frac{(t-t_i)^2}{\sigma_t^2} - \frac{2\rho(t-t_i)(a-a_i)}{\sigma_t \sigma_a} + \frac{(a-a_i)^2}{\sigma_a^2}\right)\right]. \qquad (7)$$

The parameter set, comprising τ_i, t_i, a_i, σ_t, σ_a and ρ (notice that $\phi_0$was not needed), was estimated from the measured data for the proportion of tdTomato$^+$ neutrophils in both non-tumor and PyMT-BrM3-bearing mouse brains, together with the model equations (1)-(7) described above. The standard deviation $\delta\tau_{\mathrm{LT}}$ of the mean lifetime $\langle \tau_{\mathrm{LT}} \rangle$ was computed via

$$\delta\tau_{\mathrm{LT}}{}^2 = \frac{\int_0^{\infty} (\tau_{\mathrm{LT}}(t) - \langle \tau_{\mathrm{LT}} \rangle)^2\, n(t)\, dt}{\int_0^{\infty} n(t)\, dt}\,. \qquad (8)$$

UMAP + Trajectory analysis

The manually gated PBN/TAN FCM population was exported as a separate FCS file. Variables with low variance were removed, data was randomly down-sampled to 50’000 events, and transformed (asinh(x)) using the R package scDataviz (Blighe 2021). Dimensional reduction with UMAP as well as clustering analysis were

performed using the monocle3 R package (version 1.0.0). Normalization was performed by size factor using principal component analysis. Unsupervised clustering was performed using the Leiden community detection method with the number of nearest neighbours (k) set to 100. Trajectory analysis was performed using the slingshot R package (version 2.2.0). Cluster 2 was selected as the origin. Multiple, disjoint trajectories were permitted by setting the omega parameter to TRUE.

Whole exome sequencing (WES)

WES of snap-frozen and OCT-embedded frozen tumor tissue was performed as described in (162) (Module 1b). For the validation of tumor cell lines by WES, a cell pellet of 1 x 10^6 cells was resuspended in 600 ul RLT buffer (Qiagen DNAeasy Blood&Tissue kit) and incubated at 55°C in a heating block for 1h. Genomic DNA was extracted from frozen tumor tissue and tumor cells following manufacturer's instructions (Qiagen DNAeasy Blood&Tissue kit). Sequencing of paired end, 150 base pair (2 x 150), was performed by Genewiz (South Plainfield, New Jersey, USA) on an Illumina NovaSeq 6000 sequencer (Illumina). Somatic variant calling was performed from WES data of paired tumor/cell line and PBMC samples. Raw reads (*fastq* files) were quality-control checked by FastQC and sequencing adaptors were removed by cutadapt (v2.3). The resulting reads were then aligned to the hg38 (GRCh38.95) reference genome using the Burrows-Wheeler aligner (v0.7.17). Aligned reads were sorted and written into BAM alignment files using SAMtools (v1.8) and marked for duplicates using Picard tools (v2.9.0). Somatic mutation calling was performed using MuTect2 from the GenomeAnalysisTK-4.1.0.0 (GATK4) and GATK Resource Bundle GRCh38 following best practices for somatic variant calling as described by The Broad Institute (https://gatk.broadinstitute.org/hc/en-us/articles/360035894731-Somatic-short-variant-discovery-SNVs-Indels-). Somatic variants were filtered to only retain confident calls by using the GenomeAnalysisTK FilterMutectCalls function. VCF files containing only "PASS" (filtered) variants were generated by using GenomeAnalysisTK SelectVariants (parameters: --exclude-filtered) and filtered variants were annotated using ENSEMBL Variant Effect Predictor (v96).

Protein array

Frozen CM was submitted to RayBiotech Life and analysed by the manufacturer's in-house service using L1000 Glass Slide Human Antibody Array (RayBiotech Life, AAH-BLG-1000-4). The threshold for protein detection was set to a two-fold standard deviation of the negative control, and expression values were normalized to those from complete media (DMEM-F12 + 10% FBS + 1% P/S).

TNF-α treatment

HD PBNs were resuspended at a concentration of 0.5 x 10^6 cells/ml, and 100 ul of the cell suspension was placed in a U-bottom 96 well plate. Cells were treated with 10 ng/ml TNF-α (Peprotech, 300-01A) and incubated for 5-6h at 37°C and 5% CO2. Phenotypic alterations were measured using FCM.

Software and visualization

Graphs and plots were generated using either the ggplot2 (version 3.3.6) R package or GraphPad Prism (version 9.4.1). Heatmaps were created using the ComplexHeatmap (version 2.10.0) R package. The protein interaction network was generated using the STRING platform (https://string-db.org) and visualized with iGraph (version 1.2.6).

Statistics

All biostatistics analysis were performed within R (version 4.1.1) or GraphPad Prism (version 9.4.1). Data was analyzed with the statistical test described in the corresponding figure legend. Mixed effect model calculations were performed with the R-package lmer4 and lmerTest. Statistical significance was depicted as the p-value for single comparisons and p.adj value for multiple comparisons unless otherwise stated: * <0.05, ** <0.01, *** <0.001, **** <0.0001, ns >0.05. P.adj values were obtained by correcting for multiple testing using the Benjamini-Hochberg method, unless otherwise stated.

7.3.9 Figures

Figure legends are placed on the page following the figure.

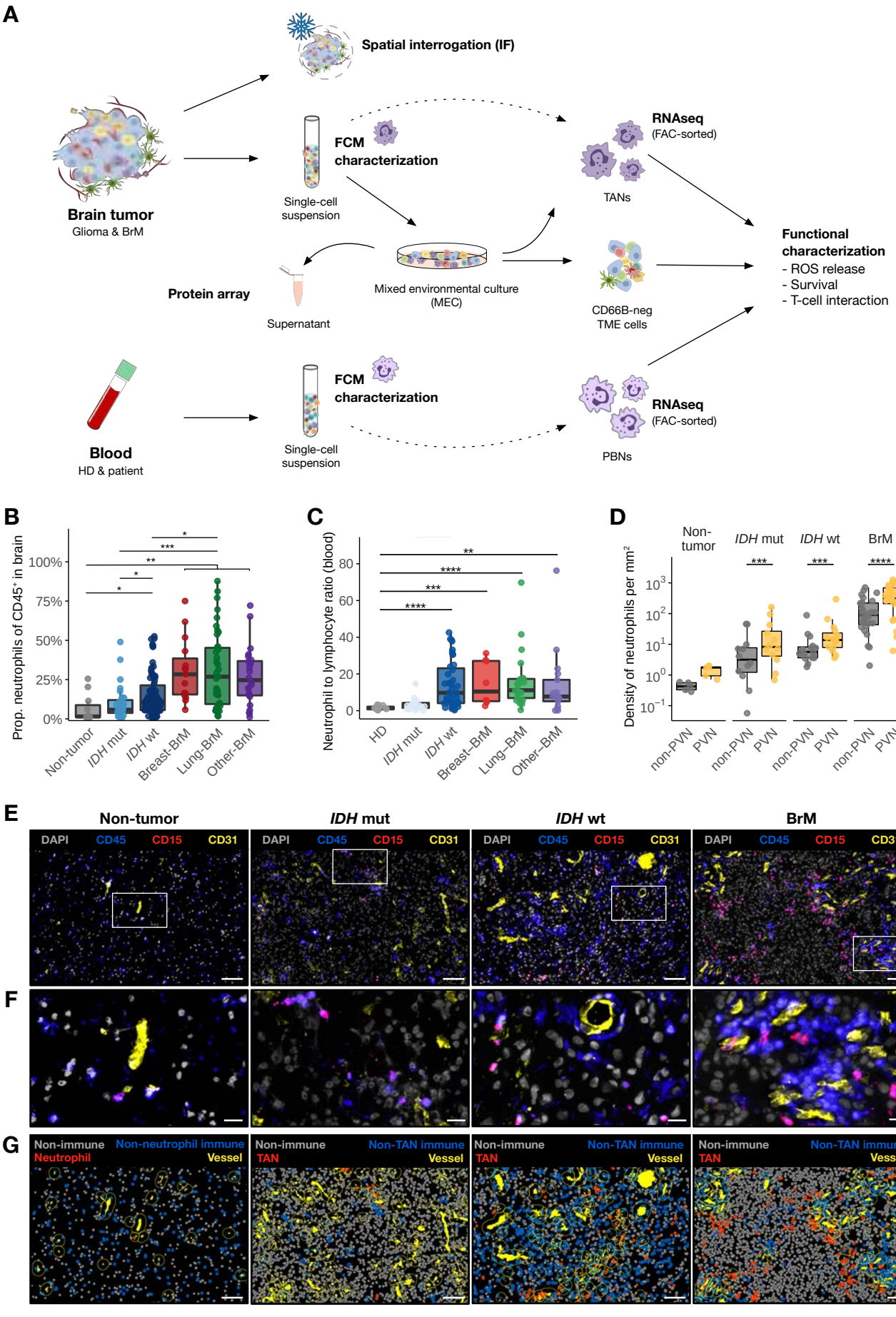

Figure 1. Neutrophils are more abundant in the TME of human BrMs than primary gliomas and preferentially localize proximal to blood vessels

(**A**) Experimental design and methodology used for analysis of human brain tumor tissue and matched blood. Abbreviations: brain metastasis (BrM), tumor-associated neutrophils (TANs), peripheral blood neutrophils (PBNs), immunofluorescence (IF), flow cytometry (FCM), fluorescence-activated cell sorting (FAC-sorting), mixed environmental culture (MEC), tumor microenvironment (TME), reactive oxygen species (ROS), healthy donor (HD). (**B**) Neutrophil proportion among $CD45^+$ immune cells in non-tumor (n=11) and tumor tissue ($n_{IDH\ mut}$=31, $n_{IDH\ wt}$=70, $n_{Breast\text{-}BrM}$=15, $n_{Lung\text{-}BrM}$=41, $n_{Other\text{-}BrM}$=24) using FCM. Wilcoxon rank-sum test. (**C**) Neutrophil to lymphocyte ratio measured in whole blood from HD (n=12) vs. brain tumor bearing patients ($n_{IDH\ mut}$=20, $n_{IDH\ wt}$=43, $n_{Breast\text{-}BrM}$=8, $n_{Lung\text{-}BrM}$=25, $n_{Other\text{-}BrM}$=17). Wilcoxon rank-sum test. P.adj values in B-C: * <0.05, ** <0.01, *** <0.001, **** <0.0001. (**D**) Density of neutrophils (per mm^2) in the non-perivascular niche (non-PVN) and PVN in non-tumor (n=5) and tumor tissue ($n_{IDH\ mut}$=12, $n_{IDH\ wt}$=15, n_{BrM}=27) using IF as shown in (E-G). Wilcoxon signed-rank test. P.adj: *** <0.001, **** <0.0001. (**E**) Representative IF images of neutrophils in relation to the vasculature in non-tumor, *IDH* mut and wt glioma, and a lung-BrM. Scale bars: 100 µm, boxed areas are shown in higher magnification in **(F**) Scale bars: 20 µm. (**G**) Cell type identification of TANs ($CD45^+$ $CD15^+$), non-TAN immune cells ($CD45^+$ $CD15^-$), non-immune ($CD45^-$) and vessels ($CD31^+$) on tissues as shown in (A). Dashed line yellow indicates the border of the PVN, corresponding to a 20 µm distance surrounding the vessel.

See also Fig S1 and Table S1A for clinical details

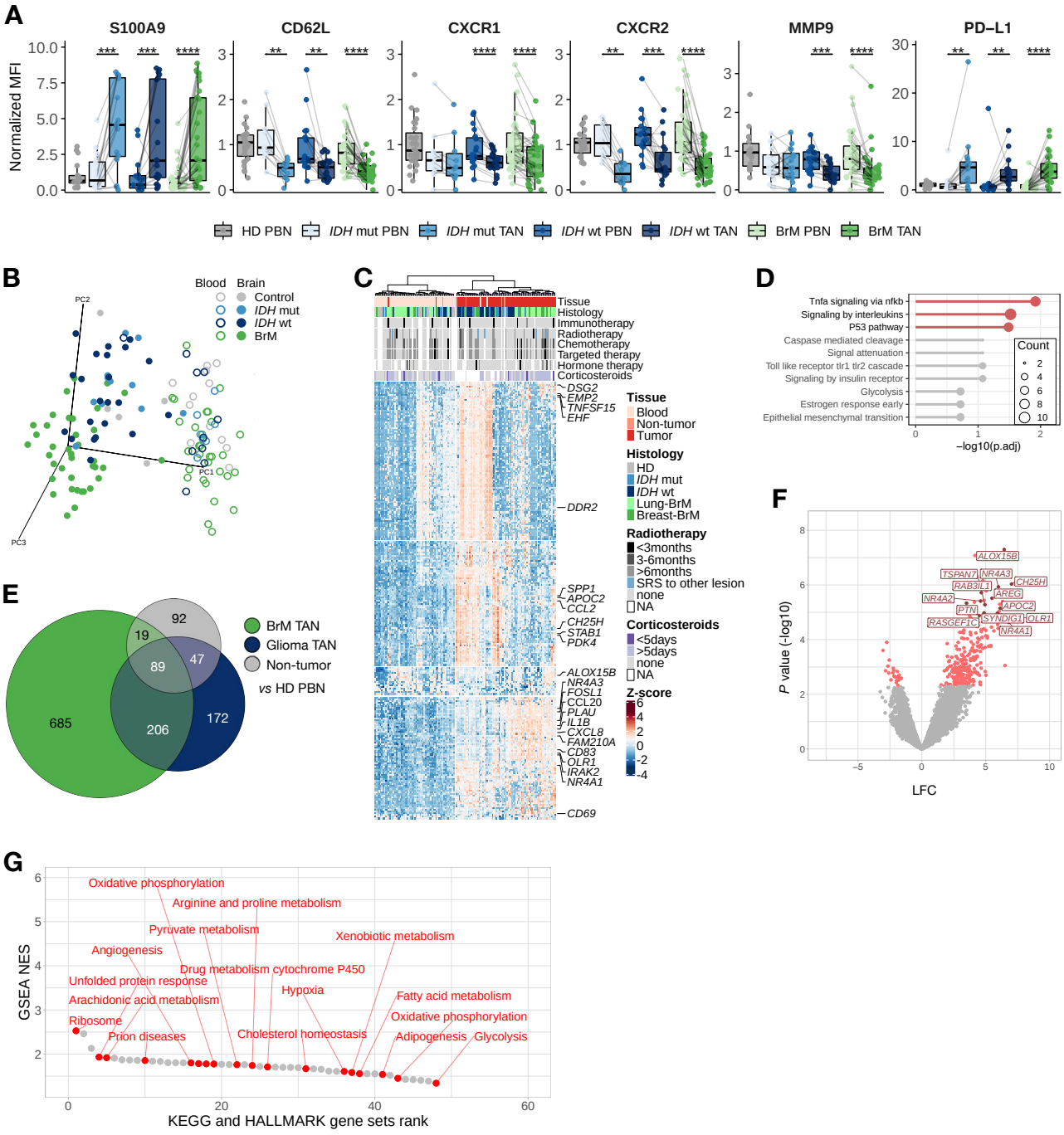
A
S100A9
CD62L
CXCR1
CXCR2
MMP9
PD–L1
Normalized MFI
HD PBN
IDH mut PBN
IDH mut TAN
IDH wt PBN
IDH wt TAN
BrM PBN
BrM TAN
B
Blood
Brain
Control
IDH mut
IDH wt
BrM
PC1
PC2
PC3
C
Tissue
Histology
Immunotherapy
Radiotherapy
Chemotherapy
Targeted therapy
Hormone therapy
Corticosteroids
DSG2
EMP2
TNFSF15
EHF
DDR2
SPP1
APOC2
CCL2
CH25H
STAB1
PDK4
ALOX15B
NR4A3
FOSL1
CCL20
PLAU
IL1B
CXCL8
FAM210A
CD83
OLR1
IRAK2
NR4A1
CD69
Tissue
Blood
Non-tumor
Tumor
Histology
HD
IDH mut
IDH wt
Lung-BrM
Breast-BrM
Radiotherapy
<3months
3-6months
>6months
SRS to other lesion
none
NA
Corticosteroids
<5days
>5days
none
NA
Z-score
D
Tnfa signaling via nfkb
Signaling by interleukins
P53 pathway
Caspase mediated cleavage
Signal attenuation
Toll like receptor tlr1 tlr2 cascade
Signaling by insulin receptor
Glycolysis
Estrogen response early
Epithelial mesenchymal transition
Count
–log10(p.adj)
E
92
19
89
47
685
206
172
BrM TAN
Glioma TAN
Non-tumor
vs HD PBN
F
P value (-log10)
LFC
ALOX15B
TSPAN7
NR4A3
CH25H
RAB3IL1
AREG
NR4A2
APOC2
PTN
RASGEF1C
SYNDIG1
OLR1
NR4A1
G
GSEA NES
KEGG and HALLMARK gene sets rank
Oxidative phosphorylation
Arginine and proline metabolism
Pyruvate metabolism
Xenobiotic metabolism
Angiogenesis
Drug metabolism cytochrome P450
Unfolded protein response
Hypoxia
Arachidonic acid metabolism
Fatty acid metabolism
Ribosome
Oxidative phosphorylation
Prion diseases
Cholesterol homeostasis
Adipogenesis
Glycolysis

Figure 2. The neutrophil phenotype is altered in the brain tissue environment

(**A**) Median fluorescence intensity (MFI) of matched PBNs and TANs from tumor-bearing patients ($n_{IDH\ mut}$ >10, $n_{IDH\ wt}$=19, n_{BrM}>31) normalized to HD PBNs (n>14). Wilcoxon signed-rank test, only comparing matched patient PBNs and TANs. P.adj values: ** <0.01, *** <0.001, **** <0.0001. (**B**) Principal component (PC) plot of neutrophil transcriptional profiles in blood (empty circles) and brain (tumor) tissue (filled circles), based on 1% most variable genes. For clinical details see Table S1B. (**C**) Unsupervised heatmap depicting the top 250 most variable neutrophil genes shown in (B), genes of interest are indicated on the right. (**D**) Over-representation analysis (ORA) of pathways from KEGG and Reactome databases on up-regulated DEGs shared between BrM PBNs and TANs *vs.* HD PBNs. (**E**) Euler diagram depicting the intersect of up-regulated DEGs in BrM TANs, glioma TANs, and non-tumor brain neutrophils *vs.* HD PBNs (cut-off: p.adj<0.05 for TANs and p<0.005 for non-tumor brain neutrophils; LFC>1). (**F**) Volcano plot showing DEGs in non-tumor brain neutrophils *vs.* HD PBNs. Highlighted are neurotrophic and metabolic genes within top 20 highest significantly up-regulated genes. (**G**) Rank plot of gene set enrichment analysis (GSEA) using KEGG and HALLMARK databases of non-tumor brain neutrophils *vs*. HD PBNs from (F) (cut-off: p.adj<0.05; NES>0).

See also Fig S2 and Tables S1B and S2

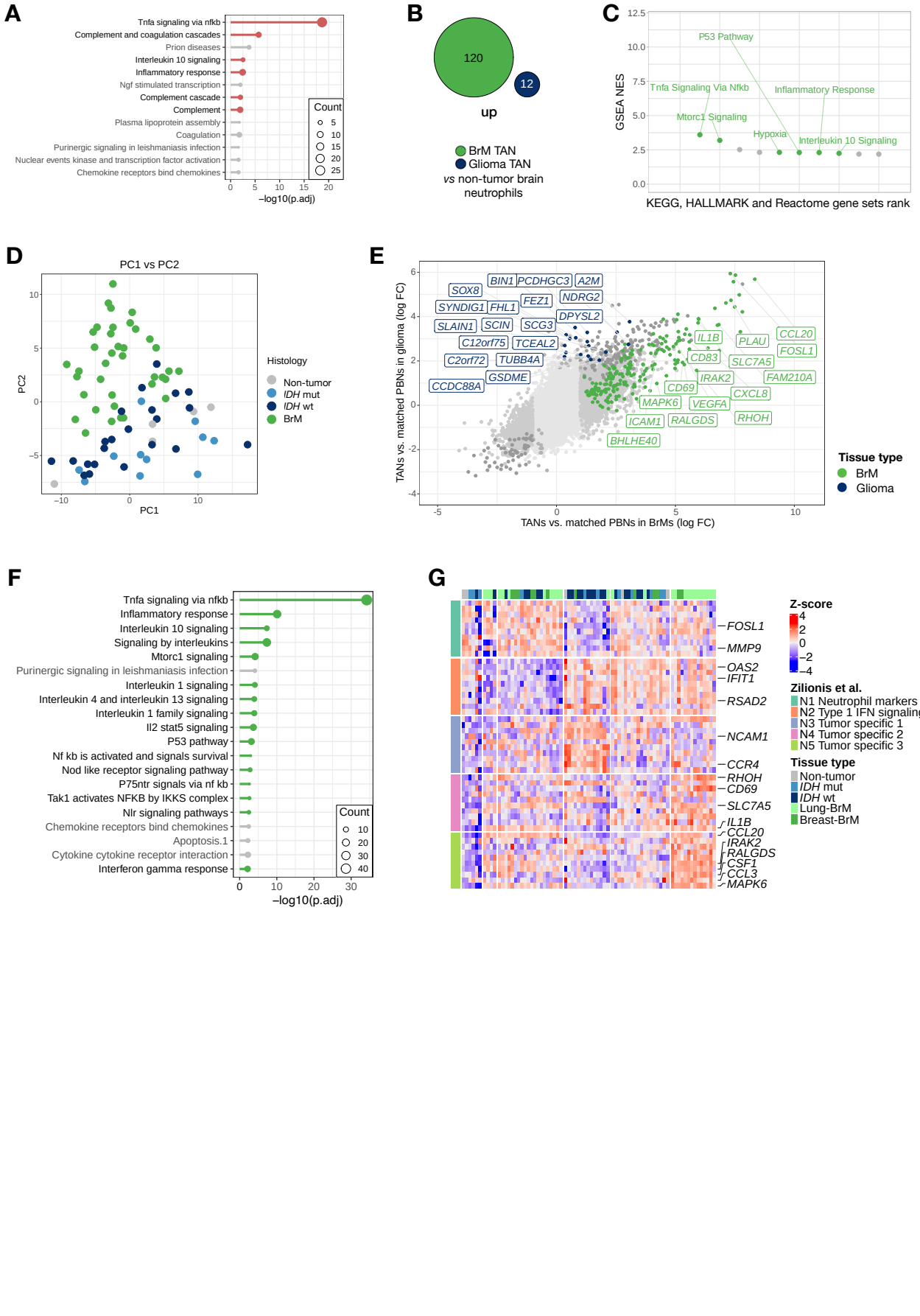
A
Tnfa signaling via nfkb
Complement and coagulation cascades
Prion diseases
Interleukin 10 signaling
Inflammatory response
Ngf stimulated transcription
Complement cascade
Complement
Plasma lipoprotein assembly
Coagulation
Purinergic signaling in leishmaniasis infection
Nuclear events kinase and transcription factor activation
Chemokine receptors bind chemokines
Count
5
10
15
20
25
0
5
10
15
20
−log10(p.adj)
B
120
12
up
BrM TAN
Glioma TAN
vs non-tumor brain
neutrophils
C
12.5
10.0
7.5
5.0
2.5
0.0
GSEA NES
P53 Pathway
Tnfa Signaling Via Nfkb
Inflammatory Response
Mtorc1 Signaling
Hypoxia
Interleukin 10 Signaling
KEGG, HALLMARK and Reactome gene sets rank
D
PC1 vs PC2
10
5
0
−5
PC2
−10
0
10
PC1
Histology
Non-tumor
IDH mut
IDH wt
BrM
E
6
4
2
0
-2
-4
TANs vs. matched PBNs in glioma (log FC)
SOX8
BIN1
PCDHGC3
A2M
NDRG2
FEZ1
SYNDIG1
FHL1
DPYSL2
SLAIN1
SCIN
SCG3
C12orf75
TCEAL2
C2orf72
TUBB4A
GSDME
CCDC88A
IL1B
PLAU
CCL20
CD83
FOSL1
SLC7A5
IRAK2
FAM210A
CD69
CXCL8
MAPK6
VEGFA
ICAM1
RALGDS
RHOH
BHLHE40
-5
0
5
10
TANs vs. matched PBNs in BrMs (log FC)
Tissue type
BrM
Glioma
F
Tnfa signaling via nfkb
Inflammatory response
Interleukin 10 signaling
Signaling by interleukins
Mtorc1 signaling
Purinergic signaling in leishmaniasis infection
Interleukin 1 signaling
Interleukin 4 and interleukin 13 signaling
Interleukin 1 family signaling
Il2 stat5 signaling
P53 pathway
Nf kb is activated and signals survival
Nod like receptor signaling pathway
P75ntr signals via nf kb
Tak1 activates NFKB by IKKS complex
Nlr signaling pathways
Chemokine receptors bind chemokines
Apoptosis.1
Cytokine cytokine receptor interaction
Interferon gamma response
Count
10
20
30
40
0
10
20
30
−log10(p.adj)
G
FOSL1
MMP9
OAS2
IFIT1
RSAD2
NCAM1
CCR4
RHOH
CD69
SLC7A5
IL1B
CCL20
IRAK2
RALGDS
CSF1
CCL3
MAPK6
Z-score
4
2
0
−2
−4
Zilionis et al.
N1 Neutrophil markers
N2 Type 1 IFN signaling
N3 Tumor specific 1
N4 Tumor specific 2
N5 Tumor specific 3
Tissue type
Non-tumor
IDH mut
IDH wt
Lung-BrM
Breast-BrM

Figure 3. Brain neutrophils are enriched in inflammatory gene signatures, which are most pronounced in BrMs

(**A**) ORA of pathways from Hallmark, KEGG and Reactome databases on up-regulated DEGs shared between non-tumor brain neutrophils, glioma and BrM TANs *vs.* HD PBNs (intersect shown in Fig. 2E). Highlighted in red are pro-inflammatory pathways. (**B**) Euler diagram of up-regulated DEGs in BrM and glioma TANs *vs.* non-tumor brain neutrophils (cut-off: p<0.005; LFC>1). (**C**) GSEA using Hallmark, KEGG and Reactome databases on DEGs in BrM TANs *vs.* non-tumor brain neutrophils. (cut-off: p.adj<0.05; -1.5>NES > 1.5). Highlighted in green are pro-inflammatory pathways. (**D**) PC plot of neutrophil transcriptional profiles in non-tumor brain tissue, glioma and BrM TANs, calculated based on top 1% most highly variable genes. (**E**) Dot plot depicting the LFC of individual DEGs between BrM/glioma TANs *vs.* matched PBNs (cut-off: p.adj<0.05). Highlighted are genes of interest that were also significantly differentially expressed in BrM *vs.* glioma TANs (cut-off: p.adj<0.05; LFC>1 or <-1; dark blue = signif. in glioma TANs *vs.* BrM TANs and glioma PBNs, light blue = signif. in glioma TANs *vs.* PBNs only, green = signif. in BrM TANs *vs.* glioma TANs and BrM PBNs, light green = signif. in BrM TANs *vs.* PBNs only, salmon pink = shared in glioma and BrM TANs). (**F**) ORA of top 20 most significant pathways from Hallmark, KEGG and Reactome databases on DEGs up-regulated specifically in BrM-TANs depicted in (E) (cut-off: p.adj<0.05; NES>0). Highlighted in green are pro-inflammatory pathways. (**G**) Heatmap depicting non-tumor neutrophils and brain-TANs aligned to the top 10 most variable genes per 'N' neutrophil cluster as defined by (122). Samples were hierarchically clustered and genes of interest are indicated on the right.

See also Fig S3 and Tables S3

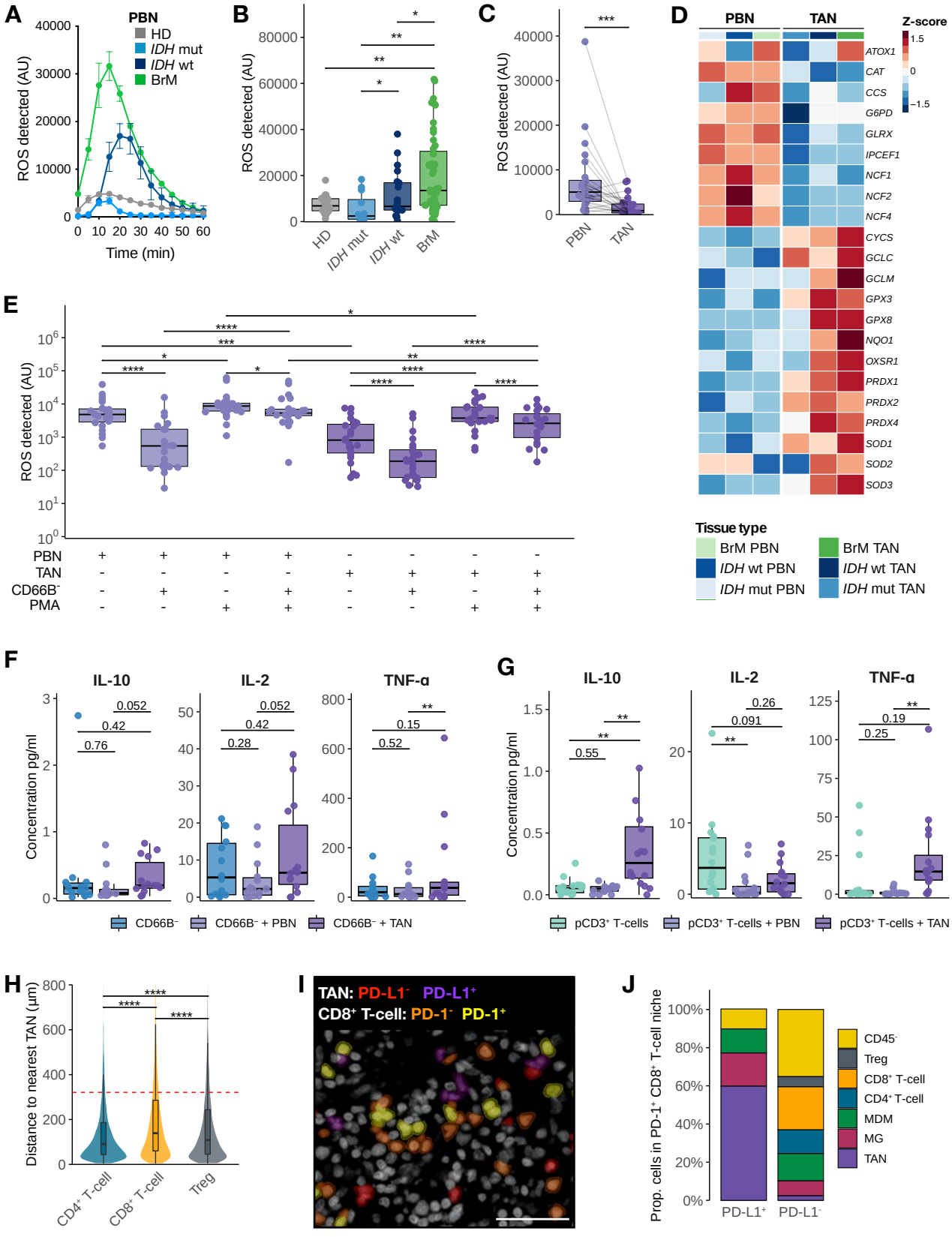
A
PBN
HD
IDH mut
IDH wt
BrM
ROS detected (AU)
Time (min)
B
ROS detected (AU)
HD
IDH mut
IDH wt
BrM
C
ROS detected (AU)
PBN
TAN
D
PBN
TAN
Z-score
ATOX1
CAT
CCS
G6PD
GLRX
IPCEF1
NCF1
NCF2
NCF4
CYCS
GCLC
GCLM
GPX3
GPX8
NQO1
OXSR1
PRDX1
PRDX2
PRDX4
SOD1
SOD2
SOD3
Tissue type
BrM PBN
IDH wt PBN
IDH mut PBN
BrM TAN
IDH wt TAN
IDH mut TAN
E
ROS detected (AU)
PBN
TAN
CD66B-
PMA
F
IL-10
IL-2
TNF-α
Concentration pg/ml
CD66B⁻
CD66B⁻ + PBN
CD66B⁻ + TAN
G
IL-10
IL-2
TNF-α
Concentration pg/ml
pCD3⁺ T-cells
pCD3⁺ T-cells + PBN
pCD3⁺ T-cells + TAN
H
Distance to nearest TAN (μm)
CD4⁺ T-cell
CD8⁺ T-cell
Treg
I
TAN: PD-L1⁻ PD-L1⁺
CD8⁺ T-cell: PD-1⁻ PD-1⁺
J
Prop. cells in PD-1⁺ CD8⁺ T-cell niche
PD-L1⁺
PD-L1⁻
CD45⁻
Treg
CD8⁺ T-cell
CD4⁺ T-cell
MDM
MG
TAN

Figure 4. The functionality of neutrophils is altered in the brain TME milieu

(**A**) Representative curves of ROS measured over time in PBNs from HD and brain tumor-bearing patients (arbitrary units, AU). (**B**) Maximum ROS detected in PBNs from HD (n=18), and tumor-bearing patients ($n_{IDH\ mut}$=12, $n_{IDH\ wt}$=20, n_{BrM}=51). Wilcoxon rank-sum test. P.adj values: * <0.05, ** <0.01. (**C**) ROS detected in matched PBNs and TANs ($n_{IDH\ mut}$=6, $n_{IDH\ wt}$=9, n_{BrM}=9). Wilcoxon signed-rank test. P-value: *** <0.001. (**D**) Heatmap depicting ROS-related, significant DEGs in BrM and glioma TANs *vs.* matched PBNs. (**E**) ROS detected in cocultures of matched PBNs and TANs with CD66B-neg TME, activation by phorbol 12-myristate 13-acetate (PMA) ($n_{IDH\ mut}$=6, $n_{IDH\ wt}$=8, n_{BrM}=9). Wilcoxon signed-rank test. P.adj values: * <0.05, ** <0.01, *** <0.001, **** <0.0001 (**F**) Cytokine concentration in pg/ml in supernatant of $CD66B^-$ cells cocultured with PBNs or TANs for 96h ($n_{IDH\ mut}$=1, $n_{IDH\ wt}$=7, n_{BrM}=6). Wilcoxon signed-rank test. P.adj value: ** <0.01. (**G**) Cytokine concentration in pg/ml in supernatant of peripheral $CD3^+$ T-cell (pCD3) cocultured with PBN or TAN for 96h ($n_{IDH\ mut}$=2, $n_{IDH\ wt}$=8, n_{BrM}=6). Wilcoxon signed-rank test. P.adj value: ** <0.01. (**H**) Distance of individual T-cells ($CD4^+$ $T\text{-cells}_{(n=53,692)}$, $CD8^+$ $T\text{-cells}_{(n=54,495)}$, $Treg_{(n=26,001)}$) to the nearest TAN in $BrM_{(n=20)}$ and *IDH* wt $glioma_{(n=7)}$ analyzed together. Dashed line indicates the average distance of all $cells_{(n=2,571,834)}$ to the nearest TAN. Wilcoxon rank-sum test. P.adj value: **** <0.0001. (**I**) Representative lung-BrM image showing IF cell type quantification of TANs ($PD\text{-}L1^-$ and $PD\text{-}L1^+$) and $CD8^+$ T-cells ($PD\text{-}1^-$ and $PD\text{-}1^+$) in BrM. Scale bar = 50 µm. (**J**) Mean proportion of cell types identified in a 20 µm radius around $PD\text{-}1^+$ $CD8^+$ $T\text{-cells}_{(n=20,697)}$ in $BrM_{(n=20)}$ and *IDH* wt $glioma_{(n=7)}$.

See also Fig S4

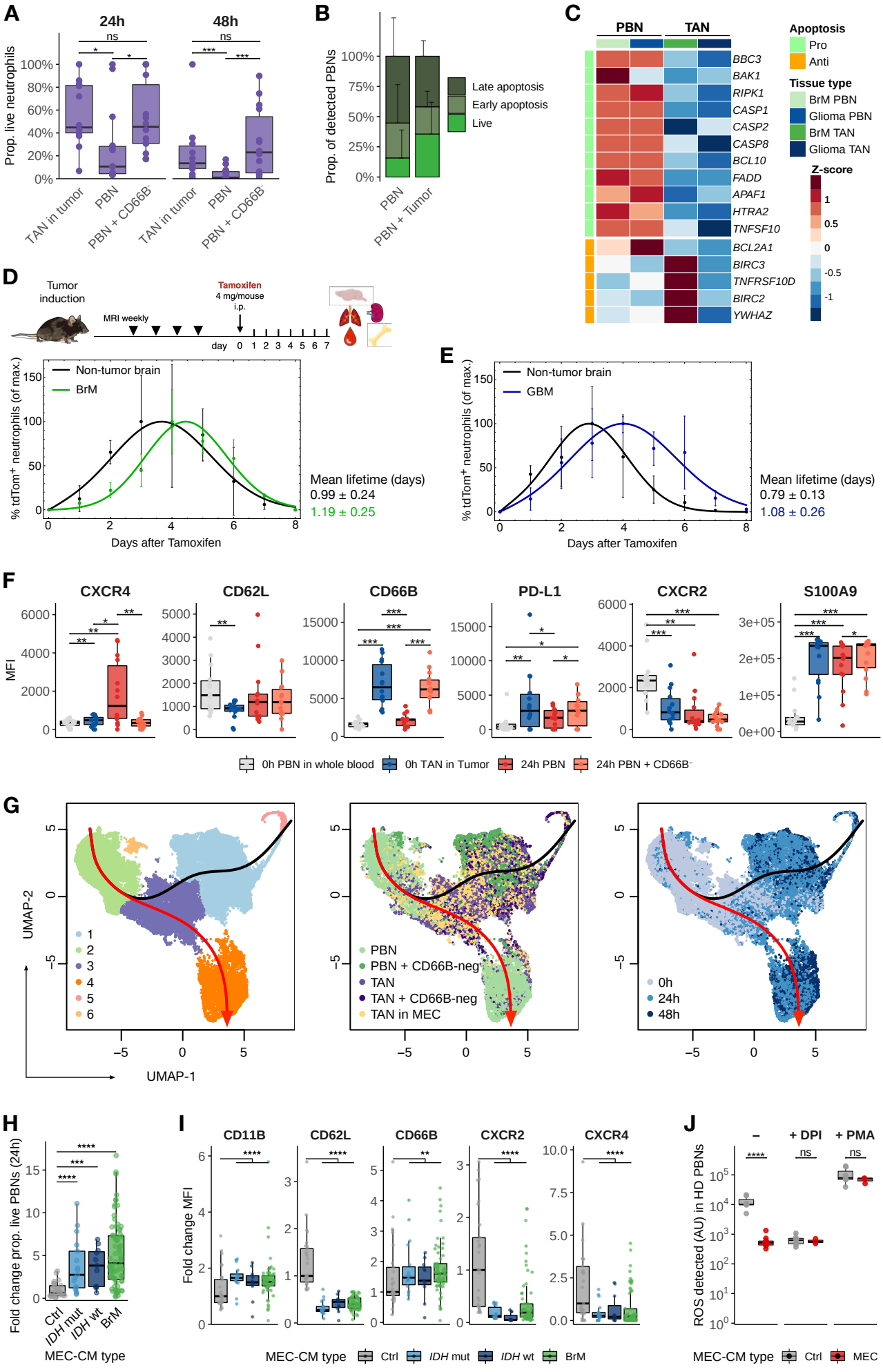
A
24h
48h
ns
Prop. live neutrophils
TAN in tumor
PBN
PBN + CD66B-
B
Prop. of detected PBNs
Late apoptosis
Early apoptosis
Live
PBN + Tumor
C
PBN
TAN
Apoptosis
Pro
Anti
Tissue type
BrM PBN
Glioma PBN
BrM TAN
Glioma TAN
Z-score
BBC3
BAK1
RIPK1
CASP1
CASP2
CASP8
BCL10
FADD
APAF1
HTRA2
TNFSF10
BCL2A1
BIRC3
TNFRSF10D
BIRC2
YWHAZ
D
Tumor induction
MRI weekly
Tamoxifen
4 mg/mouse
i.p.
day 0 1 2 3 4 5 6 7
Non-tumor brain
BrM
% tdTom+ neutrophils (of max.)
Days after Tamoxifen
Mean lifetime (days)
0.99 ± 0.24
1.19 ± 0.25
E
Non-tumor brain
GBM
% tdTom+ neutrophils (of max.)
Days after Tamoxifen
Mean lifetime (days)
0.79 ± 0.13
1.08 ± 0.26
F
CXCR4
CD62L
CD66B
PD-L1
CXCR2
S100A9
MFI
0h PBN in whole blood
0h TAN in Tumor
24h PBN
24h PBN + CD66B-
G
UMAP-2
UMAP-1
1
2
3
4
5
6
PBN
PBN + CD66B-neg
TAN
TAN + CD66B-neg
TAN in MEC
0h
24h
48h
H
Fold change prop. live PBNs (24h)
Ctrl
IDH mut
IDH wt
BrM
MEC-CM type
I
CD11B
CD62L
CD66B
CXCR2
CXCR4
Fold change MFI
MEC-CM type
Ctrl
IDH mut
IDH wt
BrM
J
–
+ DPI
+ PMA
ROS detected (AU) in HD PBNs
MEC-CM type
Ctrl
MEC

Figure 5. The brain TME affects both neutrophil survival and phenotype

(**A**) Proportion of live TANs in tumors, matched PBNs and PBNs in coculture with CD66B-neg TME population at 24h and 48h ($n_{IDH\ mut}$=5, $n_{IDH\ wt}$=5, n_{BrM}=4). Wilcoxon signed-rank test. P.adj values: * <0.05, ** <0.01, *** <0.001. (**B**) Proportion of PBNs at different viability stages, alone and in cocultures with matched tumor cells ($n_{IDH\ mut}$=2, $n_{IDH\ wt}$=2, n_{BrM}=5). (**C**) Heatmap of DEGs associated with apoptosis in glioma and BrM PBNs *vs.* matched TANs. (**D**) Experimental design in iLy6G^{tdTomato} mice and proportion of tdTomato^{+} neutrophils normalized to maximum in non-tumor and PyMT-BrM3-bearing mouse brains over 8 days. A minimum of 3 mice from 6 independent experiments are shown per timepoint, mean lifetime in days is shown on the right. (**E**) Proportion of tdTomato^{+} neutrophils normalized to maximum in Ntv-a;iLy6G^{tdTomato} non-tumor and glioblastoma (GBM) bearing mouse brains. Minimum of 3 mice from 3 independent experiments are shown per timepoint, mean lifetime in days is shown on the right. (**F**) MFI of aging and age-(in)dependent markers in PBNs over time (0h and 24h) and in the presence of CD66B^{-} TME ($n_{IDH\ mut}$=4, $n_{IDH\ wt}$=5, n_{BrM}=5). Wilcoxon signed-rank test. P.adj values: * <0.05, ** <0.01, *** <0.001 (**G**) Uniform Manifold Approximation and Projection of a 10-marker FCM panel on matched TANs and PBNs in coculture with CD66B-neg TME over 48h (CD11B, CD15, CD16, CD45, CD45, CD62L, CD66B, CXCR1, CXCR2, CXCR4). Trajectories shown based on Slingshot: red arrow; PBN-trajectory, black arrow; TAN-trajectory. (**H**) Fold change in 24h survival of HD PBNs (n=25) after culture in MEC-CM ($n_{IDH\ mut}$=4, $n_{IDH\ wt}$=4, n_{BrM}=15). Mixed effects model with MEC type as fixed effect and HD ID as random slope effect: ANOVA p-value = $4.12x10^{-8}$, p.adj values: *** <0.001, **** <0.0001 (**I**) Fold change MFI in HD PBN (n=15) cultured in MEC-CM ($n_{IDH\ mut}$=4, $n_{IDH\ wt}$=4, n_{BrM}=14) *vs.* control medium. Mixed effect model with MEC type as fixed effect and HD ID as random effect. P.adj values: ** <0.01, **** <0.0001. (**J**) ROS measured in HD PBNs (n=7) cultured in BrM MEC-CM (n=13) and treated with diphenyleneiodonium (DPI) or PMA. Wilcoxon rank-sum test. P.adj value: *** <0.001.

See also Fig S5

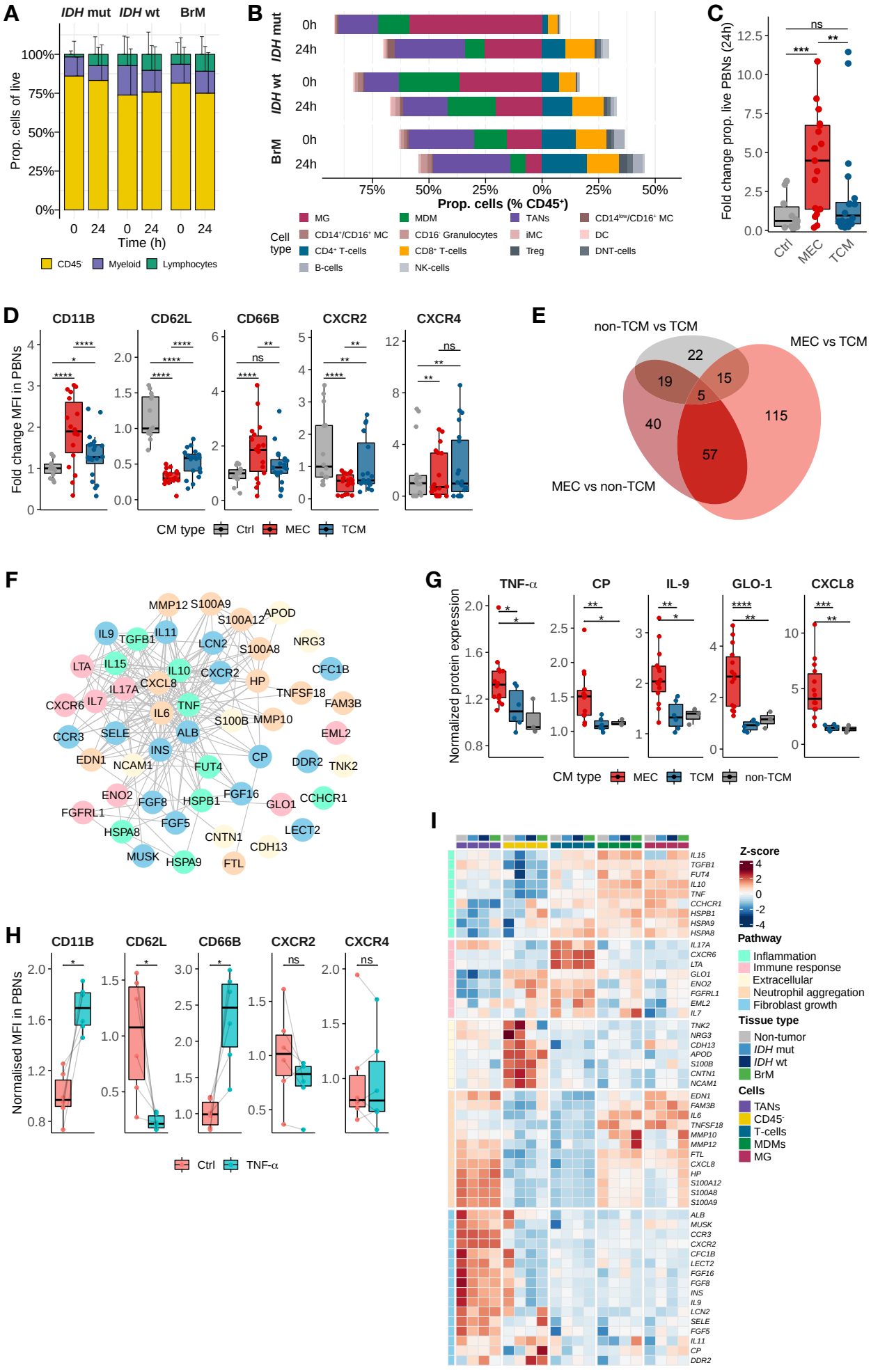
A
IDH mut
IDH wt
BrM
Prop. cells of live
100%
75%
50%
25%
0%
0
24
Time (h)
CD45-
Myeloid
Lymphocytes
B
IDH mut
IDH wt
BrM
0h
24h
75%
50%
25%
0%
Prop. cells (% CD45+)
Cell type
MG
MDM
TANs
CD14low/CD16+ MC
CD14+/CD16+ MC
CD16- Granulocytes
iMC
DC
CD4+ T-cells
CD8+ T-cells
Treg
DNT-cells
B-cells
NK-cells
C
Fold change prop. live PBNs (24h)
ns
**
***
Ctrl
MEC
TCM
D
CD11B
CD62L
CD66B
CXCR2
CXCR4
Fold change MFI in PBNs
CM type
Ctrl
MEC
TCM
E
non-TCM vs TCM
MEC vs TCM
MEC vs non-TCM
22
15
19
5
40
115
57
F
MMP12
S100A9
S100A12
APOD
IL9
TGFB1
IL11
LCN2
S100A8
NRG3
LTA
IL15
IL10
CXCR2
CFC1B
CXCL8
HP
IL17A
TNFSF18
CXCR6
IL7
TNF
FAM3B
IL6
S100B
MMP10
CCR3
SELE
ALB
EML2
EDN1
INS
CP
NCAM1
FUT4
DDR2
TNK2
ENO2
FGF8
HSPB1
FGF16
GLO1
CCHCR1
FGFRL1
FGF5
HSPA8
CNTN1
LECT2
CDH13
MUSK
HSPA9
FTL
G
TNF-α
CP
IL-9
GLO-1
CXCL8
Normalized protein expression
CM type
MEC
TCM
non-TCM
H
CD11B
CD62L
CD66B
CXCR2
CXCR4
Normalised MFI in PBNs
Ctrl
TNF-α
I
Z-score
4
2
0
-2
-4
Pathway
Inflammation
Immune response
Extracellular
Neutrophil aggregation
Fibroblast growth
Tissue type
Non-tumor
IDH mut
IDH wt
BrM
Cells
TANs
CD45-
T-cells
MDMs
MG
IL15
TGFB1
FUT4
IL10
TNF
CCHCR1
HSPB1
HSPA9
HSPA8
IL17A
CXCR6
LTA
GLO1
ENO2
FGFRL1
EML2
IL7
TNK2
NRG3
CDH13
APOD
S100B
CNTN1
NCAM1
EDN1
FAM3B
IL6
TNFSF18
MMP10
MMP12
FTL
CXCL8
HP
S100A12
S100A8
S100A9
ALB
MUSK
CCR3
CXCR2
CFC1B
LECT2
FGF16
FGF8
INS
IL9
LCN2
SELE
FGF5
IL11
CP
DDR2

Figure 6. Neutrophil alterations are induced by soluble factors in the brain TME

(**A**) Percentages of live cells in *ex vivo* MEC ($n_{IDH\ mut}$=5, $n_{IDH\ wt}$=7, n_{BrM}=13) at 0h and 24h (mean and SD). (**B**) Mean of immune cell populations as percent of $CD45^+$ cells from cultures shown in A. (**C**) Fold change in HD PBN survival (n=12) after culture in MEC- or matched tumor cell line CM (TCM, $n_{IDH\ mut}$=1, $n_{IDH\ wt}$=3, $n_{melanoma\text{-}BrM}$=2) *vs.* control medium pooled from 6 independent experiments. Mixed-effect model with CM type as fixed effect and HD ID as random slope effect: ANOVA p-value=0.0011, p.adj values: ** <0.01, *** <0.001. (**D**) Fold change MFI of indicated markers in HD PBNs shown in (C). Mixed effect model as in (C), p.adj values: * <0.05, ** <0.01, **** <0.0001. (**E**) Euler plot depicting the overlap in differentially detected proteins (cut-off: p<0.05) when comparing MEC-CM, TCM, and non-TCM. (**F**) Protein interaction network of the 51 most highly differentially expressed proteins in MEC-CM *vs.* TCM and non-TCM. Color codes based on the unbiased clustering of protein pathways in (J), with five different classes represented. (**G**) Detection of the proteins indicated (AU) normalized to control media. Wilcoxon rank-sum test, p.adj values: * <0.05, ** <0.01, *** <0.001, **** <0.0001. (**H**) Normalized MFI of indicated markers measured in HD PBNs treated with TNF-α. Wilcoxon signed-rank test, p.adj values: * <0.05. (**I**) Heatmap of gene expression levels in the main TME populations for MEC-CM specific upregulated proteins as shown in (G). T-cells include both $CD4^+$ and $CD8^+$ T-cells. Clustering by overarching protein pathways based on Wards method.

See also Fig S6 and Table S4

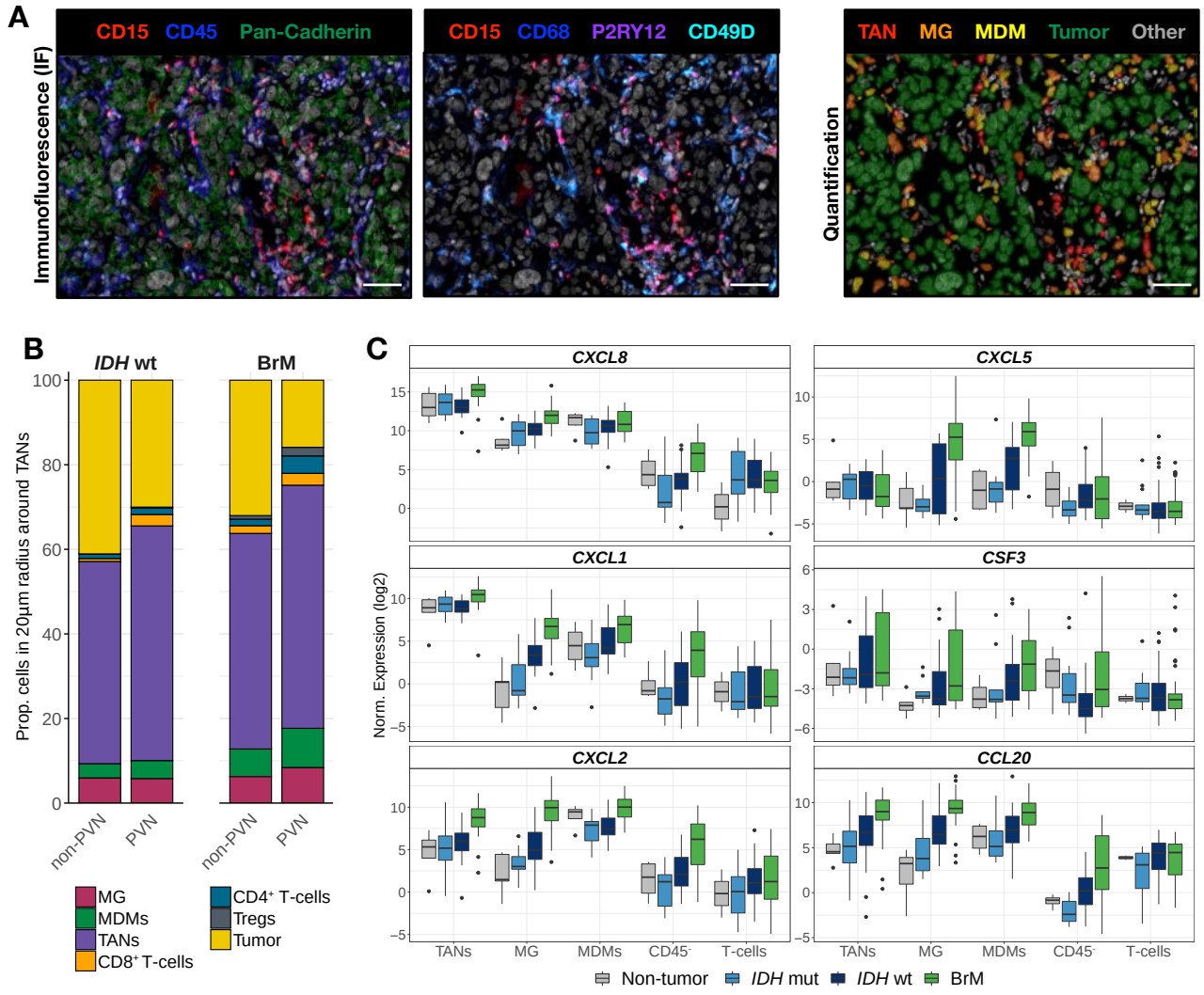
A
Immunofluorescence (IF)
CD15 CD45 Pan-Cadherin
CD15 CD68 P2RY12 CD49D
Quantification
TAN MG MDM Tumor Other
B
IDH wt
BrM
Prop. cells in 20µm radius around TANs
non-PVN
PVN
MG
MDMs
TANs
CD8+ T-cells
CD4+ T-cells
Tregs
Tumor
C
CXCL8
CXCL5
CXCL1
CSF3
CXCL2
CCL20
Norm. Expression (log2)
TANs
MG
MDMs
CD45-
T-cells
Non-tumor
IDH mut
IDH wt
BrM
D
Non-tumor
IDH mut
IDH wt
BrM
Average form factor vessel
ns
****
Neg
Pos
Presence of neutrophils in PVN
E
Angiogenesis in TANs vs. PBNs, p.adj=3.8e-02
Running Enrichment Score
Ranked List Metric
Rank in Ordered Dataset
F
VCAN
FGFR1
TIMP1
VEGFA
SPP1
CCND2
POSTN
ITGAV
APP
MSX1
FSTL1
COL3A1
PTK2
OLR1
THBD
PRG2
PDGFA
COL5A2
KCNJ8
LUM
Z-score
Tumor type
Glioma
BrM
Tissue
PBN
TAN
G
VEGFA
THBD
ICAM1
PLAUR
Neutrophils
Mean form factor
R = −0.34, p = 0.037
R = −0.34, p = 0.035
R = −0.33, p = 0.042
R = −0.049, p = 0.77
Normalized gene counts
Tissue type
Non-tumor
IDH mut
IDH wt
BrM

Figure 7. Neutrophils interact with the myeloid compartment and the brain vasculature (**A**) Representative IF image and cell type quantification by QuPath in a lung-BrM showing tumor cells (pan-cadherin^{+}), TANs (CD45^{+}, CD15^{+}), MG (CD45^{+}, CD68/P2RY12^{+}, CD49D^{-}), MDMs (CD45^{+}, CD68/P2RY12^{+}, CD49D^{+}) and 'Other' (all remaining cells). Scale bars: 50 µm. (**B**) Mean proportion of cell types identified in a 20 µm radius around TANs$_{(n=62,709)}$ in BrM$_{(n=20)}$ and *IDH* wt glioma$_{(n=7)}$. (**C**) Normalized log2-transformed expression of neutrophil-recruiting cytokines in different brain TME populations. (**D**) The mean form factor of individual vessels in the presence (Pos) or absence (Neg) of TANs in their PVN, based on IF as shown in Fig 1E-G ($n_{Non\text{-}tumor}$=5, $n_{IDH\ mut}$=12, $n_{IDH\ wt}$=15, n_{BrM}=27). Wilcoxon signed-rank test, p.adj values: **** <0.0001. (**E**) GSEA of Hallmark's Angiogenesis pathway in glioma and BrM TANs combined compared to matched PBNs. (**F**) Heatmap of individual genes of leading-edge Hallmark Angiogenesis pathway stratified by glioma and BrM PBNs and TANs. (**G**) Correlation between mean vessel form factor vs. normalized gene counts of angiogenesis-associated genes in non-tumor neutrophils, glioma, and BrM TANs using the Pearson method.

See also Fig S7

7.3.10 Supplementary figures

Figure legends are placed on the page following the supplementary figure.

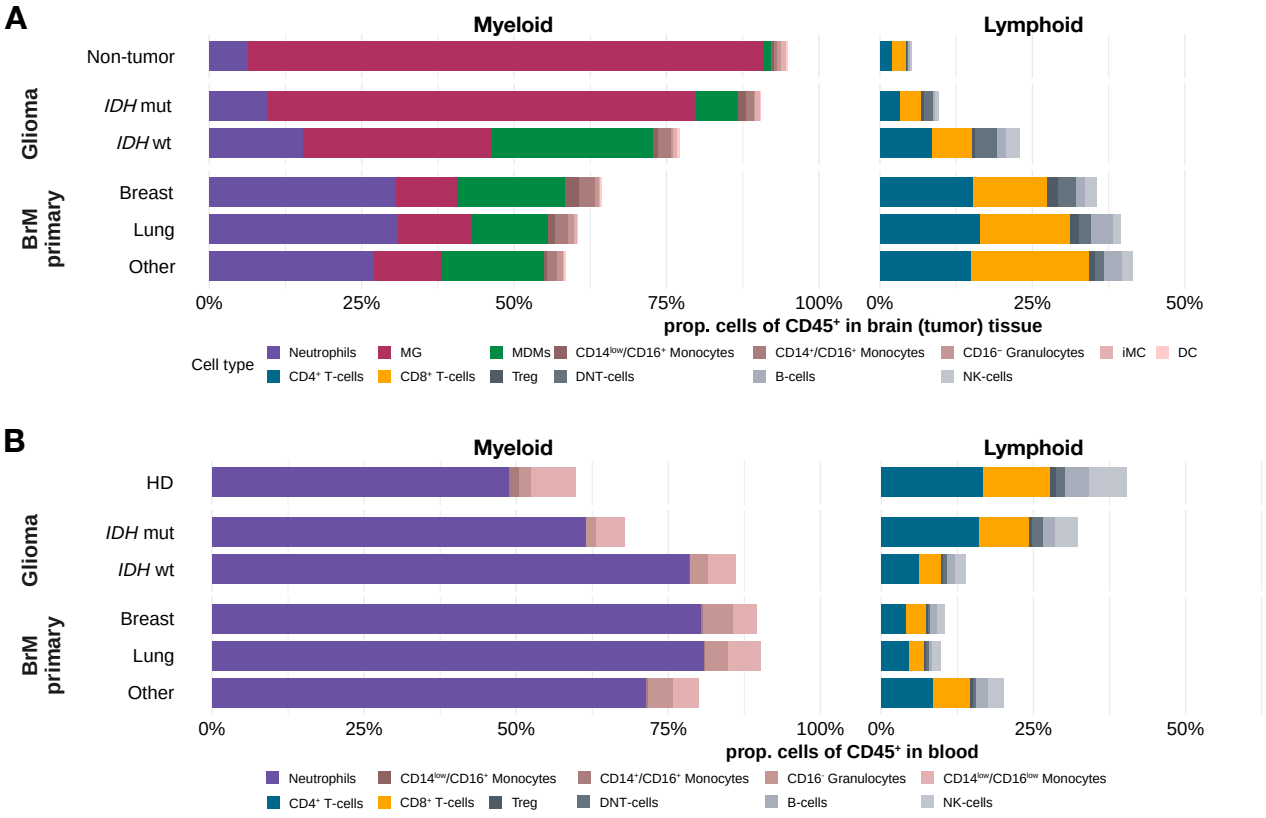

Supplementary Figure 1. Neutrophil abundance in blood and tumor microenvironment of primary and metastatic brain tumor patients, healthy individuals, and non-tumor brain tissue

(**A**) Mean of all immune cell populations in non-tumor (n=11) and tumor tissue ($n_{IDH\ mut}$=31, $n_{IDH\ wt}$=70, $n_{Breast\text{-}BrM}$=15, $n_{Lung\text{-}BrM}$=41, $n_{Other\text{-}BrM}$=24) based on flow cytometry (FCM). Microglia (MG), monocyte-derived macrophages (MDMs), immature monocytes (iMC), dendritic cells (DCs), T-regulatory cells (Tregs), double negative T-cells (DNT-cells). (**B**) Mean of immune cells in whole blood from healthy donors (HD; n=12) and brain tumor patients ($n_{IDH\ mut}$=20, $n_{IDH\ wt}$=43, $n_{Breast\text{-}BrM}$=8, $n_{Lung\text{-}BrM}$=25, $n_{Other\text{-}BrM}$=17) based on FCM.

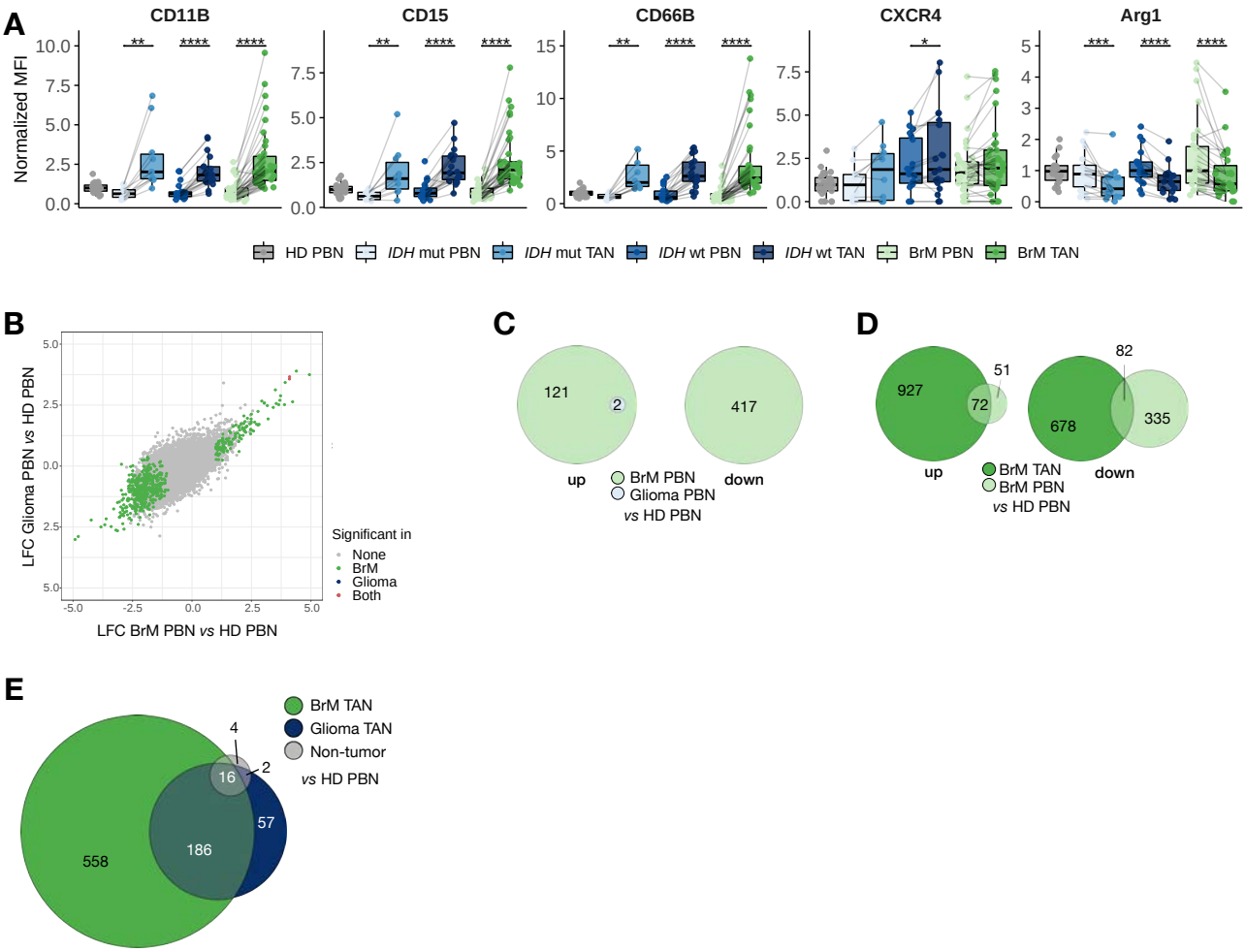
A
CD11B
CD15
CD66B
CXCR4
Arg1
Normalized MFI
HD PBN
IDH mut PBN
IDH mut TAN
IDH wt PBN
IDH wt TAN
BrM PBN
BrM TAN
B
LFC Glioma PBN vs HD PBN
LFC BrM PBN vs HD PBN
Significant in
None
BrM
Glioma
Both
C
121
2
417
up
down
BrM PBN
Glioma PBN
vs HD PBN
D
927
51
72
678
82
335
up
down
BrM TAN
BrM PBN
vs HD PBN
E
BrM TAN
Glioma TAN
Non-tumor
vs HD PBN
558
4
16
2
186
57

Supplementary Figure 2. Neutrophils in human brain (tumor) tissue differ substantially from PBNs

(**A**) Mean fluorescence intensity (MFI) of the indicated markers normalized to HD PBNs (n>14) of matched PBNs and TANs from tumor-bearing patients ($n_{IDH\ mut}$>10, $n_{IDH\ wt}$=19, n_{BrM}>31). Wilcoxon signed-rank test of matched patient neutrophils only. P.adj values: * < 0.05, ** < 0.01, *** < 0.001, **** < 0.0001. (**B**) Dot plot depicting the log-fold change (LFC) of individual genes between BrM/glioma PBNs *vs.* HD (cut-off: p.adj<0.05, BrM-specific differentially expressed genes (DEGs) shown in green, shared DEGs between glioma and BrM shown in red). (**C**) Euler diagram showing the (absence of) overlap of up- and down-regulated differentially expressed genes (DEGs) in glioma and BrM *vs.* HD PBNs from Fig. 2D (cut-off: p.adj<0.05; LFC>1 or <-1). (**D**) Euler diagram depicting the intersect of up- and down-regulated DEGs in BrM TANs and PBNs *vs.* HD PBNs (cut-off: p.adj<0.05; LFC >1 or <-1). (**E**) Euler diagram showing the intersect of down-regulated DEGs in BrM and glioma TANs, and non-tumor brain neutrophils *vs.* HD PBNs (cut-off: p.adj <0.05; LFC <-1).

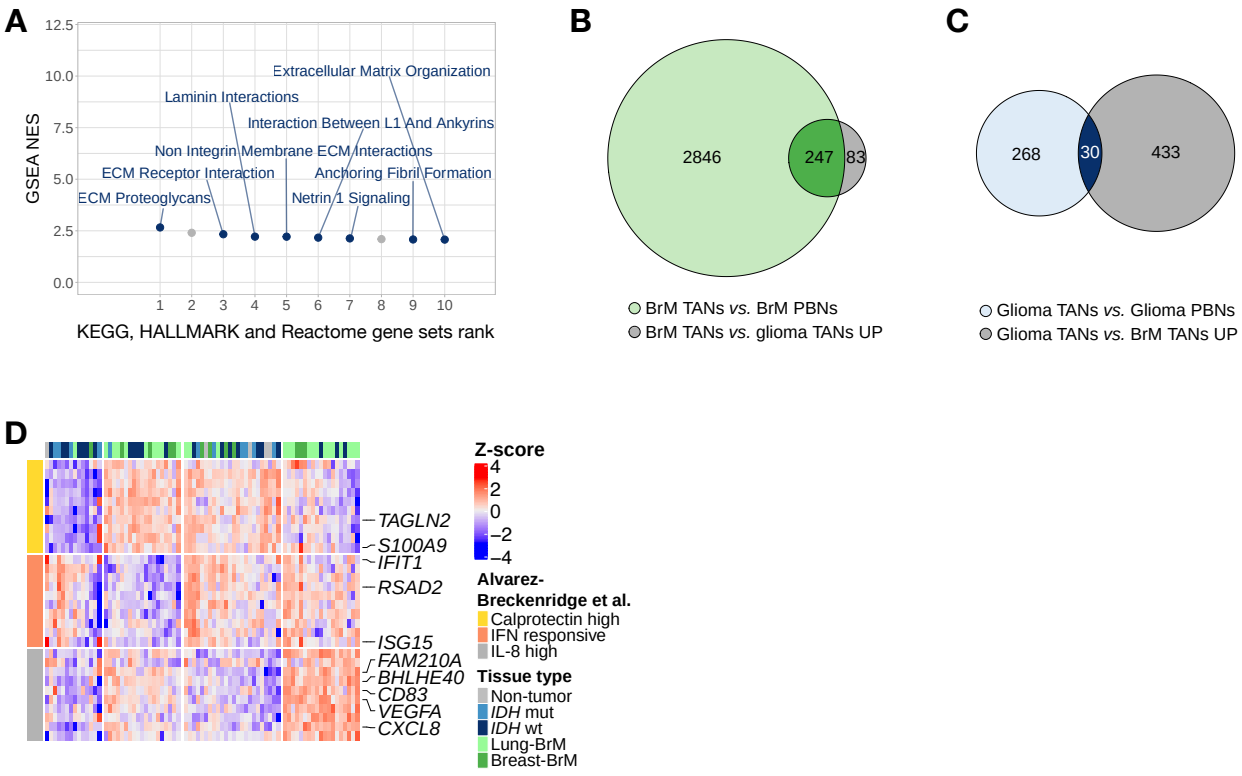
A
GSEA NES
12.5
10.0
7.5
5.0
2.5
0.0
Extracellular Matrix Organization
Laminin Interactions
Interaction Between L1 And Ankyrins
Non Integrin Membrane ECM Interactions
ECM Receptor Interaction
Anchoring Fibril Formation
ECM Proteoglycans
Netrin 1 Signaling
1 2 3 4 5 6 7 8 9 10
KEGG, HALLMARK and Reactome gene sets rank
B
2846
247
83
BrM TANs vs. BrM PBNs
BrM TANs vs. glioma TANs UP
C
268
30
433
Glioma TANs vs. Glioma PBNs
Glioma TANs vs. BrM TANs UP
D
Z-score
4
2
0
−2
−4
TAGLN2
S100A9
IFIT1
RSAD2
ISG15
FAM210A
BHLHE40
CD83
VEGFA
CXCL8
Alvarez-Breckenridge et al.
Calprotectin high
IFN responsive
IL-8 high
Tissue type
Non-tumor
IDH mut
IDH wt
Lung-BrM
Breast-BrM

Supplementary Figure 3. Glioma TANs are enriched in extracellular matrix- and IFN signaling-related transcriptional signatures

(**A**) Top 10 positively and negatively enriched gene sets from gene set enrichment analysis (GSEA) using Hallmark, KEGG and Reactome databases on DEGs comparing glioma TANs *vs.* non-tumor brain neutrophils (cut-off: p.adj<0.05; -1.5>NES>1.5). Highlighted in blue are neurotrophic and extracellular matrix-related pathways. (**B**) Euler diagrams depicting the intersect of BrM *vs*. glioma TANs and BrM TANs *vs.* their matched PBNs (cut-off: p.adj<0.05; LFC>1 or <-1). (**C**) Euler diagrams depicting the intersect of glioma *vs*. BrM TANs and glioma TANs *vs.* their matched PBNs (cut-off: p.adj<0.05; LFC>1 or <-1). (**D)** Heatmap depicting non-tumor neutrophils and brain TANs aligned to the top 10 most variable genes per cluster as defined by the Alvarez-Breckenridge scRNAseq dataset (125). Genes of interest are indicated on the right. Samples were hierarchically clustered.

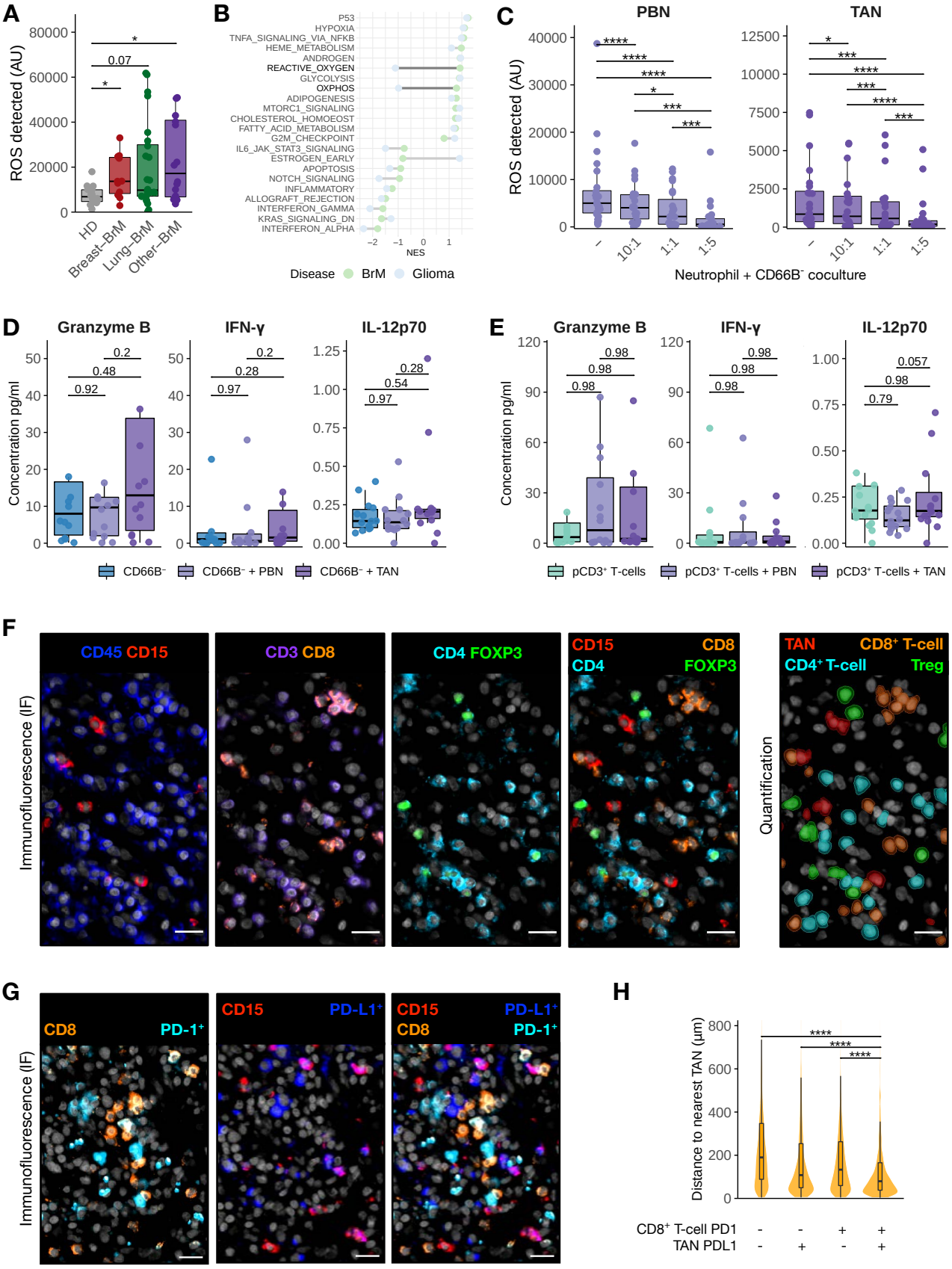
A
ROS detected (AU)
HD
Breast−BrM
Lung−BrM
Other−BrM
B
P53
HYPOXIA
TNFA_SIGNALING_VIA_NFKB
HEME_METABOLISM
ANDROGEN
REACTIVE_OXYGEN
GLYCOLYSIS
OXPHOS
ADIPOGENESIS
MTORC1_SIGNALING
CHOLESTEROL_HOMOEOST
FATTY_ACID_METABOLISM
G2M_CHECKPOINT
IL6_JAK_STAT3_SIGNALING
ESTROGEN_EARLY
APOPTOSIS
NOTCH_SIGNALING
INFLAMMATORY
ALLOGRAFT_REJECTION
INTERFERON_GAMMA
KRAS_SIGNALING_DN
INTERFERON_ALPHA
NES
Disease BrM Glioma
C
PBN
TAN
ROS detected (AU)
Neutrophil + CD66B⁻ coculture
D
Granzyme B
IFN-γ
IL-12p70
Concentration pg/ml
CD66B⁻
CD66B⁻ + PBN
CD66B⁻ + TAN
E
Granzyme B
IFN-γ
IL-12p70
Concentration pg/ml
pCD3⁺ T-cells
pCD3⁺ T-cells + PBN
pCD3⁺ T-cells + TAN
F
CD45 CD15
CD3 CD8
CD4 FOXP3
CD15 CD8 CD4 FOXP3
TAN CD8⁺ T-cell CD4⁺ T-cell Treg
Immunofluorescence (IF)
Quantification
G
CD8 PD-1⁺
CD15 PD-L1⁺
CD15 CD8 PD-L1⁺ PD-1⁺
Immunofluorescence (IF)
H
Distance to nearest TAN (µm)
CD8⁺ T-cell PD1
TAN PDL1

Supplementary Figure 4. Brain TANs show a T-cell suppressive potential which is not mediated via ROS

(**A**) ROS detected in PBNs from HD (n=18), and BrM bearing patients ($n_{Breast\text{-}BrM}$=11, $n_{Lung\text{-}BrM}$=24, $n_{Other\text{-}BrM}$=16). Wilcoxon rank-sum test. P.adj value: * <0.05. (**B**) GSEA based on Hallmark database in glioma and BrM TANs *vs.* HD PBNs. ROS-related pathways are highlighted in dark grey (cut-off p-value < 0.05). (**C**) Neutrophil ROS production in a titrated coculture with CD66B-neg TME population ($n_{IDH\ mut}$=6, $n_{IDH\ wt}$=9, n_{BrM}=9). Wilcoxon signed-rank test. P.adj value: * <0.05, *** <0.001, **** <0.0001. (**D**) Cytokine concentration in pg/ml in supernatant of $CD66B^-$ cells cocultured with either PBNs or TANs for 96h ($n_{IDH\ mut}$=1, $n_{IDH\ wt}$=7, n_{BrM}=6). Wilcoxon signed-rank test, p.adj values as shown. (**E**) Cytokine concentration in pg/ml in supernatant of peripheral $CD3^+$ T-cells (pCD3) cocultured with either PBNs or TANs for 96h ($n_{IDH\ mut}$=2, $n_{IDH\ wt}$=8, n_{BrM}=6). Wilcoxon signed-rank test, p.adj values as shown. (**F**) Representative IF image and cell type quantification of T-cells and TANs in a lung-BrM, with cell type-specific identification of TANs ($CD45^+/CD15^+$), $CD8^+$ T-cells ($CD45^+/CD3^+/CD8^+$), $CD4^+$ T-cells ($CD45^+/CD3^+/CD4^+/FOXP3^-$) and Tregs ($CD45^+/CD3^+/CD4^+/FOXP3^+$). (**G**) Representative IF image and cell type quantification of $CD8^+$ T-cells ($CD45^+/CD3^+/CD8^+$), TANs ($CD45^+/CD15^+$), PD-L1 and PD-1 in a lung-BrM sample, corresponding to the quantification shown in Fig. 4K. Scale bars in (F, G): 20 µm. (**H**) Distance of individual $CD8^+$ $T\text{-cells}_{(n=54,495)}$ to TANs stratified by their respective expression of PD-1 and PD-L1 (n_{BrM}=20, $n_{IDH\ wt}$=7 analyzed together). Wilcoxon rank-sum test. P.adj value: **** <0.0001.

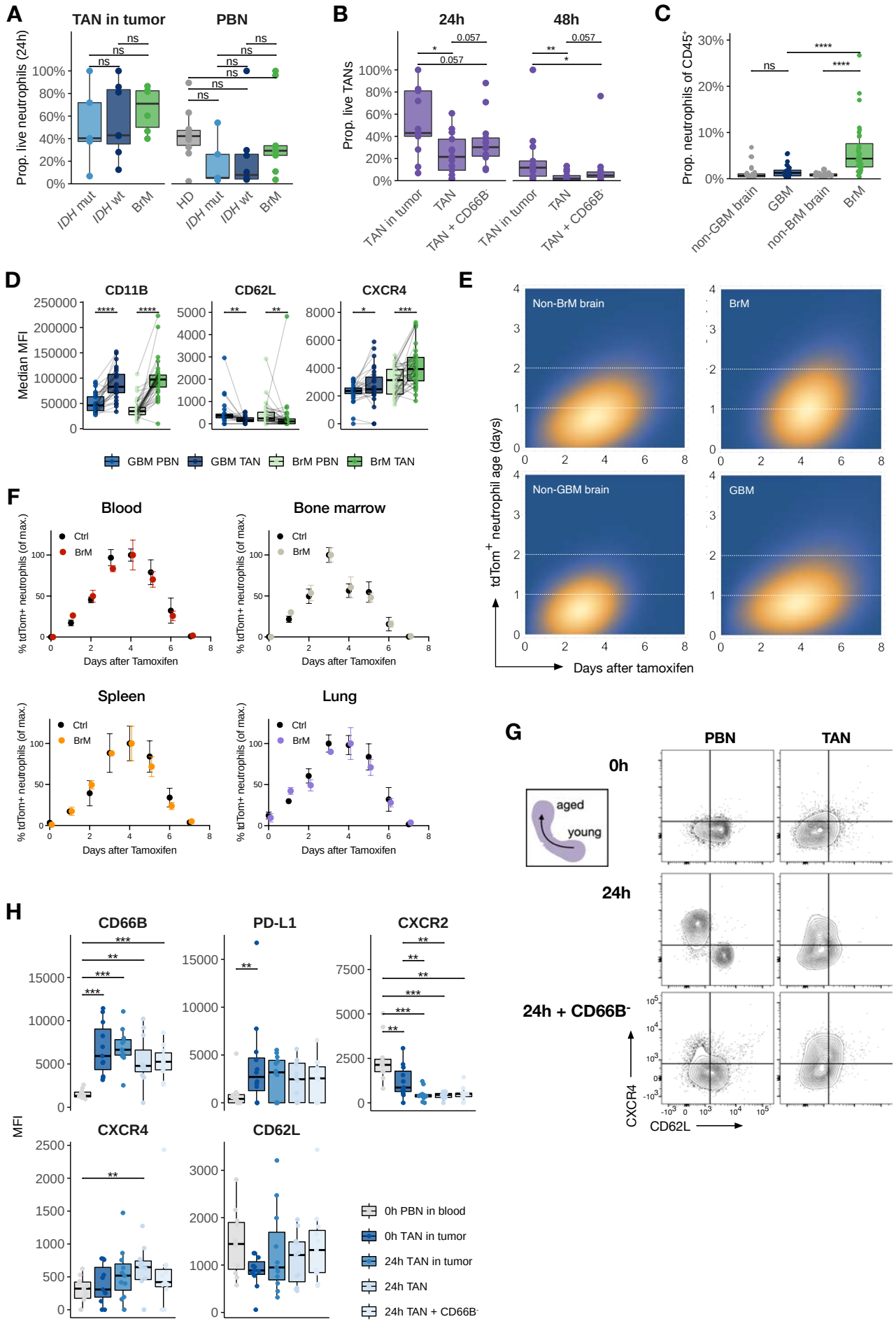
A
TAN in tumor
PBN
Prop. live neutrophils (24h)
IDH mut
IDH wt
BrM
HD
B
24h
48h
Prop. live TANs
TAN in tumor
TAN
TAN + CD66B-
C
Prop. neutrophils of CD45+
non-GBM brain
GBM
non-BrM brain
D
CD11B
CD62L
CXCR4
Median MFI
GBM PBN
GBM TAN
BrM PBN
BrM TAN
E
Non-BrM brain
BrM
Non-GBM brain
GBM
tdTom+ neutrophil age (days)
Days after tamoxifen
F
Blood
Bone marrow
Spleen
Lung
Ctrl
BrM
% tdTom+ neutrophils (of max.)
Days after Tamoxifen
G
PBN
TAN
0h
24h
24h + CD66B-
aged
young
CXCR4
CD62L
H
CD66B
PD-L1
CXCR2
CXCR4
CD62L
MFI
0h PBN in blood
0h TAN in tumor
24h TAN in tumor
24h TAN
24h TAN + CD66B-

Supplementary Figure 5. Phenotypic and lifespan alterations of TANs result from a combination of cell-intrinsic and microenvironment-mediated effects

(**A**) 24h-survival of patient TANs ($n_{IDH\ mut}$=5, $n_{IDH\ wt}$=7, n_{BrM}=6), PBNs from HD (n=10) and patient PBNs ($n_{IDH\ mut}$=5, $n_{IDH\ wt}$=8, n_{BrM}=9). (**B**) Proportion of live TANs in matched whole tumor, isolated TANs and in coculture with CD66B-neg TME populations after 24h and 48h. Wilcoxon signed-rank test. P.adj values: * <0.05, ** <0.01. (**C**) Proportion of $Ly6G^{+}$ neutrophils of $CD45^{+}$ immune cells in Ntv-a;$iLy6G^{tdTomato}$ glioblastoma $(GBM)_{(n=27)}$ and $iLy6G^{tdTomato}$ $BrM_{(n=40)}$ mouse model and non-tumor bearing control murine brain ($n_{non\text{-}GBM}$=27, $n_{non\text{-}BrM}$=39). Wilcoxon rank-sum test. P.adj values: **** <0.0001. (**D**) Median MFI of the indicated markers in Ntv-a;$iLy6G^{tdTomato}$ GBM-bearing mice (n=27) and $iLy6G^{tdTomato}$ BrM bearing mice (n=40). Wilcoxon signed-rank test. P.adj values: * <0.05, ** <0.01, *** <0.001, **** <0.0001. (**E**) Density plots of the age distribution of neutrophils in non-tumor brain, BrM and GBM models over time. (**F**) Proportion of $tdTomato^{+}$ neutrophils normalized to the maximum in a series of different non-brain tissues isolated from non-tumor (Ctrl) and BrM-bearing $iLy6G^{tdTomato}$ mice over 8 consecutive days. >3 mice are shown per timepoint from 6 individual experiments. (**G**) Representative FCM plots depicting the aging trajectory based on CXCR4 and CD62L expression in matched PBNs and TANs over time and in coculture with the CD66B-neg TME isolated from a BrM patient sample. (**H**) MFI of neutrophil markers in PBNs in whole blood *vs.* TANs over time and in the presence of the CD66B-neg TME ($n_{IDH\ mut}$=4, $n_{IDH\ wt}$=5, n_{BrM}=4). Wilcoxon signed-rank test, p.adj values: ** <0.01, *** <0.001.

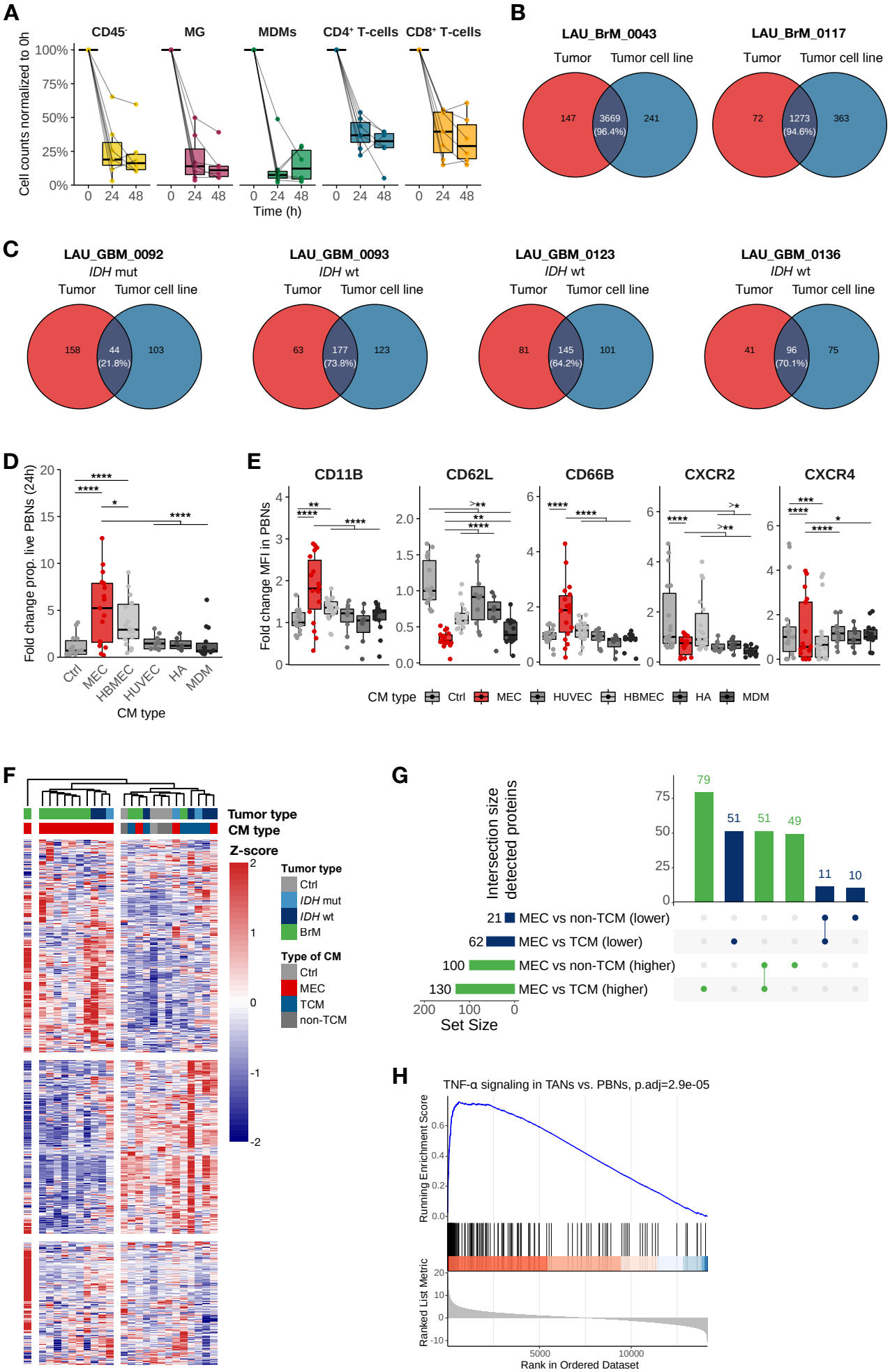
A
CD45-
MG
MDMs
CD4+ T-cells
CD8+ T-cells
Cell counts normalized to 0h
100%
75%
50%
25%
0%
0
24
48
Time (h)
B
LAU_BrM_0043
Tumor
Tumor cell line
147
3669
(96.4%)
241
LAU_BrM_0117
Tumor
Tumor cell line
72
1273
(94.6%)
363
C
LAU_GBM_0092
IDH mut
Tumor
Tumor cell line
158
44
(21.8%)
103
LAU_GBM_0093
IDH wt
Tumor
Tumor cell line
63
177
(73.8%)
123
LAU_GBM_0123
IDH wt
Tumor
Tumor cell line
81
145
(64.2%)
101
LAU_GBM_0136
IDH wt
Tumor
Tumor cell line
41
96
(70.1%)
75
D
Fold change prop. live PBNs (24h)
Ctrl
MEC
HBMEC
HUVEC
HA
MDM
CM type
E
CD11B
CD62L
CD66B
CXCR2
CXCR4
Fold change MFI in PBNs
CM type
Ctrl
MEC
HUVEC
HBMEC
HA
MDM
F
Tumor type
CM type
Z-score
Tumor type
Ctrl
IDH mut
IDH wt
BrM
Type of CM
Ctrl
MEC
TCM
non-TCM
G
Intersection size
detected proteins
79
51
51
49
11
10
21 MEC vs non-TCM (lower)
62 MEC vs TCM (lower)
100 MEC vs non-TCM (higher)
130 MEC vs TCM (higher)
Set Size
H
TNF-α signaling in TANs vs. PBNs, p.adj=2.9e-05
Running Enrichment Score
Ranked List Metric
Rank in Ordered Dataset

Supplementary Figure 6. The brain TME is a rich source of soluble factors which alter neutrophil phenotype and lifespan

(**A**) Normalized survival in % (compared to 0h) of mixed environmental culture (MEC) populations over time in culture ($n_{IDH\ mut}$=1, $n_{IDH\ wt}$=3, n_{BrM}=3). (**B**) Venn diagram of somatic mutations identified by whole exome sequencing (WES) in matched BrM MEC and tumor cell lines (n=2). (**C**) Venn diagram of somatic mutations identified by WES of *IDH* mut (n=1) and *IDH* wt gliomas (n=3) matched MEC and tumor cell lines. (**D**) Fold change in 24h-survival of HD PBNs (n=25) cultured in conditioned media (CM) of tumor naïve cell lines (non-TCM; n_{MEC}=6, $n_{HBMEC,\ HUVEC,\ HA}$=1, n_{MDM}=3) *vs*. control medium. Mixed-effect model using CM type as fixed effect and HD ID as random effect: ANOVA p-value=2.941 x 10^{7}, p.adj values: * <0.05, **** <0.0001. (**E**) Fold change MFI in HD PBN (n=12) cultured for 6 h in CM (n_{MEC}=6, $n_{HBMEC,\ HUVEC,\ HA}$ =1, n_{MDM}=3) *vs*. control medium. Mixed effect model with CM type as fixed effect and HD ID as random effect. P.adj values: * <0.05, ** <0.01, *** <0.001, **** <0.0001. (**F**) Unsupervised heatmap of proteins detected in brain tumor MEC-CM, TCM, CM from a panel of normal cell lines (non-TCM), and control media. The sample outlier is breast-BrM LAU_BrM_0092, which was not characterized by any evident difference compared to other samples based on known clinical factors. (**G**) Visualization of differentially detected proteins in glioma and BrM MEC-CM compared to tumor-conditioned media (TCM) and non-TCM. The unique $n_{proteins}$ found in individual groups and intersects are indicated on top of the bars (cut-off: p<0.05). (**H**) GSEA of TNF-α signaling pathways in glioma and BrM TANs compared to matched PBNs.

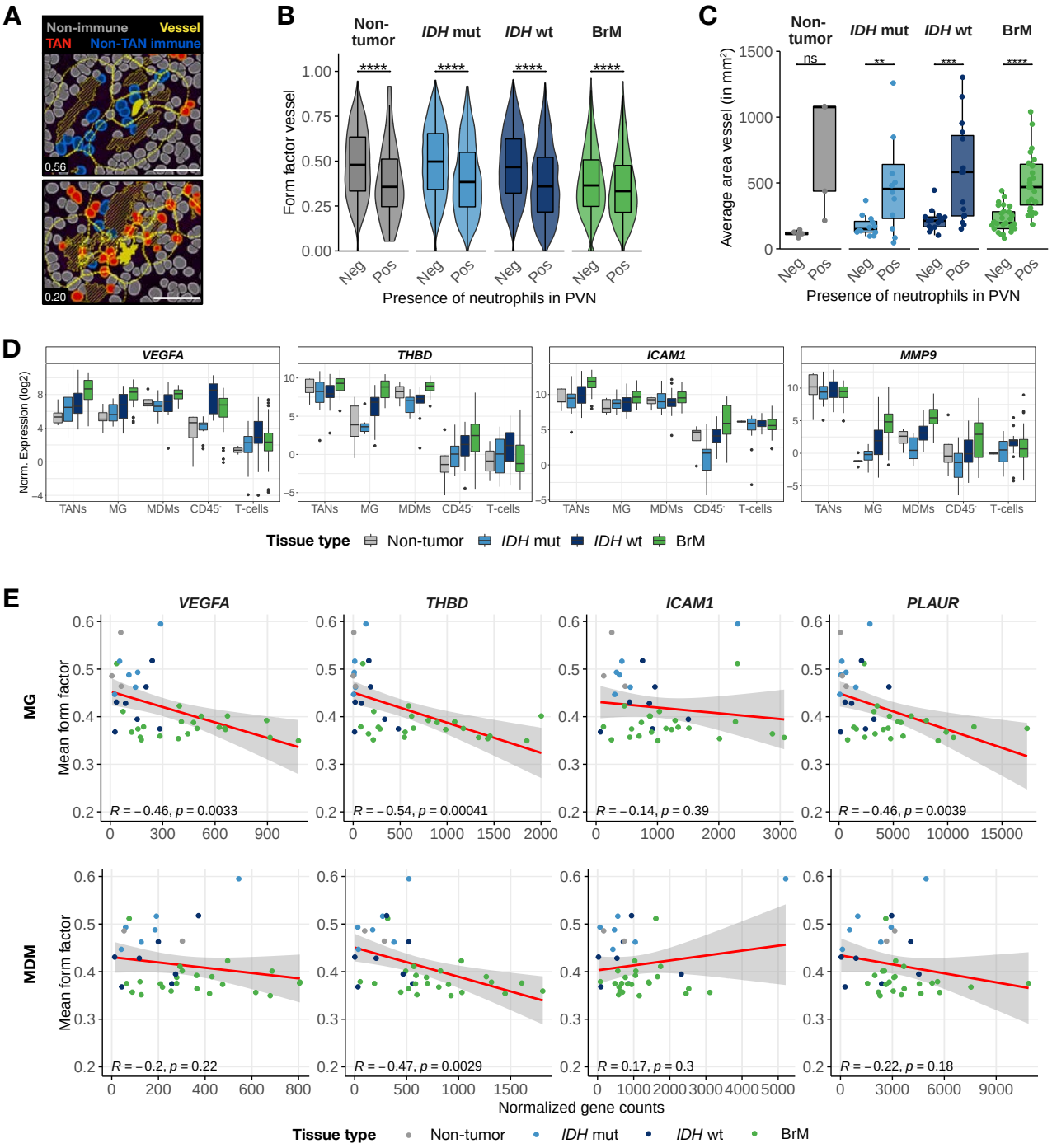
A
Non-immune
Vessel
TAN
Non-TAN immune
0.56
0.20
B
Non-tumor
IDH mut
IDH wt
BrM
Form factor vessel
Neg
Pos
Presence of neutrophils in PVN
C
Average area vessel (in mm²)
ns
Presence of neutrophils in PVN
D
VEGFA
THBD
ICAM1
MMP9
Norm. Expression (log2)
TANs
MG
MDMs
CD45-
T-cells
Tissue type
Non-tumor
IDH mut
IDH wt
BrM
E
VEGFA
THBD
ICAM1
PLAUR
MG
MDM
Mean form factor
R = −0.46, p = 0.0033
R = −0.54, p = 0.00041
R = −0.14, p = 0.39
R = −0.46, p = 0.0039
R = −0.2, p = 0.22
R = −0.47, p = 0.0029
R = 0.17, p = 0.3
R = −0.22, p = 0.18
Normalized gene counts
Tissue type
Non-tumor
IDH mut
IDH wt
BrM

Supplementary Figure 7. Brain TANs localize proximally to myeloid cells and are enriched in pro-angiogenic factors

(**A**) Representative lung-BrM IF images of vessels ($CD31^+$); inserts show the form factor value of the highlighted vessel. Scale bars: 50 µm. (**B**) Form factor of individual vessels grouped by absence (Neg, $n_{Non\text{-}tumor}$ = 35,078, $n_{IDH\ mut}$ = 54,015, $n_{IDH\ wt}$ = 62,261, n_{BrM} = 79,225) or presence (Pos, $n_{Non\text{-}tumor}$ = 67, $n_{IDH\ mut}$ = 1,630, $n_{IDH\ wt}$ = 2,745, n_{BrM} = 37,242) of TANs in the PVN from non-tumor (n=5) and tumor tissue ($n_{IDH\ mut}$=12, $n_{IDH\ wt}$=15, n_{BrM}=27). Wilcoxon signed-rank test, p.adj value: **** <0.0001. (**C**) Mean vessel size in mm^2 stratified by the presence of TANs in the PVN on the same dataset shown in (C). Wilcoxon signed-rank test, p.adj values: ** <0.01, *** <0.001, **** <0.0001. (**D**) Normalized log2-transformed gene expression of pro-angiogenic genes across main TME populations. (**E**) Correlation between mean vessel form factor *vs*. normalized gene counts of angiogenesis-associated genes in non-tumor, glioma and BrM MG and MDM using the Pearson method.

7.4 Phenotypic diversity of T-cells in primary and metastatic brain tumors revealed by multiomic interrogation

Vladimir Wischnewski [1,2], Roeltje R. Maas [1,2,3,4]*, Klara Soukup [1,2]*, Giovanni Galletti [5], Mara Kornete [1,2], Paola Guerrero Aruffo [1,2], Nadine Fournier [6], Pratyaksha Wirapati [6], Joao Lourenco [6], Alice Scarpa [5], Roy T. Daniel [4], Andreas F. Hottinger [1,8], Jean-Philippe Brouland [7], Agnese Losurdo [9], Emanuele Voulaz [10,11], Marco Alloisio [10,11], Monika E Hegi [3,4], Enrico Lugli [5], and Johanna A. Joyce [1,2,12]

[1] Department of Oncology, University of Lausanne, Lausanne, Switzerland.

[2] Ludwig Institute for Cancer Research, University of Lausanne, Switzerland.

[3] Neuroscience Research Center, Centre Hospitalier Universitaire Vaudois, Lausanne, Switzerland.

[4] Department of Neurosurgery, Centre Hospitalier Universitaire Vaudois, Lausanne, Switzerland.

[5] Laboratory of Translational Immunology, IRCCS Humanitas Research Hospital, Milan, Italy.

[6] Translational Data Science, Swiss Institute of Bioinformatics, Lausanne, Switzerland.

[7] Department of Pathology, Centre Hospitalier Universitaire Vaudois, Lausanne, Switzerland.

[8] Department of Oncology & Clinical Neurosciences, The Lundin Brain & Spine Tumor Center, Centre Hospitalier Universitaire Vaudois, Lausanne, Switzerland.

[9] Oncology Department, IRCCS Humanitas Research Hospital, Milan, Italy.

[10] Department of Biomedical Sciences, Humanitas University, Milan, Italy.

[11] Division of Thoracic, IRCCS Humanitas Research Hospital, Milan, Italy.

[12] Lead contact.

* Equal contribution

Abstract

The immune-specialized environment of the healthy brain is tightly regulated to prevent excessive neuro-inflammation. However, upon cancer development, a tissue-specific conflict between brain-preserving immune-suppression and tumor-directed immune activation may ensue. To interrogate potential roles of T-cells in this process, we profiled these cells from patients with primary or metastatic brain cancers, via integrated analyses on the single-cell and bulk population levels. We identified both interpatient similarity and variability in T cell biology, with phenotypical differences being most pronounced in a subgroup of brain metastasis (BrM) patients, characterized by accumulation of *CXCL13*-expressing CD39+ potentially tumor-reactive T-cells (pTRT). In this subgroup, high pTRT abundance was comparable to that in primary lung cancer, whereas all other brain tumors had low levels similar to

primary breast cancer. These findings indicate that T-cell-mediated tumor reactivity can occur in specific BrM, thereby providing a strategy for future patient stratification for treatment with immunotherapy.

7.5 Immunogenomic analysis of human brain metastases reveals diverse immune landscapes across genetically distinct tumors

Ángel F. Álvarez-Prado[1,2], Roeltje R. Maas[1,2,3,4]*, Klara Soukup[1,2]*, Florian Klemm[1,2], Mara Kornete[1,2], Fanny S. Krebs[1,5], Vincent Zoete[1,5], Sabina Berezowska[6], Jean-Philippe Brouland[6], Andreas F. Hottinger[1,7], Roy T. Daniel[4], Monika E. Hegi[3,4], and Johanna A. Joyce [1,2,8, #]

[1] Department of Oncology, University of Lausanne, Lausanne, Switzerland.

[2] Ludwig Institute for Cancer Research, University of Lausanne, Switzerland.

[3] Neuroscience Research Center, Centre Hospitalier Universitaire Vaudois, Lausanne, Switzerland.

[4] Department of Neurosurgery, Centre Hospitalier Universitaire Vaudois, Lausanne, Switzerland.

[5] Swiss Institute of Bioinformatics, Lausanne, Switzerland.

[6] Department of Pathology, Centre Hospitalier Universitaire Vaudois, Lausanne, Switzerland.

[7] Brain and Spine Tumor Center, Departments of Clinical Neurosciences and Oncology, Centre Hospitalier Universitaire Vaudois, Lausanne, Switzerland.

[8] Lead contact.

* Equal contribution.

AbstractBrain metastases (BrMs) are the most common form of brain tumors in adults, and frequently originate from lung and breast primary cancers. BrMs are associated with a high mortality, emphasizing the need for more effective therapies. Genetic profiling of primary tumors is increasingly used as part of the effort to guide targeted therapies against BrMs, and immune-based strategies for the treatment of metastatic cancer are gaining momentum. However, the tumor immune microenvironment (TIME) of BrM is extremely heterogeneous and whether specific genetic profiles are associated with distinct immune states remains unclear. Here, we performed an extensive characterization of the immunogenomic landscape of human BrMs by combining whole-exome/whole-genome sequencing, RNA-sequencing of immune cell populations, flow cytometry, immunofluorescence staining and tissue imaging analyses. This revealed unique TIME phenotypes in genetically distinct lung- and breast-BrMs, thereby indicating new perspectives for the development of personalized immunotherapies tailored by the genetic makeup of the tumors.

8. Discussion

The research described in this thesis focuses on interrogating the functions and phenotypes of myeloid cells in the brain TIME of primary and metastatic brain malignancies. Standard of care therapy for gliomas and BrMs is not curative, and leaves patients with a survival prospect of months to a few years (19, 22). Moreover, novel T-cell targeting therapies (e.g. ICB) have little effect in gliomas (141, 142), and currently only show promising effects in a subset of lung- and melanoma-BrMs (136-140). The lack of a robust immune response with ICB is likely in part due to the immunosuppressive TIME of brain malignancies (166). In many extracranial cancers, both tumor cells and myeloid cells have an immunosuppressive capacity and interestingly we and others have shown that myeloid cells are highly abundant in gliomas and BrMs (see Chapter 7.2 and (49, 50)). However, whether myeloid cells are immunosuppressive or confer other effector functions in human brain malignancies was not known prior to my thesis research. Therefore, we analyzed MG, MDMs, and TANs in both glioma and BrM patients and investigated whether they are differentially educated in primary vs. metastatic brain tumors.

To answer these questions, we first generated an extensive experimental pipeline for the comprehensive multi-omic interrogation of human non-tumor brain, glioma and BrM tissue, to maximize the use of these precious tissues in an integrated and orthogonal manner (see Chapter 7.1 (162)). Implementing these various analyses allowed us to explore MG and MDMs in depth, and as separate entities in the human setting for the first time. Using this powerful strategy, we discovered that MG and MDMs are educated by the brain TIME at multiple different levels, including in a diverging and brain tumor subtype-specific manner (Chapter 7.2 and (49)). Furthermore, using a similar approach but with an additional focus on the *ex vivo* functional methods described in Chapter 7.1 (162), we investigated the role of neutrophils in brain malignancies. Our main findings in this study (Chapter 7.3) revealed that neutrophils are phenotypically, transcriptionally, and functionally altered upon entry into brain tumors and these changes are predominantly induced by the myeloid cell compartment of the brain TIME via TNF-α. While both glioma and BrM

TANs confer immunosuppressive and pro-angiogenic phenotypes, BrM TANs show an additional level of pro-inflammatory alterations. In the sections below, I will discuss in further depth the major conclusions of each of these studies, along with some interesting aspects for future research.

8.1 An integrated pipeline to investigate human brain TIME

In the first Results sub-chapter of this thesis (Chapter 7.1, (162)), we designed and optimized an experimental pipeline to investigate the immune cell landscape in non-tumor brain, glioma and BrM tissues, as well as matched patient's blood. The pipeline describes a protocol for the spatial interrogation of these tissues as well as enzymatic digestion protocols to analyze the brain TIME in cell suspension. A series of experimental analyses can be performed on the digested tissue, including FCM phenotyping, fluorescence activated cell (FAC)-sorting, and bulk RNAseq. In addition, this pipeline describes the powerful strategy of using conditioned media (CM) from the brain tumor microenvironmental cultures (MEC) we derived to educate naïve circulating immune cells. This gives one the opportunity to mimic *ex vivo* the alterations that peripheral immune cells undergo upon entry into the brain TME. We also provided specific guidelines regarding the size of the tissue required for each of the different modules, to maximize the number of methods applicable per sample. This allows for cross-method validation and the possibility to assess the TIME in an orthogonal way on an individual sample basis. This experimental pipeline is not only being used in all analyses of patient samples in our lab; it has also since been implemented by many labs around the world.

The size of the brain tissue is also the most critical limitation of this pipeline, especially when investigating rare cell populations. Considering the striking contrast in TIME composition in non-tumor brain tissue or *IDH* mut glioma when compared to BrMs in particular, it may become challenging to use similar methods for the same cell types across these different samples. In addition, the different tissue types for which this pipeline was optimized have very diverse features. Particularly the high myelin content in non-tumor brain and *IDH* mut gliomas requires more stringent processing of the tissue to extract single cells and render the epitopes readily available for

antibody binding (208). In tissues with lower myelin content, this harsher treatment may have the opposite effect and data can be lost rather than gained. In our pipeline we therefore aimed to strike a balance between these extremes and emphasize that not all tissues require the same treatment to gain similar biological information. However, this also highlights the importance of using the same protocol across different tissue types as the method employed can potentially distort the biological data retrieved.

Lastly it is important to highlight that this pipeline was developed and optimized to retrieve immune cells from brain tissues. As such, enzymatic digestion might not yield a satisfying result when investigating non-immune cells. Potentially a Percoll density gradient might enable more efficient recovery of such cells (209). Since the use of distinct digestion methods for different cell types complicates the accurate investigation of interactions between these cells, we ideally need to move to a single method that allows for the extraction of all brain-associated cells at similar recovery rates. Currently such a method is not in place, and therefore this requires further investigation.

With the continuous progress of scientific methodologies, the brain TIME pipeline described in this sub-chapter will also require regular updating. Indeed, for the study described in Chapter 7.3, we have already extended several modules since the *Nature Protocols* publication in 2021 (162). The *ex vivo* module was expanded with coculture experiments of CD66B-neg MEC and peripheral T-cells with TANs and PBNs (see Chapter 7.3). We further optimized our IF pipeline into a sequential IF protocol where the same brain tumor tissue section could be re-stained up to six times (see Chapter 7.3). Although this greatly expanded the possibilities to spatially explore the brain TME, there are still limitations regarding the number of rounds and markers one can stain for. The next technologies to integrate in this pipeline would therefore be the implementation of spatial transcriptomics (210) and scRNAseq (Wischnewski et al. manuscript submitted and (125, 194, 195, 211)). These two methods would allow one to investigate cellular interactions in the brain TIME on a single cell level, while maintaining spatial information. This would allow us to generate a brain TIME

interaction atlas, similar as to what recently was reported for the immune system under homeostasis (212). In our current pipeline we either lose the spatial integrity (e.g., FCM, FAC-sorting, proteomics) or are underpowered by the number of markers we can stain (e.g., IF, sequential IF). However, these methods would not circumvent the limited availability of brain tumor tissue. To resolve this an attractive approach would be to generate glioma and BrM organoids (213, 214), which would facilitate investigating the brain TIME while easily removing or altering a specific cell population, or testing different therapeutics.

8.2 The brain TIME composition and transcriptional alterations in MG and MDMs are driven by tumor subtype

Implementing the pipeline described in Chapter 7.1 (162) we investigated MG and MDMs in non-tumor brain tissue as well as *IDH* mut and wt gliomas, and BrMs. In our study (49), along with a mass cytometry by time-of-flight (CyTOF) focused study from the Becher lab that was published in the same *Cell* issue (50), the human brain TAM compartment was separated into tumor-associated MG and MDMs in gliomas and BrMs for the first time. One of the most striking discoveries was the considerable diversity in TIME composition between the different brain tumor types. While *IDH* mut gliomas comprise almost only MG, *IDH* wt gliomas and BrMs have a much more diverse myeloid compartment with the influx of MDMs and TANs. The high abundance of TANs discovered in both *IDH* wt GBMs and BrMs was a key discovery that instigated the study described in Chapter 7.3. In BrMs specifically, the lymphoid compartment expands with substantial quantities of $CD4^+$ and $CD8^+$ T-cells. These differences in T-cell presence can potentially explain why ICB thus far only showed promising results in a subset of BrMs (136-140), but not in GBMs (141, 142). After all, ICB will not be effective in T-cell deserted tumors. In line with this, the BrM subtypes most responsive to ICB treatment were also the tumors with the highest proportion of $CD4^+$ and $CD8^+$ T-cells (i.e., lung-BrM and melanoma-BrM).

The characterization of macrophages has historically involved classification into an M1 and M2 polarization status, which since then has been much disputed (62). When assessing brain tumor-associated MG and MDMs transcriptionally, we found that

neither fitted solely within a M1 or M2 phenotype. This corresponds with the more accepted current perspective that TAMs are highly plastic and heterogeneous cells, and this has been similarly observed in other brain tumor studies (50, 79). When we compared differential gene expression in MG and MDMs, more commonalities between disease types (glioma vs. BrM) than the individual cell types (MG vs. MDM) were observed. This indicates that the difference in ontogeny has a long-lasting effect on transcriptional adaptations even in the context of cancer. However, we also observed crucial differences between BrM- and glioma-TAMs, which were predominantly associated with enrichment of extracellular remodeling and metastatic cascade-associated pathways in BrMs. Interestingly, *IDH* wt specific MDM gene signatures, including the genes *RUNX3, ACKR3, HERPUD1, FCGR2B, IL19* and others, correlated with a poor survival in both *IDH* mut and wt gliomas. In similar studies based on CyTOF, distinct transcriptional classes of MDMs were observed, each aligning with a different brain tumor subtype (50, 194). In one of these studies the presence of $CD206^{+}$ MDMs in *IDH* mut gliomas was shown to have a good prognosis in patient survival (50). Taken together this highlights that there are both cell type-specific and disease-specific transcriptional alterations in T-MG and T-MDMs, which can function as prognostic markers.

Given the poor response to ICB in gliomas, we further investigated the interaction between T-cells and TAMs. Like DCs, TAMs can exhibit an antigen presentation potential and prime the adaptive immune system to recognize and kill cancer cells (215). In gliomas, especially MDMs showed increased expression of MHC-II, which is required for antigen presentation. Additionally, pathways associated with antigen presentation were enriched in MDMs. However, this potential apparently does not positively impact ICB treatment efficiency. Not surprisingly, when cross-referencing MG and MDM bulk RNAseq data to gene sets associated with innate anti-PD-1 resistance some overlap was observed. It is important to note that T-cells are not in close spatial proximity to TAMs in gliomas, which is in part a representation of the low influx of T-cells in general. Effective antigen presentation requires APCs to bind T-cells, but for the suppression of T-cells it is less clear what the required distance between cell types is. In BrMs there is more direct contact between T-cells and TAMs,

however both $CD4^+$ and $CD8^+$ T-cells have an exhausted phenotype in these tumors. Whether they are exhausted due to chronic antigen presentation by the tumor, active immunosuppression by tumor cells, macrophages or other cells needs to be further investigated.

Given that this was predominantly prepared as a resource paper for the research community, minimal functional validation was performed in the study, which is a limitation. Functional validation is especially crucial considering that transcriptional analysis of MG and MDM in gliomas and BrMs did not give us a conclusive answer to whether TAMs generally are pro- or anti-tumorigenic and if they suppress T-cell function or not. MG and MDM would need to be FAC-sorted and cocultured with brain tumor cells to assess their cytotoxic potential. Cocultures with either tumor infiltrating T-cells or peripheral T-cells will help investigate their immunosuppressive potential. Moreover, this can help elucidate if there are meaningful functional differences between T-MG and T-MDM. While several differences are observed in their abundance, phenotype, and transcriptional activity, it is unclear whether this translates into altered functionality.

8.3 The human brain TIME stimulates an immunosuppressive and pro-angiogenic TAN phenotype

In the third Results sub-chapter we shifted our focus from MG and MDMs to TANs in brain tumors. Despite their high abundance, especially in *IDH* wt GBMs and BrMs, TANs have only minimally been studied in human brain malignancies (93, 125, 130, 131) and murine models of brain cancer (93, 110, 126-128) to date. Chapter 7.3 thus represents the first in-depth characterization of neutrophils in both gliomas and BrMs. We concluded that myeloid cells are likely the main recruiters of TANs in both tumor types, as recruitment factors are most highly expressed in these populations and increase with tumor grade. Some of the recruitment factors we identified (e.g., CXCL1, CXCL2, CXCL5, IL-8) are well-described chemoattractants produced by tumor cells in other cancers (91), but in the context of brain malignancies their expression does not compare to that produced by TANs and TAMs. TAMs have been described as important regulators of neutrophil recruitment in several murine cancer models (216-

219). Depletion of macrophages was mostly associated with increased neutrophil recruitment (216-218). However, in the case of increased TAM activation or migration, higher TAN recruitment was observed in both cancer (219, 220) and inflammatory contexts (221-223). In brain tumors, TAN recruitment by TAMs has not been explicitly studied to date, and *ex* vivo experiments will be required to validate that TAMs can indeed effectively recruit neutrophils. This could be performed using cell migration assays, for example. Additionally, it is important to note that the recruitment factor analysis was performed from bulk RNAseq data, in samples isolated from enzymatically digested brain tumors. As we did not FAC-separate distinct non-tumor $CD45^-$ populations (e.g., astrocytes, oligodendrocytes, neurons, endothelial cells), this may affect our interpretation of the contribution of TAN recruitment by tumor cells and/or non-immune brain resident cells. For example, endothelial cells play a crucial role in neutrophil recruitment in many cancers (224) as well as neuroinflammation (225, 226).

Through our extensive comparison of PBNs and TANs in patient samples, we could detect a robust pro-inflammatory and activated phenotype, combined with a prolonged survival in TANs. This phenotype was completely independent of tumor type and grade. Even in non-tumor brain, transcriptional adaptations in neutrophils were readily detected, indicating rapid adjustment to the altered metabolic environment. Similar to TAMs (Chapter 7.2 (49)), additional layers of pro-inflammatory transcriptional changes were observed in brain tumor TANs. They were most prominent in BrM TANs and TNF-a mediated. Interestingly, the BrM subtype is also of importance as lung-BrM TANs transcriptionally cluster with scRNAseq data of primary lung cancer TANs, while breast-BrM TANs did not. Such rapid tissue-specific adaptations of neutrophils have similarly been reported in several other organ types (79, 122, 124, 227). These data clearly indicate that the brain environment, brain tumor type, and BrM subtype all contribute to transcriptional alterations in TANs. Initially we hypothesized that comparing glioma- and BrM-TANs transcriptionally would help identify the role of neutrophils in the formation of metastasis specifically. However, aside from their pro-angiogenic gene expression, there were no BrM-TAN specific pathways identified that indicated potential functions aiding in the formation of metastasis (e.g., epithelial

mesenchymal transition, extracellular matrix remodeling). This was similar for BrM-PBNs, where only broad pro-inflammatory signatures were observed in comparison to HD PBNs. Interestingly, in a lung cancer mouse model, pro-tumoral transcriptional alterations in neutrophils could already be observed in the bone marrow (228). To date, this result has not been validated in human studies. Moreover, one obvious limitation of the murine study is that SiglecF, the phenotypic marker the authors used to distinguish pro- and anti-tumoral neutrophils (228) is not expressed by human neutrophils (229). Additionally, it is plausible that pro-metastatic attributes of neutrophils are not due to transcriptional changes per se, but rather post-translational alterations regarding their granule content, for example. Since neutrophils have such low transcriptional activity (121), they have been excluded from many RNAseq analyses to date. Therefore, pathway databases (e.g., Hallmark, KEGG, GO-BP, REACTOME) might not be very familiar with transcriptional changes in neutrophils and how they relate to their functionality. This highlights that the role of TANs in human gliomas and BrMs requires further exploration on additional functional levels.

Even though distinct transcriptional alterations were observed depending on the brain tumor subtype, functionally TANs behaved similarly. Interestingly, ROS detection was decreased in TANs from both gliomas and BrMs compared to matched PBNs. Neutrophils decreased their ROS production immediately upon contact with the brain TME or associated soluble factors, indicating suppression of neutrophil ROS release by the brain TME. This is in contrast with a study by Yee et al. showing that increased ROS production by TANs was associated with tumor cytotoxicity in a mouse model of GBM (110). Similar observations were made in other cancer mouse models (108, 109, 115, 230). Here it needs to be stressed that murine and human neutrophils are intrinsically different, also with regards to the MPO-ROS activation pathway and baseline MPO levels (129). In humans certain phosphatase-binding subunits are crucial for the regulation of ROS, which are not relevant in mice (231). It has been established that the TME can scavenge ROS or suppress its production (232) and in our MEC-CM protein analysis several proteins were detected that can suppress ROS (i.e., Ceruloplasmin (182, 183), GLO-1 (184)). Further experiments could be proposed, for example to inhibit these factors in the MEC-CM and assess the effect on ROS

production by PBNs. Of note, although ROS detection was decreased in glioma and BrM TANs, an increase in ROS was measured in BrM PBNs specifically. Similar findings were observed in PBNs of patients with metastatic breast cancer (180).

As we did not detect a direct anti-tumoral response, we interrogated if TANs are pro-tumoral via suppression of T-cell function. Phenotypically we could establish that TANs are likely immunosuppressive as their PD-L1 expression is increased compared to PBNs. Expression of Arg1 is decreased in TANs, which can either be indicative of decreased Arg1 production, or the release of Arg1 to the extracellular space, which may mediate T-cell inhibition (119). In direct cocultures of T-cells with TANs, the cytokine profile of both tumor infiltrating and peripheral T-cells was skewed to a Treg-like profile. Moreover, no cytotoxic $CD8^+$ T-cell associated cytokines were detected. More importantly, $PD\text{-}1^+$ $CD8^+$ T-cells reside in close spatial proximity to $PD\text{-}L1^+$ TANs, which would be required for effective immunosuppression via the PD-1 – PD-L1 axis. Taken together, these data suggest that brain TANs may have pro-tumorigenic capacity by suppressing $CD8^+$ T-cells and simultaneously stimulating Tregs. This is in concordance with previous studies in mouse models of both hepatocellular cancer (233, 234) and BrMs (93). The next steps should be to test if the cytotoxic capacity of $CD8^+$ T-cells is truly suppressed by TANs in an *ex vivo* coculture system. Glioma and BrM tumor cell lines would need to be transduced with a tumor antigen (e.g., NY-ESO) and matched peripheral $CD8^+$ T-cells transduced with the TCR recognizing the tumor antigen. Consecutively, non-matched glioma/BrM-TANs would need to be isolated and cocultured with the transduced tumor cell line and $CD8^+$ T-cells. Using a similar setup, the proliferation of $CD8^+$ T-cells in the presence and absence of TANs should be assessed. Future research should also be pointed towards targeting the immunosuppressive phenotype of TANs directly. Here one could consider PD-L1 blockade (234, 235), or Arginine supplementation in *ex vivo* culture systems of microenvironmental cultures (MEC), or in the transduced model as described above. Interestingly, arginine supplementation has thus far shown promising results in reversing peripheral immune suppression in GBM patients (236). In tumor infiltrating T-cells of several cancer types, mixed observations have been made regarding the efficacy of Arginine supplementation (237-239). Therefore, the effect of both anti-PD-

L1 and Arginine supplementation in gliomas and BrMs needs to be further investigated.

Aside from their immunosuppressive phenotype we additionally observed a pro-angiogenic phenotype in TANs, with increased expression of pro-angiogenic genes (e.g., *THBD, ICAM1, VEGFA, MMP9)* in TANs from *IDH* wt glioma and BrMs. Furthermore, expression levels were correlated with the degree of vessel deformity in individual samples. Moreover, TANs are more abundant in the perivascular niche of highly deformed and leaky vessels. Although these data allude to a pro-angiogenic phenotype of TANs, more extensive analysis needs to be conducted to confirm a functional relationship between TANs and endothelial cells. The observed phenotype also does not rule out that the BBB is altered due to non-TAN related reasons. In addition, the increased abundance of TANs in the perivascular niche of deformed and leakier vessels may be due to easier access into the brain. To address the relationship between the BBB and TANs in more depth, more extensive IF analysis could be performed, linking expression intensity of pro-angiogenic proteins by TANs to receptor expression in endothelial cells. A more comprehensive approach would be the use of spatial transcriptomics. With this method phenotypic and transcriptional single cell data can be obtained without losing spatial information. This would allow us to take a more unbiased approach by mapping receptor-ligand interactions between the BBB and the TME while also taking the degree of deformity and astrocyte and pericyte coverage of the vessels into account. Other approaches to validate a functional relationship between TANs and the BBB would be to target the pro-angiogenic phenotype of TANs in *ex vivo* coculture systems of HBMECs with TANs. Anti-VEGF treatment has been implemented in several clinical studies including in GBM-bearing patients (160, 161). Although the pro-angiogenic TAN phenotype under anti-VEGF therapy has not been studied extensively, there are indications in both GBM (130) and other tumors (240, 241) that TANs are involved in its therapy resistance. Thus, only targeting angiogenesis by anti-VEGF will not suffice and additional pro-angiogenic pathways in neutrophils would need to be inhibited. Several other pro-angiogenic markers either do not have an available inhibitor (e.g., ICAM-1 (242)) or they are crucial for the coagulation cascade (e.g., THBD (243)). However, there are several

selective inhibitors available for MMP9 which effectively target neutrophils, which may be worth evaluating (113, 244).

To determine which potentially targetable factors are responsible for the observed TAN phenotype and longevity, we designed *ex vivo* experiments of PBNs either in coculture with MEC, or cultured in CM from MEC. As both experimental setups were aimed to recapitulate and assess brain TAN-like features (e.g., prolonged survival, activated phenotype), we characterized the protein expression in CM from whole tumor MEC. This MEC-education effect was driven by TNF-a and several other pro-inflammatory proteins, which were predominantly produced by MG and MDMs. TNF-a is associated with an activated neutrophil phenotype that can both be pro- (220, 245) and anti-tumoral (92, 180). Another MEC-associated protein, IL-9, could directly be linked to TAN longevity (185). Several factors (e.g. Ceruloplasmin and GLO-1) can suppress ROS production and were discussed above. Interesting next steps will be to investigate if any of these MEC-associated proteins are targetable and can revert the immunosuppressive and pro-angiogenic TAN phenotypes. One experiment to follow up on is to supply PBNs with a cocktail of the MEC-associated proteins, as was done with TNF-a alone. With this approach the soluble proteins responsible for inducing different aspects of the TAN phenotype can be further narrowed down. Another experimental setup would involve the depletion of potential TAN-educating proteins from the MEC-CM, and subsequently assessing the neutrophil phenotype after co-culture with MEC, or after culturing in MEC-CM. This can further aid in the identification of targets to therapeutically modulate TANs. Alternatively, instead of targeting MEC-CM proteins, another interesting option would be to target the TME populations secreting these soluble proteins. Indeed, given that MG and MDMs were identified as the main producers of these proteins, the reeducation of macrophages via CSF-1R inhibition might indirectly impact the neutrophil phenotype and survival in brain tumors.

As these *ex vivo* experiments require large quantities of human brain tumor tissue, murine brain tumor models may facilitate the execution of several of the experiments proposed. Thus far we observed that part of the TAN phenotype and their prolonged survival in murine tumors is similar to the human setting. However, we would first need

to investigate if both the immunosuppressive and pro-angiogenic phenotypes are present in murine GBM and BrM models, if they are similarly educated by MEC-CM, and if MEC-associated proteins in mouse models show overlap with our human results. Considering the substantial differences between human and murine neutrophils (129), one needs to be critical when using mouse models to study neutrophil function with the goal of translating such findings back to the clinic. While at the transcriptional level, there is relevant overlap between mouse and human neutrophils (122), at the post-translational level, there are several crucial differences (129). For our specific study, several of our findings may be challenging to reproduce, because in murine models i) the circulating neutrophil population is far smaller, ii) the MPO-ROS pathway has different requirements, iii) several chemoattractants found in humans (e.g., IL-8, CCL13) are absent, iv) and Arg1 is not constitutively expressed as is the case in human neutrophils (129). However, for rigorous *in vivo* functional studies, we are still heavily dependent on animal models. For the next steps in the study described in Chapter 7.3, murine brain tumor models could help answer if the recruitment of neutrophils can be inhibited by blocking recruitment factors that are conserved between human and mice. This would circumvent targeting TANs directly and prevent potential immunosuppressive and pro-angiogenic neutrophils from populating the brain TME. Brain tumor-bearing mouse models could additionally show if suppression of neutrophil recruitment would affect tumor growth and animal survival.

Taken together, the research in this thesis has contributed to the first comprehensive interrogation of the TIME in non-tumor brain, glioma and BrM immune landscape in humans, with a specific focus on myeloid cells. By studying individual patient samples both on the single cell level and in their undisrupted spatial context, we aimed to interrogate their role in the TIME in an orthogonal manner. We found that MG, MDMs and TANs all show disease specific transcriptional alterations, which are most pronounced in BrMs. Even though TAMs and TANs have extensive differences in their phenotypes, functionality, and longevity under homeostasis, in the context of brain tumors they additionally converge towards several similarities. While for MG and MDM we observe indications of an immunosuppressive phenotype at the transcriptional level, in TANs this became more apparent on both the functional and

spatial levels. The TAN and TAM phenotypes further allude to tumorigenic functions based on the expression of pro-angiogenic genes. Additionally, we concluded that TANs were predominantly educated by TAMs, through pro-inflammatory proteins. Considering that they colocalize in both *IDH* wt gliomas and BrMs, this further strengthens the notion of a myeloid niche within brain malignancies. Further studies will be instructive to identify potential targets that can prevent neutrophils and TAMs from assuming these immunosuppressive and pro-angiogenic phenotypes within the brain TME.

The extent to which TAMs and TANs collaborate to form a pro-tumoral environment is poorly studied, particularly in the brain TME. However, we do know that TAMs and TANs are very plastic cells that in a number of studies have been associated with therapy resistance (130, 246, 247). Additionally, depletion of TAMs can lead to an increase of TANs (216-218), and conversely, effective TAN depletion is dependent on TAM function (248). This raises the question as to whether their plasticity allows one myeloid cell population to take over the pro-tumoral functions of the other. While we observed that MG, MDMs and TANs all showed increased expression of pro-angiogenic genes, the specific pro-angiogenic pathways were not identical. Similarly, the immunosuppressive phenotype appears to be mediated by PD-L1 in TANs, while MG and MDMs express PD-L1 at very low levels, or not at all. These shared phenotypes, which are nonetheless moderated via different pathways, could further bolster a synergistic immunosuppressive and pro-angiogenic niche. Additionally, these perspectives highlight that TAMs and TANs should perhaps be targeted simultaneously (217) to truly alter the pro-tumoral niche that is generated by myeloid cells, and to prevent potential therapy resistance that can be induced by the remaining myeloid cell population. Therefore, it would be of great interest to further study the complex interactions between myeloid cells, particularly in the context of ICB and anti-angiogenic therapies. As it currently stands, this is both lacking in the general cancer field as well as in brain tumors specifically. Such studies will be invaluable to identify new therapeutic targets, and to further our understanding of the factors determining the efficiency of cancer therapies, as well as the mechanisms underlying therapeutic resistance.

9. References

1. Mtui E, Gruener G, Dockery P. Fitzgerald's Clinical Neuroanatomy and Neuroscience. 8th ed: Elsevier; 2020.
2. Bonfanti L, Charvet CJ. Brain Plasticity in Humans and Model Systems: Advances, Challenges, and Future Directions. Int J Mol Sci. 2021;22(17).
3. Allen NJ, Lyons DA. Glia as architects of central nervous system formation and function. Science (New York, NY). 2018;362(6411):181-5.
4. Allen NJ, Eroglu C. Cell Biology of Astrocyte-Synapse Interactions. Neuron. 2017;96(3):697-708.
5. Nortley R, Attwell D. Control of brain energy supply by astrocytes. Curr Opin Neurobiol. 2017;47:80-5.
6. Durkee CA, Araque A. Diversity and Specificity of Astrocyte-neuron Communication. Neuroscience. 2019;396:73-8.
7. Prinz M, Jung S, Priller J. Microglia Biology: One Century of Evolving Concepts. Cell. 2019;179(2):292-311.
8. Krüger-Genge A, Blocki A, Franke RP, Jung F. Vascular Endothelial Cell Biology: An Update. Int J Mol Sci. 2019;20(18).
9. Arvanitis CD, Ferraro GB, Jain RK. The blood-brain barrier and blood-tumour barrier in brain tumours and metastases. Nature reviews Cancer. 2020;20(1):26-41.
10. Van Dyken P, Lacoste B. Impact of Metabolic Syndrome on Neuroinflammation and the Blood-Brain Barrier. Front Neurosci. 2018;12:930.
11. Chowdhury EA, Noorani B, Alqahtani F, Bhalerao A, Raut S, Sivandzade F, et al. Understanding the brain uptake and permeability of small molecules through the BBB: A technical overview. J Cereb Blood Flow Metab. 2021;41(8):1797-820.
12. Forrester JV, McMenamin PG, Dando SJ. CNS infection and immune privilege. Nat Rev Neurosci. 2018;19(11):655-71.
13. Da Mesquita S, Fu Z, Kipnis J. The Meningeal Lymphatic System: A New Player in Neurophysiology. Neuron. 2018;100(2):375-88.
14. Oliver G, Kipnis J, Randolph GJ, Harvey NL. The Lymphatic Vasculature in the 21(st) Century: Novel Functional Roles in Homeostasis and Disease. Cell. 2020;182(2):270-96.
15. Hu X, Deng Q, Ma L, Li Q, Chen Y, Liao Y, et al. Meningeal lymphatic vessels regulate brain tumor drainage and immunity. Cell Res. 2020;30(3):229-43.
16. Song E, Mao T, Dong H, Boisserand LSB, Antila S, Bosenberg M, et al. VEGF-C-driven lymphatic drainage enables immunosurveillance of brain tumours. Nature. 2020;577(7792):689-94.
17. Matthews HK, Bertoli C, de Bruin RAM. Cell cycle control in cancer. Nat Rev Mol Cell Biol. 2022;23(1):74-88.
18. Hanahan D. Hallmarks of Cancer: New Dimensions. Cancer discovery. 2022;12(1):31-46.
19. Ostrom QT, Cioffi G, Waite K, Kruchko C, Barnholtz-Sloan JS. CBTRUS Statistical Report: Primary Brain and Other Central Nervous System Tumors Diagnosed in the United States in 2014-2018. Neuro-oncology. 2021;23(12 Suppl 2):iii1-iii105.
20. Louis DN, Perry A, Wesseling P, Brat DJ, Cree IA, Figarella-Branger D, et al. The 2021 WHO Classification of Tumors of the Central Nervous System: a summary. Neuro-oncology. 2021;23(8):1231-51.

21. Bollig-Fischer A, Michelhaugh S, Ali-Fehmi R, Mittal S. The molecular genomics of metastatic brain tumours. OA Mol Oncol. 2013;1(1).
22. Cagney DN, Martin AM, Catalano PJ, Redig AJ, Lin NU, Lee EQ, et al. Incidence and prognosis of patients with brain metastases at diagnosis of systemic malignancy: a population-based study. Neuro-oncology. 2017;19(11):1511-21.
23. Vogelbaum MA, Brown PD, Messersmith H, Brastianos PK, Burri S, Cahill D, et al. Treatment for Brain Metastases: ASCO-SNO-ASTRO Guideline. J Clin Oncol. 2022;40(5):492-516.
24. Valiente M, Ahluwalia MS, Boire A, Brastianos PK, Goldberg SB, Lee EQ, et al. The Evolving Landscape of Brain Metastasis. Trends Cancer. 2018;4(3):176-96.
25. Achrol AS, Rennert RC, Anders C, Soffietti R, Ahluwalia MS, Nayak L, et al. Brain metastases. Nature Reviews Disease Primers. 2019;5(1):5.
26. Barnholtz-Sloan JS, Sloan AE, Davis FG, Vigneau FD, Lai P, Sawaya RE. Incidence proportions of brain metastases in patients diagnosed (1973 to 2001) in the Metropolitan Detroit Cancer Surveillance System. J Clin Oncol. 2004;22(14):2865-72.
27. Lamba N, Wen PY, Aizer AA. Epidemiology of brain metastases and leptomeningeal disease. Neuro-oncology. 2021;23(9):1447-56.
28. Sacks P, Rahman M. Epidemiology of Brain Metastases. Neurosurg Clin N Am. 2020;31(4):481-8.
29. Cahill J, LoBiondo-Wood G, Bergstrom N, Armstrong T. Brain tumor symptoms as antecedents to uncertainty: an integrative review. J Nurs Scholarsh. 2012;44(2):145-55.
30. van Breemen MS, Wilms EB, Vecht CJ. Epilepsy in patients with brain tumours: epidemiology, mechanisms, and management. The Lancet Neurology. 2007;6(5):421-30.
31. Chan V, Sahgal A, Egeto P, Schweizer T, Das S. Incidence of seizure in adult patients with intracranial metastatic disease. Journal of neuro-oncology. 2017;131(3):619-24.
32. Noh T, Walbert T. Brain metastasis: clinical manifestations, symptom management, and palliative care. Handb Clin Neurol. 2018;149:75-88.
33. Larjavaara S, Mäntylä R, Salminen T, Haapasalo H, Raitanen J, Jääskeläinen J, et al. Incidence of gliomas by anatomic location. Neuro-oncology. 2007;9(3):319-25.
34. Barajas RF, Jr., Cha S. Metastasis in Adult Brain Tumors. Neuroimaging Clin N Am. 2016;26(4):601-20.
35. Stensjøen AL, Berntsen EM, Jakola AS, Solheim O. When did the glioblastoma start growing, and how much time can be gained from surgical resection? A model based on the pattern of glioblastoma growth in vivo. Clin Neurol Neurosurg. 2018;170:38-42.
36. Weller M, van den Bent M, Preusser M, Le Rhun E, Tonn JC, Minniti G, et al. EANO guidelines on the diagnosis and treatment of diffuse gliomas of adulthood. Nature reviews Clinical oncology. 2021;18(3):170-86.
37. Hegi ME, Liu L, Herman JG, Stupp R, Wick W, Weller M, et al. Correlation of O6-methylguanine methyltransferase (MGMT) promoter methylation with clinical outcomes in glioblastoma and clinical strategies to modulate MGMT activity. J Clin Oncol. 2008;26(25):4189-99.

38. Stupp R, Hegi ME, Mason WP, van den Bent MJ, Taphoorn MJ, Janzer RC, et al. Effects of radiotherapy with concomitant and adjuvant temozolomide versus radiotherapy alone on survival in glioblastoma in a randomised phase III study: 5-year analysis of the EORTC-NCIC trial. Lancet Oncol. 2009;10(5):459-66.
39. Hanahan D, Weinberg RA. The hallmarks of cancer. Cell. 2000;100(1):57-70.
40. Quail DF, Joyce JA. Microenvironmental regulation of tumor progression and metastasis. Nat Med. 2013;19(11):1423-37.
41. Hanahan D, Weinberg RA. Hallmarks of cancer: the next generation. Cell. 2011;144(5):646-74.
42. Quail DF, Joyce JA. The Microenvironmental Landscape of Brain Tumors. Cancer Cell. 2017;31(3):326-41.
43. Bejarano L, Jordao MJC, Joyce JA. Therapeutic Targeting of the Tumor Microenvironment. Cancer discovery. 2021;11(4):933-59.
44. Watkins S, Robel S, Kimbrough IF, Robert SM, Ellis-Davies G, Sontheimer H. Disruption of astrocyte-vascular coupling and the blood-brain barrier by invading glioma cells. Nature communications. 2014;5:4196.
45. Dubois LG, Campanati L, Righy C, D'Andrea-Meira I, Spohr TC, Porto-Carreiro I, et al. Gliomas and the vascular fragility of the blood brain barrier. Front Cell Neurosci. 2014;8:418.
46. Hinshaw DC, Shevde LA. The Tumor Microenvironment Innately Modulates Cancer Progression. Cancer research. 2019;79(18):4557-66.
47. Chen DS, Mellman I. Oncology meets immunology: the cancer-immunity cycle. Immunity. 2013;39(1):1-10.
48. Parham P. The immune system. 5th ed: W. W. Norton & Company; 2021.
49. Klemm F, Maas RR, Bowman RL, Kornete M, Soukup K, Nassiri S, et al. Interrogation of the Microenvironmental Landscape in Brain Tumors Reveals Disease-Specific Alterations of Immune Cells. Cell. 2020;181(7):1643-60.e17.
50. Friebel E, Kapolou K, Unger S, Nunez NG, Utz S, Rushing EJ, et al. Single-Cell Mapping of Human Brain Cancer Reveals Tumor-Specific Instruction of Tissue-Invading Leukocytes. Cell. 2020;181(7):1626-42 e20.
51. Demaria O, Cornen S, Daëron M, Morel Y, Medzhitov R, Vivier E. Harnessing innate immunity in cancer therapy. Nature. 2019;574(7776):45-56.
52. Ginhoux F, Greter M, Leboeuf M, Nandi S, See P, Gokhan S, et al. Fate mapping analysis reveals that adult microglia derive from primitive macrophages. Science (New York, NY). 2010;330(6005):841-5.
53. Chen P, Hsu WH, Chang A, Tan Z, Lan Z, Zhou A, et al. Circadian Regulator CLOCK Recruits Immune-Suppressive Microglia into the GBM Tumor Microenvironment. Cancer discovery. 2020;10(3):371-81.
54. Zhang Q, Wang J, Yao X, Wu S, Tian W, Gan C, et al. Programmed Cell Death 10 Mediated CXCL2-CXCR2 Signaling in Regulating Tumor-Associated Microglia/Macrophages Recruitment in Glioblastoma. Front Immunol. 2021;12:637053.
55. Liu H, Sun Y, Zhang Q, Jin W, Gordon RE, Zhang Y, et al. Pro-inflammatory and proliferative microglia drive progression of glioblastoma. Cell Rep. 2021;36(11):109718.
56. Gautier EL, Shay T, Miller J, Greter M, Jakubzick C, Ivanov S, et al. Gene-expression profiles and transcriptional regulatory pathways that underlie the identity and diversity of mouse tissue macrophages. Nat Immunol. 2012;13(11):1118-28.

57. Bennett ML, Bennett FC, Liddelow SA, Ajami B, Zamanian JL, Fernhoff NB, et al. New tools for studying microglia in the mouse and human CNS. Proceedings of the National Academy of Sciences of the United States of America. 2016;113(12):E1738-46.
58. Bowman RL, Klemm F, Akkari L, Pyonteck SM, Sevenich L, Quail DF, et al. Macrophage Ontogeny Underlies Differences in Tumor-Specific Education in Brain Malignancies. Cell Rep. 2016;17(9):2445-59.
59. Kenkhuis B, Somarakis A, Kleindouwel LRT, van Roon-Mom WMC, Höllt T, van der Weerd L. Co-expression patterns of microglia markers Iba1, TMEM119 and P2RY12 in Alzheimer's disease. Neurobiol Dis. 2022;167:105684.
60. Haynes SE, Hollopeter G, Yang G, Kurpius D, Dailey ME, Gan WB, et al. The P2Y12 receptor regulates microglial activation by extracellular nucleotides. Nat Neurosci. 2006;9(12):1512-9.
61. Zhu C, Kros JM, van der Weiden M, Zheng P, Cheng C, Mustafa DA. Expression site of P2RY12 in residential microglial cells in astrocytomas correlates with M1 and M2 marker expression and tumor grade. Acta Neuropathol Commun. 2017;5(1):4.
62. Ginhoux F, Schultze JL, Murray PJ, Ochando J, Biswas SK. New insights into the multidimensional concept of macrophage ontogeny, activation and function. Nat Immunol. 2016;17(1):34-40.
63. Cassetta L, Pollard JW. Tumor-associated macrophages. Curr Biol. 2020;30(6):R246-r8.
64. Pyonteck SM, Akkari L, Schuhmacher AJ, Bowman RL, Sevenich L, Quail DF, et al. CSF-1R inhibition alters macrophage polarization and blocks glioma progression. Nat Med. 2013;19(10):1264-72.
65. Quail DF, Bowman RL, Akkari L, Quick ML, Schuhmacher AJ, Huse JT, et al. The tumor microenvironment underlies acquired resistance to CSF-1R inhibition in gliomas. Science (New York, NY). 2016;352(6288):aad3018.
66. Akkari L, Bowman RL, Tessier J, Klemm F, Handgraaf SM, de Groot M, et al. Dynamic changes in glioma macrophage populations after radiotherapy reveal CSF-1R inhibition as a strategy to overcome resistance. Science translational medicine. 2020;12(552).
67. Klemm F, Möckl A, Salamero-Boix A, Alekseeva T, Schäffer A, Schulz M, et al. Compensatory CSF2-driven macrophage activation promotes adaptive resistance to CSF1R inhibition in breast-to-brain metastasis. Nat Cancer. 2021;2(10):1086-101.
68. De Boeck A, Ahn BY, D'Mello C, Lun X, Menon SV, Alshehri MM, et al. Glioma-derived IL-33 orchestrates an inflammatory brain tumor microenvironment that accelerates glioma progression. Nature communications. 2020;11(1):4997.
69. Wang YC, Wang X, Yu J, Ma F, Li Z, Zhou Y, et al. Targeting monoamine oxidase A-regulated tumor-associated macrophage polarization for cancer immunotherapy. Nature communications. 2021;12(1):3530.
70. Gangoso E, Southgate B, Bradley L, Rus S, Galvez-Cancino F, McGivern N, et al. Glioblastomas acquire myeloid-affiliated transcriptional programs via epigenetic immunoediting to elicit immune evasion. Cell. 2021;184(9):2454-70.e26.
71. Guldner IH, Wang Q, Yang L, Golomb SM, Zhao Z, Lopez JA, et al. CNS-Native Myeloid Cells Drive Immune Suppression in the Brain Metastatic Niche through Cxcl10. Cell. 2020;183(5):1234-48.e25.

72. Geraldo LH, Xu Y, Jacob L, Pibouin-Fragner L, Rao R, Maissa N, et al. SLIT2/ROBO signaling in tumor-associated microglia and macrophages drives glioblastoma immunosuppression and vascular dysmorphia. J Clin Invest. 2021;131(16).
73. Chen P, Zhao D, Li J, Liang X, Li J, Chang A, et al. Symbiotic Macrophage-Glioma Cell Interactions Reveal Synthetic Lethality in PTEN-Null Glioma. Cancer Cell. 2019;35(6):868-84.e6.
74. Quail DF, Amulic B, Aziz M, Barnes BJ, Eruslanov E, Fridlender ZG, et al. Neutrophil phenotypes and functions in cancer: A consensus statement. J Exp Med. 2022;219(6).
75. Adrover JM, Nicolas-Avila JA, Hidalgo A. Aging: A Temporal Dimension for Neutrophils. Trends Immunol. 2016;37(5):334-45.
76. Lahoz-Beneytez J, Elemans M, Zhang Y, Ahmed R, Salam A, Block M, et al. Human neutrophil kinetics: modeling of stable isotope labeling data supports short blood neutrophil half-lives. Blood. 2016;127(26):3431-8.
77. Pillay J, den Braber I, Vrisekoop N, Kwast LM, de Boer RJ, Borghans JA, et al. In vivo labeling with 2H2O reveals a human neutrophil lifespan of 5.4 days. Blood. 2010;116(4):625-7.
78. Tofts PS, Chevassut T, Cutajar M, Dowell NG, Peters AM. Doubts concerning the recently reported human neutrophil lifespan of 5.4 days. Blood. 2011;117(22):6050-2; author reply 3-4.
79. Ballesteros I, Rubio-Ponce A, Genua M, Lusito E, Kwok I, Fernández-Calvo G, et al. Co-option of Neutrophil Fates by Tissue Environments. Cell. 2020;183(5):1282-97.e18.
80. Cupp MA, Cariolou M, Tzoulaki I, Aune D, Evangelou E, Berlanga-Taylor AJ. Neutrophil to lymphocyte ratio and cancer prognosis: an umbrella review of systematic reviews and meta-analyses of observational studies. BMC Med. 2020;18(1):360.
81. Starzer AM, Steindl A, Mair MJ, Deischinger C, Simonovska A, Widhalm G, et al. Systemic inflammation scores correlate with survival prognosis in patients with newly diagnosed brain metastases. Br J Cancer. 2021;124(7):1294-300.
82. Zhang L, Hu Y, Chen W, Tian Y, Xie Y, Chen J. Pre-stereotactic radiosurgery neutrophil-to-lymphocyte ratio is a predictor of the prognosis for brain metastases. Journal of neuro-oncology. 2020;147(3):691-700.
83. Chim ST, Sanfilippo P, O'Brien TJ, Drummond KJ, Monif M. Pretreatment neutrophil-to-lymphocyte/monocyte-to-lymphocyte ratio as prognostic biomarkers in glioma patients. J Neuroimmunol. 2021;361:577754.
84. Kowanetz M, Wu X, Lee J, Tan M, Hagenbeek T, Qu X, et al. Granulocyte-colony stimulating factor promotes lung metastasis through mobilization of Ly6G+Ly6C+ granulocytes. Proceedings of the National Academy of Sciences of the United States of America. 2010;107(50):21248-55.
85. Casbon AJ, Reynaud D, Park C, Khuc E, Gan DD, Schepers K, et al. Invasive breast cancer reprograms early myeloid differentiation in the bone marrow to generate immunosuppressive neutrophils. Proceedings of the National Academy of Sciences of the United States of America. 2015;112(6):E566-75.
86. Coffelt SB, Kersten K, Doornebal CW, Weiden J, Vrijland K, Hau CS, et al. IL-17-producing gammadelta T cells and neutrophils conspire to promote breast cancer metastasis. Nature. 2015;522(7556):345-8.

87. Kohanbash G, McKaveney K, Sakaki M, Ueda R, Mintz AH, Amankulor N, et al. GM-CSF promotes the immunosuppressive activity of glioma-infiltrating myeloid cells through interleukin-4 receptor-α. Cancer research. 2013;73(21):6413-23.
88. Bayne LJ, Beatty GL, Jhala N, Clark CE, Rhim AD, Stanger BZ, et al. Tumor-derived granulocyte-macrophage colony-stimulating factor regulates myeloid inflammation and T cell immunity in pancreatic cancer. Cancer Cell. 2012;21(6):822-35.
89. Quail D, Joyce J. Obesity alters the lung myeloid cell landscape to enhance breast cancer metastasis through IL5 and GM-CSF. Nature Cell Biologie. 2017.
90. Xiao Y, Cong M, Li J, He D, Wu Q, Tian P, et al. Cathepsin C promotes breast cancer lung metastasis by modulating neutrophil infiltration and neutrophil extracellular trap formation. Cancer Cell. 2021;39(3):423-37.e7.
91. SenGupta S, Subramanian BC, Parent CA. Getting TANned: How the tumor microenvironment drives neutrophil recruitment. J Leukoc Biol. 2019;105(3):449-62.
92. Finisguerra V, Di Conza G, Di Matteo M, Serneels J, Costa S, Thompson AA, et al. MET is required for the recruitment of anti-tumoural neutrophils. Nature. 2015;522(7556):349-53.
93. Zhang L, Yao J, Wei Y, Zhou Z, Li P, Qu J, et al. Blocking immunosuppressive neutrophils deters pY696-EZH2-driven brain metastases. Science translational medicine. 2020;12(545).
94. Fujii T, Rehman H, Chung SY, Shen J, Newman J, Wu V, et al. Treatment with Granulocyte-colony Stimulating Factor (G-CSF) is not associated with Increased Risk of Brain Metastasis in Patients with De Novo Stage IV Breast Cancer. J Cancer. 2021;12(18):5687-92.
95. Mollinedo F. Neutrophil Degranulation, Plasticity, and Cancer Metastasis. Trends Immunol. 2019;40(3):228-42.
96. Phillipson M, Kubes P. The Healing Power of Neutrophils. Trends Immunol. 2019;40(7):635-47.
97. Uhl B, Vadlau Y, Zuchtriegel G, Nekolla K, Sharaf K, Gaertner F, et al. Aged neutrophils contribute to the first line of defense in the acute inflammatory response. Blood. 2016;128(19):2327-37.
98. Houghton AM, Rzymkiewicz DM, Ji H, Gregory AD, Egea EE, Metz HE, et al. Neutrophil elastase-mediated degradation of IRS-1 accelerates lung tumor growth. Nat Med. 2010;16(2):219-23.
99. Spiegel A, Brooks MW, Houshyar S, Reinhardt F, Ardolino M, Fessler E, et al. Neutrophils Suppress Intraluminal NK Cell-Mediated Tumor Cell Clearance and Enhance Extravasation of Disseminated Carcinoma Cells. Cancer discovery. 2016;6(6):630-49.
100. Bausch D, Pausch T, Krauss T, Hopt UT, Fernandez-del-Castillo C, Warshaw AL, et al. Neutrophil granulocyte derived MMP-9 is a VEGF independent functional component of the angiogenic switch in pancreatic ductal adenocarcinoma. Angiogenesis. 2011;14(3):235.
101. Szczerba BM, Castro-Giner F, Vetter M, Krol I, Gkountela S, Landin J, et al. Neutrophils escort circulating tumour cells to enable cell cycle progression. Nature. 2019;566(7745):553-7.
102. Jorgensen I, Rayamajhi M, Miao EA. Programmed cell death as a defence against infection. Nature Reviews Immunology. 2017;17(3):151-64.

103. Park J, Wysocki RW, Amoozgar Z, Maiorino L, Fein MR, Jorns J, et al. Cancer cells induce metastasis-supporting neutrophil extracellular DNA traps. Science translational medicine. 2016;8(361):361ra138.
104. Rayes RF, Mouhanna JG, Nicolau I, Bourdeau F, Giannias B, Rousseau S, et al. Primary tumors induce neutrophil extracellular traps with targetable metastasis promoting effects. JCI Insight. 2019;5(16).
105. Inoue M, Nakashima R, Enomoto M, Koike Y, Zhao X, Yip K, et al. Plasma redox imbalance caused by albumin oxidation promotes lung-predominant NETosis and pulmonary cancer metastasis. Nature communications. 2018;9(1):5116.
106. Yang L, Liu Q, Zhang X, Liu X, Zhou B, Chen J, et al. DNA of neutrophil extracellular traps promotes cancer metastasis via CCDC25. Nature. 2020;583(7814):133-8.
107. Jiang ZZ, Peng ZP, Liu XC, Guo HF, Zhou MM, Jiang D, et al. Neutrophil extracellular traps induce tumor metastasis through dual effects on cancer and endothelial cells. Oncoimmunology. 2022;11(1):2052418.
108. Granot Z, Henke E, Comen EA, King TA, Norton L, Benezra R. Tumor entrained neutrophils inhibit seeding in the premetastatic lung. Cancer Cell. 2011;20(3):300-14.
109. Gershkovitz M, Caspi Y, Fainsod-Levi T, Katz B, Michaeli J, Khawaled S, et al. TRPM2 Mediates Neutrophil Killing of Disseminated Tumor Cells. Cancer research. 2018;78(10):2680-90.
110. Yee PP, Wei Y, Kim SY, Lu T, Chih SY, Lawson C, et al. Neutrophil-induced ferroptosis promotes tumor necrosis in glioblastoma progression. Nature communications. 2020;11(1):5424.
111. Cools-Lartigue J, Spicer J, McDonald B, Gowing S, Chow S, Giannias B, et al. Neutrophil extracellular traps sequester circulating tumor cells and promote metastasis. J Clin Invest. 2013;123(8):3446-58.
112. Demers M, Wong SL, Martinod K, Gallant M, Cabral JE, Wang Y, et al. Priming of neutrophils toward NETosis promotes tumor growth. Oncoimmunology. 2016;5(5):e1134073.
113. Albrengues J, Shields MA, Ng D, Park CG, Ambrico A, Poindexter ME, et al. Neutrophil extracellular traps produced during inflammation awaken dormant cancer cells in mice. Science (New York, NY). 2018;361(6409).
114. Takeshima T, Pop LM, Laine A, Iyengar P, Vitetta ES, Hannan R. Key role for neutrophils in radiation-induced antitumor immune responses: Potentiation with G-CSF. Proceedings of the National Academy of Sciences of the United States of America. 2016;113(40):11300-5.
115. Rice CM, Davies LC, Subleski JJ, Maio N, Gonzalez-Cotto M, Andrews C, et al. Tumour-elicited neutrophils engage mitochondrial metabolism to circumvent nutrient limitations and maintain immune suppression. Nature communications. 2018;9(1):5099.
116. Mensurado S, Rei M, Lança T, Ioannou M, Gonçalves-Sousa N, Kubo H, et al. Tumor-associated neutrophils suppress pro-tumoral IL-17+ γδ T cells through induction of oxidative stress. PLoS Biol. 2018;16(5):e2004990.
117. Schmielau J, Finn OJ. Activated granulocytes and granulocyte-derived hydrogen peroxide are the underlying mechanism of suppression of t-cell function in advanced cancer patients. Cancer research. 2001;61(12):4756-60.

118. Vonwirth V, Bülbül Y, Werner A, Echchannaoui H, Windschmitt J, Habermeier A, et al. Inhibition of Arginase 1 Liberates Potent T Cell Immunostimulatory Activity of Human Neutrophil Granulocytes. Front Immunol. 2020;11:617699.
119. Czystowska-Kuzmicz M, Sosnowska A, Nowis D, Ramji K, Szajnik M, Chlebowska-Tuz J, et al. Small extracellular vesicles containing arginase-1 suppress T-cell responses and promote tumor growth in ovarian carcinoma. Nature communications. 2019;10(1):3000.
120. Coffelt SB, Wellenstein MD, de Visser KE. Neutrophils in cancer: neutral no more. Nature reviews Cancer. 2016;16(7):431-46.
121. Garratt LW. Current Understanding of the Neutrophil Transcriptome in Health and Disease. Cells. 2021;10(9).
122. Zilionis R, Engblom C, Pfirschke C, Savova V, Zemmour D, Saatcioglu HD, et al. Single-Cell Transcriptomics of Human and Mouse Lung Cancers Reveals Conserved Myeloid Populations across Individuals and Species. Immunity. 2019;50(5):1317-34.e10.
123. Azizi E, Carr AJ, Plitas G, Cornish AE, Konopacki C, Prabhakaran S, et al. Single-Cell Map of Diverse Immune Phenotypes in the Breast Tumor Microenvironment. Cell. 2018;174(5):1293-308.e36.
124. Veglia F, Hashimoto A, Dweep H, Sanseviero E, De Leo A, Tcyganov E, et al. Analysis of classical neutrophils and polymorphonuclear myeloid-derived suppressor cells in cancer patients and tumor-bearing mice. J Exp Med. 2021;218(4).
125. Alvarez-Breckenridge C, Markson SC, Stocking JH, Nayyar N, Lastrapes M, Strickland MR, et al. Microenvironmental Landscape of Human Melanoma Brain Metastases in Response to Immune Checkpoint Inhibition. Cancer Immunol Res. 2022;10(8):996-1012.
126. Magod P, Mastandrea I, Rousso-Noori L, Agemy L, Shapira G, Shomron N, et al. Exploring the longitudinal glioma microenvironment landscape uncovers reprogrammed pro-tumorigenic neutrophils in the bone marrow. Cell Rep. 2021;36(5):109480.
127. Wang PF, Zhang YX, Su J, Yao K, Li SW, Huang GR, et al. Neutrophil depletion enhances the therapeutic effect of PD-1 antibody on glioma. Aging (Albany NY). 2020;12(15):15290-301.
128. Liu Y, Kosaka A, Ikeura M, Kohanbash G, Fellows-Mayle W, Snyder LA, et al. Premetastatic soil and prevention of breast cancer brain metastasis. Neuro-oncology. 2013;15(7):891-903.
129. Eruslanov EB, Singhal S, Albelda SM. Mouse versus Human Neutrophils in Cancer: A Major Knowledge Gap. Trends Cancer. 2017;3(2):149-60.
130. Jiguet-Jiglaire C, Boissonneau S, Denicolai E, Hein V, Lasseur R, Garcia J, et al. Plasmatic MMP9 released from tumor-infiltrating neutrophils is predictive for bevacizumab efficacy in glioblastoma patients: an AVAglio ancillary study. Acta Neuropathol Commun. 2022;10(1):1.
131. Liang J, Piao Y, Holmes L, Fuller GN, Henry V, Tiao N, et al. Neutrophils promote the malignant glioma phenotype through S100A4. Clin Cancer Res. 2014;20(1):187-98.
132. Thommen DS, Schumacher TN. T Cell Dysfunction in Cancer. Cancer Cell. 2018;33(4):547-62.
133. Ribas A, Wolchok JD. Cancer immunotherapy using checkpoint blockade. Science (New York, NY). 2018;359(6382):1350-5.

134. Dagogo-Jack I, Shaw AT. Tumour heterogeneity and resistance to cancer therapies. Nature reviews Clinical oncology. 2018;15(2):81-94.
135. Alexandrov LB, Nik-Zainal S, Wedge DC, Aparicio SAJR, Behjati S, Biankin AV, et al. Signatures of mutational processes in human cancer. Nature. 2013;500(7463):415-21.
136. Goldberg SB, Schalper KA, Gettinger SN, Mahajan A, Herbst RS, Chiang AC, et al. Pembrolizumab for management of patients with NSCLC and brain metastases: long-term results and biomarker analysis from a non-randomised, open-label, phase 2 trial. Lancet Oncol. 2020;21(5):655-63.
137. Mansfield AS, Herbst RS, de Castro G, Jr., Hui R, Peled N, Kim DW, et al. Outcomes With Pembrolizumab Monotherapy in Patients With Programmed Death-Ligand 1-Positive NSCLC With Brain Metastases: Pooled Analysis of KEYNOTE-001, 010, 024, and 042. JTO Clin Res Rep. 2021;2(8):100205.
138. Powell SF, Rodríguez-Abreu D, Langer CJ, Tafreshi A, Paz-Ares L, Kopp HG, et al. Outcomes With Pembrolizumab Plus Platinum-Based Chemotherapy for Patients With NSCLC and Stable Brain Metastases: Pooled Analysis of KEYNOTE-021, -189, and -407. J Thorac Oncol. 2021;16(11):1883-92.
139. Tawbi HA, Forsyth PA, Hodi FS, Algazi AP, Hamid O, Lao CD, et al. Long-term outcomes of patients with active melanoma brain metastases treated with combination nivolumab plus ipilimumab (CheckMate 204): final results of an open-label, multicentre, phase 2 study. Lancet Oncol. 2021;22(12):1692-704.
140. Long GV, Atkinson V, Lo S, Sandhu S, Guminski AD, Brown MP, et al. Combination nivolumab and ipilimumab or nivolumab alone in melanoma brain metastases: a multicentre randomised phase 2 study. Lancet Oncol. 2018;19(5):672-81.
141. Cloughesy TF, Mochizuki AY, Orpilla JR, Hugo W, Lee AH, Davidson TB, et al. Neoadjuvant anti-PD-1 immunotherapy promotes a survival benefit with intratumoral and systemic immune responses in recurrent glioblastoma. Nat Med. 2019;25(3):477-86.
142. Reardon DA, Brandes AA, Omuro A, Mulholland P, Lim M, Wick A, et al. Effect of Nivolumab vs Bevacizumab in Patients With Recurrent Glioblastoma: The CheckMate 143 Phase 3 Randomized Clinical Trial. JAMA Oncol. 2020;6(7):1003-10.
143. O'Rourke DM, Nasrallah MP, Desai A, Melenhorst JJ, Mansfield K, Morrissette JJD, et al. A single dose of peripherally infused EGFRvIII-directed CAR T cells mediates antigen loss and induces adaptive resistance in patients with recurrent glioblastoma. Science translational medicine. 2017;9(399).
144. Brown CE, Badie B, Barish ME, Weng L, Ostberg JR, Chang WC, et al. Bioactivity and Safety of IL13Rα2-Redirected Chimeric Antigen Receptor CD8+ T Cells in Patients with Recurrent Glioblastoma. Clin Cancer Res. 2015;21(18):4062-72.
145. Morse MA, Gwin WR, 3rd, Mitchell DA. Vaccine Therapies for Cancer: Then and Now. Target Oncol. 2021;16(2):121-52.
146. Liau LM, Ashkan K, Tran DD, Campian JL, Trusheim JE, Cobbs CS, et al. First results on survival from a large Phase 3 clinical trial of an autologous dendritic cell vaccine in newly diagnosed glioblastoma. J Transl Med. 2018;16(1):142.
147. Wen PY, Reardon DA, Armstrong TS, Phuphanich S, Aiken RD, Landolfi JC, et al. A Randomized Double-Blind Placebo-Controlled Phase II Trial of Dendritic Cell

Vaccine ICT-107 in Newly Diagnosed Patients with Glioblastoma. Clin Cancer Res. 2019;25(19):5799-807.
148. Weller M, Butowski N, Tran DD, Recht LD, Lim M, Hirte H, et al. Rindopepimut with temozolomide for patients with newly diagnosed, EGFRvIII-expressing glioblastoma (ACT IV): a randomised, double-blind, international phase 3 trial. Lancet Oncol. 2017;18(10):1373-85.
149. Platten M, Bunse L, Wick A, Bunse T, Le Cornet L, Harting I, et al. A vaccine targeting mutant IDH1 in newly diagnosed glioma. Nature. 2021;592(7854):463-8.
150. Keskin DB, Anandappa AJ, Sun J, Tirosh I, Mathewson ND, Li S, et al. Neoantigen vaccine generates intratumoral T cell responses in phase Ib glioblastoma trial. Nature. 2019;565(7738):234-9.
151. Bracci PM, Rice T, Hansen HM, Francis SS, Lee S, McCoy LS, et al. Pre-surgery immune profiles of adult glioma patients. Journal of neuro-oncology. 2022;159(1):103-15.
152. Coniglio SJ, Eugenin E, Dobrenis K, Stanley ER, West BL, Symons MH, et al. Microglial stimulation of glioblastoma invasion involves epidermal growth factor receptor (EGFR) and colony stimulating factor 1 receptor (CSF-1R) signaling. Mol Med. 2012;18(1):519-27.
153. Lin C-C, Gil-Martin M, Bauer TM, Naing A, Lim DW-T, Sarantopoulos J, et al. Abstract CT171: Phase I study of BLZ945 alone and with spartalizumab (PDR001) in patients (pts) with advanced solid tumors. Cancer research. 2020;80(16_Supplement):CT171-CT.
154. Butowski N, Colman H, De Groot JF, Omuro AM, Nayak L, Wen PY, et al. Orally administered colony stimulating factor 1 receptor inhibitor PLX3397 in recurrent glioblastoma: an Ivy Foundation Early Phase Clinical Trials Consortium phase II study. Neuro-oncology. 2016;18(4):557-64.
155. von Roemeling CA, Wang Y, Qie Y, Yuan H, Zhao H, Liu X, et al. Therapeutic modulation of phagocytosis in glioblastoma can activate both innate and adaptive antitumour immunity. Nature communications. 2020;11(1):1508.
156. Zhang Y, Guoqiang L, Sun M, Lu X. Targeting and exploitation of tumor-associated neutrophils to enhance immunotherapy and drug delivery for cancer treatment. Cancer Biol Med. 2020;17(1):32-43.
157. Boivin G, Faget J, Ancey P-B, Gkasti A, Mussard J, Engblom C, et al. Durable and controlled depletion of neutrophils in mice. Nature communications. 2020;11(1):2762.
158. Emblem KE, Mouridsen K, Bjornerud A, Farrar CT, Jennings D, Borra RJ, et al. Vessel architectural imaging identifies cancer patient responders to anti-angiogenic therapy. Nat Med. 2013;19(9):1178-83.
159. Kickingereder P, Brugnara G, Hansen MB, Nowosielski M, Pflüger I, Schell M, et al. Noninvasive Characterization of Tumor Angiogenesis and Oxygenation in Bevacizumab-treated Recurrent Glioblastoma by Using Dynamic Susceptibility MRI: Secondary Analysis of the European Organization for Research and Treatment of Cancer 26101 Trial. Radiology. 2020;297(1):164-75.
160. Chinot OL, Wick W, Mason W, Henriksson R, Saran F, Nishikawa R, et al. Bevacizumab plus radiotherapy-temozolomide for newly diagnosed glioblastoma. N Engl J Med. 2014;370(8):709-22.

161. Gilbert MR, Dignam JJ, Armstrong TS, Wefel JS, Blumenthal DT, Vogelbaum MA, et al. A randomized trial of bevacizumab for newly diagnosed glioblastoma. N Engl J Med. 2014;370(8):699-708.
162. Maas RR, Soukup K, Klemm F, Kornete M, Bowman RL, Bedel R, et al. An integrated pipeline for comprehensive analysis of immune cells in human brain tumor clinical samples. Nat Protoc. 2021;16(10):4692-721.
163. Mohile NA, Messersmith H, Gatson NT, Hottinger AF, Lassman A, Morton J, et al. Therapy for Diffuse Astrocytic and Oligodendroglial Tumors in Adults: ASCO-SNO Guideline. J Clin Oncol. 2022;40(4):403-26.
164. Sperduto PW, Mesko S, Li J, Cagney D, Aizer A, Lin NU, et al. Survival in Patients With Brain Metastases: Summary Report on the Updated Diagnosis-Specific Graded Prognostic Assessment and Definition of the Eligibility Quotient. J Clin Oncol. 2020;38(32):3773-84.
165. Desbaillets N, Hottinger AF. Immunotherapy in Glioblastoma: A Clinical Perspective. Cancers (Basel). 2021;13(15).
166. Sampson JH, Gunn MD, Fecci PE, Ashley DM. Brain immunology and immunotherapy in brain tumours. Nature reviews Cancer. 2020;20(1):12-25.
167. Quail DF, Olson OC, Bhardwaj P, Walsh LA, Akkari L, Quick ML, et al. Obesity alters the lung myeloid cell landscape to enhance breast cancer metastasis through IL5 and GM-CSF. Nature cell biology. 2017;19(8):974-87.
168. Andersen BM, Faust Akl C, Wheeler MA, Chiocca EA, Reardon DA, Quintana FJ. Glial and myeloid heterogeneity in the brain tumour microenvironment. Nature reviews Cancer. 2021;21(12):786-802.
169. Hedrick CC, Malanchi I. Neutrophils in cancer: heterogeneous and multifaceted. Nat Rev Immunol. 2022;22(3):173-87.
170. Shaul ME, Fridlender ZG. Tumour-associated neutrophils in patients with cancer. Nature reviews Clinical oncology. 2019;16(10):601-20.
171. Wellenstein MD, Coffelt SB, Duits DEM, van Miltenburg MH, Slagter M, de Rink I, et al. Loss of p53 triggers WNT-dependent systemic inflammation to drive breast cancer metastasis. Nature. 2019;572(7770):538-42.
172. Peng Z, Liu C, Victor AR, Cao DY, Veiras LC, Bernstein EA, et al. Tumors exploit CXCR4(hi)CD62L(lo) aged neutrophils to facilitate metastatic spread. Oncoimmunology. 2021;10(1):1870811.
173. Glodde N, Bald T, van den Boorn-Konijnenberg D, Nakamura K, O'Donnell JS, Szczepanski S, et al. Reactive Neutrophil Responses Dependent on the Receptor Tyrosine Kinase c-MET Limit Cancer Immunotherapy. Immunity. 2017;47(4):789-802.e9.
174. Bodac A, Meylan E. Neutrophil metabolism in the cancer context. Semin Immunol. 2021:101583.
175. Garcia-Navas R, Gajate C, Mollinedo F. Neutrophils drive endoplasmic reticulum stress-mediated apoptosis in cancer cells through arginase-1 release. Scientific reports. 2021;11(1):12574.
176. Wang JF, Wang YP, Xie J, Zhao ZZ, Gupta S, Guo Y, et al. Upregulated PD-L1 delays human neutrophil apoptosis and promotes lung injury in an experimental mouse model of sepsis. Blood. 2021;138(9):806-10.
177. Summers C, Rankin SM, Condliffe AM, Singh N, Peters AM, Chilvers ER. Neutrophil kinetics in health and disease. Trends Immunol. 2010;31(8):318-24.

178. Brostjan C, Oehler R. The role of neutrophil death in chronic inflammation and cancer. Cell Death Discov. 2020;6:26.
179. Casanova-Acebes M, Pitaval C, Weiss LA, Nombela-Arrieta C, Chevre R, N AG, et al. Rhythmic modulation of the hematopoietic niche through neutrophil clearance. Cell. 2013;153(5):1025-35.
180. Comen E, Wojnarowicz P, Seshan VE, Shah R, Coker C, Norton L, et al. TNF is a key cytokine mediating neutrophil cytotoxic activity in breast cancer patients. NPJ Breast Cancer. 2016;2:16009.
181. Vieira SM, Lemos HP, Grespan R, Napimoga MH, Dal-Secco D, Freitas A, et al. A crucial role for TNF-alpha in mediating neutrophil influx induced by endogenously generated or exogenous chemokines, KC/CXCL1 and LIX/CXCL5. Br J Pharmacol. 2009;158(3):779-89.
182. Chapman AL, Mocatta TJ, Shiva S, Seidel A, Chen B, Khalilova I, et al. Ceruloplasmin is an endogenous inhibitor of myeloperoxidase. J Biol Chem. 2013;288(9):6465-77.
183. Golenkina EA, Viryasova GM, Galkina SI, Gaponova TV, Sud'ina GF, Sokolov AV. Fine Regulation of Neutrophil Oxidative Status and Apoptosis by Ceruloplasmin and Its Derivatives. Cells. 2018;7(1).
184. Xue M, Rabbani N, Momiji H, Imbasi P, Anwar MM, Kitteringham N, et al. Transcriptional control of glyoxalase 1 by Nrf2 provides a stress-responsive defence against dicarbonyl glycation. Biochem J. 2012;443(1):213-22.
185. Chowdhury K, Kumar U, Das S, Chaudhuri J, Kumar P, Kanjilal M, et al. Synovial IL-9 facilitates neutrophil survival, function and differentiation of Th17 cells in rheumatoid arthritis. Arthritis Res Ther. 2018;20(1):18.
186. Winkler F, Kozin SV, Tong RT, Chae SS, Booth MF, Garkavtsev I, et al. Kinetics of vascular normalization by VEGFR2 blockade governs brain tumor response to radiation: role of oxygenation, angiopoietin-1, and matrix metalloproteinases. Cancer Cell. 2004;6(6):553-63.
187. Izumi Y, Xu L, di Tomaso E, Fukumura D, Jain RK. Tumour biology: herceptin acts as an anti-angiogenic cocktail. Nature. 2002;416(6878):279-80.
188. De Palma M, Biziato D, Petrova TV. Microenvironmental regulation of tumour angiogenesis. Nature reviews Cancer. 2017;17(8):457-74.
189. Hao Q, Chen Y, Zhu Y, Fan Y, Palmer D, Su H, et al. Neutrophil depletion decreases VEGF-induced focal angiogenesis in the mature mouse brain. J Cereb Blood Flow Metab. 2007;27(11):1853-60.
190. Ajikumar A, Long MB, Heath PR, Wharton SB, Ince PG, Ridger VC, et al. Neutrophil-Derived Microvesicle Induced Dysfunction of Brain Microvascular Endothelial Cells In Vitro. Int J Mol Sci. 2019;20(20).
191. Qiu YM, Zhang CL, Chen AQ, Wang HL, Zhou YF, Li YN, et al. Immune Cells in the BBB Disruption After Acute Ischemic Stroke: Targets for Immune Therapy? Front Immunol. 2021;12:678744.
192. Wang S, Song R, Wang Z, Jing Z, Wang S, Ma J. S100A8/A9 in Inflammation. Front Immunol. 2018;9:1298.
193. Quintero-Fabian S, Arreola R, Becerril-Villanueva E, Torres-Romero JC, Arana-Argaez V, Lara-Riegos J, et al. Role of Matrix Metalloproteinases in Angiogenesis and Cancer. Front Oncol. 2019;9:1370.
194. Gonzalez H, Mei W, Robles I, Hagerling C, Allen BM, Hauge Okholm TL, et al. Cellular architecture of human brain metastases. Cell. 2022;185(4):729-45.e20.

195. Sudmeier LJ, Hoang KB, Nduom EK, Wieland A, Neill SG, Schniederjan MJ, et al. Distinct phenotypic states and spatial distribution of CD8(+) T cell clonotypes in human brain metastases. Cell Rep Med. 2022;3(5):100620.
196. Ozawa T, Riester M, Cheng YK, Huse JT, Squatrito M, Helmy K, et al. Most human non-GCIMP glioblastoma subtypes evolve from a common proneural-like precursor glioma. Cancer Cell. 2014;26(2):288-300.
197. Becher OJ, Hambardzumyan D, Fomchenko EI, Momota H, Mainwaring L, Bleau AM, et al. Gli activity correlates with tumor grade in platelet-derived growth factor-induced gliomas. Cancer research. 2008;68(7):2241-9.
198. Holland EC, Hively WP, DePinho RA, Varmus HE. A constitutively active epidermal growth factor receptor cooperates with disruption of G1 cell-cycle arrest pathways to induce glioma-like lesions in mice. Genes Dev. 1998;12(23):3675-85.
199. Gut G, Herrmann MD, Pelkmans L. Multiplexed protein maps link subcellular organization to cellular states. Science (New York, NY). 2018;361(6401).
200. Sternberg SR. Biomedical Image-Processing. Computer. 1983;16(1):22-34.
201. Bankhead P, Loughrey MB, Fernandez JA, Dombrowski Y, McArt DG, Dunne PD, et al. QuPath: Open source software for digital pathology image analysis. Scientific reports. 2017;7(1):16878.
202. Schmidt U, Weigert M, Broaddus C, Myers G, editors. Cell Detection with Star-Convex Polygons2018; Cham: Springer International Publishing.
203. Stoltzfus CR, Filipek J, Gern BH, Olin BE, Leal JM, Wu Y, et al. CytoMAP: A Spatial Analysis Toolbox Reveals Features of Myeloid Cell Organization in Lymphoid Tissues. Cell Rep. 2020;31(3):107523.
204. Baddeley A, Turner R. spatstat: An R package for analyzing spatial point patterns. J Stat Softw. 2005;12(6):1-42.
205. Dobin A, Davis CA, Schlesinger F, Drenkow J, Zaleski C, Jha S, et al. STAR: ultrafast universal RNA-seq aligner. Bioinformatics. 2013;29(1):15-21.
206. Li B, Dewey CN. RSEM: accurate transcript quantification from RNA-Seq data with or without a reference genome. BMC Bioinformatics. 2011;12:323.
207. Hambardzumyan D, Amankulor NM, Helmy KY, Becher OJ, Holland EC. Modeling Adult Gliomas Using RCAS/t-va Technology. Transl Oncol. 2009;2(2):89-95.
208. Gritsenko PG, Atlasy N, Dieteren CEJ, Navis AC, Venhuizen JH, Veelken C, et al. p120-catenin-dependent collective brain infiltration by glioma cell networks. Nature cell biology. 2020;22(1):97-107.
209. Swartzlander DB, Propson NE, Roy ER, Saito T, Saido T, Wang B, et al. Concurrent cell type-specific isolation and profiling of mouse brains in inflammation and Alzheimer's disease. JCI Insight. 2018;3(13).
210. Ravi VM, Will P, Kueckelhaus J, Sun N, Joseph K, Salié H, et al. Spatially resolved multi-omics deciphers bidirectional tumor-host interdependence in glioblastoma. Cancer Cell. 2022;40(6):639-55.e13.
211. Ratz M, von Berlin L, Larsson L, Martin M, Westholm JO, La Manno G, et al. Clonal relations in the mouse brain revealed by single-cell and spatial transcriptomics. Nature Neuroscience. 2022;25(3):285-94.
212. Shilts J, Severin Y, Galaway F, Müller-Sienerth N, Chong Z-S, Pritchard S, et al. A physical wiring diagram for the human immune system. Nature. 2022;608(7922):397-404.

213. Jacob F, Salinas RD, Zhang DY, Nguyen PTT, Schnoll JG, Wong SZH, et al. A Patient-Derived Glioblastoma Organoid Model and Biobank Recapitulates Inter- and Intra-tumoral Heterogeneity. Cell. 2020;180(1):188-204.e22.
214. Mansour AA, Gonçalves JT, Bloyd CW, Li H, Fernandes S, Quang D, et al. An in vivo model of functional and vascularized human brain organoids. Nat Biotechnol. 2018;36(5):432-41.
215. Muntjewerff EM, Meesters LD, van den Bogaart G. Antigen Cross-Presentation by Macrophages. Front Immunol. 2020;11:1276.
216. Kumar V, Donthireddy L, Marvel D, Condamine T, Wang F, Lavilla-Alonso S, et al. Cancer-Associated Fibroblasts Neutralize the Anti-tumor Effect of CSF1 Receptor Blockade by Inducing PMN-MDSC Infiltration of Tumors. Cancer Cell. 2017;32(5):654-68.e5.
217. Nywening TM, Belt BA, Cullinan DR, Panni RZ, Han BJ, Sanford DE, et al. Targeting both tumour-associated CXCR2(+) neutrophils and CCR2(+) macrophages disrupts myeloid recruitment and improves chemotherapeutic responses in pancreatic ductal adenocarcinoma. Gut. 2018;67(6):1112-23.
218. Pahler JC, Tazzyman S, Erez N, Chen YY, Murdoch C, Nozawa H, et al. Plasticity in tumor-promoting inflammation: impairment of macrophage recruitment evokes a compensatory neutrophil response. Neoplasia. 2008;10(4):329-40.
219. Jung K, Heishi T, Khan OF, Kowalski PS, Incio J, Rahbari NN, et al. Ly6Clo monocytes drive immunosuppression and confer resistance to anti-VEGFR2 cancer therapy. J Clin Invest. 2017;127(8):3039-51.
220. Peng ZP, Jiang ZZ, Guo HF, Zhou MM, Huang YF, Ning WR, et al. Glycolytic activation of monocytes regulates the accumulation and function of neutrophils in human hepatocellular carcinoma. J Hepatol. 2020;73(4):906-17.
221. De Filippo K, Dudeck A, Hasenberg M, Nye E, van Rooijen N, Hartmann K, et al. Mast cell and macrophage chemokines CXCL1/CXCL2 control the early stage of neutrophil recruitment during tissue inflammation. Blood. 2013;121(24):4930-7.
222. Liang X, Gupta K, Quintero JR, Cernadas M, Kobzik L, Christou H, et al. Macrophage FABP4 is required for neutrophil recruitment and bacterial clearance in Pseudomonas aeruginosa pneumonia. Faseb j. 2019;33(3):3562-74.
223. Bijnen M, Josefs T, Cuijpers I, Maalsen CJ, van de Gaar J, Vroomen M, et al. Adipose tissue macrophages induce hepatic neutrophil recruitment and macrophage accumulation in mice. Gut. 2018;67(7):1317-27.
224. Wieland E, Rodriguez-Vita J, Liebler SS, Mogler C, Moll I, Herberich SE, et al. Endothelial Notch1 Activity Facilitates Metastasis. Cancer Cell. 2017;31(3):355-67.
225. Wu F, Zhao Y, Jiao T, Shi D, Zhu X, Zhang M, et al. CXCR2 is essential for cerebral endothelial activation and leukocyte recruitment during neuroinflammation. J Neuroinflammation. 2015;12:98.
226. Wu F, Zou Q, Ding X, Shi D, Zhu X, Hu W, et al. Complement component C3a plays a critical role in endothelial activation and leukocyte recruitment into the brain. J Neuroinflammation. 2016;13:23.
227. Grieshaber-Bouyer R, Radtke FA, Cunin P, Stifano G, Levescot A, Vijaykumar B, et al. The neutrotime transcriptional signature defines a single continuum of neutrophils across biological compartments. Nature communications. 2021;12(1):2856.

228. Engblom C, Pfirschke C, Zilionis R, Da Silva Martins J, Bos SA, Courties G, et al. Osteoblasts remotely supply lung tumors with cancer-promoting SiglecF(high) neutrophils. Science (New York, NY). 2017;358(6367).
229. Pfirschke C, Engblom C, Gungabeesoon J, Lin Y, Rickelt S, Zilionis R, et al. Tumor-Promoting Ly-6G(+) SiglecF(high) Cells Are Mature and Long-Lived Neutrophils. Cell Rep. 2020;32(12):108164.
230. Zhong J, Li Q, Luo H, Holmdahl R. Neutrophil-derived reactive oxygen species promote tumor colonization. Communications Biology. 2021;4(1):865.
231. Bagaitkar J, Matute JD, Austin A, Arias AA, Dinauer MC. Activation of neutrophil respiratory burst by fungal particles requires phosphatidylinositol 3-phosphate binding to p40phox in humans but not in mice. Blood. 2012;120(16):3385-7.
232. Weinberg F, Ramnath N, Nagrath D. Reactive Oxygen Species in the Tumor Microenvironment: An Overview. Cancers (Basel). 2019;11(8).
233. Cheng Y, Li H, Deng Y, Tai Y, Zeng K, Zhang Y, et al. Cancer-associated fibroblasts induce PDL1+ neutrophils through the IL6-STAT3 pathway that foster immune suppression in hepatocellular carcinoma. Cell Death Dis. 2018;9(4):422.
234. Deng H, Kan A, Lyu N, He M, Huang X, Qiao S, et al. Tumor-derived lactate inhibit the efficacy of lenvatinib through regulating PD-L1 expression on neutrophil in hepatocellular carcinoma. J Immunother Cancer. 2021;9(6).
235. Kaltenmeier C, Yazdani HO, Morder K, Geller DA, Simmons RL, Tohme S. Neutrophil Extracellular Traps Promote T Cell Exhaustion in the Tumor Microenvironment. Front Immunol. 2021;12:785222.
236. Sippel TR, White J, Nag K, Tsvankin V, Klaassen M, Kleinschmidt-DeMasters BK, et al. Neutrophil degranulation and immunosuppression in patients with GBM: restoration of cellular immune function by targeting arginase I. Clin Cancer Res. 2011;17(22):6992-7002.
237. Szefel J, Ślebioda T, Walczak J, Kruszewski WJ, Szajewski M, Ciesielski M, et al. The effect of l-arginine supplementation and surgical trauma on the frequency of myeloid-derived suppressor cells and T lymphocytes in tumour and blood of colorectal cancer patients. Adv Med Sci. 2022;67(1):66-78.
238. Heys SD, Ogston K, Miller I, Hutcheon AW, Walker LG, Sarker TK, et al. Potentiation of the response to chemotherapy in patients with breast cancer by dietary supplementation with L-arginine: results of a randomised controlled trial. Int J Oncol. 1998;12(1):221-5.
239. Satoh Y, Kotani H, Iida Y, Taniura T, Notsu Y, Harada M. Supplementation of l-arginine boosts the therapeutic efficacy of anticancer chemoimmunotherapy. Cancer Sci. 2020;111(7):2248-58.
240. Schiffmann LM, Fritsch M, Gebauer F, Günther SD, Stair NR, Seeger JM, et al. Tumour-infiltrating neutrophils counteract anti-VEGF therapy in metastatic colorectal cancer. Br J Cancer. 2019;120(1):69-78.
241. Itatani Y, Yamamoto T, Zhong C, Molinolo AA, Ruppel J, Hegde P, et al. Suppressing neutrophil-dependent angiogenesis abrogates resistance to anti-VEGF antibody in a genetic model of colorectal cancer. Proceedings of the National Academy of Sciences of the United States of America. 2020;117(35):21598-608.
242. Bui TM, Wiesolek HL, Sumagin R. ICAM-1: A master regulator of cellular responses in inflammation, injury resolution, and tumorigenesis. J Leukoc Biol. 2020;108(3):787-99.

243. Lentz SR, Sadler JE. Inhibition of thrombomodulin surface expression and protein C activation by the thrombogenic agent homocysteine. J Clin Invest. 1991;88(6):1906-14.
244. Wei P, Wang K, Luo C, Huang Y, Misilimu D, Wen H, et al. Cordycepin confers long-term neuroprotection via inhibiting neutrophil infiltration and neuroinflammation after traumatic brain injury. J Neuroinflammation. 2021;18(1):137.
245. Shan ZG, Chen J, Liu JS, Zhang JY, Wang TT, Teng YS, et al. Activated neutrophils polarize protumorigenic interleukin-17A-producing T helper subsets through TNF-α-B7-H2-dependent pathway in human gastric cancer. Clin Transl Med. 2021;11(6):e484.
246. Wisdom AJ, Hong CS, Lin AJ, Xiang Y, Cooper DE, Zhang J, et al. Neutrophils promote tumor resistance to radiation therapy. Proceedings of the National Academy of Sciences of the United States of America. 2019;116(37):18584-9.
247. Ruffell B, Coussens LM. Macrophages and therapeutic resistance in cancer. Cancer Cell. 2015;27(4):462-72.
248. Bruhn KW, Dekitani K, Nielsen TB, Pantapalangkoor P, Spellberg B. Ly6G-mediated depletion of neutrophils is dependent on macrophages. Results Immunol. 2016;6:5-7.